UNIVERSITÀ
DEGLI STUDI
DI PADOVA

Sede Amministrativa: Università degli Studi di Padova

Dipartimento di Territorio e Sistemi Agro Forestali (T.e.S.A.F.)

SCUOLA DI DOTTORATO DI RICERCA IN: TERRITORIO AMBIENTE RISORSE E SALUTE (T.A.R.S.)
INDIRIZZO: TECNOLOGIE MECCANICHE DEI PROCESSI AGRICOLI E FORESTALI

CICLO XXVI

SOIL-TYRE INTERACTION ANALYSIS FOR AGRICULTURAL TRACTORS: MODELLING OF TRACTION PERFORMANCE AND SOIL DAMAGE

Direttore della Scuola : Ch.mo Prof. Mario Aristide Lenzi
Coordinatore d'indirizzo : Ch.mo Prof. Luigi Sartori
Supervisore : Ch.mo Prof. Luigi Sartori
Correlatore : Dr. Etienne Diserens

Dottorando : Andrea Battiato

Index

Abstract

Tillage operations in farming often require high traction forces applied by tractor wheels. These interact with topsoil via a stress system along the contact surface, this interaction resulting in soil and tyre deformation. Topsoil is subject to normal and tangential stresses at the contact surface. The tangential stress rises sharply with increasing traction force and may cause topsoil among tyre lugs to fail, with the consequent formation of a strengthless layer strongly exposed to erosion and an underlying layer where shear deformations contribute to the alteration of soil structure functionalities.

This work aimed to investigate mechanical conditions along the soil-tyre contact surface which lead to topsoil damage. These conditions are analysed in the light of simulations with a soil-tyre interaction model and discussed on the basis of results of specific experimental tests. A semi-empirical model of interaction between the soil and a pneumatic wheel was adapted to simulate the traction performance of mechanical front-wheel drive MFWD vehicles, taking into account the load transfer effect, the multi-pass effect, and the theoretical speed ratio between the front and the rear axles. This model was employed to simulate (i) the traction performance of tractors in terms of drawbar pull, motion resistance due to soil compaction, traction coefficient and traction efficiency as a function of slip, wheel load and tyre inflation pressure; (ii) soil stress paths along the contact surface with tyres; and (iii) the risk of soil failure corresponding to a defined slip level. Several traction tests were performed on four agricultural soils of different texture (clay, clay loam, silty loam, and loamy sand). Four tractors of wide ranging power (40.4 kW, 65 kW, 110 kW, and 123 kW) and weight (25.3 kN, 40 kN, 66.7 kN, and 68 kN) were used. Tractor configurations were varied by changing tyre inflation pressure and tractor weight, and by using dual tyres. Slip normally ranged between 0% and 35%, only in some cases higher values, up to 58%, were reached. The shearing effect on the topsoil due to slip of tractor tyres was investigated on the silty loam agricultural field by measuring longitudinal topsoil displacements along the driving corridors during traction tests. A system of strips orthogonal to the tractor track was spray-painted on the soil surface to enable easy visualisation of the topsoil displacements.

The changes in soil hydraulic properties owing to deformation caused by the passage of the 40 kN tractor, both in a self-propelled condition without wheel slip, and with high drawbar pull (21.8 kN) and high wheel slip (27%), were compared in the clay loam agricultural field. The mechanical properties of the topsoil were determined in situ on the basis of vertical plate-penetration tests and horizontal plate-shear deformation tests with a tractor-mounted bevameter. Soil stress-strain conditions at contact with a traction tyre were reproduced in the laboratory by means of a direct simple shear box. A Geonor shear box was modified in order to carry out hydraulic conductivity measurements in saturated conditions while shearing the soil sample.

Simulations with the soil-tractor interaction model matched measured traction performance with general good agreement (overall mean error of 12% and overall mean residual of 3.30 kN). As soon as the soil failure condition, as simulated by the model, was approached along the soil-tyre contact surface, longitudinal topsoil displacements measured in the silty loam agricultural field clearly increased. The slip values at which soil failure was reached were identified for three configurations of the 40 kN tractor. These slip values should be regarded as indicative limits not to be exceeded in tillage operations in order to avoid topsoil damage in the conditions under consideration.

The stress state at the soil-tyre contact surface increased significantly, mostly in terms of shear stress, when the tractor moved with slip rather than without slip. As a consequence, the severity of tractor-traffic-induced

soil degradation increased appreciably. The change in soil structure and hydraulic properties measured in the clay loam agricultural field was more pronounced in the first 0.15 m where the total porosity decreases by 11% without slip and 29% with slip, with a reduction in macropores of about 60% and 100%, respectively. The saturated hydraulic conductivity of the shallow topsoil (0 - 0.04 m) turned out to be reduced by about 66% without slip and about 98% with 27% slip.

The results of the simple shear tests confirmed that shear deformations may contribute to damage topsoil structure functionalities, decreasing, in most cases, hydraulic conductivity. However, in the samples of clay, clay loam and silty loam, the major decrease in hydraulic conductivity was caused by the deformation during compression. Moreover, it emerged that the effects of shearing on the saturated hydraulic conductivity are mainly controlled by the volumetric strain coupled to the shear strain, and the variation in voids volume of the pore system affects the hydraulic conductivity more than a pure distortional deformation which may alter the water pathways in the sample.

The validated approach for modelling tractor traction performance and predicting topsoil damage from the shearing effect due to tyre slip was used as a framework for developing a new Excel module for the third edition of the TASC V3.0.xlsm software: www.agrartechnik-agroscope.ch. This module also provides the power-wheel slip relationship. Four practical tests were set up for the user to enable a fast, simple and reliable mechanical characterisation of topsoil behaviour. Different tractor configurations, soil textures and conditions can be confronted. The limit beyond which topsoil damage is expected to occur is reported in terms of net traction and wheel slip. TASC V3.0 offers a valuable support tool for identifying tractor configurations and soil conditions which optimise traction, resulting in increased fuel saving, reduced tyre wear and limited topsoil damage.

Riassunto

Le lavorazioni dei terreni agricoli in molti casi richiedono elevate forze di trazione sviluppate dalle ruote dei trattori. Uno pneumatico da trazione interagisce con il terreno attraverso un sistema di tensioni lungo la superficie di contatto tra lo pneumatico e il terreno, tale interazione genera deformazioni sia nel terreno che nello pneumatico. Il terreno viene assoggettato a tensioni normali e tangenziali alla superficie di contatto con lo pneumatico. Le tensioni tangenziali aumentano repentinamente all'aumentare della forza di trazione e possono portare il terreno compresso tra le costolature del battistrada dello pneumatico in condizioni di rottura (effetto di taglio del terreno). Ciò determina la formazione di uno strato superficiale di terreno privo di resistenza meccanica e, quindi, fortemente esposto ai fenomeni erosivi, e uno strato sottostante in cui l'effetto delle deformazioni di taglio contribuisce ad alterare le funzionalità della struttura del terreno.

Obiettivo di questo lavoro è l'indagine delle condizioni meccaniche all'interfaccia di contatto tra il terreno e lo pneumatico che generano suddetto danneggiamento del terreno. Tali condizioni meccaniche sono state analizzate e discusse sulla base di simulazioni con un modello di interazione terreno-pneumatico e secondo i risultati di specifiche prove sperimentali. Un modello semiempirico di interazione tra il terreno e una ruota pneumatica è stato adattato per simulare le prestazioni di trazione di trattori MFWD, considerando l'effetto di trasferimento del carico sulla ruota, l'effetto del passaggio multiplo sul terreno e il rapporto delle velocità teoriche tra gli assi anteriore e posteriore. Il modello è stato utilizzato per simulare (i) le prestazioni di trazione di trattori MFWD in termini di trazione netta, resistenza al movimento dovuta al compattamento del terreno, coefficiente di trazione ed efficienza di trazione, in funzione dello slittamento degli pneumatici, del carico sulla ruota e della pressione di gonfiaggio degli pneumatici; (ii) i percorsi di tensione del terreno lungo la superficie di contatto con lo pneumatico e (iii) il rischio di raggiungimento delle condizioni di rottura del terreno in corrispondenza di un definito slittamento. Numerose prove di trazione sono state eseguite su quattro terreni agricoli di differente tessitura (terreno argilloso, franco argilloso, franco limoso e sabbioso franco), utilizzando quattro trattori aventi potenza di 40.4 kW, 65 kW, 110 kW e 123 kW e peso di 25.3 kN, 40 kN, 66.7 kN e 68 kN. La configurazione dei trattori è stata variata modificando la pressione di gonfiaggio degli pneumatici, il peso del trattore e utilizzando doppi pneumatici. Lo slittamento è stato controllato in un intervallo di valori generalmente compresi tra 0% e 35%, in alcuni casi sono stati raggiunti valori più elevati fino a un massimo del 58%. L'effetto di taglio del terreno, dovuto allo slittamento degli pneumatici da trazione, è stato studiato sul terreno agricolo franco limoso attraverso la misura degli spostamenti longitudinali del terreno lungo i corridoi di esecuzione delle prove di trazione. Un sistema di strisce ortogonali al corridoio di avanzamento del trattore è stato tracciato con una vernice spray sulla superficie del suolo, al fine di visualizzare in modo semplice gli spostamenti del terreno.

Le alterazioni delle proprietà idrauliche del terreno causate dalle deformazioni indotte dal passaggio del trattore di 40 kN sono state confrontate in un terreno franco argilloso in assenza di slittamento e con elevato slittamento (27%) e forza di trazione netta (21.8 kN). Le proprietà meccaniche del terreno sono state determinate in situ sulla base di prove di compressione verticale e prove di deformazione di taglio in direzione orizzontale eseguite con un bevameter installato su di un trattore. Le condizioni di tensione e deformazione del terreno al contatto con lo pneumatico sono state riprodotte in laboratorio per mezzo di una scatola di taglio semplice diretto della Geonor. Essa è stata modificata al fine di eseguire delle misure di conducibilità idraulica in condizioni di saturazione durante la fase di taglio del provino di terreno.

Le simulazioni con il modello di interazione terreno-trattore hanno riprodotto le misure delle prestazioni di trazione con elevata fedeltà (errore medio del 12% e scarto medio di 3.3 kN). Quando la condizione di rottura del terreno (simulata dal modello) è stata raggiunta lungo la superficie di contatto terreno-pneumatico, gli spostamenti longitudinali misurati sulla superficie del terreno franco limoso sono aumentati in maniera evidente. I valori di slittamento corrispondenti al raggiungimento della condizione di rottura del terreno sono stati definiti per tre configurazioni del trattore di 40 kN. Tali valori, che possono essere considerati come limiti indicativi nelle condizioni analizzate, non dovrebbero essere superati nelle operazioni di lavorazione del terreno, al fine di evitarne il danneggiamento.

Lo stato di stress al contatto terreno-pneumatico è aumentato significativamente in presenza di slittamento, principalmente in termini di tensioni di taglio, con un conseguente aumento apprezzabile del danneggiamento del terreno indotto dal traffico del trattore. Le alterazioni della struttura e delle proprietà idrauliche misurate nel terreno franco argilloso sono risultate più evidenti nei primi 0.15 m di profondità dove è stata misurata una riduzione di porosità totale dell'11% in assenza di slittamento e del 29% in presenza di slittamento, con una corrispondente diminuzione della macroporosità rispettivamente del 60% e del 100%. Le deformazioni indotte dalle ruote del trattore hanno ridotto la conducibilità idraulica in condizioni di saturazione dello strato più superficiale di terreno (0 - 0.04 m) di circa il 66% in assenza di slittamento e di circa il 98% in presenza di uno slittamento del 27%.

I risultati delle prove eseguite con la scatola di taglio semplice hanno confermato che le deformazioni di taglio possono contribuire al danneggiamento delle funzionalità della struttura del terreno, riducendo, in molti casi, la conducibilità idraulica. Tuttavia, nei terreni argilloso, franco argilloso e franco limoso la riduzione complessiva di conducibilità idraulica è stata quasi esclusivamente causata dal processo di compressione. La variazione della conducibilità idraulica durante il processo di taglio è stata principalmente controllata dalle deformazioni volumetriche abbinate a quelle di taglio. La variazione di porosità ha influenzato la conducibilità idraulica più della deformazione distorsionale che può alterare i percorsi idraulici all'interno del provino.

L'approccio proposto per la modellazione delle prestazioni di trazione e l'identificazione delle condizioni di danneggiamento del terreno dovute all'effetto di taglio causato dallo slittamento degli pneumatici da trazione è stato convalidato sperimentalmente e utilizzato per lo sviluppo di un nuovo modulo Excel per la terza edizione del software TASC V3.0.xlsm: www.agrartechnik-agroscope.ch.

Questo modulo simula anche la relazione tra potenza erogata dal motore e slittamento delle ruote. Per permettere agli utilizzatori una semplice e affidabile caratterizzazione meccanica del terreno, sono state messe a punto quattro pratiche prove di campo. L'applicazione consente di confrontare numerose configurazioni del trattore, su vari terreni con differenti condizioni. Il limite oltre il quale è previsto un danneggiamento del terreno è riportato in termini di trazione netta e slittamento. Il TASC V3.0 rappresenta un valido supporto per identificare le configurazioni del trattore e le condizioni del terreno che ottimizzano le prestazioni di trazione, con conseguente riduzione dei consumi di carburante e limitazione dell'usura degli pneumatici e del danneggiamento del terreno.

Main nomenclature

a	Parameter of the parabolic equation which defines the shape of the contact surface [m^{-1}]
A	Intercept of the soil critical state line [kPa]
b	Contact patch smaller dimension (tyre width) or diameter of the compression plate [m]
c	Soil cohesion [kPa]
DP	Drawbar pull [kN]
D_{rim}	Rim diameter [m]
ds	Infinitesimal area of the soil-tyre contact surface [m^2]
dp_v	Elementary vertical load on the tyre [kN]
e_0	Eccentricity of the centre of the wheel relative to the rear point of the contact surface [m]
e_t	Eccentricity of the soil reaction relative to the wheel centre [m]
FC	Gravimetric fuel consumption [kg h^{-1}]
GT	Gross traction [kN]
h	Height of the drawbar [m]
$i_{front/rear}$	Slip of the front/rear wheel [%]
j	Soil shear displacement [m]
k	Shear deformation modulus [m]
K	Modulus of deformation [kN $m^{-(n+2)}$]
K_c	Cohesive modulus of deformation [kN $m^{-(n+1)}$]
K_{carc}	Carcass stiffness [kN m^{-1}]
K_s	Theoretical speed ratio
K_{sat}	Hydraulic conductivity of soil in saturated condition [m s^{-1}]
K_v	Coefficient of vertical stiffness of the tyre for unit length of the contact surface [kN m^{-2}]
K_φ	Frictional modulus of deformation [kN $m^{-(n+2)}$]
L	Wheelbase of the tractor [m]
M	Slope of the soil critical state line
M_{GT}	Driving torque corresponding to the required gross traction [kN m]
M_r	Resistance moment [kN m]
n	Exponent of deformation
NT	Net traction [kN]
p	Soil mean stress [kPa]
P_{in}	Tyre inflation pressure [kPa]
$P_{input\ on\ wheel}$	Power input on the drive wheel [kW]
PR	Penetration resistance [N]
PTO	Power-take-off [kW]
$P_{tractive\ wheel}$	Tractive power of the drive wheel [kW]
$P_{tractive\ tractor}$	Tractive power of the tractor [kW]
p_s	Vertical soil pressure [kPa]
q	Soil deviatoric stress [kPa]
r	Radius vector from the wheel centre [m]
R	Unloaded radius of the wheel [m]
R_c	Soil compaction resistance [kN]
R_{GT}	Distance from the centre of the wheel to the point where the gross traction is applied [m]
R_r	Rolling radius of the wheel [m]
s	Soil matric suction [kPa]
SFC	Specific fuel consumption (drawbar power basis) [kg kW^{-1} h^{-1}]
T	Total driving torque [kN m]
V	Absolute velocity [m s^{-1}]

V_a	Actual forward velocity of the wheel [m s^{-1}]
V_{aj}	Tangential projection of the actual forward velocity of the wheel [m s^{-1}]
V_j	Slip velocity [m s^{-1}]
V_ω	Velocity relative to the centre of the wheel [m s^{-1}]
$V_{\omega j}$	Tangential projection of the velocity relative to the centre of the wheel [m s^{-1}]
W	Vertical component of the total soil reaction / wheel load [kN]
W_0	Wheel load in stationary condition [kN]
x	Horizontal coordinate [m]
x_0	Length of the soil-tyre contact surface in the horizontal direction [m]
z	Vertical coordinate (soil sinkage) [m]
z_0	Rut depth [m]

Greek letters

α	Angle between the tangent to the infinitesimal area of soil-tyre contact and the *x*-axis [°]
$\alpha_{V\omega}$	Angle between the vertical axis and the position of the radius-vector [°]
$\alpha_{\omega j}$	Angle between the velocity relative to the wheel centre and its tangential projection [°]
γ	Soil unit weight [kN m^{-3}]
δ	Tyre vertical deflection [m]
Δ	Deflection of the tyre on a hard surface [m]
ΔK_p	Inflation pressure dependence of the tyre [kN m^{-1} kPa^{-1}]
ε_s	Soil shear strain
ε_v	Soil volumetric strain
ε_z	Soil vertical strain
η_{PD}	Power delivery efficiency
$\eta_{tr\ wheel}$	Traction efficiency of the drive wheel
$\eta_{tr\ tractor}$	Traction efficiency of the tractor
θ	Soil volumetric water content [%]
μ_{tr}	Traction coefficient
σ	Normal stress at soil-tyre contact [kPa]
σ_v	Vertical pressure on the tyre [kPa]
σ_1	Soil greatest principal stress [kPa]
σ_3	Soil smallest principal stress [kPa]
τ	Soil shear stress [kPa]
τ_{max}	Soil strength [kPa]
φ	Angle of soil shear resistance [°]
ω	Angular velocity of the wheel [s^{-1}]

Some definitions

(sources: International Society for Terrain-Vehicle Systems ISTVS Standards and ASABE Distinguished Lecture Series)

Compaction: the densification of soil by means of mechanical manipulation which results in the reduction of air voids in the soil.

Drawbar coefficient (or traction coefficient): the ratio of drawbar pull to gross vehicle weight.

Drawbar efficiency (or traction efficiency): the product of drawbar pull and vehicle speed divided by power input to the traction elements. It representes the fraction of power delivered to the traction elements that is available as drawbar power.

Drawbar power: the product of drawbar pull and vehicle speed.

Drawbar pull: the force available for external work in a direction parallel to the horizontal surface over which the vehicle is moving.

Four-wheel drive (4WD) tractor: a tractor with powered front and rear axles. The tyres are all equal in diameter, and the tractor is steered by a center frame articulation joint or, less frequently, by coordinated front and rear steer wheels. It is assumed to not have a suspension system.

Mechanical front-wheel drive (MFWD) tractor: a tractor with powered front and rear axles. The front tyres are smaller in diameter than the rear tyres, and the tractor is steered with the front wheels. It is assumed to not have a front suspension system unless specifically indicated to the contrary.

Motion resistance, external: The resistance to movement of a vehicle provided by the surface on and through which it moves.

Motion resistance, internal: The resistance to movement of a vehicle provided by the internal friction of its moving parts and the energy losses in the traction elements.

Net tractive effort (or net traction): the total force output of the traction device acting parallel to the surface of the soil and in the direction of travel.

Power delivery efficiency: the ratio of delivered tractive power (drawbar power) to tractor input power from the engine, it represents the fraction of power produced by the engine of a tractor that is available as tractive power. In order to consider the engine power input, the equivalent PTO (power-take-off) power can be used.

Rolling circumference: the distance traveled on a rigid surface by the wheel or track in one complete revolution. The rolling circumference may vary with changes in load, speed, or tyre pressure. The rolling radius is given by the rolling circumference divided by 2π.

Self-propulsion point (or self-propelled point): The point on a drawbar pull-slip curve at which the vehicle is just able to propel itself (i.e. zero drawbar pull)

Slip (or travel reduction): an indication of how the speed of the traction elements differs from the forward speed of the vehicle. Slip is defined by the equation:

$$i = \frac{\varpi R_r - V_a}{\varpi R_r}$$

where:

i = slip

R_r = rolling radius

ω = angular velocity of the wheel, or number of revolutions per unit time divided by 2π for a track

V_a = actual forward velocity of vehicle or wheel axle

Soil strength: the resistance of a soil to an applied stress. The strength varies with moisture content and the nature, arrangement, and size distribution of the soil particles, and the test itself.

Specific fuel consumption: the ratio of the fuel consumption expressed in kg h^{-1} (gravimetric) or l h^{-1} (volumetric) to the engine power input, or alternatively to the drawbar power.

Tyre contact area: the portion of the tyre in contact with the supporting surface. Interruptions of the contact area due to tread patterns are considered part of the contact area.

Tyre deflection: any inward radial displacement of a point on the tyre surface from its position on the inflated but unloaded tyre, unless otherwise specified.

Traction element (transport element): any element of a vehicle that is designed to provide support and/or traction for a vehicle travelling on a surface (e.g. tyres, tracks, feet, screws, etc.).

Two-wheel drive (2WD) tractor: a tractor whose rear axle only is powered. The front tyres are smaller in diameter than the rear tyres, and the tractor is steered with the front wheels. It is assumed to not have a suspension system.

Mathemata mathematicis scribuntur
Mathematics is written for mathematicians
Nicolaus Copernicus - De revolutionibus orbium coelestium

Preface

This work presents an analysis of two important issues in tillage management: the choice of the tractor configuration which best matches the soil characteristics and conditions, and the prevention of soil damage due to tractor traffic.

The first issue is recognised to be of high interest since it significantly affects the efficiency of the locomotion on soils which controls the fuel consumption, as well as the time required for tillage operations. Furthermore, an inefficient locomotion on soil entails energy loss which turns out in additional harmful consequences such as a rapid wear of the tyre tread and a severe soil deformation.

The second issue has long been studied as soil plastic deformations induced by traffic of agricultural machines are responsible for several detrimental consequences, such as a potential yield reduction, an increase in soil erosion due to enhanced surface runoff, and a greater energy required for tilling the soil.

With regard to the first issue, the innovative contribution of this research consists in the development and experimental substantiation of a practical physical-based model for simulating the traction performance, in terms of drawbar pull, traction coefficient, traction efficiency and motion resistance due to soil compaction, of agricultural mechanical front-wheel drive MFWD tractors. The model presented consistently simulates the influence of the tyre inflation pressure and the wheel load on the traction performance of MFWD tractors, furthermore, it reproduces reliably the dependence of the traction performance on the soil strength.

Thanks to all this valuable information, the model represents a worthwhile aid for the choice of a proper tractor configuration.

The prevention of soil damage due to tractor traffic is analysed with particular regard to the effects of the wheel slip on the topsoil. These effects, as pointed out by results presented in this study, need to gain more attention in the future, in order to develop more appropriate models to prevent soil damage.

The harmful consequences due to the application of a high traction force and a high wheel slip on the topsoil are clearly shown in terms of soil deformations, reduction of soil porosity, alteration of the soil pore structure, and degradation of the soil hydraulic conductivity.

A mechanistic approach aimed to define the mechanical condition at soil-tyre contact which leads to a topsoil damage due to the shearing effect from the tread of the tyre is presented.

This monograph is organized in two main parts. The first part is dedicated to: i) the presentation of the problem and the analysis of the previous contributions; ii) the description of the model of tractor-soil interaction; iii) the exposition of the experimental technique used for full-scale traction tests; iv) the discussion of results of the traction tests in the widely differentiated conditions considered, with special focus on the role of the tyre inflation pressure, the wheel load, and the soil strength, in controlling the traction performance of the tractor-terrain system.

The second part presents the analysis of the effects of the wheel slip on the topsoil on the basis of three tests: i) in the field test 1, the topsoil deformation is taken under consideration, and a mechanistic approach to define the stress condition which leads to a topsoil damage and the corresponding slip value is described; ii) the field test 2 aimed to evaluate the soil stress state at the soil-tyre contact area in two conditions, viz., the passage of a tractor without and with slip, to assess the soil deformation arising from these two treatments, and to determine the effects of such a deformation on the water movement in the soil; iii) the third test is a laboratory test aimed to reproduce the soil stress paths under a tyre and measure the saturated hydraulic conductivity as affected by a compression process and a subsequent shear phase.

General conclusions of this study are drawn in Chapter 3.

The results of this work were used for developing a practical Excel module for the third version of the application TASC V3.0.xlsm (Tyres/Tracks And Soil Compaction) which is introduced in Chapter 4 at the end of this monograph.

1. Simulation of traction performance of mechanical front-wheel drive (MFWD) tractors

1.1 Introduction

1.1.1 The pneumatic wheel: function and structure

The wheel of a tractor is generally required to perform different functions such as supporting and cushioning the vehicle, providing sufficient traction in driving and braking conditions, and besides, it must assure adequate steering control and stability.

Except for the gravimetric as well as the aerodynamic forces, these latter becoming negligible at low velocity, the major forces and moments controlling the motion of a tractor on a terrain are applied through the tyre-ground contact. A proper understanding of the way the tyre interacts with the soil surface is, therefore, an essential step to improve the performance of the tractor and the ride and handling behaviour.

Tractor tyres are asked to perform both in road and in off-road conditions, therefore, they match the two main problems in the mechanics of tyres, i.e. the interaction with a hard surface such as a road, and the interaction with a deformable surfaces such as a tilled soil.

A pneumatic tyre is a toroidal air-filled flexible structure. The main element of its structure is the carcass which is made up of several layers of flexible cords enclosed in a matrix of rubber compounds (Fig. 1 and Fig. 2). The cords can be of different composition, natural fabric, synthetic, or metallic. They are anchored around the beads which are made of steel wires. The beads represent a sort of foundations for the carcass, moreover, they provide adequate seating of the tyre on the rim.

The rubber compounds of a tyre are a mixture of different rubber types and chemicals. The main rubber compounds are the natural rubber (NR), the styrene butadiene rubber (SBR), the butadiene rubber (BR), and the butyl rubber (IIR). The rubber is mixed to various additives in order to improve the characteristics of softness, strength and durability of the tyre. Different compounds are used for the parts of the tyre such as the sidewall and the tread, as a function of the work they must perform.

The behaviour of a tyre is affected, to a great extent, by the characteristic of the carcass. There are two main types of tyre carcass constructions: diagonal and radial.

The first has a diagonal cord ply from bead to bead (Fig. 1) with the different layers of cord ply that cross each other in opposite direction. The main advantage of such a structure is a strong and durable sidewall of the tyre. As a drawback, the tyre is stiffer, has a higher rolling resistance and a smaller contact surface than a tyre with a radial structure.

In a radial tyre (Fig. 2) the cord plies are arranged at 90 degrees (radially) to the direction of travel and the tread is strengthened with belts of diagonal design. This particular structure allows the sidewalls and the tread to work as two independent features of the tyre. The tyre sidewalls are thinner and softer than in a diagonal tyre, they provide higher ride comfort, but, as a drawback, are more sensitive to damage. Other advantages of a radial tyre are the large contact surface, the low rolling resistance and the low heat build up.

Furthermore, a radial tyre applies a relatively uniform ground pressure over the entire contact area, whilst a diagonal tyre exerts a ground pressure which varies greatly from point to point due to a complex localized wiping motion of the tread elements.

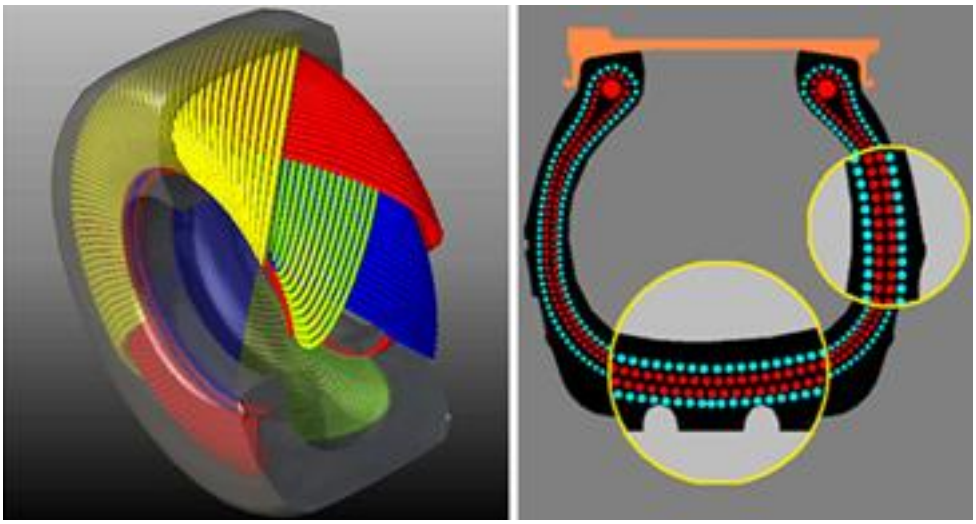

Fig. 1: Structure of a diagonal tyre (source: www.michelinag.com).

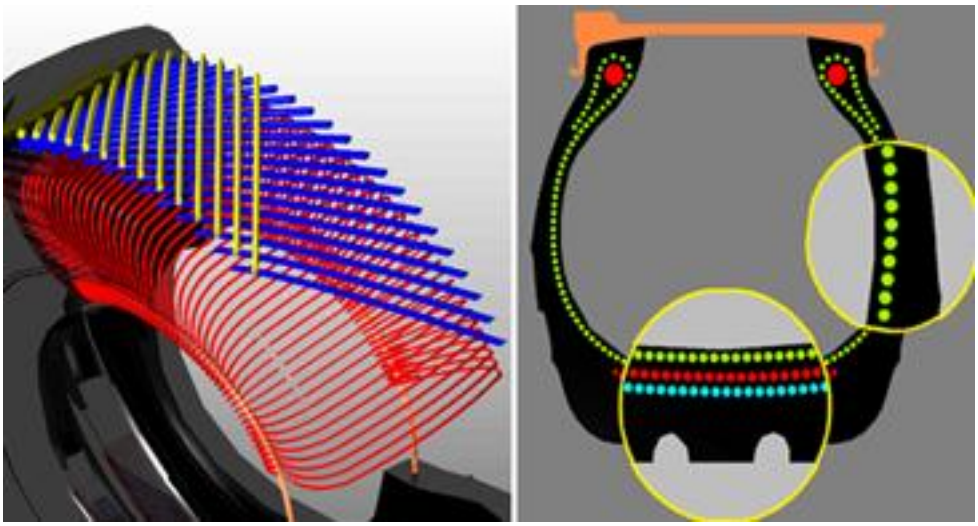

Fig. 2: Structure of a radial tyre (source: www.michelinag.com).

1.1.2 Soil-tyre interaction for a driven wheel

A driven wheel converts the applied torque into traction. This latter is defined as the total force output of the wheel acting parallel to the wheeling surface and in the direction of travel. Fig. 3a and 3b show the system of forces acting on a rigid drive wheel when it moves on a rigid surface or on a soft surface, respectively. The resisting forces acting on a tractor are the internal resistance of the wheels, the resistance due to wheel-soil interaction, the grade resistance, the obstacle resistance, and the aerodynamic resistance. An additional factor of resistance is due to the use of an implement. Assuming a flat wheeling surface with no obstacles and neglecting the aerodynamic resistance because of the low velocities considered, resisting forces reduce to the internal resistance and the resistance due to interaction with soil.

The internal resistance of the wheel corresponds to the rolling resistance of the tyre which depends on the hysteresis in tyre materials due to the deflection when operating. During the rolling, in fact, the tyre is deflected and the normal pressure in the front half of the contact surface is higher than that in the rear half. As a consequence, a rolling resistance moment is generated due to the fact that the resultant of the normal pressure lies in the front half of the tyre-ground contact surface. The rolling resistance of a tyre depends on

several factors related to the structure of the tyre and the conditions of operation such as the inflation pressure, the load, the temperature, the speed and the ground condition.

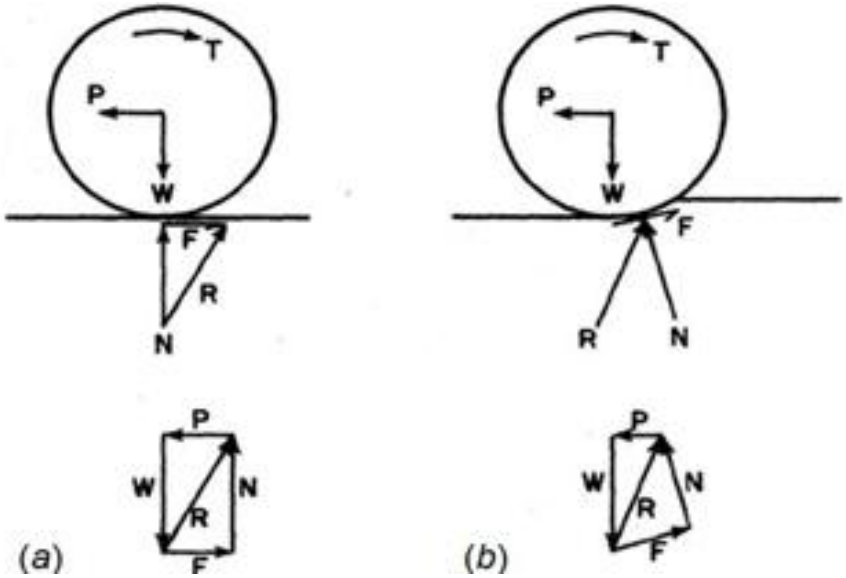

Fig. 3: System of forces acting on a rigid drive wheel: (a) on a rigid surface, (b) on a yielding surface (source: Hovland, 1973).

The resistance due to wheel-soil interaction is the most significant one for off-road locomotion, and determines, to a great extent, the mobility of a vehicle over terrains. It mainly corresponds to the soil compaction resistance. This latter, according to the Bekker's theory (Bekker, 1956), is due to the vertical work done in making a rut equal to that left after the wheel passage. In soft terrain where wheel sinkage is significant, Bekker suggested that a bulldozing resistance acting in front of the wheel should be taken into consideration, in addition to the compaction resistance.

The net traction or drawbar pull is the force available to pull something and is equal to the difference between the traction force developed by the wheel and the resultant resisting force acting on the wheel in the same direction. In off-road locomotion the pure wheeling condition (slip = 0) (Fig. 4) is generally not respected, in fact, since soil is a deformable body, as soon as it is stressed, it deforms, this deformation resulting in wheel slip. The relationship between developed traction force and wheel slip (Fig. 5) characterises the traction performance of a wheel-soil system depending on the soil stress-strain behaviour, the tyre size and stiffness, the load acting on the wheel as well as the driving speed.

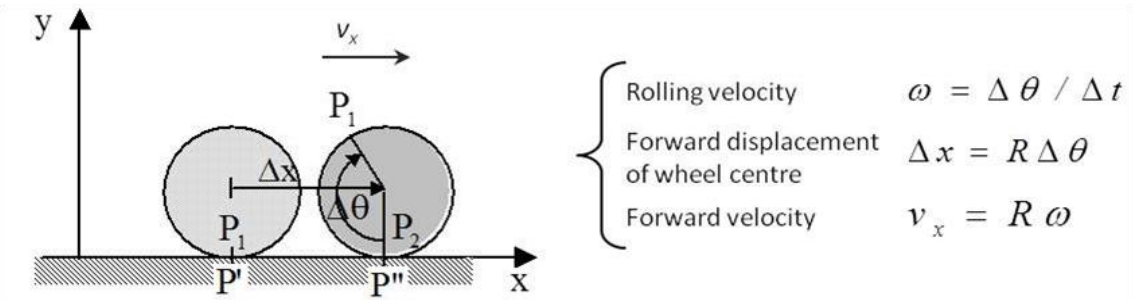

Fig. 4: Pure wheeling condition (slip = 0).

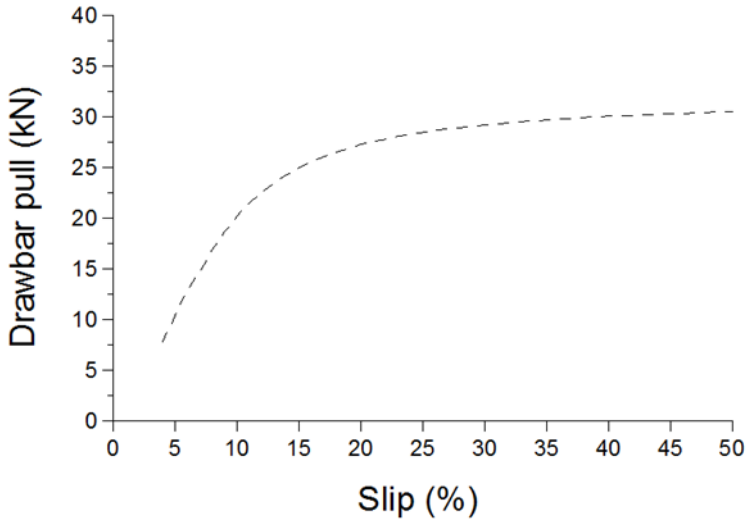

Fig. 5: Drawbar pull-wheel slip relationship.

The complex process of the development of traction is based on the mechanical interaction between two media: the soil and the wheel. They interact in terms of stresses and strains according to their own constitutive laws. A proper analysis and simulation of the traction force generated by a wheel running on a deformable soil should be, therefore, based on a reliable characterisation of the mechanical behaviour of the two media. An element of complexity in the mechanical characterisation of both the tyre and the soil is due to the fact that their interaction is not quasi-static since several dynamic factors are involved.

Over the years, a variety of methods, ranging from empirical to theoretical, for predicting the performance of tracked and wheeled vehicles over unprepared terrain have been proposed. According to Wong (1989) and Upadhyaya and Rosa (1997), the methods for predicting wheel-soil performance can be divided into three main groups: analytical, empirical, and semi-empirical methods.

1.1.3 Analytical models of soil-tyre interaction

The analytical models have the potential of examining in details single aspects of the mechanics of vehicle-terrain interaction, on the basis of the constitutive laws which describe the soil and wheel mechanical behaviour.

They use numerical methods such as the finite difference methods (FDM) (Karafiath and Nowaizki, 1978), or the finite element method (FEM) (Aubel, 1994; Fervers 1997; Liu and Wong, 1996).

The FEM has been widely used for simulating the wheel-soil interaction, it is free of a priori assumptions and shows very good correlation with test results. However, using FEM, it is hard to simulate the large deformations, flow, and cracks that appear in the soil (Asaf et al., 2006). Moreover, at least four to five parameters are required for the soil constitutive models used in FEM (Rubinstein et al., 1994; Shoop, 2001). These parameters are usually of difficult determination, particularly in situ. A method for determining such parameters by means of in situ tests was proposed by Rubinstein et al. (1994).

In the early applications of the finite element method for the simulation of the tyre-soil interaction, the soil was assumed either a linear or a nonlinear elastic continuum and the determination of the solution required the stress state at the soil-tyre contact to be defined as an input (Perumpral et al., 1971; Yong and Fattah, 1976). The function of the finite element method was, therefore, limited to simulate the stress state in the soil, for a given distribution of the normal and shear stress over the soil-tyre contact (Wong, 1977).

Nowadays the possibilities of application of the finite element method to the simulation of the soil-tyre interaction are significantly advanced. Moreover, a variety of constitutive models for the mechanical characterisation of the soil are available. The Drucker-Prager cap model and the Cam-Clay model are two of the widely used, although the Mohr-Coulomb yield model is also employed in some cases (Liu and Wong, 1996; Liu et al., 1999; Seta et al., 2003; Ferves, 2004; Zhang et al., 2005). The geometry of the contact patch and the stress state at the soil-tyre contact can now be easily simulated with the finite element method.
Another analytical model is the discrete element model (DEM), introduced by Cundall (1971). It can be used for describing the behaviour of granular material and its interaction with rigid bodies (Asaf et al., 2006). Thanks to the possibility of modelling large plastic deformations and discontinuities in materials, this method may represent a proper tool for describing the dynamic aspects involved in the soil-tyre interaction.
Due to the dynamic behaviour between the particles, the forces generated between them depend on their overlap and contact law (Cundall and Strack, 1979). In Cundall and Strack's work the particles are spheres or discs. The relationship among the particles is described by a contact law obtained by a combination of springs, dampers, coulomb friction, coulomb damping, or also additional forces.
Studies reported by Oida et al. (1999) and by Fujii et al. (2003) have shown a good agreement between the simulation of the soil-wheel interaction and the experimental results. A DEM model of track link-soil interaction with good quantitative and qualitative results was reported by Asaf et al. (2005).
In spite of valid recent applications of the discrete element method to investigate the mechanics of vehicle-terrain interaction (Shigeta and Aruga, 2005; Asaf et al., 2006), it is in its early stage of development at the present time (Wong, 2010).
The simulation of the soil-tyre interaction based on the finite element method or the discrete element method has been shown to be in qualitative agreement with results collected on certain types of terrain, however, they cannot provide the off-road vehicle engineer with a realistic tool for design and performance evaluation of the vehicle-terrain system (Wong, 2010).
Several challenging issues facing these computational methods have to be further developed, and, at the present time, it is suggested that the primary role of computer simulation models is to provide vehicle engineers with reliable tools for comparing off-road vehicle performance on a relative basis (Wong, 2008).

1.1.4 Empirical models of soil-tyre interaction

In the empirical models of soil-tyre interaction the soil is characterised by simple measurements or field observations. The development of an empirical method is based on the execution of several tests with selected representative vehicles on different soils of interest. An empirical relationship between the vehicle performance and the soil characteristics can be defined on the basis of the experimental results.
The first empirical methods based on the cone index were developed during World War II by the U.S. Army Waterways Experiment Station (WES) to easily asses the vehicle mobility on a "go/no go" basis. Further developments led to the NATO Reference Mobility Model (NRMM).
The cone index is defined as the force per unit cone base area (pressure) applied to push a 30° circular cone with a 3.23 cm^2 base area into the soil with a recommended rate of penetration of approximately 3 cm/s. The cone index is obtained using a cone penetrometer (Fig. 6), and the performance of a vehicle is then correlated with the cone index or its derivatives. Modern penetrometers can monitor and store the force applied and the penetration depth of the cone.

Another index of high interest for characterising the variation in soil strength due to repeated vehicular traffic is the remoulding index (RI). It is defined as the ratio of the cone index of a soil after remoulding to that before remoulding. The product of the remoulding index (RI) and the cone index (CI) is indicated as the rating cone index (RCI), and is used to define the soil strength under repeated vehicular traffic.

Fig. 6: The cone penetrometer (source: www.globalsecurity.org).

The WES-method (Knight and Rula, 1961) is based on dimensionless vehicle parameters such as the wheel numerics calculated from the wheel dimension and slip and based on simple wheel models. Different wheel numerics have been developed by several institutions, based on empirical observations on the wheel-soil interaction. The early approaches aimed to assess the minimum CI-value which allows a given vehicle to move “go/no go”. Models based on a simple wheel numeric were presented by Freitag (1965), and by Turnage (1972a) who differentiated the wheel numeric for sand and clay soils and added a width factor in the model for clay soils. Further developments were presented by Rowland (1975), Paul (1984), Turnage (1972b, 1978, 1984), Brixius (1987), and Li et al. (1990). A model which has been widely used is that presented by Wismer and Luth (1973) who introduced the Janosi and Hanamoto’s soil shear equation (Janosi and Hanamoto, 1961) and the slip in the mobility model. A further improvement was introduced by Gee-Glough (1980) with a soil shear factor.

In the context of the empirical models, Rowland (1972; 1975) introduced the concept of mean maximum pressure (MMP) defined as the mean value of the maximum pressure occurring under all of the roadwheel stations. A set of desired values of the mean maximum pressure for different conditions was proposed by Rowland (1975) in order to evaluate whether a given vehicle with a specific value of MMP has adequate mobility on a certain terrain.

According to the equations of the mean maximum pressure method, the MMP doesn’t depend on the soil conditions. Wong (1989) has shown, on the contrary, that the soil characteristics strongly influence the pressure distribution.

Wong (1994) pointed out that the values of MMP calculated using Rowland’s equations differ significantly from those measured, furthermore, the effects of vehicle design parameters on the value of MMP are not accurately represented on many types of terrain. Another limit of Rowland’s approach is that it can be used only to evaluate the performance of a vehicle on a soft ground on a “go/no go” basis since it doesn’t provide a quantitatively prediction of the performance of a vehicle in terms of motion resistance, thrust, drawbar pull, and tractive efficiency under a given operating condition (Wong, 1989).

The empirical methods have been object of several criticisms by different authors (Holm et al. 1987; Wong, 1984; Golob 1981; Schmid 1995). Limits of the standard mobility models due to the presence of vegetation were remarked by Maclaurin (1981). Upadhyaya and Wulfsohn (1990) didn't observe any correlation between the wheel performance and the penetration resistance of the soil, whilst only a weak correlation (r = 0.24) between the penetration resistance and the wheel performance during the thaw period was reported by Shoop (1993). Moreover, the modelling of the trafficability on frictional soils is recognised to be difficult (Gee-Clough 1978; Reece and Peca, 1981). In addition, Turnage (1978) and Maclaurin (1981) remarked that special tyres need their own modelling.

1.1.5 Semi-empirical models of soil-tyre interaction

In view of the limitation of computational and empirical methods, mathematical models for parametric analysis of the performance of off-road vehicles have been developed, these models belong to the semi-empirical approach to the study of tyre-soil interaction. A pioneering effort in this area was made by Bekker (Bekker, 1956, 1960, 1969). Subsequently, a series of computer-aided methods for parametric analysis of the performance and design of both tracked vehicles and off-road wheeled vehicles, from a traction perspective, have been presented (Onafeko and Reece, 1967; Wong and Reece, 1967a and b; Fujimoto, 1977; Wong et al., 1984; Wong and Preston.Thomas, 1986 and 1988; Wong, 1992; Gao and Wong, 1994; Wong, 1995, 1998, 2007, 2008; Schmid 1995; Shmulevich and Osetinsky, 2003; Osetinsky and Shmulevich, 2004; Wong and Huang, 2005, 2006, 2008).

These methods are based on a description of the physical processes involved in the vehicle-soil interaction, and take into account the design features which affect the performance of a vehicle, and the soil mechanical behaviour under compression, shear and repetitive loading.

They have been verified by field tests on various types of terrains. Moreover, since they are suitable for comparing different design solutions or for optimizing design parameters, they have been successfully used to assist vehicle manufacturers in the development of new products.

A normal load is applied on the soil surface by the tractor wheels, this load results in sinkage and, as a consequence, in a rise in motion resistance. The torque acting on the wheel generates a shearing action at the tyre-soil contact which turns out in the development of traction force and slip.

A proper knowledge of the normal pressure-sinkage and shear stress-shear displacement relationships of the soil is of prime importance for the simulation of the traction performance of the tractor-soil system.

Furthermore, the soil under a vehicle which moves in straight line motion, undergoes a repetitive loading of the consecutive wheels in a multiaxle wheeled vehicle. To realistic predict the performance of an off-road vehicle, the response of the terrain to repetitive loading should also be measured (Wong et al., 1982; Wong et al., 1984; Wong, 1989; Wong, 2008).

1.1.5.1 The bevameter technique for soil mechanical characterisation

Bekker (1960 and 1969) and Wong and Bekker (1985) introduced a technique for measuring the response of a soil to loading due to the interaction with an off-road vehicle. This technique is usually referred to as the bevameter technique and is based on two types of tests: the plate penetration tests and the shear tests. The penetration tests are executed by simulating the soil-wheel contact area with a plate of suitable size, and the pressure-sinkage relationship of the soil is measured (Fig. 7). This test allow the simulation of the distribution of the normal pressure on the soil-wheel interface and the wheel sinkage. In order to minimize the

uncertainty in applying the pressure-sinkage relationship measured experimentally to the simulation of the full-scale soil-wheel interaction, it is recommended that the size of the plate used in the tests is comparable to that of the contact area of the tyre (Wong, 1989; Wong et al., 1984).

In the shear tests, the shearing action of a tyre is simulated by means of a shear ring or a shear plate (Fig. 8 8). This test provides the shear stress-shear displacement relationship and the shear strength of a soil. These data are required for simulating the shear stress distribution over the soil-tyre contact surface and the traction force-slip relationship of the wheel. Fig. 9 shows the basic features of a bevameter (Bekker, 1969). The normal load is applied to the compression plate or to the shear plate by a hydraulic ram. In the plate penetration tests a plate of circular shape is commonly used and the relationship between the applied pressure and the sinkage of the plate is recorded (Fig. 9).

In the shear tests, a shear loading is applied to the soil surface by means of a shear ring, under different normal pressures. The shear stress-shear displacement relationship and the parameters of shear strength of the soil are derived from the experimental relationship between the torque applied and the angular displacement of the shear ring (Fig. 9).

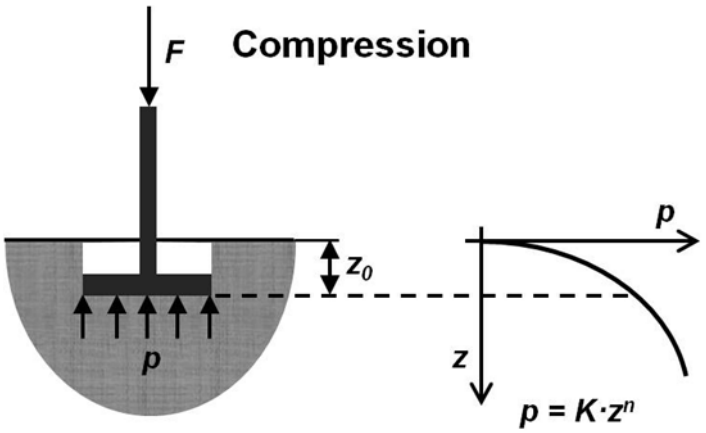

Fig. 7: The penetration test (redrawn from: AS²TM, AESCO, 2003).

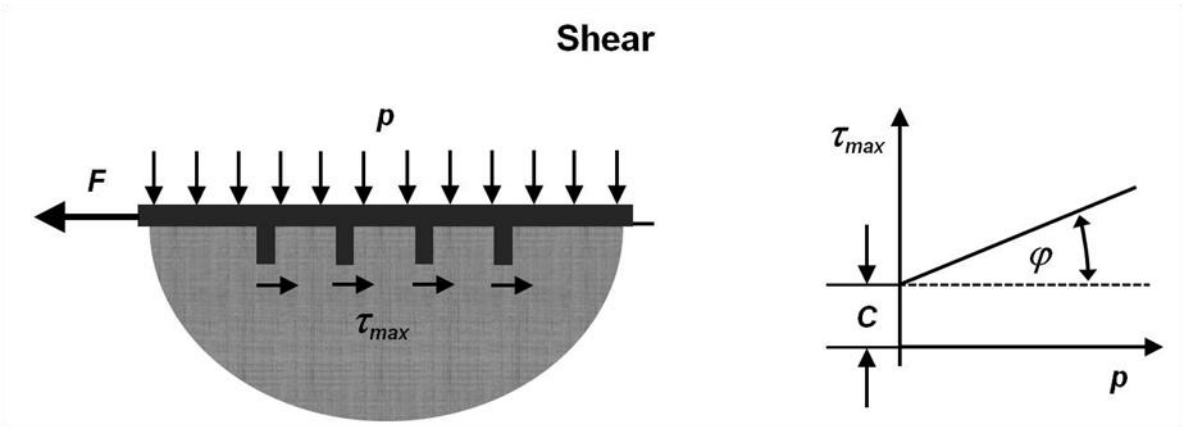

Fig. 8: The shear test (redrawn from: AS²TM, AESCO, 2003).

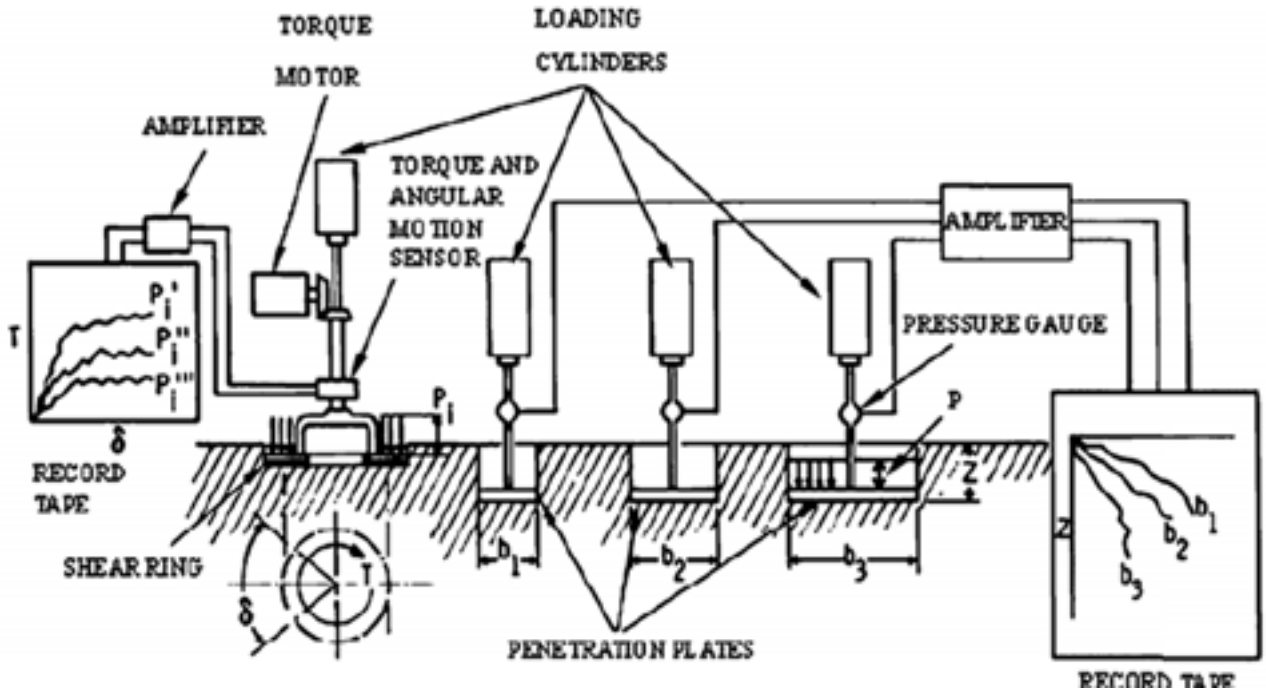

Fig. 9: Schematic view of a bevameter for measuring terrain properties (source: Bekker, 1969).

Several mathematical functions have been proposed for characterising the pressure-sinkage relationship of the soil. For a soil which is considered to be homogeneous, at least within the depth of interest, typical forms of the pressure-sinkage relationship are those shown in Fig. 10.

An empirical equation to characterise the pressure-sinkage relationship in homogeneous soils was proposed by Bekker (1969). Bekker's equation is based on three parameters: K_φ, and K_c which have variable dimension, and n which is dimensionless.

Another equation which characterises the pressure-sinkage relationship in homogeneous soils was proposed by Reece (1965) based on two dimensionless parameters, K'_φ, and K'_c and introducing the weight density of the terrain γ and the soil cohesion c.

For organic terrains with a mat of living vegetation on the surface and with a layer of saturated peat beneath it, a mathematical model for the pressure-sinkage relationship was developed by Wong et al. (1979), Wong et al. (1982), and Wong (1989).

Mathematical models has been also developed to characterise the pressure-sinkage relationship of snow covers with ice layers (Wong, 1989; Wong and Preston-Thomas, 1983; Wong and Irwin, 1992).

When a tractor move in straight line motion, the soil is subjected to a repetitive loading due to the passage of the front and the rear wheels. An example of response to repetitive normal load of a sandy terrain is reported in Fig. 11. Based on experimental observations on homogeneous soils, organic soils, and on snow, the pressure-sinkage relationship during both unloading and reloading may by approximated by a linear function that represents the average response of the terrain (Wong, 1989; Wong et al., 1984; Wong 2008).

As an alternative to a repetitive loading test (Fig. 11), in order to take the multi-pass effect into account, the pressure-sinkage relationship of the soil can be measured on the undisturbed soil as well as on the rut left from the passage of the front wheel (Bekker, 1969).

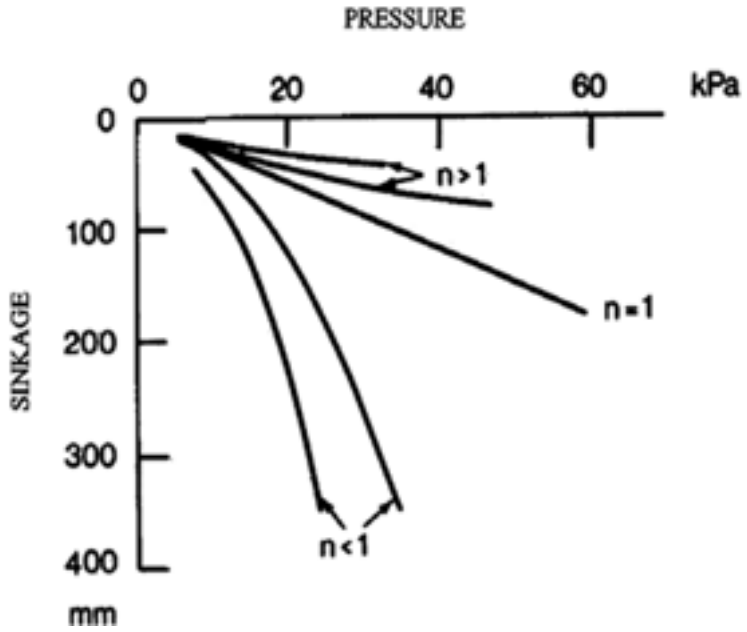

Fig. 10: Pressure-sinkage relationship for various homogeneous soils (source: Bekker, 1969).

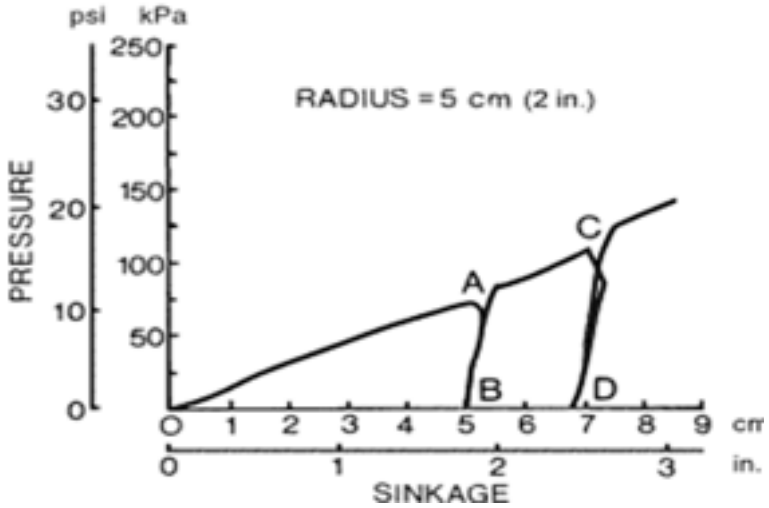

Fig. 11: Response of a sandy terrain to repetitive normal load applied with a circular plate (radius 5 10^{-2} m) (source: Wong, 1989).

The determination of the soil shear stress-displacement curve is of primary importance to describe traction force with increasing slip. With regard to this, results of horizontal plate shear deformation tests can be employed (Bekker, 1956). Two main types of mechanical behaviour can be observed (Fig. 12), for loose sand, saturated clay, dry fresh snow and most of the disturbed soils, the shear stress-displacement relationship exhibits a hardening phase followed by a plastic phase. In this case, the shear stress at first increases with the shear displacement, and then approaches a constant value. Janosi and Hanamoto (1961) have proposed a mathematical function to describe such a shear stress-displacement relationship.

Compacted sand, silt and loam, and frozen snow, may exhibit a brittle behaviour with softening, in which shear stress initially increases rapidly reaching a peak of maximum stress at a particular shear displacement, and then decreases approaching a residual value. A mathematical description of such a behaviour was presented by Wong and Preston-Thomas (1983) and Wong (1989). It depends on additional parameters

such as the ratio of the residual shear stress to the maximum shear stress and the shear displacement where the maximum shear stress occurs (Fig. 12).

As for the normal pressure, in order to simulate the traction performance of a vehicle moving in straight line motion, the response of the soil to repetitive shearing of consecutive tyres should be considered.

Fig. 13 shows the response of a dry sand to repetitive shearing under a constant normal load (Wong et al., 1984; Wong, 1989). The shear stress-shear displacement relationship during the repetitive application of the shear load does not vary significantly from that measured in the first shear load. Similar results were reported by Keira (1979) who measured the shearing force developed beneath a rectangular shear plate under a cyclic normal load.

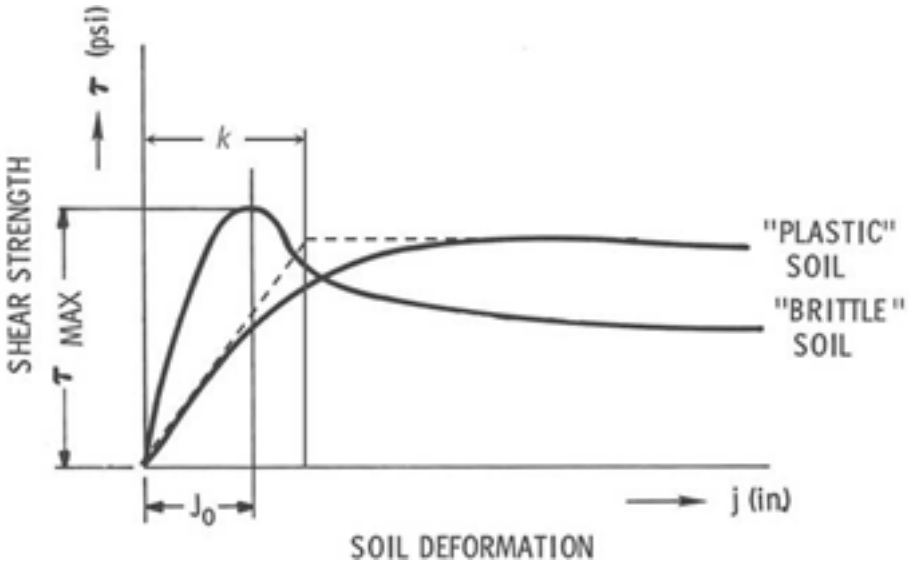

Fig. 12: Soil shear stress-deformation relationship (source: Bekker, 1969).

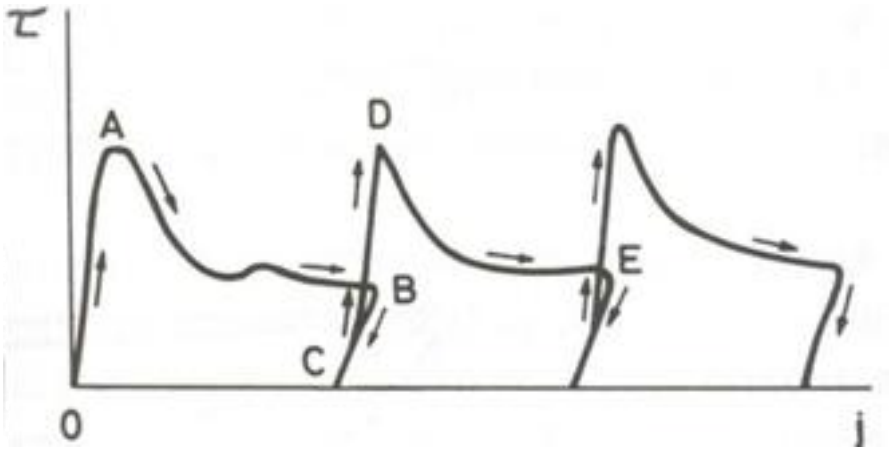

Fig. 13: Response to repetitive shear loading of a dry sand (source: Wong, 2008).

1.1.5.2 Semi-empirical models of soil-wheel interaction for a rigid wheel

One of the earliest parametrical approach to the mechanics of wheel-soil interaction for a rigid wheel was proposed by Bekker (1956; 1969). The mechanics of a rigid wheel over unprepared terrains is still of interest, as a pneumatic tyre may behave like a rigid rim in soft terrain, furthermore, rigid wheels are still used under certain circumstances, such as in the paddy field.

Bekker (1959; 1969) developed a method for predicting the motion resistance of a rigid wheel assuming that the terrain reaction at all points on the contact patch is purely radial and is equal to the normal pressure beneath a horizontal plate at the same depth in a pressure-sinkage test with a bevameter (Fig. 14). This assumption for the stress distribution implies that the motion resistance of a rigid wheel is due to the vertical work done in making a rut of depth z_0. This motion resistance is referred to as the soil compaction resistance R_c. Once the rut depth of the wheel is calculated, the tractive effort and the slip can be determined. To evaluate the relationship between the tractive effort and slip of a rigid wheel, the development of shear displacement along the wheel-soil interface has to be determined first. The shear displacement developed along the contact area of a rigid wheel may be determined based on the analysis of the slip velocity V_j. For a rigid wheel, the slip velocity V_j of a point on the rim relative to the terrain is the tangential component of the absolute velocity V at the same point (Fig. 15).

The derivation of the shear displacement j along the wheel-soil interface as a function of the angle θ (Fig. 15) and the slip i was described by Wong and Reece (1967). Based on the relationship between the shear stress and the shear displacement discussed previously, the shear stress distribution along the contact area of a rigid wheel can be determined (Wong and Reece, 1967). The total tractive effort can be determined by integrating the horizontal component of tangential stress over the entire contact area. The vertical component of the shear stress on the contact area supports part of the vertical load on the wheel. This fact has been neglected in the first simplified approach proposed by Bekker (1956). In a more complete analysis of wheel-soil interaction, the effect of shear stress should be taken into consideration (Wong, 1989; Wong and Reece, 1967).

The first approach to mechanics of rigid wheel-soil interaction presented by Bekker (1956; 1969) was further improved by Onafeko and Reece (1967) and modified by Wong and Reece (1967a, 1967b). More recently, another model for simulating the tractive performance of a driven rigid wheel on soft ground, based on the analysis of soil-wheel interaction, was presented by Muro (1993).

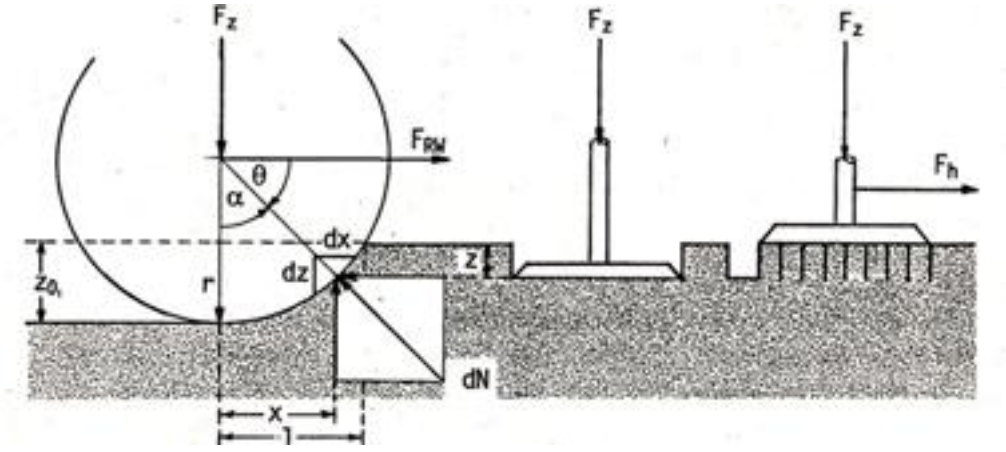

Fig. 14: Simplified soil-tyre interaction model: stress along the contact surface (source: Bekker, 1956).

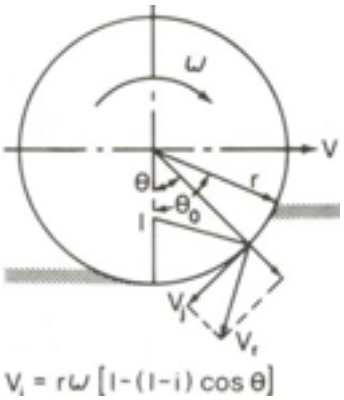

Fig. 15: Development of shear displacement under a rigid wheel (source: Wong, 2008).

1.1.5.3 Semi-empirical models of soil-wheel interaction for a pneumatic wheel

The semi-empirical approach was also applied to the analysis of the pneumatic wheel-soil interaction (Bekker, 1960; Fujimoto, 1977; Schmid, 1995; Shmulevich and Osetinsky, 2003).

A central problem of the tyre-soil interaction is the distribution of the pressure along the contact area. This depends on the deformations of the tyre-soil system which are described by the tyre-soil contact surface. While the maximum sinkage z_0 results from the equilibrium condition in the vertical direction, the type of shape of the contact surface is an assumption in all the models based on Bekker's theory (Schmid, 1995).

The simplest approach (Fig. 16*a*) assumes the contact surface as the combination of the section of a circle and a straight horizontal secant (Bekker, 1960; Wong, 1989). In another approach reported by Fujimoto (1977), the elastic tyre is replaced by a bigger rigid wheel within the area of ground contact (Fig. 16*b*).

A parabolic configuration of the tyre-soil contact surface (Fig. 16*c*) with the apex at the front point of contact was proposed by Schmid (1995).

More recently, Shmulevich and Osetinsky (2003) assumed that the contact surface can be represented in parabolic form in the longitudinal direction with the apex at the rear point of contact. This parabolic model approximates the circle-section very tightly allowing, moreover, an elegant and simple mathematical treatment.

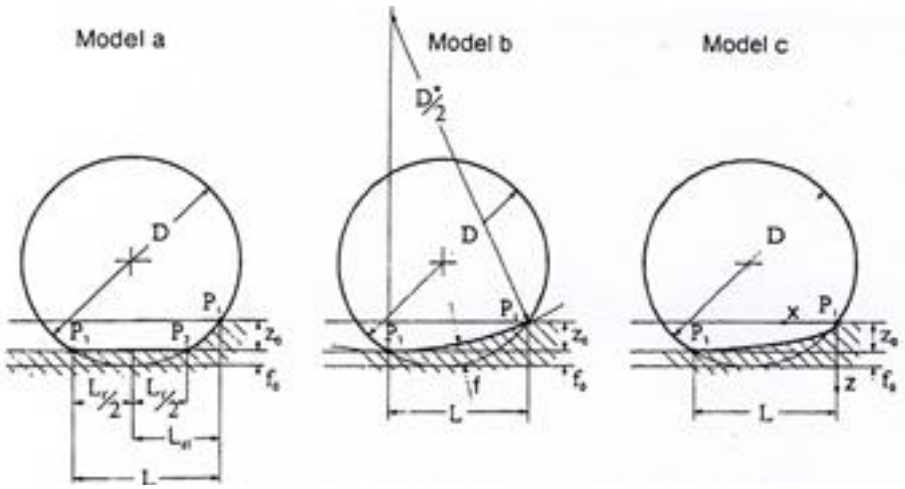

Fig. 16: Shape of the soil-tyre contact surface: (a) flat contact surface, (b) the elastic tyre is replaced by a bigger rigid wheel, (c) parabolic contact surface (source: Schmid, 1995).

The semi-empirical models represent a physical-based approach to the mechanics of wheel-soil interaction still valid and suitable for practical applications. Most of these models analyse the wheel-soil interaction considering a single wheel instead of a system of wheels, like in multi-wheel-drive vehicles. Experimental data to study the single wheel-soil interaction were often obtained by means of traction tests with a single wheel tester on a soil bin (Onafeko and Reece, 1967; Burt et al., 1979; Muro, 1993) or on field (Upadhyaya et al., 1989; Upadhyaya et al., 1997; Shmulevich and Osetinsky, 2003), in this latter case the single wheel tester was usually connected to a tractor. The single wheel tester allows a proper monitoring and control of all parameters of interest, furthermore, the use of a soil bin assures a homogeneous condition of soil. When a multi-wheel-drive vehicles, like a mechanical front-wheel drive MFWD tractor, is considered, the wheel-soil interaction model must be adapted by introducing effects such as: the behaviour of soil under repetitive loading (Muro, 1997), often referred to as multi-pass effect, the progressive transfer of load from the front axle to the rear axle when a traction force is developed, and the relationship between the slip of the front and rear wheels when the tractor moves with locked differential. The adaptation of a single wheel-soil model to a multi-wheel-drive system can be used to simulate the traction performance of a tractor-soil system. This results in a variety of practical and valuable applications such as the selection of the best tractor configuration as well as the definition of the optimal range of slip, as a function of the soil characteristics and conditions, in order to optimize the traction performance in tillage operations. The optimization of the traction development mechanism of a tractor can lead to a reduction of energetic losses due to wheel slip, with a decrease in fuel consumption, a limitation of wear of the tyre tread, and a reduction of the time required for tillage operations.

Among the tyre-soil interaction models presented recently, the model introduced by Shmulevich and Osetinsky (2003) has shown a very good correlation with results reported in literature (Pope, 1969; Shmulevich, 1975; Gee-Clough, 1976; Muro, 1993; Du Plessis and Venter, 1993; Thangavadivelu, 1994), and experimental data obtained with a single wheel tester on concrete, on a sand and on a tilled soil. This model considers the load transfer effect affecting a drive wheel in a multi-drive-wheel vehicle and, therefore, offers the opportunity to be adapted in order to develop a comprehensive tool for predicting off-road vehicle performance. In spite of the successful qualitative validation reported by the authors, a need for further verification by additional experimental data under experimental conditions different from those considered by the authors, and on different soils, is recognised (Osetinsky and Shmulevich, 2003). Furthermore, the possible application of this model to simulate the traction performance of multi-wheel-drive vehicles, like MFWD tractors which are very widespread in Europe, is of high interest for practical applications and therefore needs to be studied.

1.1.6 Aims of the research

The main aims of this work can be summarized as follows:

I. Development of a tractor-soil interaction model for predicting the traction performance of mechanical front-wheel drive MFWD tractors, based on the approach to tyre-soil interaction proposed by Shmulevich and Osetinsky (2003).

II. Setting of an experimental technique to perform full-scale tractor traction tests with MFWD tractors on agricultural soils.

III. Experimental substantiation of the model for simulating the traction performance of MFWD tractors on the basis of traction tests with four tractors of power ranging between 40 kW and 123 kW, under different configurations, in four locations presenting different soil textures ranging from clay to loamy sand.

IV. Evaluation of the overall accuracy of the tractor-soil interaction model to predict the traction performance of the four tractors considered, in terms of drawbar pull as a function of the slip.

1.2 Materials and methods

1.2.1 Modelling of traction performance of a mechanical front-wheel drive (MFWD) tractor

1.2.1.1 The Shmulevich and Osetinsky model of soil-tyre interaction

The stress-strain interaction at soil-tyre contact was analysed by means of a model which simulates traction performance of a deformable wheel (Shmulevich and Osetinsky, 2003; Osetinsky and Shmulevich, 2004). The main forces acting on the wheel are shown in Fig. 17.

The model assumes the soil to behave as a plastic non-linear medium, the wheel to roll in steady-state motion at a low velocity, and the tyre to deformation in linear elasticity. The soil-tyre contact surface in the longitudinal direction has a parabolic form with the apex at the rear point of contact *A* (Fig. 17), moreover, as illustrated in Fig. 18, the wheel-soil interaction is two dimensional (plane-strain problem). This latter assumption implies that the rut depth is the same across the width, and the width is the same along the contact surface, moreover all values are referred to the unit width of the wheel.

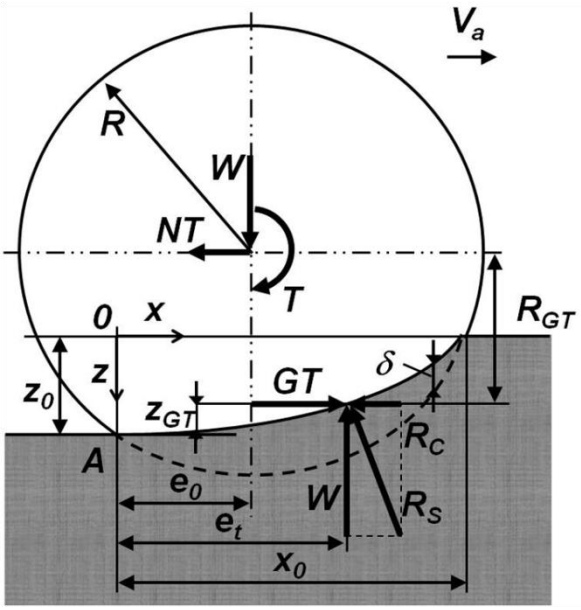

Fig. 17: Interaction between soil and a driven pneumatic wheel (redrawn from: Osetinsky and Shmulevich, 2004).

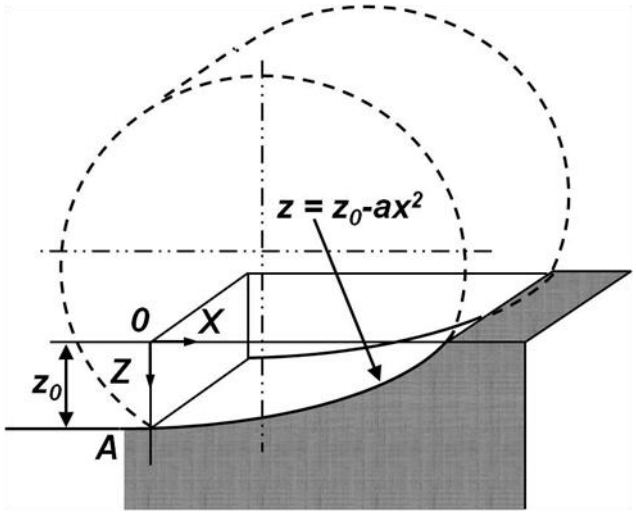

Fig. 18: The parabolic contact surface (redrawn from: Osetinsky and Shmulevich, 2004).

According to the assumptions of the model, the rut formed under the wheel is caused by the vertical load applied to the wheel and depends on the configuration of the wheel-soil contact surface. The parabolic equation which describes the soil-tyre contact surface in the longitudinal direction is:

$$z = z_0 - ax^2 \tag{1}$$

where z_0 is the rut depth, a is the parameter which controls the convexity of the parabolic function while x is the horizontal coordinate.

According to Bekker's theory (Bekker, 1960), the normal soil pressure along the soil-tyre contact surface is assumed to be equal to the normal soil pressure beneath the compression plate at the same depth. The vertical soil pressure-sinkage relationship for a plate penetrating into homogeneous terrain is described as:

$$p_s = \left(\frac{K_c}{b} + K_\varphi \right) z^n \tag{2}$$

In this, p_s is the vertical soil pressure under the plate, z is the soil sinkage, n is the exponent of deformation, b is the contact patch smaller dimension (width of the tyre or diameter of the round compression plate), whereas K_c and K_φ are respectively the cohesive modulus and the frictional modulus of deformation.

The contact surface in the proposed parabolic form is found from the equilibrium of the wheel in the vertical direction. The vertical component of the total soil reaction must equilibrate the wheel load W, this condition being expressed as follows:

$$W = \int_0^{x_0} p_s b \, dx \tag{3}$$

in which x_0 is the maximum value of the horizontal coordinate according to Fig. 17.

The normal soil pressure is here defined as in equation 2 and the previous integral can be written as:

$$W = b \left(\frac{K_c}{b} + K_\varphi \right) \int_0^{x_0} z^n \, dx \tag{4}$$

Values of K_c, K_φ and n are derived experimentally on the basis of vertical plate penetration tests.

Integral 4 is solved by means of a series expansion of function 1 limited to the second term, similarly to the approach reported by Wong (2008):

$$\left(z_0 - ax^2 \right)^n = z_0^n - anz_0^{n-1} x^2 \tag{5}$$

This way the force equilibrium results in:

$$W = \frac{K_c + bK_\varphi}{3} z_0^n \sqrt{\frac{z_0}{a}} (3 - n) \tag{6}$$

In order to match the parabolic configuration of the contact surface to the deflection of the moving pneumatic wheel, its state of equilibrium in the vertical direction is analysed. Tyre mechanical behaviour is assumed to be linear elastic. The stiffness is defined, according to Lines and Murphy (1991), as the sum of two components, the carcass stiffness K_{carc} and the product $\Delta K_p \, P_{in}$, where ΔK_p is the inflation pressure dependence of the tyre and P_{in} is the inflation pressure. Therefore the stiffness has a constant component and a component which varies with the inflation pressure.

The elementary vertical load dp_v and the vertical pressure σ_v acting on the tyre contact area of width b and length dx can be expressed as:

$$dp_v = K_v \delta dx \tag{7}$$

$$\sigma_v = \frac{dp_v}{bdx} = \frac{K_v \delta}{b} \tag{8}$$

here δ is the tyre vertical deflections and K_v is the coefficient of vertical stiffness of the tyre for unit length of the contact surface. The tyre vertical deflection is defined geometrically according to Fig. 19:

$$\delta = \sqrt{R^2 - (x - e_0)^2} - \sqrt{R^2 - e_0^2} + ax^2 \tag{9}$$

where R is the unloaded radius of the wheel and e_0 is the eccentricity of the centre of the wheel relative to the rear point of the contact surface, this latter defined as:

$$e_0 = \frac{x_0}{2}\left[1 - a\left(\sqrt{\frac{4R^2}{1+(ax_0)^2} - x_0^2}\right)\right] \tag{10}$$

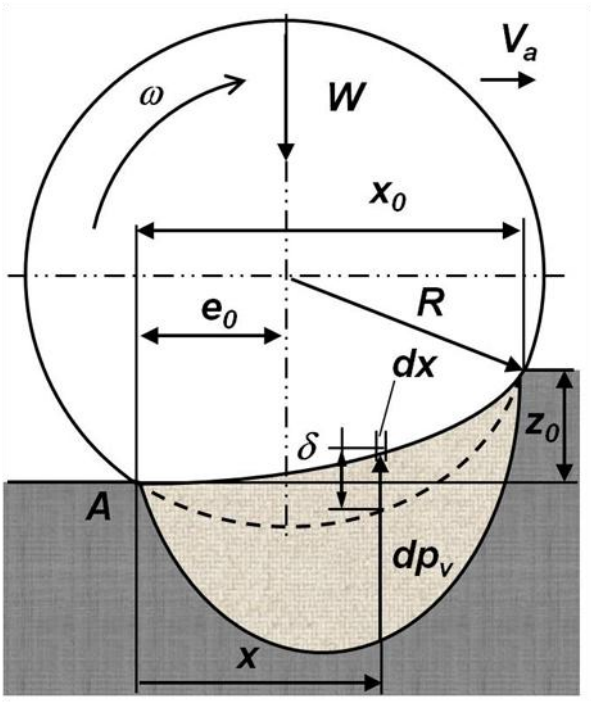

Fig. 19: Force equilibrium of the moving pneumatic wheel (redrawn from: Osetinsky and Shmulevich, 2004).

The coefficient of vertical stiffness of the tyre for unit length of the contact surface K_v is given by:

$$K_v = \frac{W}{R^2 \arcsin\left(\frac{x_0}{2R}\right) - \frac{x_0}{2}(R - \Delta)} \tag{11}$$

where Δ is the deflection of the pneumatic wheel on a hard surface and is calculated as:

$$\Delta = \frac{W}{(\Delta K_p P_{in} + K_{carc})} \tag{12}$$

The same equilibrium condition in equation 3 can be expressed in terms of the tyre stress state according to its stress–deflection relationship:

$$W = \int_0^{x_0} K_v \delta dx \tag{13}$$

According to equations 9, 10 and 11, integral 13 results in the following analytical solution:

$$W = K_v \left\{ \frac{a x_0^3}{3} - \sqrt{R^2 - e_0^2}\left(x_0 - \frac{e_0}{2} \right) + \frac{x_0 - e_0}{2}\sqrt{R^2 - (x_0 - e_0)^2} + \frac{R^2}{2}\left[\arcsin\left(\frac{x_0 - e_0}{R} \right) + \arcsin\left(\frac{e_0}{R} \right) \right] \right\} \tag{14}$$

The rut depth z_0 and the parameter a which define the soil-tyre contact surface are determined by simultaneously solving equations 6 and 14.

In order to calculate the relationship between the traction force and the slip of a moving wheel, usually referred to as traction performance, the development of the shear displacement along the wheel-soil interface has to be determined first, for which purpose a similar analysis for a rigid wheel, described by Wong and Reece (1967), can be used.

The absolute velocity of any circumferential point *B* on the wheel can be found according to Fig. 20:

$$V = V_a + V_\omega \tag{15}$$

here V is the absolute velocity, V_a is the actual forward velocity of the wheel and V_ω is the velocity relative to the centre of the wheel.

The absolute velocity of point *B* can be resolved into its normal and tangential components. The magnitude of the slip velocity V_j can be derived as the sum of the projections of the absolute velocity components on the tangential axis *j*, whose positive direction corresponds to that of the angular velocity of the wheel:

$$V_j = V_{\omega j} - V_{aj} \tag{16}$$

where V_{aj} is the tangential projection of the actual velocity of the wheel and $V_{\omega j}$ is the tangential projection of the velocity of point B relative to the centre of the wheel.

The slip velocity can be expressed as follows:

$$V_j = \omega r \cos \alpha_{\omega j} - V_a \cos \alpha \tag{17}$$

where r is the radius vector from the wheel centre, $\alpha_{\omega j}$ is the angle between the velocity of point *B* relative to the centre of the wheel and its projection on the *j* axis (Fig. 20), α is the angle between the *x*-axis and the tangent at point *B*, and ω is the angular velocity of the wheel corresponding to:

$$\omega = \frac{d(\alpha_{V\omega})}{dt} \tag{18}$$

in which $\alpha_{V\omega}$ is the angle between the vertical axis and the position of the radius vector to the current point on the soil-tyre contact surface.

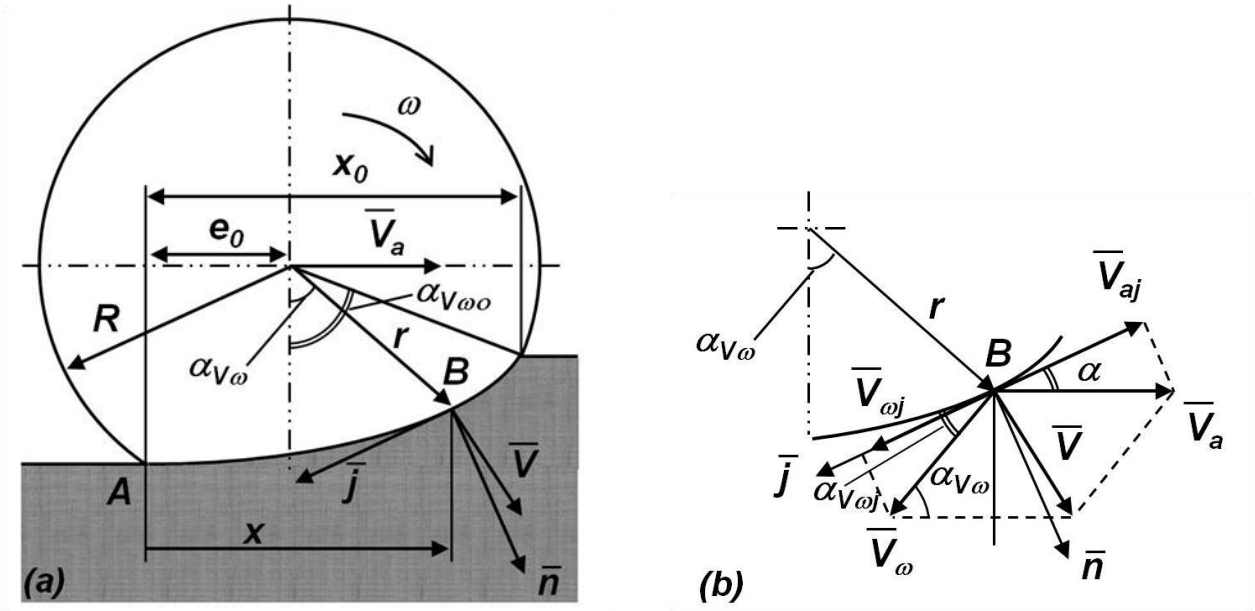

Fig. 20: Kinematic of a moving wheel: (a) absolute velocity of a circumferential point B, (b) evaluation of slip velocity of point B (redrawn from: Osetinsky and Shmulevich, 2004).

The soil shear displacement at point *B* can be found by integrating the slip velocity over time:

$$j = \int_0^t V_j dt \tag{19}$$

where *j* is the shear displacement of the soil at point *B*.

According to equations 17 and 18, integral 19 corresponds to:

$$j = \int_{\alpha_{V\omega}}^{\alpha_{V\omega 0}} \left(r\cos\alpha_{\omega j} - \frac{V_a}{\omega}\cos\alpha \right) d(\alpha_{V\omega}) \tag{20}$$

Since the configuration of the contact surface is known, all geometrical relationships are found in trigonometric and differential geometry terms as function of *x* (Appendix 1). Integral 20 can be rewritten as:

$$j = \int_x^{x_0} \frac{\left[ax(x-2e_0) + \sqrt{R^2 - e_0^2} - \frac{V_a}{\omega} \right] \left[ax(x-2e_0) + \sqrt{R^2 - e_0^2} \right]}{\sqrt{1+(2ax)^2} \left[\left(\sqrt{R^2 - e_0^2} - ax^2 \right)^2 + (x-e_0)^2 \right]} dx \tag{21}$$

The wheel slip *i* relates the actual forward velocity and the angular velocity of the wheel:

$$i = \frac{\varpi R_r - V_a}{\varpi R_r} \tag{22}$$

where R_r is the rolling radius of the wheel (ASAE S296.2).

Since an analytical solution of integral 21 results to be complicated, a numerical approach is adopted.

Fig. 21 shows elementary forces acting at soil-tyre contact according to Osetinsky and Shmulevich (2004). The horizontal and vertical components of the elementary force are given by:

$$p_h = (\sigma ds)\sin\alpha - (\tau ds)\cos\alpha \tag{23}$$

$$p_v = (\sigma ds)\cos\alpha + (\tau ds)\sin\alpha \tag{24}$$

where σ and τ are the normal stress and the tangential stress at the soil-tyre contact respectively.

Moreover, it results that (Fig. 21):

$$ds \sin\alpha = bdz \tag{25}$$

and

$$ds \cos\alpha = bdx \tag{26}$$

The shear stress at each point of the contact surface depends on the normal stress, the soil cohesion *c*, the angle of soil shear resistance *φ*, the soil shear deformation modulus *k*, and the soil shear displacement *j* along the contact surface. This dependence is described by the equation proposed by Janosi and Hanamoto (1961):

$$\tau = (c + \sigma \tan\varphi)\left(1 - e^{-j/k}\right) \tag{27}$$

The normal stress at each point of the contact surface is given by:

$$\sigma = \frac{\sigma_v - c\left(1 - e^{-j/k}\right)2ax}{1 + tg\varphi\left(1 - e^{-j/k}\right)2ax} \tag{28}$$

in which σ_v is the vertical component of the surface traction defined as in equation 8.

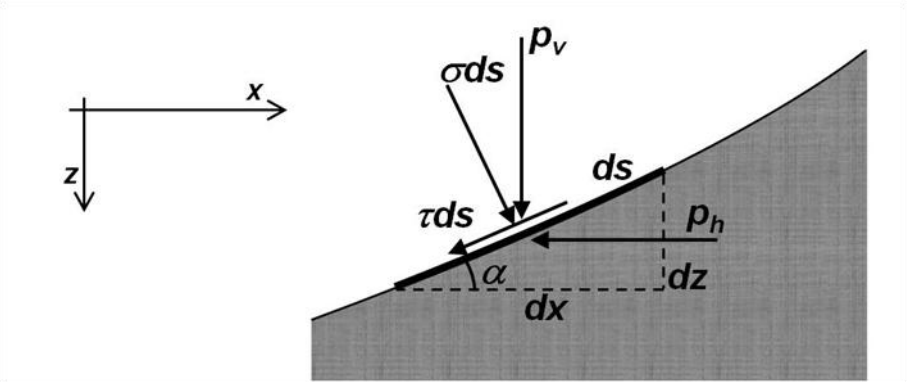

Fig. 21: Soil normal and tangential stresses on the contact surface with tyre (redrawn from: Osetinsky and Shmulevich, 2004).

The gross traction *GT* is obtained by integrating with a numerical approach the horizontal components p_h of the elementary force over the contact surface:

$$GT = \int_{x}^{x_0} p_h \tag{29}$$

according to equations 23, 25, 26, 27, and 28, this condition is rewritten as:

$$GT = \int_{x}^{x_0} \frac{\sigma_v\left[2ax - \tan\varphi\left(1 - e^{-j/k}\right)\right] - c\left(1 - e^{-j/k}\right)\left[(2ax)^2 + 1\right]}{1 + 2ax\left(1 - e^{-j/k}\right)\tan\varphi} b dx \tag{30}$$

According to the initial assumptions, the main resisting forces acting on a tractor when driving on flat terrain are represented by the internal resistance of the running gear and the resistance due to the interaction with terrain. Since the latter is, to a great extent, the most significant (Bekker, 1960; Wong, 2008), at least in first

approximation the internal resistance can be neglected. The resistance due to the interaction with terrain, according to Fig. 17, corresponds to the soil compaction resistance R_c. Additional soil bulldozing resistance has to be taken into account in soft soils where wheel sinkage is significant. In all the cases considered in this study the bulldozing effect was reliably expected not to occur because of the limited wheel sinkage values.

According to the approach presented by Bekker (1960) for a rigid wheel, the soil compaction resistance is calculated as the vertical work done in making a rut of depth z_0:

$$R_c = \int_0^{z_0} p_s b dz \tag{31}$$

where p_s is given by equation 2. Integral 31 results in:

$$R_c = \left(K_c + bK_\varphi\right)\frac{z_0^{n+1}}{n+1} \tag{32}$$

The net traction *NT* is finally calculated as:

$$NT = GT - R_c \tag{33}$$

The vertical component of the total soil reaction R_s equilibrates the load acting on the wheel and has a forward eccentricity relative to the wheel centre (Fig. 17). The eccentricity e_t relative to the rear point *A* of soil-tyre contact (Fig. 17) can be calculated from the equilibrium of the moving wheel. According to equation 7 it must result that:

$$We_t = \int_0^{x_0} K_v \delta x dx \tag{34}$$

Integral 34 is solved as reported in Appendix 2 and gives the following expression of e_t:

$$e_t = \frac{K_v}{W}\left\{\frac{z_0^2}{4a} + \frac{\sqrt{R^2-\left(x_0-e_0\right)^2}}{3}\left[\left(x_0-e_0\right)\left(x_0+\frac{e_0}{2}\right)-R^2\right] + \frac{\sqrt{R^2-e_0^2}}{3}\left(R^2+\frac{e_0^2}{2}-\frac{3}{2}x_0^2\right)\right.$$

$$\left. + \frac{R^2 e_0}{2}\left[\arcsin\left(\frac{x_0-e_0}{R}\right)+\arcsin\left(\frac{e_0}{R}\right)\right]\right\} \tag{35}$$

Both the wheel load and the vertical soil reaction produce a couple of forces, resulting in the resistance moment M_r opposite to the motion of the wheel:

$$M_r = W(e_t - e_0) \tag{36}$$

The point z_{GT} where the gross traction *GT* is applied (Fig. 17), can be found from the equilibrium of the moments acting on infinitesimal elements of the contact surface:

$$z_{GT} = \frac{1}{GT}\int_0^{x_0} \tau b z dx \tag{37}$$

which according to equations 1 and 27 can be rewritten as:

$$z_{GT} = \frac{1}{GT}\int_0^{x_0} (c + p_s \tan\varphi)(1 - e^{-j/k})(z_0 - ax^2)bdx \tag{38}$$

Similarly to integral 30, integral 38 needs a numerical approach.

The distance R_{GT} from the centre of the wheel to the point where the gross traction is applied can be calculated geometrically as follows:

$$R_{GT} = \sqrt{R^2 - e_0^2} - z_{GT} \tag{39}$$

The driving torque M_{GT} needed to achieve the required value of gross traction can be calculated as:

$$M_{GT} = GT\,\mathrm{R} \tag{40}$$

The total driving torque T should support the moment caused by the gross traction M_{GT} and the resistance moment M_r:

$$T = M_{GT} + M_r \tag{41}$$

The power input on the wheel is then given by the product of the total driving torque and the angular velocity of the wheel:

$$P_{inputon\,wheel} = T\omega \tag{42}$$

The tractive power is defined as the product of the net traction force and the actual forward velocity of the drive wheel:

$$P_{tractive\,wheel} = NTV_a \tag{43}$$

The traction efficiency of a drive wheel, which expresses the ratio of output power to input power of the wheel, is given by:

$$\eta_{tr\ wheel} = \frac{P_{tractive\,wheel}}{P_{inputon\,wheel}} = \frac{NTV_a}{T\omega} \tag{44}$$

The model described can be also used to simulate the traction performance of a system of dual tyres. In this case the dual tyres are considered, at least in first approximation, as one tyre having width and stiffness given by the sum of those of the two independent tyres.

1.2.1.2 Soil-tyre interaction model adapted for a mechanical front-wheel drive (MFWD) tractor

The soil-tyre interaction model was adapted to a MFWD tractor by considering the multi-pass effect, the dynamic wheel load due to the load transfer effect and the theoretical speed ratio K_s which controls the relationship between the slip of the front wheel i_{front} and that of the rear wheel i_{rear} of a tractor moving in straight line motion with rigid coupling between the front and the rear axles.

The multi-pass effect was considered by means of a differentiated mechanical characterisation of soil interacting with the front wheel and soil interacting with the rear wheel. Soil parameters were derived with bevameter tests before tractor passage as well as on the rut left from the passage of the front wheel, according to Bekker (1960).

When the net traction force is developed, the repartition of the tractor load between the front and the rear axles differs from that in stationary state due to a transfer of load toward the rear axle. Such effect is referred

to as load transfer effect and causes the rear axle load to rise when net traction increases with an opposite effect to the front axle. The dynamic wheel load was considered on the basis of the equilibrium condition of the tractor body (Fig. 22), as follows:

$$W_f = W_{0,f} - \Delta W \tag{45}$$

for the front wheel and

$$W_r = W_{0,r} + \Delta W \tag{46}$$

for the rear wheel.

The terms $W_{0,f}$ and $W_{0,r}$ are the stationary wheel loads on the front wheel and rear wheel respectively, whereas W_f and W_r are the wheel loads in dynamic conditions on the front wheel and rear wheel, respectively. The term ΔW is the difference between the wheel load in stationary and dynamic condition due to the load transfer effect. According to Fig. 22, ΔW is calculated as:

$$\Delta W = \frac{T_f + T_r + \left(NT_f + NT_r\right)\left(h - R_{r,r}\right) + NT_f\left(R_{r,r} - R_{r,f}\right)}{L} \tag{47}$$

in which T_f, NT_f, $R_{r,f}$ and T_r, NT_r, $R_{r,r}$ are, in order, the total driving torque, the net traction, and the rolling radius of the front wheel and the rear wheel respectively, h is the height of the drawbar measured on the field in the operating configuration, and L is the wheelbase of the tractor.

Equation 47 is derived assuming the rolling radius to be a good approximation of the height of the wheel hub and to be constant, and the rut depth small enough to be neglected in the calculation. This equation is valid when the pulling force is applied horizontally, which means that the total tractor weight remains constant, and only its distribution between the front and rear axles changes.

For a tractor with rigid coupling between the front and the rear axles, the ratio of the angular speed of the front wheel to that of the rear wheel, commonly referred to as the theoretical speed ratio K_s, is fixed, and therefore there is a precise relationship between the slip of the front wheel i_{front} and that of the rear wheel i_{rear} in straight line motion:

$$i_{front} = 1 - \frac{\left(1 - i_{rear}\right)}{K_s} \tag{48}$$

Preliminary tests with the MFWD tractors in the configurations considered have indicated values of K_s very close to 1, with a minimum of 0.993 and a maximum of 1.013, allowing a simplified analysis in which the slip of the front wheel and that of the rear wheel are assumed to be the same.

The traction performance of the tractor-soil system is given by the sum of the traction performances obtained for the two axles.

The net traction force developed by the tractor, usually referred to as drawbar pull, is given by the sum of the net traction of the drive wheels:

$$DP = \sum NT \tag{49}$$

When the tractor works in two wheel drive mode, the drawbar pull can be calculated as the sum of the net traction of the drive wheels minus the soil compaction resistance acting on the towed wheels.

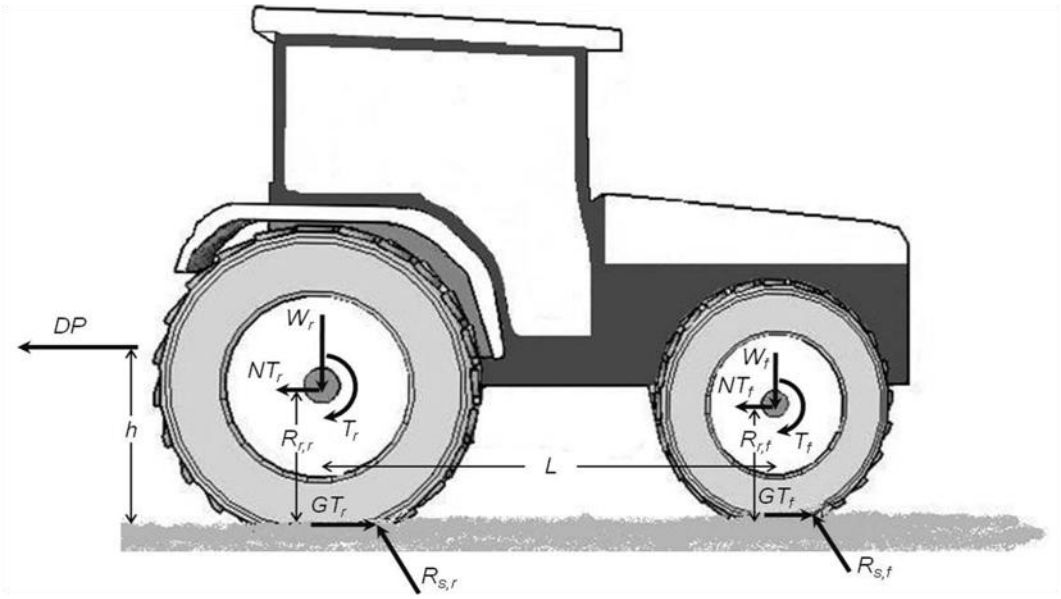

Fig. 22: Forces on a MFWD tractor.

The tractive power of the tractor is defined as the product of the drawbar pull and the actual forward velocity:

$$P_{tractivetractor} = DP\,V_a \tag{50}$$

The traction performance is often expressed in terms of the traction coefficient μ_{tr}, this latter defined as the drawbar pull *DP* to tractor weight $W_{tractor}$ ratio:

$$\mu_{tr} = \frac{DP}{W_{tractor}} \tag{51}$$

The traction efficiency of the tractor can be defined as:

$$\eta_{tr\,tractor} = \frac{DP\,V_a}{\sum T\omega} \tag{52}$$

which represents the fraction of power delivered to the tractor wheels that is available as tractive power.
The power delivery efficiency is defined as the ratio of the delivered tractive power to the tractor input power from the engine, and represents the fraction of power produced by the engine of a tractor that is available as tractive power (Shell et al., 1997; Turner et al., 1997). In order to consider the engine power input, the equivalent PTO (power-take-off) power can be used (Zoz et al., 2002), then the power delivery efficiency can be defined as:

$$\eta_{PD} = \frac{DP\,V_a}{Equivalent\ PTO\ power} \tag{53}$$

The model described was written in a Visual Basic code. The main steps of the calculation of traction performance are reported in the flowchart in Fig. 23. The calculation procedure can be divided into two main steps: the first defines the soil-tyre contact surface and the second calculates the traction performance in terms of gross traction, soil compaction resistance, net traction and total driving torque. Since a variation in slip in the range considered causes the tractor weight to distribute differently between the front and the rear axles, the calculation is repeated until a defined $slip_f$ value is reached.

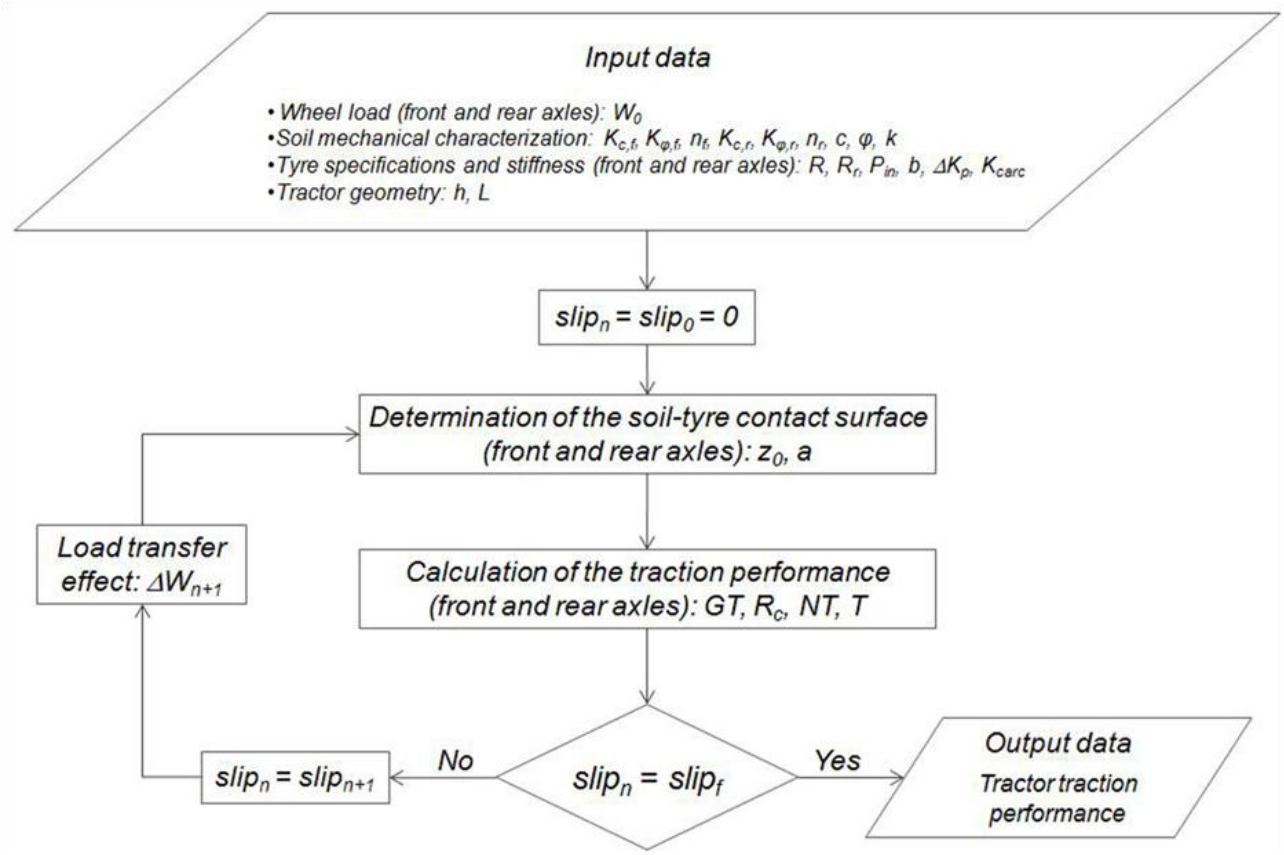

Fig. 23: Flowchart of the calculation procedure for tractor traction performance.

1.2.2 Experimental validation

1.2.2.1 Traction tests

Several traction tests were carried out with a MFWD Hürlimann H488 DT 65 kW tractor weighing 40 kN (tractor A). Such a tractor was chosen as a reference machine for this study.

Additional traction tests were carried out with a FIAT 50-66 DTS tractor of 40.4 kW weighing 25.3 kN (tractor B), a John Deere 6920 tractor of 110 kW weighing 66.7 kN (tractor C), and a John Deere 6930 tractor of 123 kW weighing 68 kN (tractor D).

The pulling force was obtained by means of a second tractor used as braking machine. In this case were used different tractors having weight always higher than the pulling tractor.

The pulling tractor and the braking tractor were connected by a steel cable and moved aligned as sketched in Fig. 24. Corridors 4 m wide and 70 m long were marked out in the field. The corridors were navigated in steady-state motion, controlling the drawbar pull developed by the pulling tractor with the braking tractor.

The pulling tractor moved in a rectilinear direction with locked differential, which allowed the highest traction performance to be achieved. The drawbar pull was varied from one corridor to the next, as was, therefore, the slip, which ranged between 0% and 35%, only in some cases higher values, up to 58%, were reached. The traction force was measured by load cells of capacity 50 kN and 200 kN (HBM U2B, Darmstadt, Germany) in section with the steel cable used to connect the two tractors (Fig. 25), the actual forward velocity was measured by a 100 Hz radar velocity sensor (Dickey-john RVS2, Auburn, Illinois, U.S.A.) in Fig. 26, whereas the wheel rolling velocity was registered by means of a wireless wheel speed sensor of two pulses per wheel revolution set on a rear wheel of the pulling tractor (Fig. 27).

All these parameters were recorded and displayed by an automatic acquisition system in the braking tractor. The load acting on the wheels in the stationary condition was measured with flat bed wheel load scales (Haenni WL 103, Jegenstorf, Switzerland).

In order to measure fuel consumption, the pulling tractor was fitted with an external fuel tank and a switch for changing between the internal and external fuel tanks (Fig. 28). The fuel consumption was measured as the difference in weight of the external fuel tank before and after driving along a corridor.

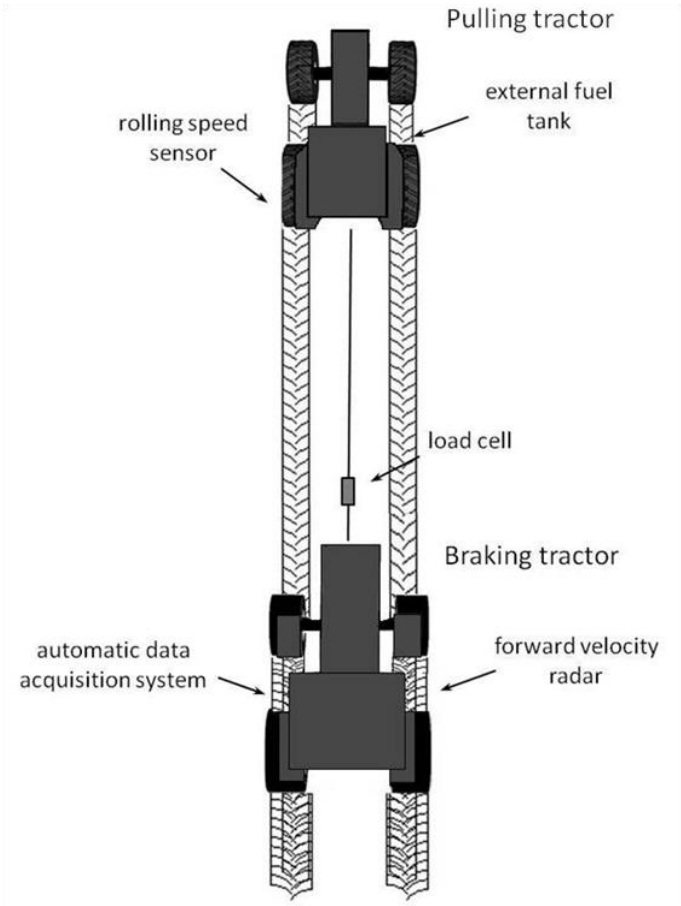

Fig. 24: Tractor pulling test layout.

Fig. 25: The 50 kN load cell for the measurement of pulling force.

Fig. 26: The 100 Hz radar velocity sensor.

Fig. 27: The wireless wheel speed sensor of two pulses per wheel revolution.

Fig. 28: The external tank for the measurement of the fuel consumption and the switch for changing between the internal and external fuel tanks.

Different tractor configurations were considered by changing the tyre inflation pressure, the wheel load, or by using dual tyres. The wheel load was changed by ballasting the tractor both at the front and at the back. The inflation pressure of the tyres was varied from 50 kPa to 160 kPa. A tyre pressure gauge (Motometer Mühlacker-Lomersheim, Germany) was used to measure the pressure.

A list of configurations of tractor A considered in this study is reported in Table 1. Configurations of tractors B, C, and D, are listed in Table 2, Table 3 and Table 4, respectively.

A mosaic of images from the tractor traction tests in the different locations with different tractors and configurations is reported in Fig. 29.

Table 1: Configurations of tractor A (reference tractor).

Tractor	Configuration	Tyre F / R / DF / DR*	Wheel load [kN] C / CL / SL / LS**	Tyre Pressure [kPa] C / CL / SL / LS**
Hürlimann H488 DT 65 kW	1	F R	9.1 / 9.1 / 9.1 / 9.1 10.9 / 10.9 / 10.9 / 10.9	60 / 60 / 60 / 60 60 / 60 / 60 / 60
	2	F R	9.1 / 9.1 / 9.1 / 9.1 10.9 / 10.9 / 10.9 / 10.9	160 / 160 / 160 / 160 160 / 160 / 160 / 160
	3	F R	10.3 / 10.3 / 10.3 / - 14.3 / 14.3 / 14.3 / -	60 / 60 / 60 / - 60 / 60 / 60 / -
	4	F R	10.3 / 10.3 / 10.3 / - 14.3 / 14.3 / 14.3 / -	160 / 160 / 160 / - 160 / 160 / 160 / -
	5	F R DR	- / - / 9.1 / 9.0 - / - / 12.7 / 12.6	- /- / 60 / 80 - / - / 60 / 80 - / - / 60 / 80
	6	F R DR	- / - / 9.1 / 9.0 - / - / 12.7 / 12.6	- / - / 160 / 160 - / - / 160 / 160 - / - / 160 / 160
	7	F R DR	- / - / 9.1 / 8.0 - / - / 16.1 / 24.4	- / - / 60 / 80 - / - / 60 / 80 - / - / 60 / 80
	8	F R DR	- / - / 9.1 / 8.0 - / - / 16.1 / 24.4	- / - / 160 / 160 - / - / 160 / 160 - / - / 160 / 160
	9	F R DF DR	- / - / 10.3 / - - / - / 12.8 / -	- /- / 60 / - - / - / 60 / - - / - / 60 / - - / - / 60 / -
	10	F R DF DR	- / - / 10.3 / - - / - / 12.8 / -	- /- / 160 / - - / - / 160 / - - / - / 160 / - - / - / 160 / -
	11	F R DF DR	- / - / 11.3 / - - / - / 16.4 / -	- /- / 60 / - - / - / 60 / - - / - / 60 / - - / - / 60 / -
	12	F R DF DR	- / - / 11.3 / - - / - / 16.4 / -	- /- / 160 / - - / - / 160 / - - / - / 160 / - - / - / 160 / -

* F = Front tyre (380/85R24); R = Rear tyre (420/85R34); DF = Dual front tyre (11.2R28); DR = Dual rear tyre (11.2R42)

** C = Clay; CL = Clay loam; SL = Silty loam; LS = Loamy sand

Table 2: Configurations of tractor B.

Tractor	Configuration	Tyre F / R / DF / DR*	Wheel load [kN] C / CL / SL / LS**	Tyre Pressure [kPa] C / CL / SL / LS**
FIAT 50-66 DTS 40.4 kW	1	F R	- / 5.8 / - / - - / 6.3 / - / -	- / 60 / - / - - / 90 / - / -
	2	F R	- / 5.8 / - / - - / 6.3 / - / -	- / 160 / - / - - / 180 / - / -
	3	F R	- / 7.0 / - / - - / 10.7 / - / -	- / 60 / - / - - / 90 / - / -
	4	F R	- / 7.0 / - / - - / 10.7 / - / -	- / 160 / - / - - / 180 / - / -

* F = Front tyre (8.3R24); R = Rear tyre (230/95R36); DF = Dual front tyre; DR = Dual rear tyre
** C = Clay; CL = Clay loam; SL = Silty loam; LS = Loamy sand

Table 3: Configurations of tractor C.

Tractor	Configuration	Tyre F / R / DF / DR*	Wheel load [kN] C / CL / SL / LS**	Tyre Pressure [kPa] C / CL / SL / LS**
John Deere 6920 110 kW	1	F R	- / 14.1 / - / - - / 19.1 / - / -	- / 50 / - / - - / 50 / - / -
	2	F R	- / 14.1 / - / - - / 19.1 / - / -	- / 140 / - / - - / 140 / - / -

* F = Front tyre (540/65R28); R = Rear tyre (650/65R38); DF = Dual front tyre; DR = Dual rear tyre
** C = Clay; CL = Clay loam; SL = Silty loam; LS = Loamy sand

Table 4: Configurations of tractor D.

Tractor	Configuration	Tyre F / R / DF / DR*	Wheel load [kN] C / CL / SL / LS**	Tyre Pressure [kPa] C / CL / SL / LS**
John Deere 6930 123 kW	1	F R	- / - / - / 14.7 - / - / - / 19.3	- / - / - / 60 - / - / - / 60
	2	F R	- / - / - / 14.7 - / - / - / 19.3	- / - / - / 140 - / - / - / 180
	3	F R	- / - / - / 14.3 - / - / - / 31.0	- / - / - / 60 - / - / - / 60
	4	F R	- / - / - / 14.3 - / - / - / 31.0	- / - / - / 140 - / - / - / 180

* F = Front tyre (540/65R28); R = Rear tyre (650/65R38); DF = Dual front tyre; DR = Dual rear tyre
** C = Clay; CL = Clay loam; SL = Silty loam; LS = Loamy sand

(a)

(b)

(c)

(d)

Fig. 29: Tractor pulling tests: (a) tractor B on the clay loam field with wheat stubble (Tänikon -CH), (b) tractor A on the clay loam field with wheat stubble (Tänikon), (c) tractor C on the clay loam field with wheat stubble (Tänikon), (d) tractor A on the silty loam field with corn stubble (Frauenfeld - CH).

1.2.2.2 Soil characterisation

The traction tests were carried out on four sites having different soil textures: a clay field with corn stubble in Tänikon, Ettenhausen (CH) [47° 28’ 52” N, 8° 54’ 14” E], a clay loam field with wheat stubble in Tänikon [47° 29’ 0” N, 8° 54’ 44” E], a silty loam field with corn stubble in Frauenfeld (CH) [47° 34’ 32” N, 8° 52’ 20” E], and a loamy sand field with corn stubble in Witzwil (CH) [46° 59’ 30” N, 7° 03’ 24” E]. Physical and mechanical parameters of topsoil (0-0.1 m depth) of the four sites are reported in Table 5.

The volumetric water content θ was measured by means of a time domain reflectometry (TDR) device (E.S.I. Environmental sensors MP-917, Sidney, Canada) with two-rod single diode probes (Fig. 30) at 0.1 m depth. The water potential at 5 and 10 cm depth was measured with field tensiometers, while the penetration resistance was measured with a penetrometer fitted with a 6 mm wide screwdriver n. 4. as tip. (Fig. 31).

Mechanical soil parameters required for the soil-tyre interaction simulation were obtained on the basis of the soil pressure-sinkage relationship in vertical plate penetration tests and the soil shear stress-displacement relationship in horizontal plate shear deformation tests (Bekker, 1960) with a tractor-mounted Bevameter (Fig. 32) (Diserens and Steinmann, 2003). The bevameter has a massive frame with a central jack using the hydraulic system of the tractor. A laptop and a datalogger are used for the automatic acquisition of the data during the tests. A load cell of capacity 50 kN is used to measure the applied vertical force, a torque cell of 2 kNm is used to measure the applied torque. The vertical soil sinkage is measured by means of an ultrasound sensor which stands on a tripod frame and reflects its signal on a specific plate on top of the link to the

compression plate. The rotation of the lugged plate (Fig. 32), used in the shear deformation tests, is measured by a tachometer. The vertical plate penetration tests are executed with two circular plates of diameter 0.2 and 0.3 m (Fig. 33). In such a way the influence of the width of the contact area on the soil pressure-sinkage relationship is analysed. The experimental relationship was fitted with equation 2 and parameters K_c, K_φ and n were determined according to the fitting procedure described by Wong (1980).

Table 5: Physical and mechanical parameters of topsoil in the four locations considered.

Soil property 0-0.10 m depth	C*	CL	SL	LS
Sand [%]	20	31	20	84.2
Silt [%]	32	34	53	7.6
Clay [%]	48	35	27	5.7
Texture	Clay	Clay loam	Silty loam	Loamy sand
Volumetric water content θ [%]	27.0	28.4	40.2	15.2
Matric suction s [kPa]	6.11	9.45	1.27	57.40
Penetration resistance PR [N]	91.7	124.6	47.1	106.9
Cohesive modulus of deformation (front) $K_{c,f}$ [kN/m$^{(n+1)}$]	2354.1	4554.8	298.2	1208.2
Frictional modulus of deformation (front) $K_{\varphi,f}$ [kN/m$^{(n+2)}$]	-4130.0	-3036.5	479.0	-805.5
Exponent of deformation (front) n_f	1.01	0.90	0.77	0.81
Cohesive modulus of deformation (rear) $K_{c,r}$ [kN/m$^{(n+1)}$]	2168.9	4554.8	298.2	1208.2
Frictional modulus of deformation (rear) $K_{\varphi,r}$ [kN/m$^{(n+2)}$]	-3498.3	-3036.5	479.0	-805.5
Exponent of deformation (rear) n_r	0.79	0.90	0.77	0.81
Cohesion c [kPa]	24.4	5.0	15.9	29.2
Angle of shear resistance φ [°]	18.0	30.0	25.6	6.4
Shear deformation modulus k [m]	0.014	0.010	0.010	0.012

*C = Clay; CL = Clay loam; SL = Silty loam; LS = Loamy sand

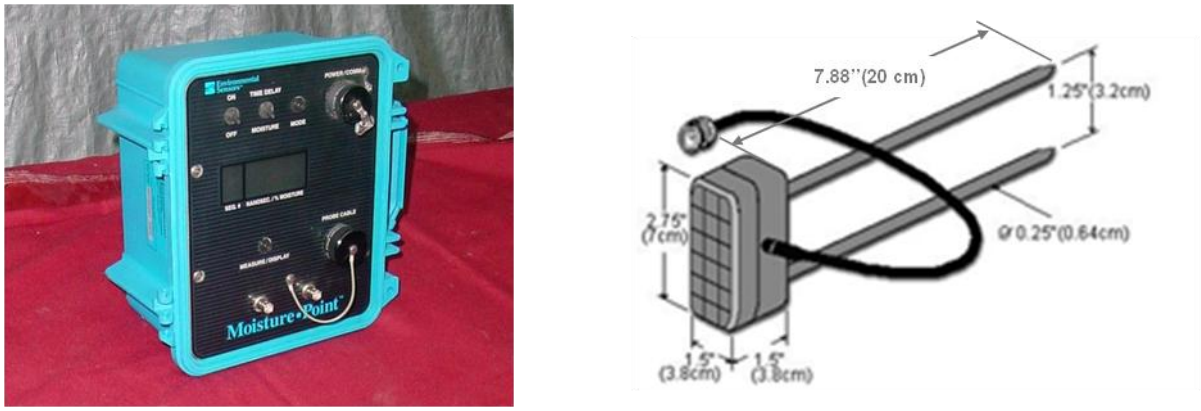

Fig. 30: The time domain reflectometry (TDR) device (E.S.I. Environmental sensors MP-917), with two-rod single diode probes (www.esica.com).

Fig. 31: The penetrometer fitted with a 6 mm wide screwdriver n. 4. used for measuring the soil penetration resistance.

Fig. 32: The tractor-mounted bevameter.

Fig. 34 shows the experimental and the fitted soil pressure-sinkage relationship for the four terrains considered, obtained with the compression plate of 0.2 m in diameter. The same relationship obtained with the compression plate of 0.3 m in diameter is reported in Fig. 35. In Fig. 34 and in Fig. 35 the first load corresponds to the test executed before the passage of the tractor, whilst the second load refers to the test execute on the rut left from the passage of the front wheel. The compression velocity was around 2 10^{-3} m/s, according to the indications reported by Bekker (1956).

Fig. 33: The circular plate of diameter 0.3 m used for soil penetration tests.

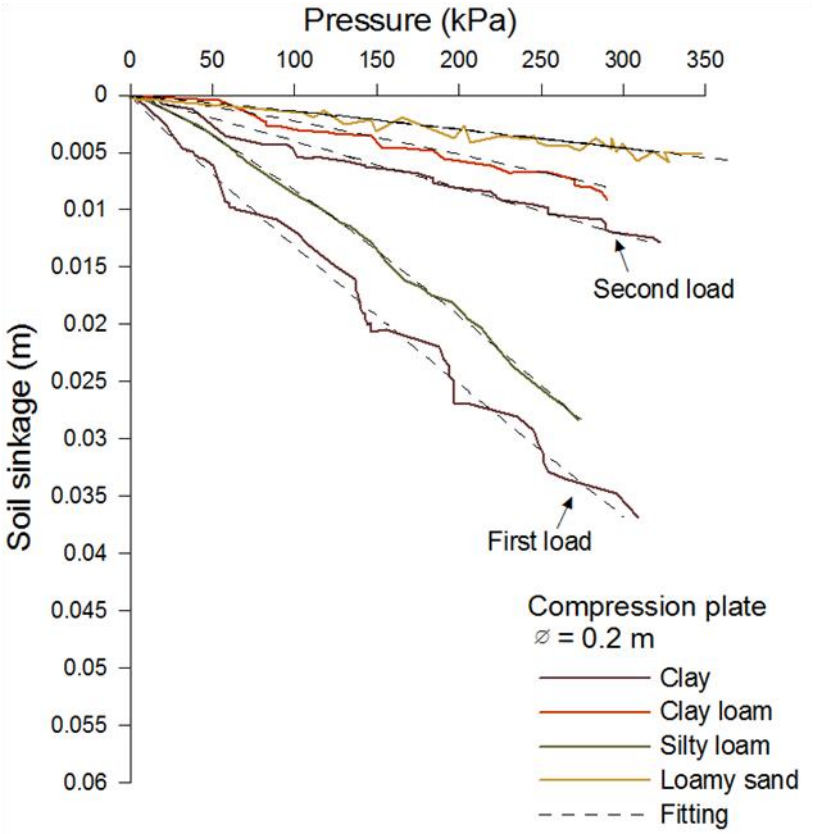

Fig. 34: Experimental and fitted pressure-sinkage relationship for the four terrains considered from bevameter tests with the compression plate of 0.2 m in diameter.

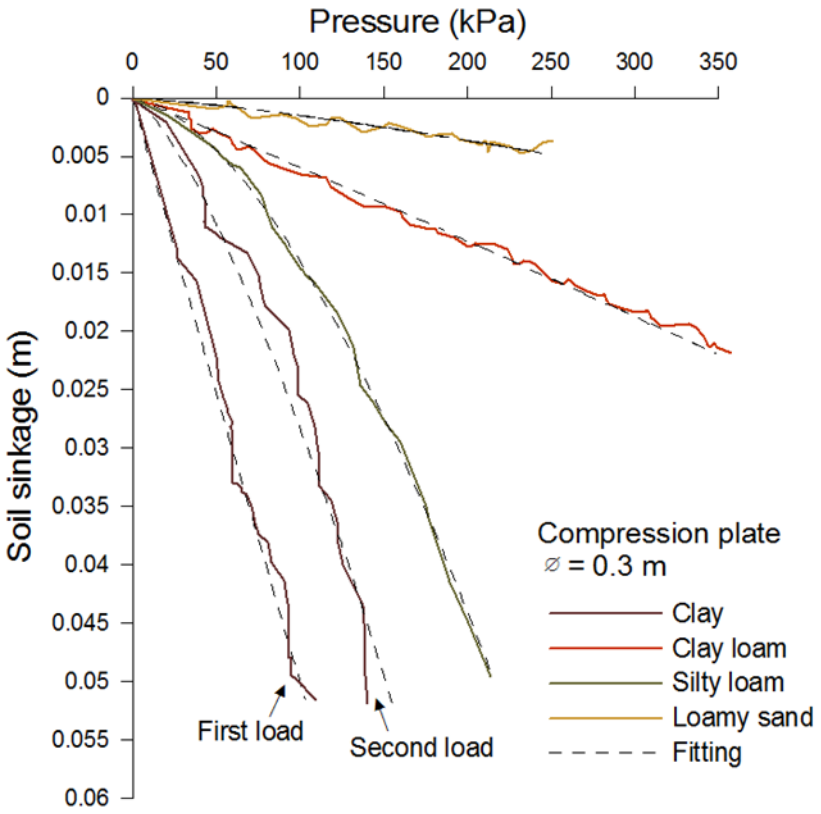

Fig. 35: Experimental and fitted pressure-sinkage relationship for the four terrains considered from bevameter tests with the compression plate of 0.3 m in diameter.

In the horizontal plate shear deformation tests it is used a lugged plate (Fig. 36) on which a torque is applied and the relationship between torque and rotation of the plate (i.e. soil displacement) is measured. Such a relationship is measured under different vertical pressures and maximum values are used in order to derive the Mohr-Coulomb failure envelope. The experimental relationship is fitted with equation 27 and soil strength parameters are derived according to the procedure described by Wong (1980). In Fig. 37 is reported the experimental shear stress-displacement relationship obtained for the silty loam, compared with the fitted one. In Fig. 38 is reported the failure envelope for the four terrains considered.

In order to consider the multi-pass effect, i.e. the different behaviour of soil interacting with the front wheel and the rear wheel, the vertical plate penetration tests and the horizontal plate shear deformation tests were executed before tractor passage as well as on the rut left from the passage of the front wheel. Parameters K_c, K_φ and n calculated before and after the passage of the front wheel changed significantly in the clay soil, but not in the other soils which were widely trafficked, consequently, they were differentiated for soil interacting with the front wheel ($K_{c,f}$, $K_{\varphi,f}$, n_f) and soil interacting with the rear wheel ($K_{c,r}$, $K_{\varphi,r}$, n_r), as reported in Table 5. The shear parameters c, φ and k did not change significantly before and after the passage of the front wheel in all locations and for these a unique characterisation was adopted (Table 5).

Fig. 36: The lugged plate for shear deformation tests.

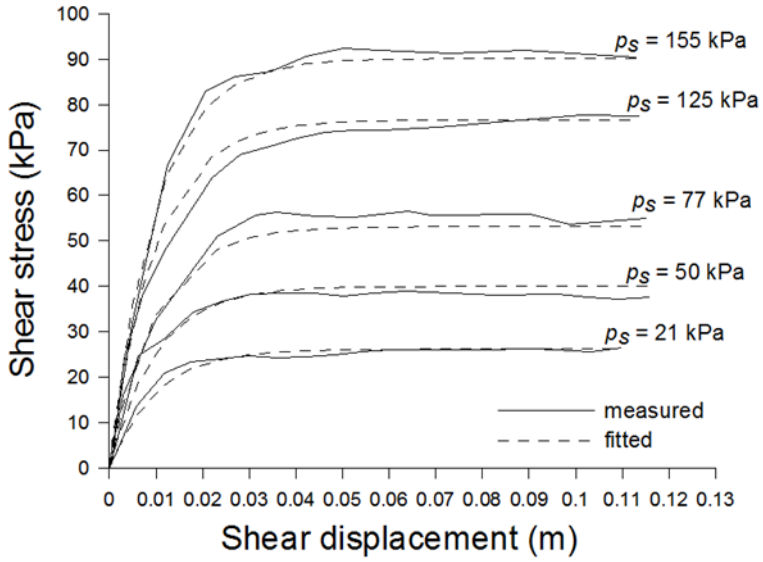

Fig. 37: Experimental and fitted shear stress-displacement relationship from bevameter tests on a silty loam.

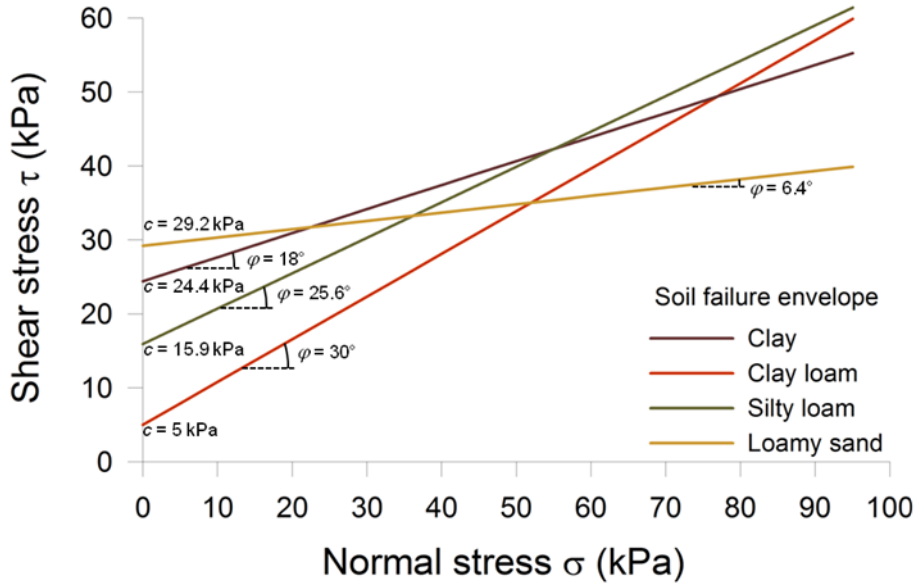

Fig. 38: Failure envelope according to Mohr-Coulomb for the four terrains considered.

1.2.2.3 Tyre characterisation

The tyre rolling radius R_r was determined according to the ASAE Standard S296.2, as the distance travelled per revolution of the wheel divided by 2π when operating at the specified zero condition. This latter was here assumed as the vehicle operating in self-propelled condition on a hard surface, such as a smooth road, according to Wismer and Luth (1973).

This condition allows the travel reduction (slip) to have a fixed base not depending on the test condition (soil strength) (Wismer and Luth, 1973).

Moreover the difference in measured rolling radii between a hard surface and a test surface is small under normal agricultural soil conditions (untilled soil) and thus makes little difference in the final results (Zoz and Grisso, 2003).

Fig. 39 shows the variation of the rolling radius with the inflation pressure and the wheel load for the front wheel (tyre 380/85R24) and the rear wheel (tyre 420/85R34) of tractor A.

As in the model of Osentinsky and Shmulevich (2004), the tyre stiffness was derived on the basis of the tyre dimensions according to the empirical relationship proposed by Lines and Murphy (1991).

In one case the radial stiffness of a 420/85R34 tyre was measured in stationary condition (Fig. 40). Here the wheel load was ranged between 4.9 kN and 22.2 kN by ballasting the tractor, and the inflation pressure was varied between 60 kPa and 160 kPa.

Vertical deflection of the tyre was measured by means of a laser distance meter (Leica DISTO A8, Leica Geosystems AG, Heerbrugg, CH) fixed to the tractor frame.

An example of the tractor parameters used for the simulation of the traction performance of tractor A in configurations 1, 2, 3 and 4 (Table 1), is reported in Table 6.

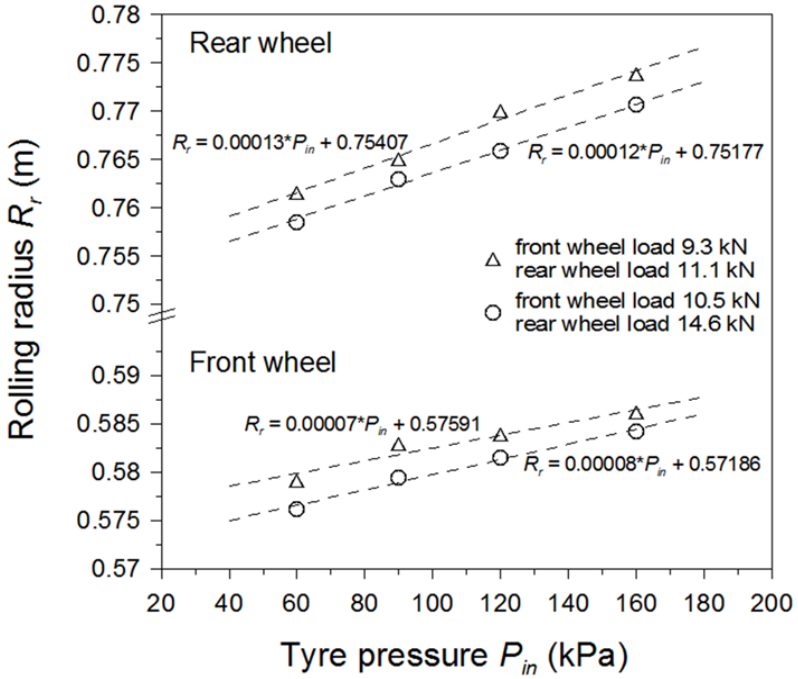

Fig. 39: Rolling radius at different inflation pressures and wheel loads for the front wheel (tyre 380/85R24) and the rear wheel (tyre 420/85R34) of tractor A.

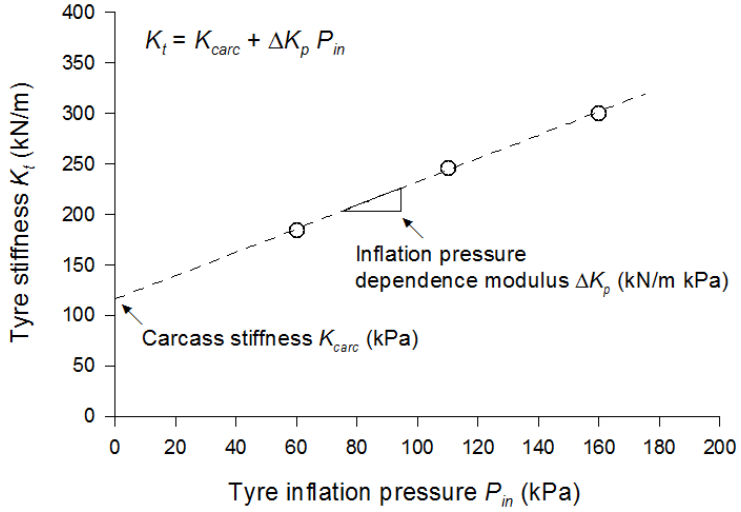

Fig. 40: Experimental and fitted tyre stiffness at different inflation pressures for the rear wheel (tyre 420/85R34) of tractor A.

Table 6: Parameters of tractor A used for simulating the traction performance in configurations 1, 2, 3 and 4.

Wheelbase L [m]	2.34			
Tyre (front - rear)	380/85R24 - 420/85R34			
Tyre width b (front - rear) [m]	0.38 - 0.44			
Tyre unloaded radius R (front - rear) [m]	0.63 - 0.79			
Rim diameter D_{rim} (front - rear) [m]	0.61 - 0.86			
Tyre carcass stiffness K_{carc} (front - rear) [kN m^{-1}]	129.5 - 111.8			
Pressure dependence of tyre ΔK_p (front - rear) [kN m^{-1} kPa^{-1}]	1.22 - 2.00			
Configuration	1	2	3	4
Height of the drawbar h [m]	0.80	0.83	0.71	0.77
Stationary wheel load W_0 (front - rear) [kN]	9.1 - 10.9	9.1 - 10.9	10.3 - 14.3	10.3 - 14.3
Tyre rolling radius R_r (front - rear) [m]	0.58 - 0.76	0.59 - 0.77	0.58 - 0.76	0.58 - 0.77
Tyre inflation pressure P_{in} (front - rear) [kPa]	60 - 60	160 - 160	60 - 60	160 - 160
Tyre stiffness (front - rear) [kN m^{-1}]	203 - 232	325 - 432	203 - 232	325 - 432

1.3 Results

1.3.1 Simulation of traction performance of mechanical front-wheel drive (MFWD) tractors

1.3.1.1 Soil-tyre contact surface and stress state

A simulation of the soil-tyre contact surface for the front and rear wheel of tractor A in configuration 1 on the clay soil is reported in Fig. 41 for slip values of 5%, 10%, 15%, and 20%. In the same figure is also reported the distribution of the slip velocity V_j along the soil-tyre contact. The load acting on the front wheel is lower than that acting on the rear wheel (9.1 kN and 10.9 kN respectively), however, it is distributed on a smaller contact surface, this fact makes for a deeper rut under the front wheel than under the rear one. Due to the load transfer effect, the wheel load acting on the front and rear wheel varies as a function of the drawbar pull and the slip. The wheel load on the front wheel decreases with increasing slip, whilst the wheel load on the rear wheel increases with slip. As a consequence, the rut depth of the front wheel decreases with slip whilst the rut depth of the rear wheel increases with slip. The length of the contact surface also varies with the wheel load, becoming longer when the wheel load increases, and shorter when the wheel load decreases. The variation of the wheel load with slip for the front and rear wheel of tractor A in configuration 1 (Table 1) on the clay soil (Table 5) is reported in Fig. 42. In the condition considered, the wheel load acting on the front wheel in stationary condition is 9.1 kN and that acting on the rear wheel is 10.9 kN. When a drawbar pull is developed, the load acting on the front wheel decreases progressively to 4.3 kN at a slip of 35%, whilst the load acting on the rear wheel rises up to 16.1 kN at a slip of 35% (Fig. 42). The wheel load does not vary till a slip of 4% is reached (Fig. 42), this slip value corresponds to the self-propulsion point (self-propelled point), that is the point on a drawbar pull-slip curve at which the vehicle is just able to propel itself (i.e. zero drawbar pull). Beyond a slip of 4%, the wheel load is progressively transferred from the front axle to the rear one, and this transfer shows a high gradient in the range of slip values from 4% to 15%, which is the same range where the drawbar pull rises very sharply. At higher values of slip, the transfer of load from the front axle to the rear one drops, and the wheel load tends to a constant value (horizontal asymptote of the wheel load-slip curve). In this range of slip also the drawbar pull increases slightly with slip, and tends to a constant value which is its maximum value. According to equation 47, the sum of the wheel loads acting on the wheels of the tractor doesn't vary because the drawbar pull is assumed to be applied horizontally. In Fig. 43 is reported the variation of the rut depth of the front and rear wheel of tractor A in configuration 1 (Table 1) on the clay soil (Table 5), as a function on the slip. According to the variation of wheel load, the rut depth of both the front and the rear wheel doesn't change till a slip of 4% is reached, beyond this value the rut depth of the front wheel reduces significantly from 0.036 m to 0.023 m, whilst the rut depth of the rear wheel becomes deeper from 0.013 m to 0.016 m. When the load transfer effect reduces and the wheel load tends towards a constant value, also the rut depth shows an asymptotic behaviour. Similarly to the rut depth, also the length of the contact surface, reported in Fig. 44, varies with slip due to the load transferred from the front to the rear axle. In the same case considered in Fig. 42 and Fig. 43, the length of the soil-tyre contact surface remains constant as long as a slip of 4% is not exceeded. In this range of slip values the length of the contact surface of the front wheel is 0.52 m, and that of the rear wheel is 0.56 m. Beyond a slip of 4%, the length of the contact surface of the front wheel decreases tending to a value of 0.37 m, whilst the length of the contact surface of the rear wheel increases tending towards a value of 0.67 m.

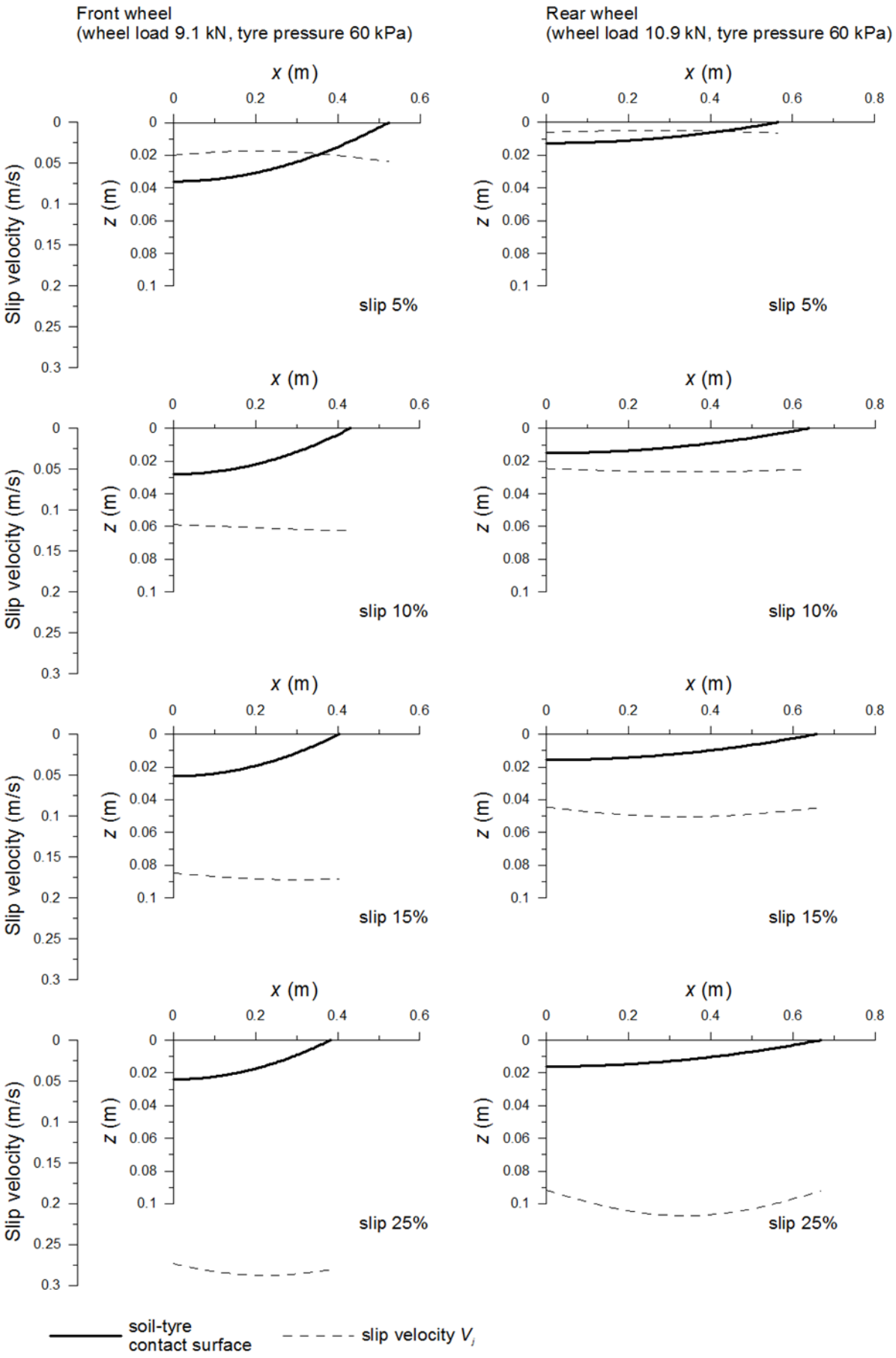

Fig. 41: Simulation of the distribution of the slip velocity along the soil-tyre contact surface for the front and rear wheel of tractor A in configuration 1 (Table 1) on the clay soil.

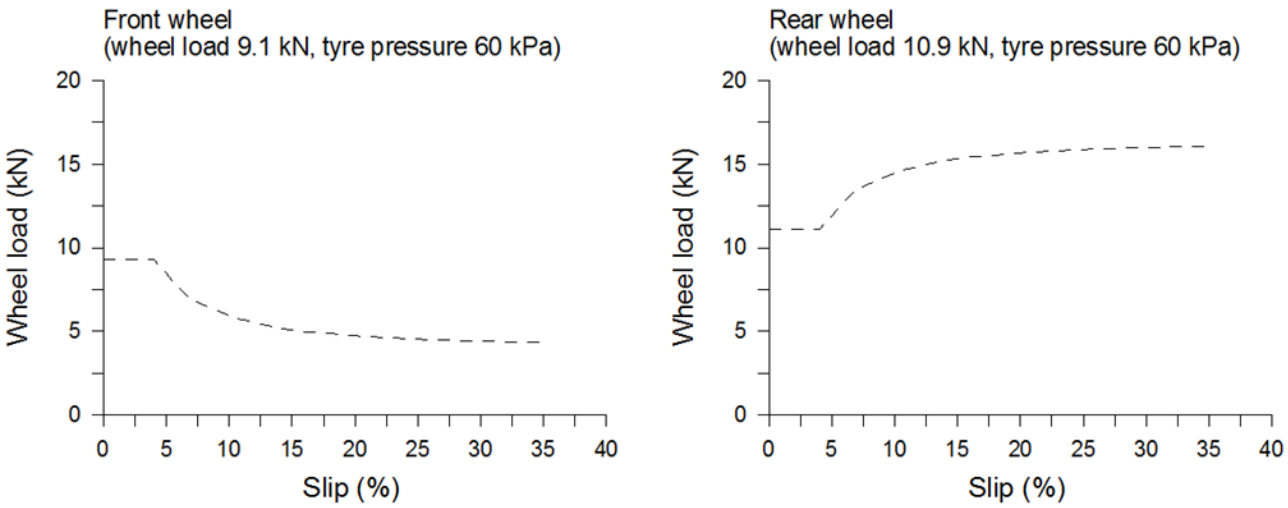

Fig. 42: Simulation of the variation of the wheel load with slip for the front and rear wheel of tractor A in configuration 1 (Table 1) on the clay soil.

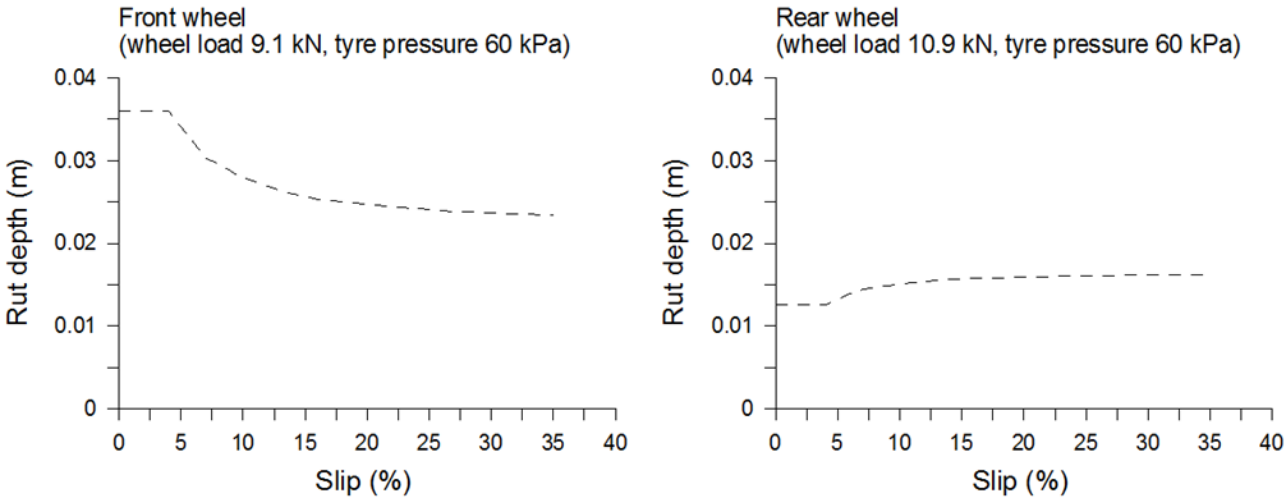

Fig. 43: Simulation of the variation of the rut depth with slip for the front and rear wheel of tractor A in configuration 1 (Table 1) on the clay soil.

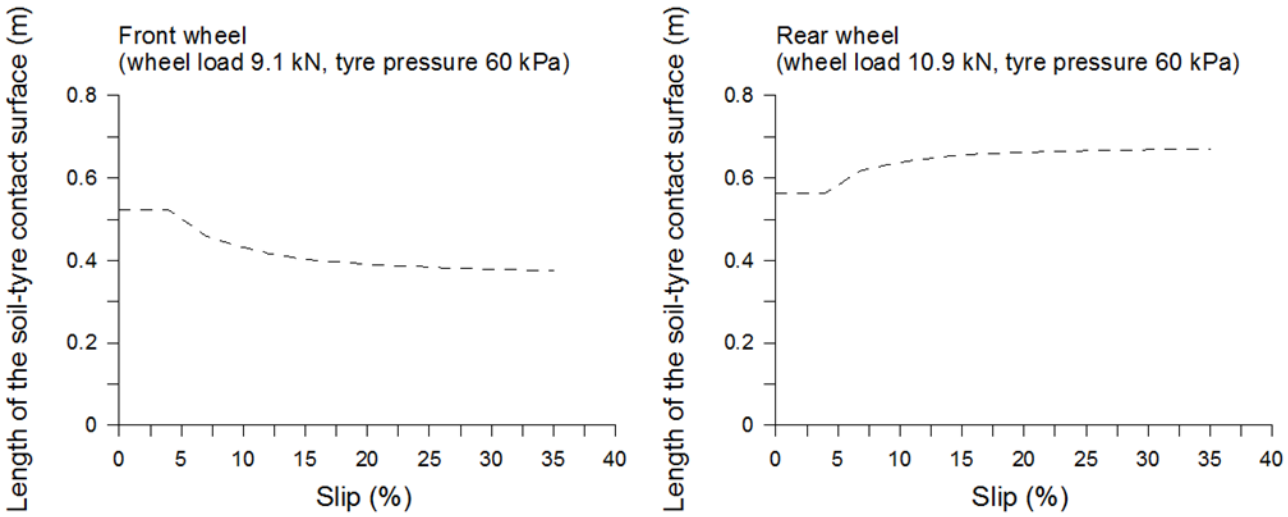

Fig. 44: Simulation of the variation of the length of the soil-tyre contact surface with slip for the front and rear wheel of tractor A in configuration 1 (Table 1) on the clay soil.

The rut depth and the length of the contact surface define the geometry of the soil-tyre contact surface, their values are the result of the stress-strain interaction between the two media, which is simulated by the model presented in the previous section. Among the other factors, this interaction depends on the wheel load and the stiffness of both the tyre and the soil. A given increase of wheel load may turn out in a deeper rut depth, to a greater or lesser extent, depending on the difference of stiffness between the soil and the tyre. If the soil stiffness is much higher than that of the tyre, like in the case of a hard soil surface trafficked by tyres at a low pressure, an increase in wheel load is likely to produce a big deflection of the tyre, with a consequent increase in contact length, rather than resulting in a deeper rut due to a greater penetration of the tyre into the soil. The opposite case is represented by a highly inflated tyre on a very soft surface, in this condition an increase in wheel load is more likely to produce a much deeper rut than a greater deflection of the tyre. This latter, in fact, behaves similarly to a rigid wheel and the length of the contact surface increases mainly due to a deeper sinkage of the wheel into the soil.

The slip velocity V_j, reported in Fig. 41, is calculated as the sum of the projections of the absolute velocity components on the tangential axis *j*, whose positive direction corresponds to that of the wheel angular velocity (Fig. 20). The slip velocity varies along the soil-tyre contact surface, and its value, according to equation 17, depends on the geometry of the contact surface, in particular it is a function of: the radius vector from the wheel centre *r*, the angle $\alpha_{\omega j}$ between the velocity of the point considered relative to the centre of the wheel and its projection on the *j* axis, and the angle α between the *x*-axis and the tangent at the point considered (Fig. 20). Furthermore, the slip velocity depends on the actual forward velocity of the wheel V_a, as well as on the angular velocity of the wheel ω (Fig. 20), therefore, it varies with the slip, defined as in equation 22, which relates the actual forward velocity and the angular velocity of the wheel. The highest slip velocity along the soil-tyre contact surface of the front wheel ranges from 0.048 m/s, at a slip of 5%, to 0.29 m/s at a slip of 25%. The slip velocity along the rear wheel is lower than along the front wheel, this fact finds an explanation in the different geometrical configuration of the soil-tyre contact surface of the front and rear wheel, i.e. the different tyre deflection, soil sinkage, and ratio between the rut depth and the length of the contact surface. The geometry of the contact surface is controlled by the two parameters, z_0 and *a*, which define the parabola. The highest slip velocity along the soil-tyre contact surface of the rear wheel ranges from 0.01 m/s, at a slip of 5%, to 0.21 m/s at a slip of 25%.

Fig. 45 reports the simulation of the distribution of the soil shear displacement along the soil-tyre contact surface of the front and rear wheel of tractor A in configuration 1 on the clay soil. The soil shear displacement is calculated by integrating the slip velocity over time, as in equation 19. It increases along the soil-tyre contact surface from the front contact point to the last contact point which correspond to the maximum value of *x* and the origin of the axes ($x = 0$), respectively. The variation is nearly linear and the magnitude of the shear displacement rises with slip according to the increase in slip velocity.

The maximum shear displacement under the front tyre ranges from 0.02 m, at a slip of 5%, to 0.11 m, at a slip of 25%. Under the rear wheel, the maximum shear displacement turned out to vary in the range from 0.01 m to 0.14 m for slip values of 5% and 25%, respectively. The shear displacement depends on both the slip velocity and the length of the contact surface. A higher slip velocity makes for a greater shear displacement, this result is pointed out by the greater shear displacement under the front wheel compared to the rear wheel at a slip less than or equal to 15%. A longer contact surface generates a greater shear displacement, this effect is evident when the shear displacement under the front wheel is compared to that

under the rear wheel at a slip of 25%. Here, in spite of a higher slip velocity under the front wheel than under the rear wheel (Fig. 41), the maximum shear displacement occurs under the rear wheel due to a longer contact surface, or, analogously, a longer time of contact between the soil and the wheel. The effect of the higher slip velocity under the front wheel seems to prevail till a slip value of about 15% is reached, beyond this value the maximum shear displacement results higher under the rear wheel, this indicating a greater influence of the length of the contact surface.

The stress distribution along the soil-tyre contact surface of the front wheel and rear wheel of tractor A in the same condition considered above, is reported in Fig. 46. The stress state is shown for slip values from 5% to 25% in terms of normal stress σ, and shear stress τ. The first is given by equation 28, whilst the second is described by equation 27. Furthermore, the soil strength τ_{max} is also shown, this latter is defined as:

$$\tau_{max} = (c + \sigma \tan\varphi) \tag{54}$$

and represents the soil failure condition under a given normal pressure. The soil strength is also the highest value of the shear stress at the soil-tyre contact surface, being the horizontal asymptote of equation 27.

The normal stress at the soil-tyre contact surface varies with slip due to the load transfer effect, particularly, it decreases under the front wheel and increases under the rear wheel. At a slip of 5% the maximum normal stress σ is 66.8 kPa under the front wheel, and 66.4 kPa under the rear wheel. At a slip of 25% the maximum normal stress under the front wheel drops to 43.8 kPa, whilst the maximum normal stress under the rear wheel rises to 79.3 kPa.

The shear stress τ increases with the normal stress and the soil shear displacement, according to equation 27. When the slip increases, the shear stress approaches the soil strength, at first at the rear point of the contact surface, corresponding to x = 0. The maximum shear stress under the front wheel ranges from 26.4 kPa at a slip of 5%, to 37.8 kPa at a slip of 25%. In this case the increase in shear displacement prevails on the reduction in normal stress, and the peak of shear stress under the front wheel increases with slip. The same shear stress rises sharply under the rear wheel, from 10.5 kPa, at a slip of 5%, to 49.7 kPa, at a slip of 25%.

The soil strength along the soil-tyre contact surface changes according to the variation of the normal stress, therefore, it drops with slip under the front wheel, and rises with slip under the rear wheel. Peak values of the soil strength range from 46.4 kPa to 38.6 kPa under the front wheel at slip of 5% and 25%, respectively, and from 46.0 kPa to 50.2 kPa under the rear wheel at 5% and 25% of slip, respectively.

The stress state at the contact surface is the result of the interaction between the soil and the tyre and controls the traction performance of the wheel or of the tractor, in a four-wheel system. In order to better understand the variation of the soil stress state at the soil-tyre contact, a representation of the stress paths along the contact surface may be of great help.

In Fig. 47, soil stress paths along the contact surface with the tyre, for the front and the rear wheel of tractor A in the same condition considered above, are represented in terms of mean stress $p = (\sigma_1+\sigma_3)/2$ and deviatoric stress $q = (\sigma_1-\sigma_3)/2$. The terms σ_1 and σ_3 are respectively, the greatest principal stress, and the smallest principal stress, which are univocally defined when the tangent plane to each point of the soil-tyre contact surface is assumed as the critical plane, i.e. the plane on which the ratio τ/σ is maximum.

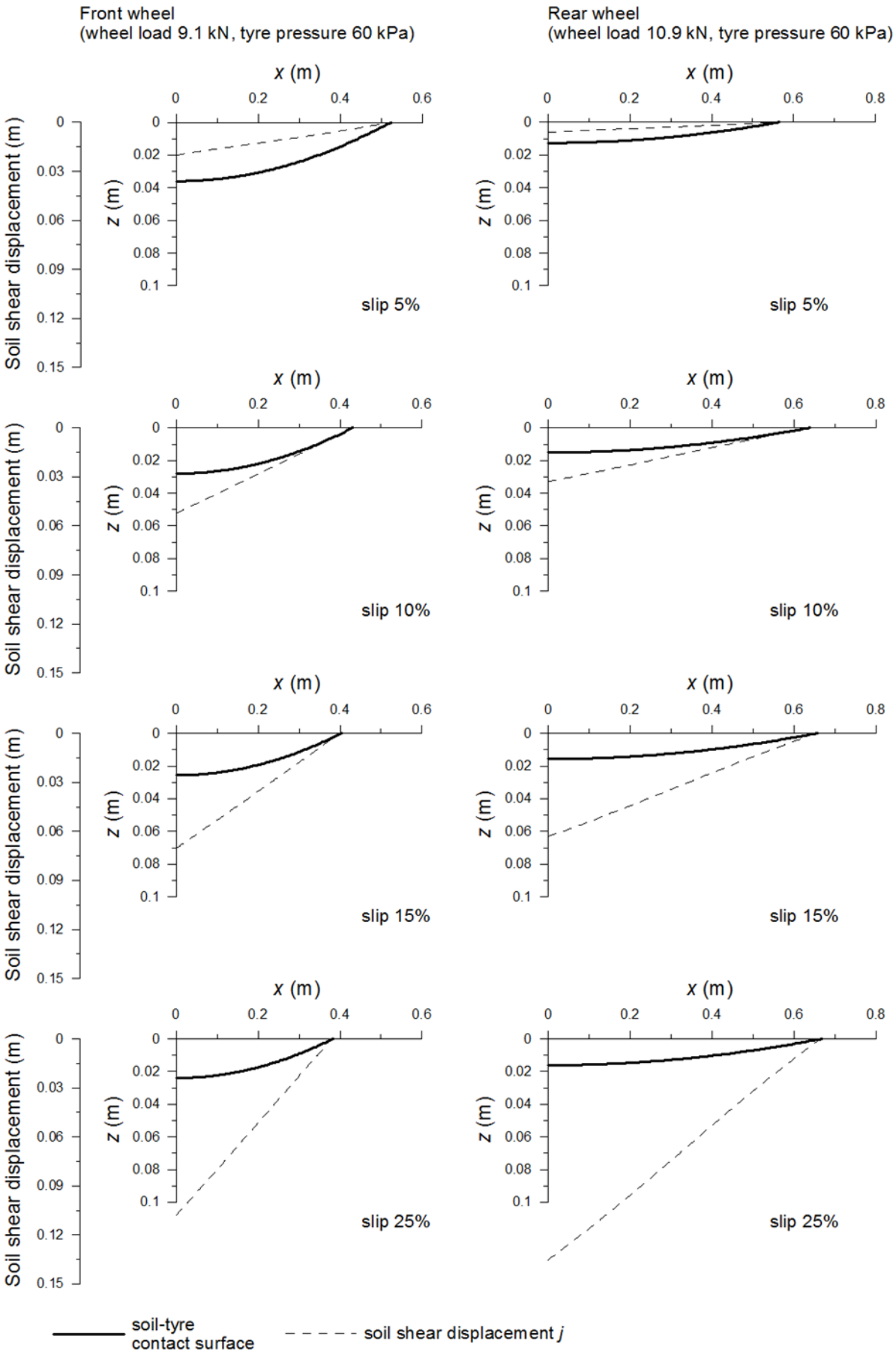

Fig. 45: Simulation of the distribution of the soil shear displacement along the soil-tyre contact surface for the front and rear wheel of tractor A in configuration 1 (Table 1) on the clay soil.

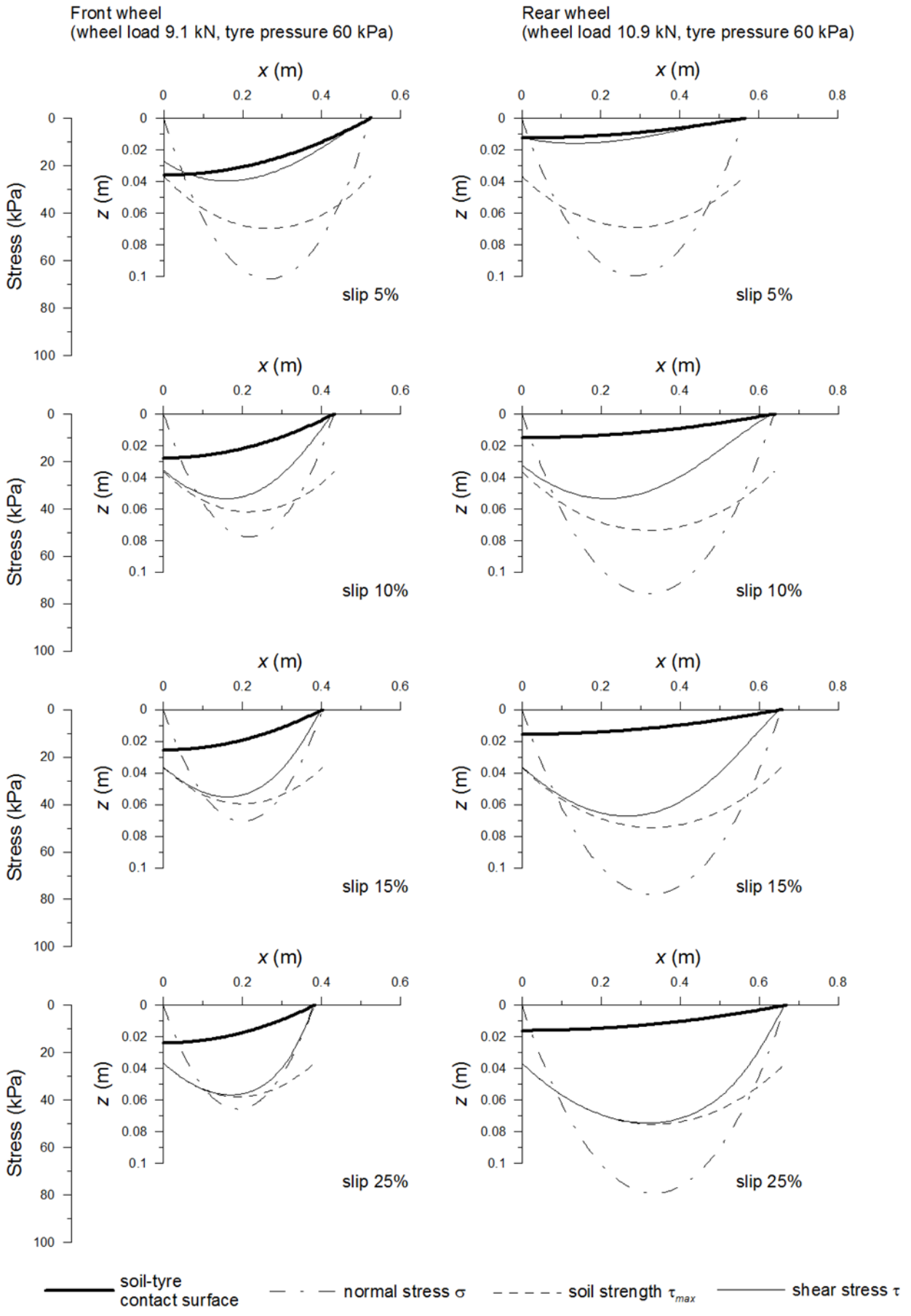

Fig. 46: Simulation of the distribution of the normal stress, the shear stress and the soil strength along the soil-tyre contact surface for the front and rear wheel of tractor A in configuration 1 (Table 1) on the clay soil.

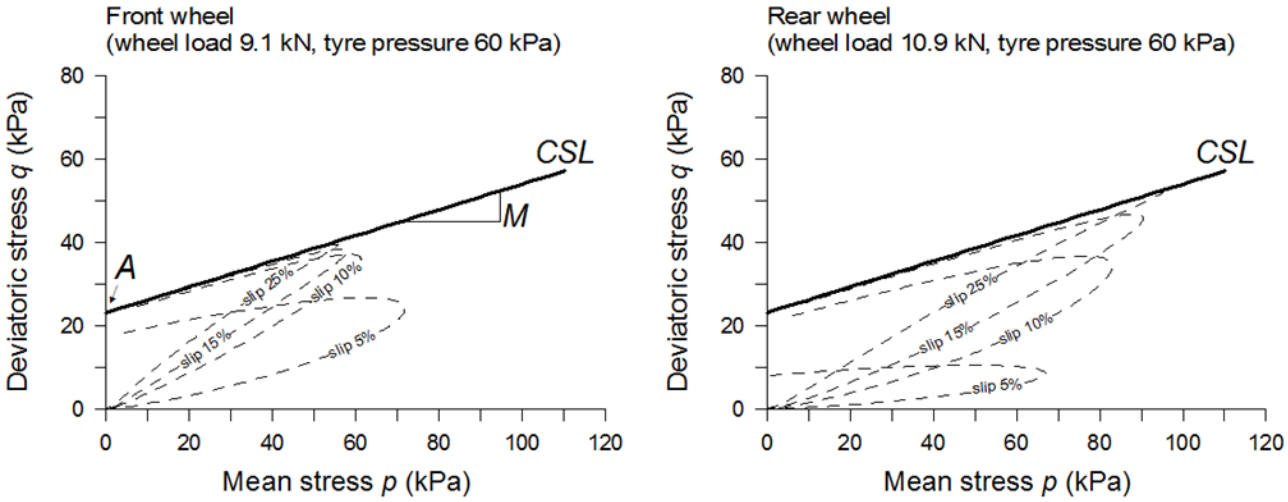

Fig. 47: Soil critical state line CSL and simulation of the stress paths along the soil-tyre contact surface, at different slip, for the front and rear wheel of tractor A in configuration 1 (Table 1) on the clay soil.

Intercept *A* and slope *M* of the critical state line *CSL* were derived as a function of the soil cohesion *c* and the angle of soil shear resistance φ for a plane stress state:

$$A = c\cos\varphi \tag{55}$$

$$M = \sin\varphi \tag{56}$$

The stress paths at slip of 5%, 10%, 15% and 25% indicated that the soil stress state varies significantly along the contact surface and with slip for both the front wheel and the rear wheel. Moreover, the last point of the stress path, which corresponds to the rear contact point, turned out to be the closest to the critical state condition. At a slip of 15%, a wide part of the soil stress path lay on the critical state line *CSL,* indicating that the critical state condition is fully reached.

1.3.1.2 Motion resistance

The distribution of the motion resistance of tractor A on the clay soil is shown in Fig. 48 for slip values ranging from 5% to 25% and for tyre inflation pressure ranging from 60 kPa to 160 kPa. The motion resistance due to soil compaction is defined as in equation 32 and corresponds to the vertical work done in making a rut of depth z_0. In the conditions represented in Fig. 48, the motion resistance increases with the tyre inflation pressure and decreases with slip.

The motion resistance assumes a value of 1.24 kN at a slip of 5% and tyre inflation pressure of 60 kPa, and a value of 1.82 kN at the same slip and tyre pressure of 160 kPa. At a slip of 25%, the motion resistance assumes a value of 0.87 kN for tyre pressure of 60 kPa and a value of 1.37 kN for tyre pressure of 160 kPa. With regard to the influence of the tyre pressure, a higher inflation pressure results in a reduced surface of contact between the tyre and the soil, thus the wheel load is distributed on a smaller area and the normal stress applied on the soil rises. This fact produces a deeper sinkage of the wheel into the soil and a deeper rut. The soil reaction to compaction (motion resistance) is a monotonically increasing function of the sinkage of the wheel (equation 32), therefore it increases with the rut depth and with the tyre inflation pressure. The influence of the slip on the motion resistance is explained on the basis of the load transfer effect, the higher the slip is, the greater are the drawbar pull and the load transferred from the front axle to the rear axle, since the contact area under the rear wheel is, to a great extent, greater than that under the front wheel, the load

transferred causes the rut depth of the front wheel to reduce and the rut depth of the rear wheel to increase, however, the first effect turns out to be much bigger than the second (Fig. 43). As a result, the overall rut depth, sum of that under the front wheel and that under the rear wheel, drops with slip and so does the motion resistance.

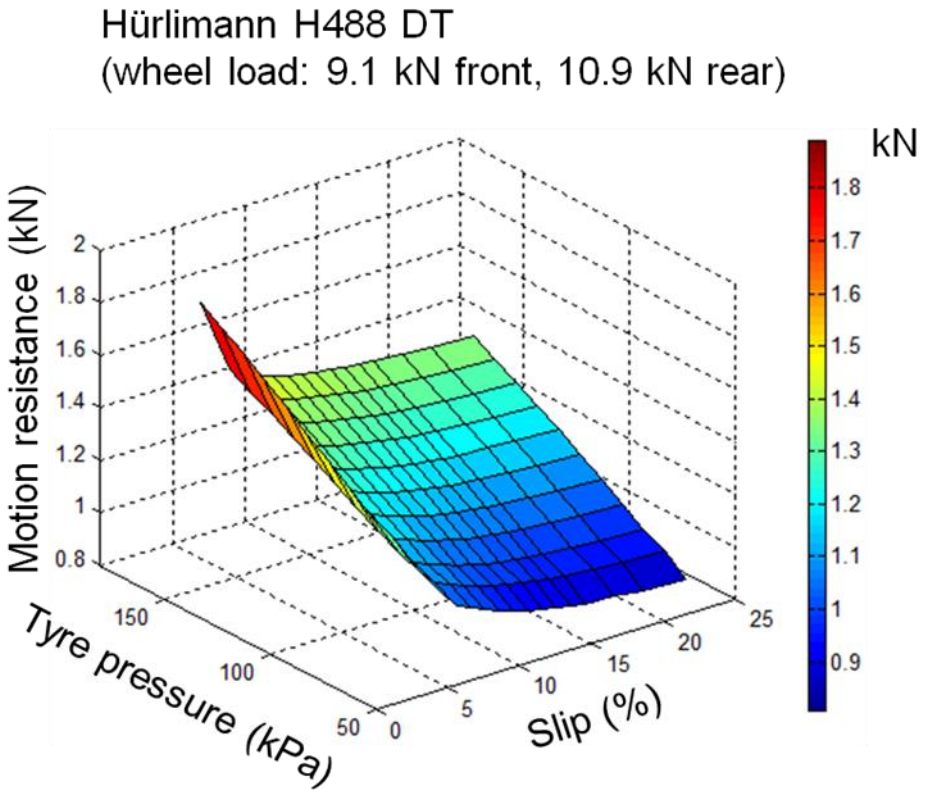

Fig. 48: Simulation of the motion resistance of tractor A (tractor weight 40 kN) on the clay soil for slip values ranging from 5% to 25% and for tyre inflation pressure ranging from 60 kPa to 160 kPa.

The simulation of the motion resistance of tractor A on the clay soil for slip values ranging from 5% to 25% and for tractor weight ranging from 40 kN to 56 kN is reported in Fig. 49. Here the inflation pressure of the tyres is assumed equal to 60 kPa, and the ratio of the load of the front axle to that of the rear axle is assumed constant and equal to that of the tractor without any ballast (0.83). The motion resistance decreases with slip, as already seen in Fig. 48, and increases with the wheel load and thus with the tractor weight. At a slip of 5% and a tractor weight of 40 kN (unballasted), the motion resistance is 1.24 kN, at the same slip and a tractor weight of 56 kN the motion resistance assumes a value of 1.82 kN. At a slip of 25% and a tractor weight of 40 kN the motion resistance is equal to 0.87 kN, at the same slip and a tractor weight of 56 kN the motion resistance assumes a value of 1.34 kN. The influence of the tractor weight on the motion resistance finds an explanation in the greater sinkage of the wheel and the deeper rut which makes for bigger motion resistance (equation 32).

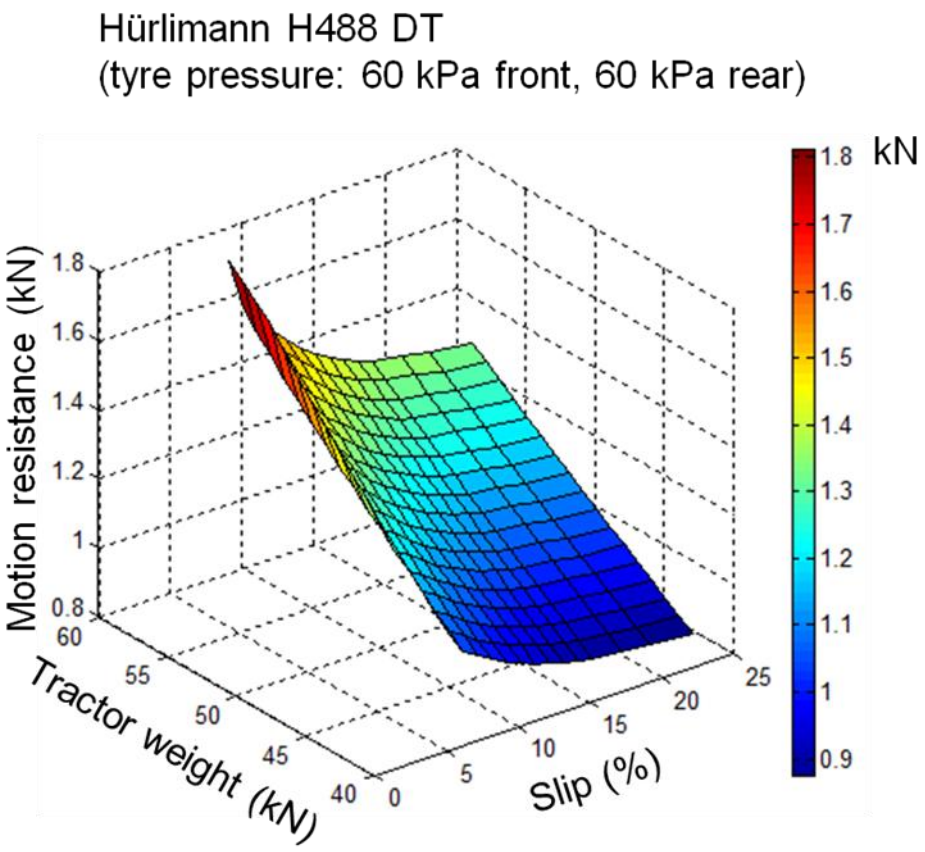

Fig. 49: Simulation of the motion resistance of tractor A (tyre pressure 60 kPa) on the clay soil for slip values ranging from 5% to 25% and for tractor weight ranging from 40 kN to 56 kN.

1.3.1.3 Drawbar pull and traction coefficient

The simulation of the traction performance of tractor A on the clay soil in terms of drawbar pull as a function of the slip in the range from 5% to 25%, and as a function of the tyre inflation pressure in the range from 60 kPa to 160 kPa, is shown in Fig. 50.

In the case considered, the tractor weight is 40 kN (unballasted), thus the conditions simulated are those from configuration 1 to configuration 2 in Table 1. The drawbar pull developed by the tractor rises sharply when slip increases, for instance, it varies from 7.8 kN at a slip of 5% to 28.1 kN at a slip of 25%, at a tyre pressure of 60 kPa, and from 11 kN at a slip of 5% to 23.2 kN at a slip of 25%, at a tyre pressure of 160 kPa. This result depends mainly on the increase of soil shear displacement (Fig. 45) and, as a consequence, on the increase of shear stress along the soil-tyre contact surface (Fig. 46), with slip.

The drawbar pull reduces with increasing tyre inflation pressure due to a less extended contact surface and a deeper rut depth which makes for a higher soil compaction resistance.

At a slip of 5%, the drawbar pull is 7.8 kN at a tyre pressure of 60 kPa, and 11 kN at a tyre pressure of 160 kPa. At a slip of 25%, the drawbar pull varies from 28.1 kN at a tyre pressure of 60 kPa, to 23.2 kN at a tyre pressure of 160 kPa.

In Fig. 51 the drawbar pull of tractor A on the clay soil is simulated as a function of the slip in the range from 5% to 25%, and as a function of the tractor weight ranging from 40 kN to 56 kN. The tractor weight can be controlled relatively easily by means of ballasts at the front and at the rear axle of the tractor.

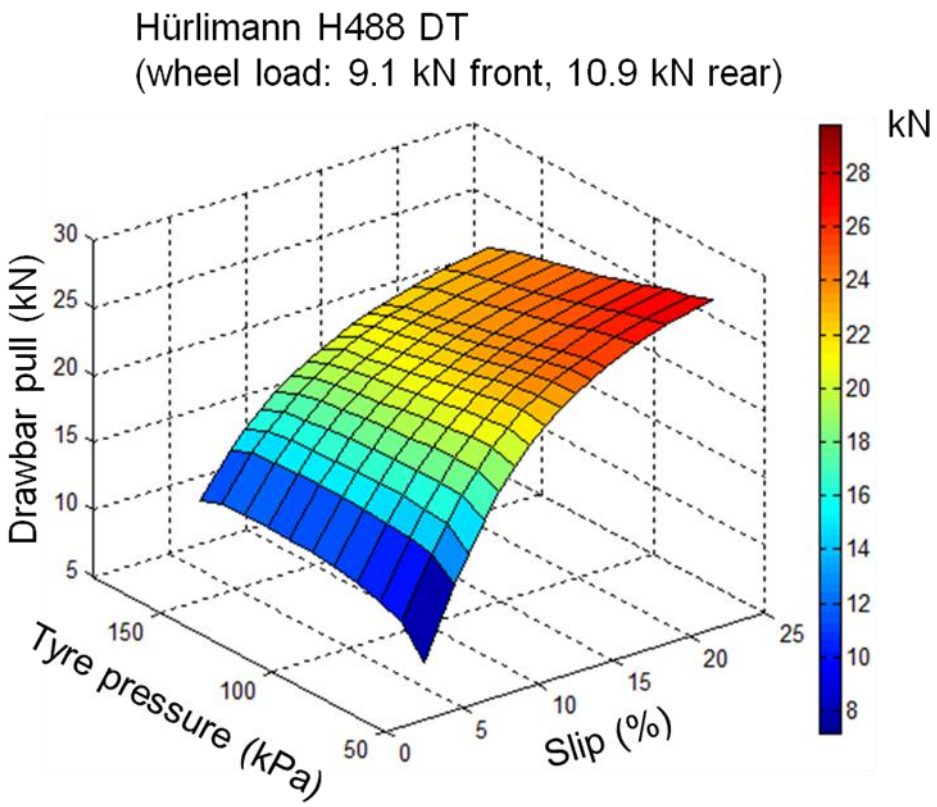

Fig. 50: Simulation of the drawbar pull of tractor A (tractor weight 40 kN) on the clay soil for slip values ranging from 5% to 25% and for tyre inflation pressure ranging from 60 kPa to 160 kPa.

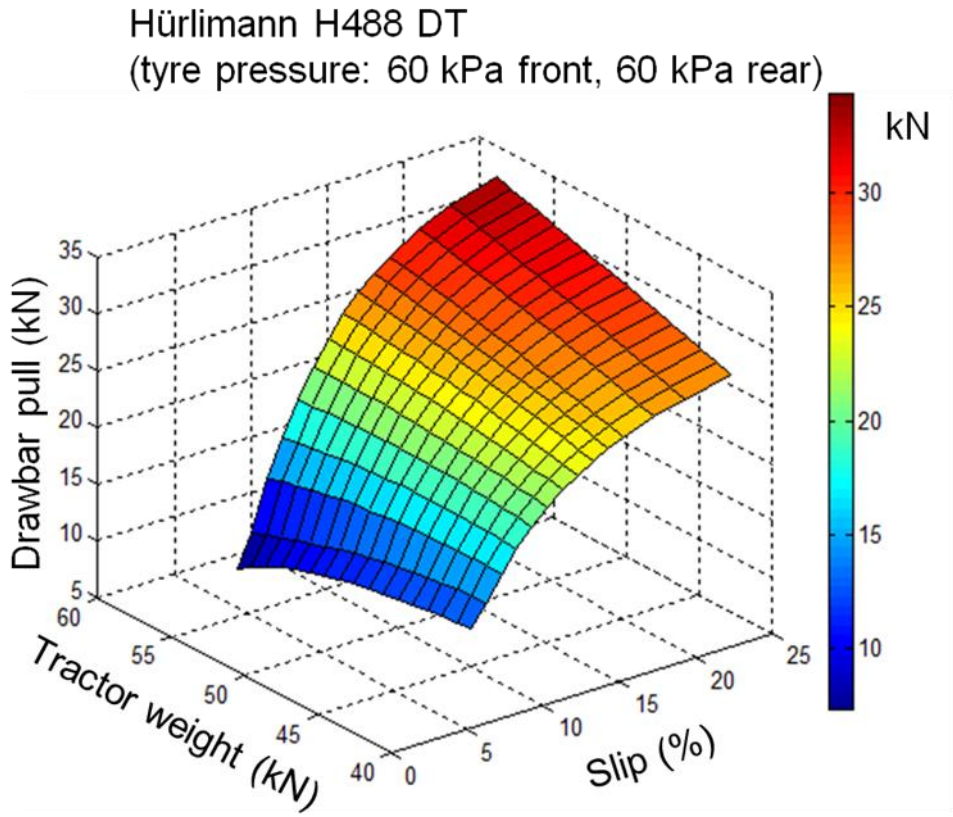

Fig. 51: Simulation of the drawbar pull of tractor A (tyre pressure 60 kPa) on the clay soil for slip values ranging from 5% to 25% and for tractor weight ranging from 40 kN to 56 kN.

The influence of the tractor weight, as well as that of the tyre pressure, on the traction performance of a MFWD tractor is, therefore, of high interest in practical applications and will be discussed in detail in chapter 1.3.3. The increase in tractor weight is simulated by assuming the ratio of the load of the front axle to that of the rear axle to be constant and equal to that without any ballast (0.83).

At low slip the drawbar pull decreases with increasing the tractor weight, for instance, at a slip of 5%, the drawbar pull of the tractor is 12.9 kN at a tractor weight of 40 kN (without ballast), and 7.1 kN at a tractor weight of 56 kN (with ballast). This tendency is inverted at higher slip where an increase in tractor weight results in a remarkable increase in drawbar pull. For instance, at a slip of 25%, the drawbar pull is 28.1 kN at a tractor weight of 40 kN, and 34.6 kN at a tractor weight of 56 kN. At a slip of 10% the drawbar pull varies only slightly with the tractor weight, assuming values of 20.2 kN and 20.4 kN for a tractor weight of 40 kN and 56 kN, respectively.

A simulation of the traction performance of tractor A on the clay soil in terms of the traction coefficient is reported in Fig. 52. Here the traction coefficient is defined according to equation 51 and is simulated as a function of the slip in the range from 5% to 25%, and as a function of the tyre inflation pressure in the range from 60 kPa to 160 kPa. The tractor is considered unballasted (tractor weight 40 kN). The traction coefficient increases with slip and decreases with the increase in tyre pressure at slip higher than 7%, below this value an increase in tyre pressure makes for a higher traction coefficient. At a slip of 5%, the traction coefficient assumes values of 0.19 and 0.27 at tractor weights of 40 kN and 56 kN, respectively. When a slip of 25% is considered, the traction coefficient turns out to be 0.69 and 0.57 at tractor weights of 40 kN and 56 kN respectively.

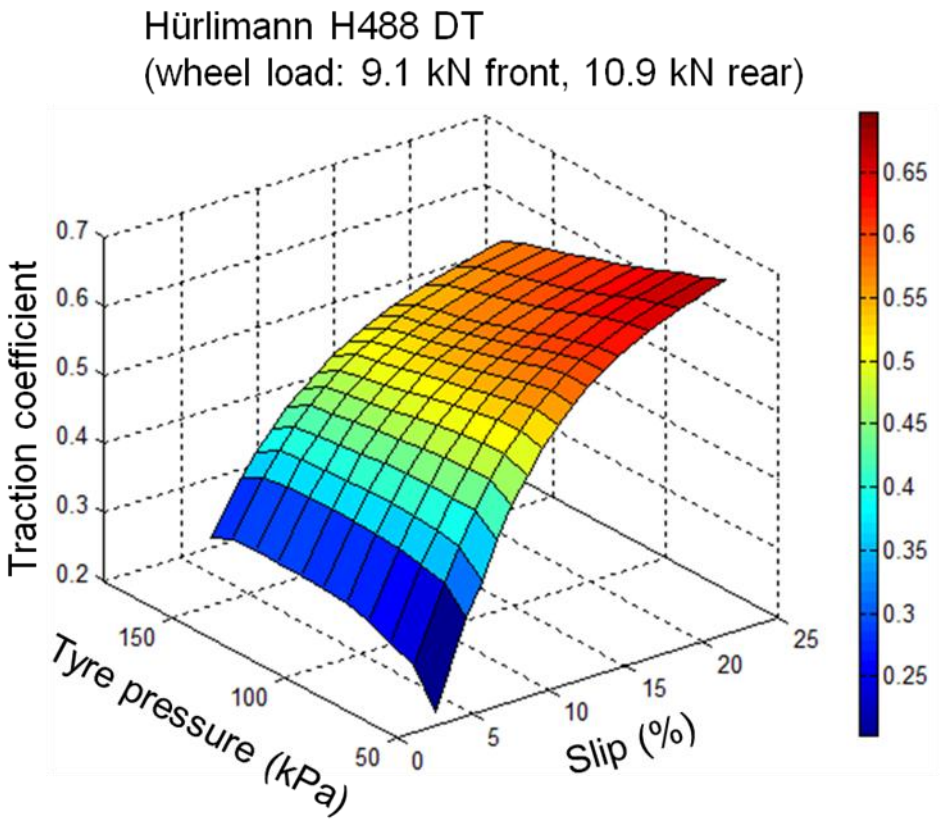

Fig. 52: Simulation of the traction coefficient of tractor A (tractor weight 40 kN) on the clay soil for slip values ranging from 5% to 25% and for tyre inflation pressure ranging from 60 kPa to 160 kPa.

The simulated distribution of the traction coefficient of tractor A on the clay soil, for slip values ranging between 5% and 25%, and tractor weight ranging between 40 kN and 56 kN, is shown in Fig. 53. In the simulation, the ratio of the load of the front axle to that of the rear axle is assumed constant and equal to that of the tractor without any ballast (0.83). The traction coefficient clearly increases with slip and decreases with the tractor weight, in this latter case, the decrease is sharper at low slip and steadier at high slip. In spite of an increase in drawbar pull (Fig. 51), the rise in tractor weight turns out in a lower traction coefficient (Fig. 53). At a slip of 5% the traction coefficient varies from 0.32, for a tractor weight of 40 kN, to 0.13, for a tractor weight of 56 kN. The corresponding values of drawbar pull (Fig. 51) are 12.9 kN and 7.1 kN for tractor weights of 40 kN and 56 kN, respectively. At a slip of 25% the traction coefficient varies from 0.69, for a tractor weight of 40 kN, to 0.61, for a tractor weight of 56 kN. The corresponding values of drawbar pull (Fig. 51) are 28.1 kN and 34.6 kN for tractor weights of 40 kN and 56 kN, respectively.

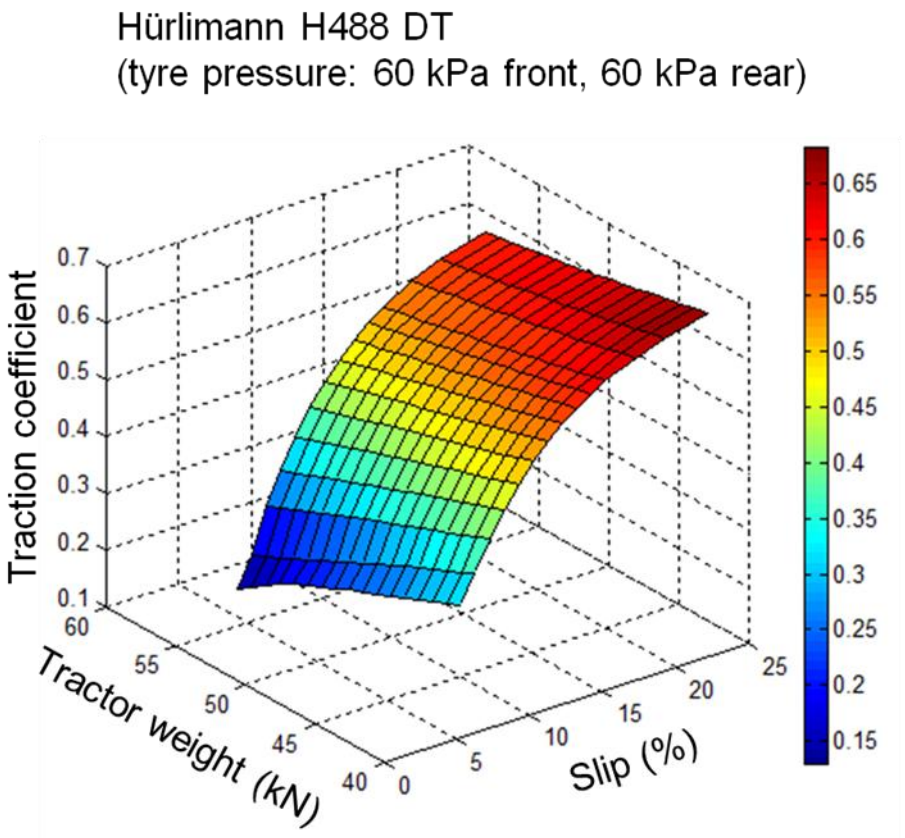

Fig. 53: Simulation of the traction coefficient of tractor A (tyre pressure 60 kPa) on the clay soil for slip values ranging from 5% to 25% and for tractor weight ranging from 40 kN to 56 kN.

1.3.1.4 Traction efficiency

The traction efficiency, or tractive efficiency, defined as in equation 52, is simulated as a function of the slip in the range between 5% and 25% and as a function of the tyre pressure in the range between 60 kPa to 160 kPa, in Fig. 54. The traction efficiency sharply rises at low slip, and reaches a peak in the range of slip between 8% and 12%, beyond this peak, it decreases progressively with slip. The increase in tyre pressure makes for lower values of traction efficiency in the whole range of slip considered. At a tyre pressure of 60 kPa, the traction efficiency assumes a value of 0.73 at a slip of 5%, it reaches a peak of 0.86 at a slip of 10%, and afterwards it drops to 0.77 at a slip of 25%. The traction efficiency represents the percentage of

power delivered to the tractor wheels that is available as tractive power and the shape of its distribution as a function of the slip depends on the fact that, at low slip, a little increase in slip, and hence in soil shear displacement, turns out in a great increase in traction force, this resulting in a overall rise in traction efficiency. Beyond a certain limit, depending on all the factors affecting the tractor-terrain interaction but, to a great extent, on the soil shear stress-displacement relationship (Fig. 37), an increase in slip and in soil shear displacement turns out in a slight increase in traction force with an overall reduction in traction efficiency. The knowledge of the range of slip which corresponds to the optimal traction efficiency is of high interest in practical applications since it represents the best way to convert tractor energy into traction work.

Fig. 55 shows the simulation of the traction efficiency of tractor A (tyre pressure 60 kPa) on the clay soil for slip values ranging from 5% to 25% and for tractor weight ranging from 40 kN to 56 kN. At low slip, the traction efficiency reduces abruptly with the tractor weight. At a slip of 5% the traction efficiency is 0.83 for a tractor weight of 40 kN and 0.63 for a tractor weight of 56 kN. The peak of traction efficiency (0.86) is reached at a slip of 10% for a tractor weight of 40 kN. The same peak drops to 0.83 and is reached at a slip of 13% for a tractor weight of 56 kN. At a slip of 25% the traction efficiency results 0.77 at both a tractor weight of 40 kN and a tractor weight of 56 kN.

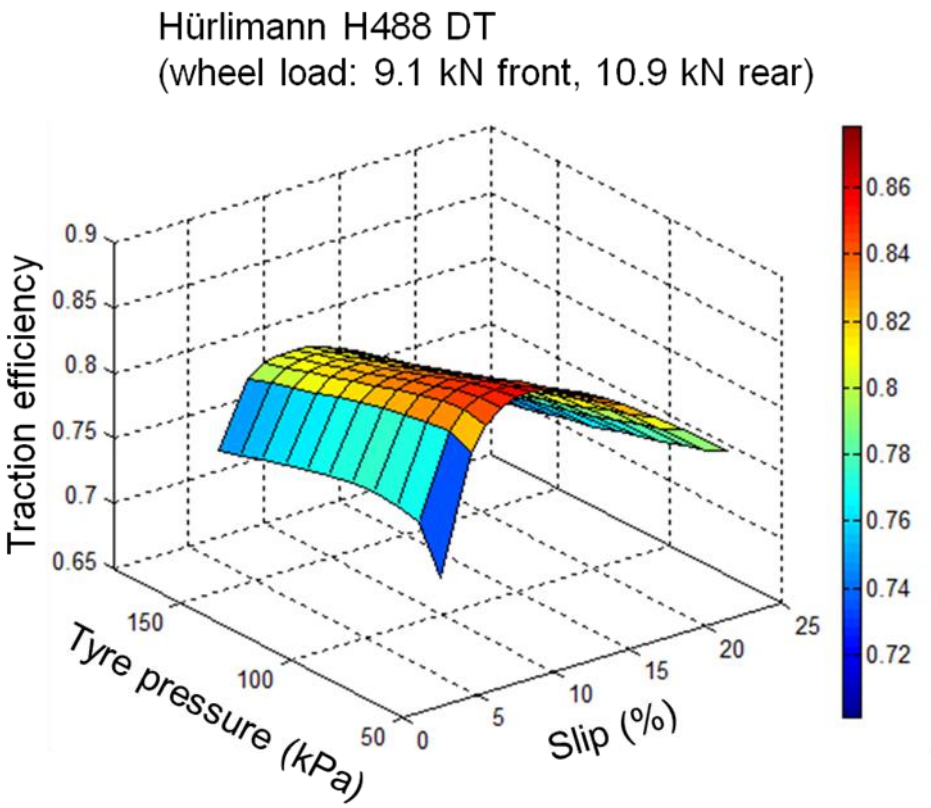

Fig. 54: Simulation of the traction efficiency of tractor A (tractor weight 40 kN) on the clay soil for slip values ranging from 5% to 25% and for tyre inflation pressure ranging from 60 kPa to 160 kPa.

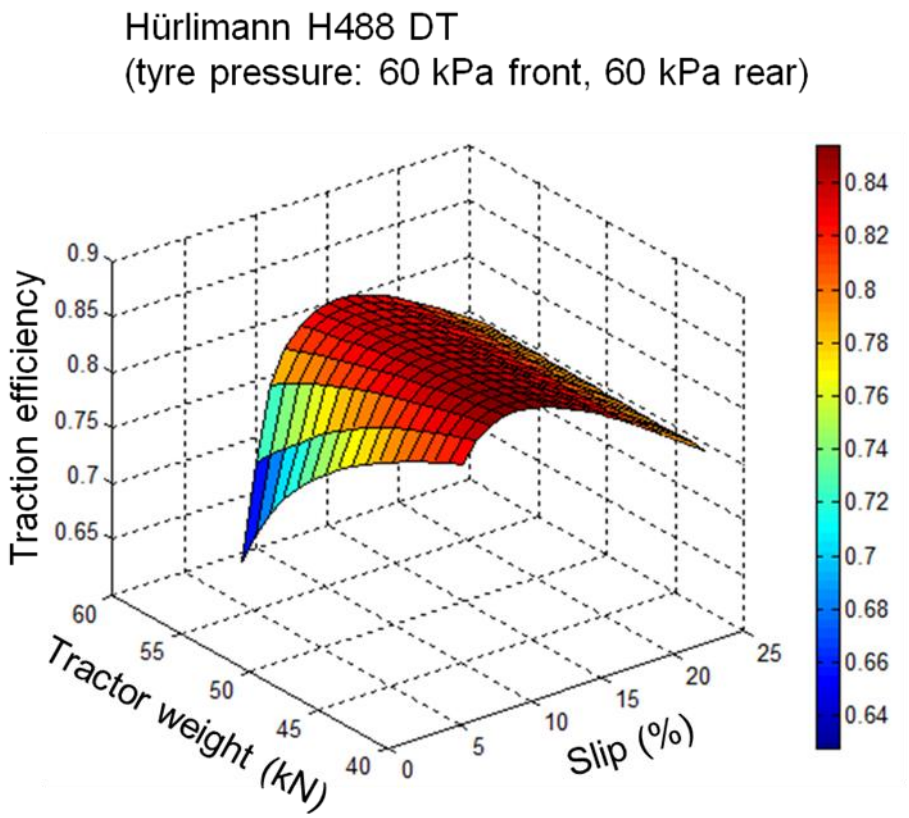

Fig. 55: Simulation of the traction efficiency of tractor A (tyre pressure 60 kPa) on the clay soil for slip values ranging from 5% to 25% and for tractor weight ranging from 40 kN to 56 kN.

1.3.2 Results of the experimental validation

In Fig. 56 the tyre contact area measured in stationary condition is confronted with the contact area predicted by the model, for different tyres, at various wheel loads and contact pressures, on the clay soil. The contact area in stationary condition was measured according to Diserens (2011). The simulation matches the experimental data with a mean error of 0.04, and maximum and minimum error of 0.07 and 0.01, respectively.

The data reported in Fig. 56 were obtained by Diserens (2011), under soil conditions almost analogous to that considered in the traction tests (Table 5). Although the model used considers the wheel to move at low velocity rather than in a static condition, the simulation also reproduces the area of the contact surface in static condition with considerable accuracy.

Fig. 57 reports the measured and the simulated drawbar pull for the tractors A, B, and C, on the clay loam (Table 5). Here the influence of tractor size and power on traction performance results evident. As expected, more powerful and bigger sized tractors have higher traction performance. The bigger the tractor size is, the heavier and more powerful the tractor is and the bigger the tyre dimensions usually are, this resulting in increasing wheel load, tyre contact surface with soil, and traction force. According to the traction that a tractor is able to produce, the engine must provide the power required. A comparison between the measured and simulated traction performance, in terms of drawbar pull, of tractor A on the clay, is presented in Fig. 58. Results of the measured and simulated drawbar pull of tractor A on the clay loam, on the silty loam, and on the loamy sand are presented in Fig. 59, Fig. 60, and Fig. 61 (Appendix 3), respectively.

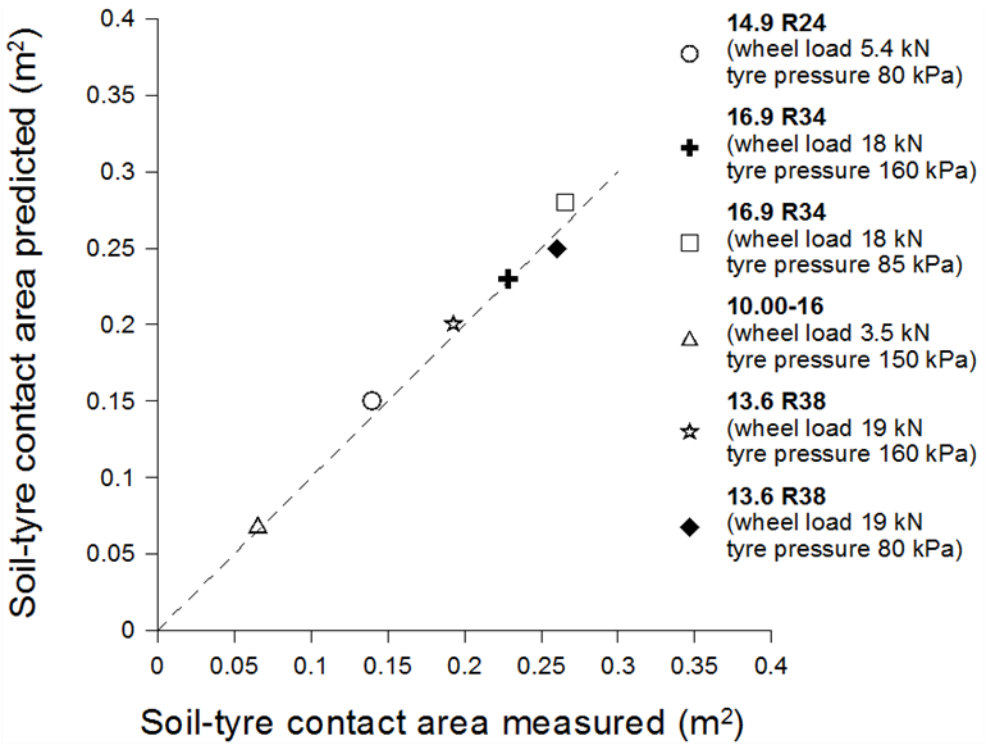

Fig. 56: Measured and simulated contact area of different agricultural tyres at various wheel loads and inflation pressures on the clay soil.

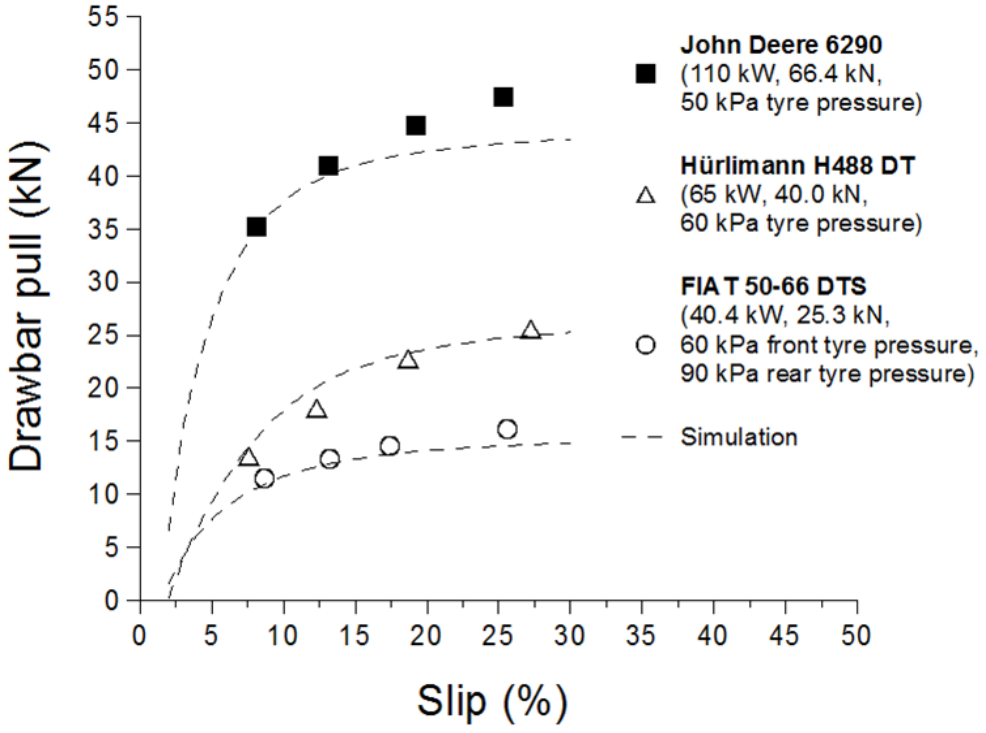

Fig. 57: Measured and simulated drawbar pull of the tractors A, B, and C, on the clay loam.

In Fig. 62 (Appendix 3) is compared the measured and simulated drawbar pull of tractor B on the clay loam. The same comparison is reported in Fig. 63 and Fig. 64 (Appendix 3) for the tractor C on the clay loam, and for the tractor D on the loamy sand, respectively. The simulated drawbar pull of tractor A on the clay matches the measured drawbar pull with an overall good agreement, with a slight underestimation in configuration 3

(Fig. 58*c*). On the clay loam, the simulated drawbar pull underestimates the measured data only at a low slip in configuration 3 (Fig. *59c*). On the silty loam, the traction performance of tractor A is simulated consistently in configurations 1 and 2 (Fig. 60*a* and 60*b*), whilst in configurations 3 and 4 (Fig. 60*c* and 60*d*) the traction performance is rather underestimated at a low slip. In configurations 5, 6, 7, 8, 9, 10, and 12 (Fig. 60*e*, 60*f*, 60*g*, 60*h*, 60*i*, 60*j*, and 60*l*), where dual tyres are used, the traction performance is slightly overestimated. On the loamy sand, the drawbar pull of tractor A is simulated with high fidelity in configurations 1, 2, 3 and 4 (Fig. 61*a*, 61*b*, 61*c*, and 61*d*). The accuracy of the simulation decreases significantly when dual tyres are used, as in configurations 7 and 8, where an evident underestimation of the traction performance is shown (Fig. 61*e* and 61*f*). The traction performance of tractor B on the clay loam is rather underestimated only in configuration 3 (Fig. 62*c*), and a general good agreement between measured and simulated drawbar pull is shown. The traction performance of tractor B on the clay loam is a little underestimated in configuration 1 (Fig. 63*a*) and overestimated in configuration 2 (Fig. 63*b*). With regard to the traction performance of tractor D on the loamy sand, a rather evident overestimation is shown in configuration 1 (Fig. 64*a*), as well as, a clear underestimation is presented in configurations 3 and 4 (Fig. 64*c* and 64*d*), at least at a low slip. In configuration 2 (Fig. 64*b*) the simulation matches the experimental data with high fidelity.

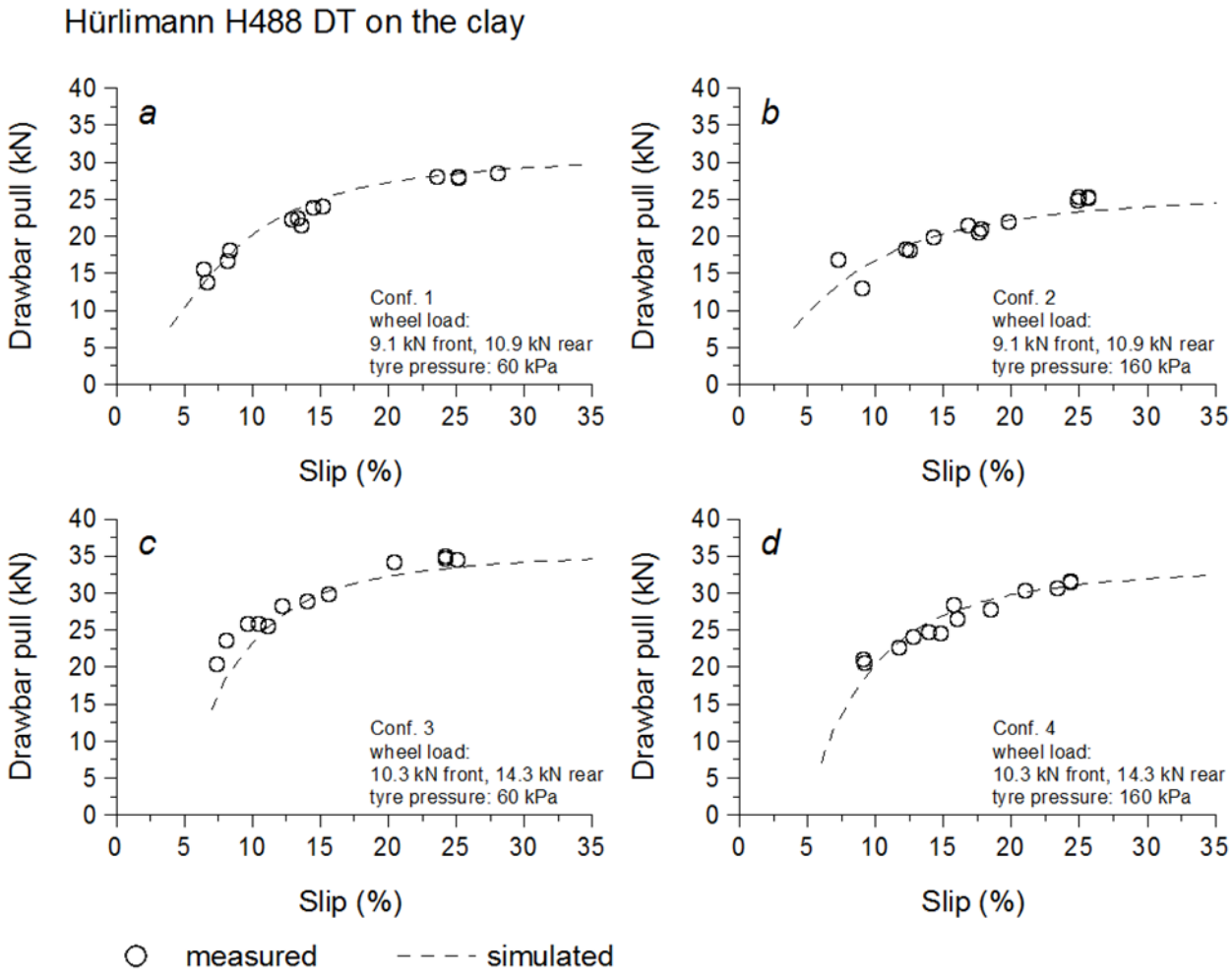

Fig. 58: Measured and simulated drawbar pull of tractor A on the clay.

An overview of the agreement between measured and simulated drawbar pull for the tractor A in the four soils considered is reported in Fig. 65, for configurations 1, 2, 3 and 4 (Table 1). In the cases considered, the overall mean error is 0.12 and the overall mean residual is 2.24 kN. The minimum and maximum mean errors for the single configurations are 0.02 and 0.53, obtained in configuration 2 on the loamy sand (Fig. 61*b*), and in configuration 3 on the silty loam (Fig. 60*c*), respectively. The minimum and maximum overall mean residual for the single configurations are 0.31 kN and 8.82 kN, also obtained in configuration 2 on the loamy sand (Fig. 61*b*), and in configuration 3 on the silty loam (Fig. 60*c*), respectively.

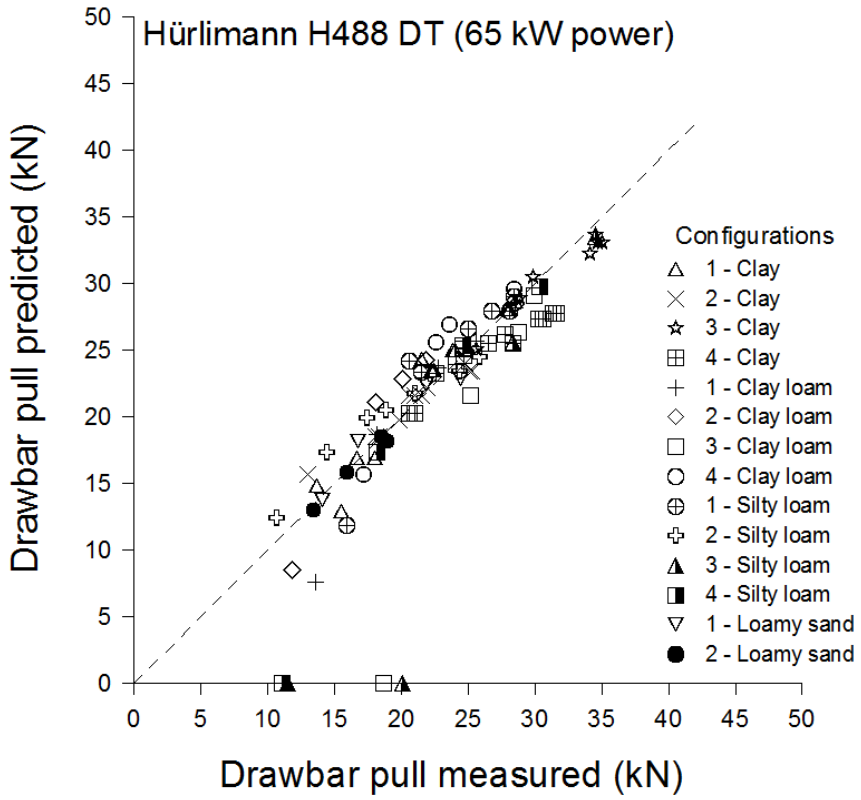

Fig. 65: Comparison between measured and simulated drawbar pull of tractor A in configurations 1, 2, 3 and 4 (Table 1), on the four sites considered (Table 5).

In Fig. 66 an overview is shown of the agreement between measured and simulated drawbar pull for the tractor A on the silty loam and on the loamy sand in configurations 5, 6, 7, 8, 9, 10, 11, and 12 (Table 1). In the cases reported, the overall mean error is 0.09 and the overall mean residual is 2.36 kN. The minimum and maximum mean errors and mean residuals for the single configurations are 0.03 and 0.33, and 0.54 kN and 7.54 kN, respectively. These values are obtained on the loamy sand, in configurations 6 and 7 (Fig. 61*d* and 61*e*), respectively.

The same comparison between measured and simulated traction performance is reported in Fig. 67 for the tractor B on the clay loam, in configuration 1, 2, 3, and 4. Here the overall mean error is 0.06 and the overall mean residual is 0.84 kN. The minimum and maximum mean errors and mean residuals for the single configurations are 0.01 and 0.09, and 0.16 kN and 1.61 kN, respectively.

The minimum and maximum values of the mean error are obtained in configurations 4 and 2, respectively. The minimum and maximum values of the mean residual are obtained in configurations 4 and 3, respectively.

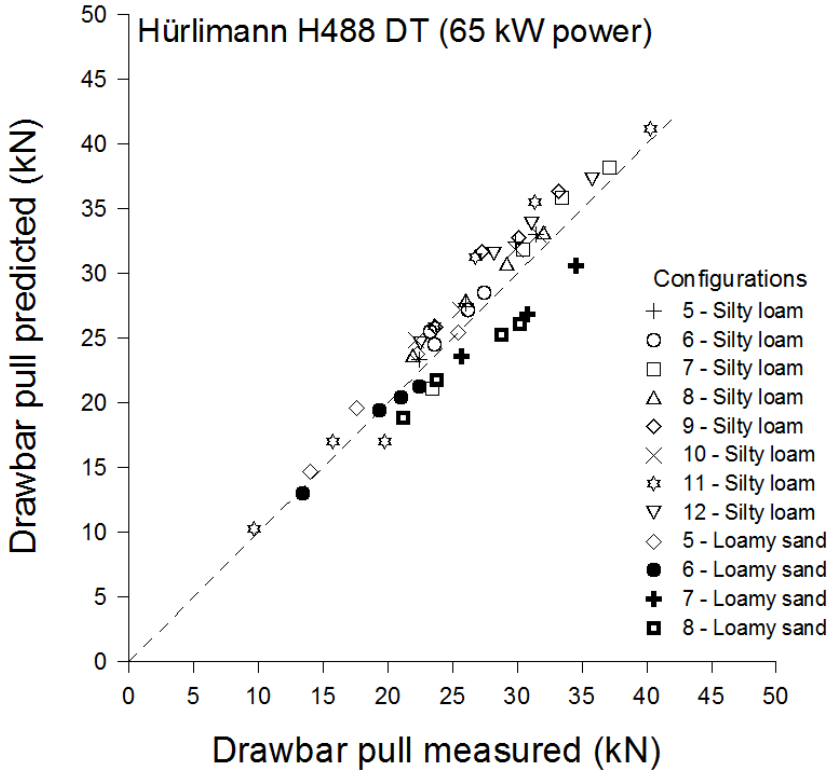

Fig. 66: Comparison between measured and simulated drawbar pull of tractor A in configurations 5,6,7,8,9,10,11 and 12 (Table 1), on the silty loam and the loamy sand (Table 5).

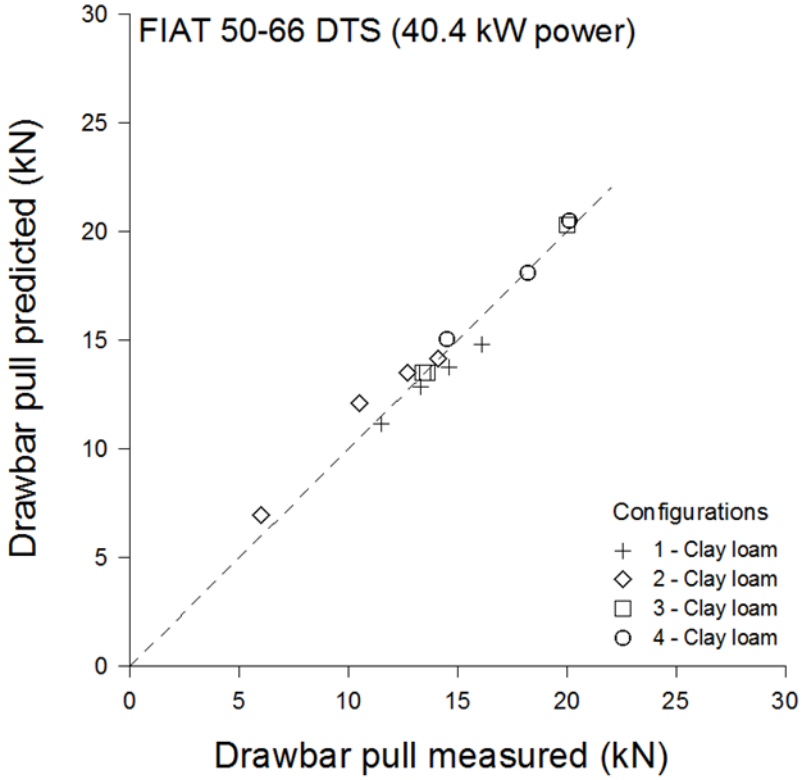

Fig. 67: Comparison between measured and simulated drawbar pull of tractor B on the clay loam (Table 5), for the different configurations considered (Table 2).

With regard to tractor C, the overview of the comparison between measured and simulated traction performance on the clay loam (Table 5), for configurations 1 and 2 (Table 3), is shown in Fig. 68. In the cases considered, the overall mean error is 0.07 and the overall mean residual is 2.39 kN. Maximum and minimum values are 0.10 and 0.05, for the mean error referred to single configurations, and 2.07 kN and 2.71kN, for the mean residual referred to single configurations. The minimum value of both the mean error and the mean residual is obtained in configuration 1 (Fig. 63*a*), whilst the maximum is obtained in configuration 2 (Fig. 63*b*).

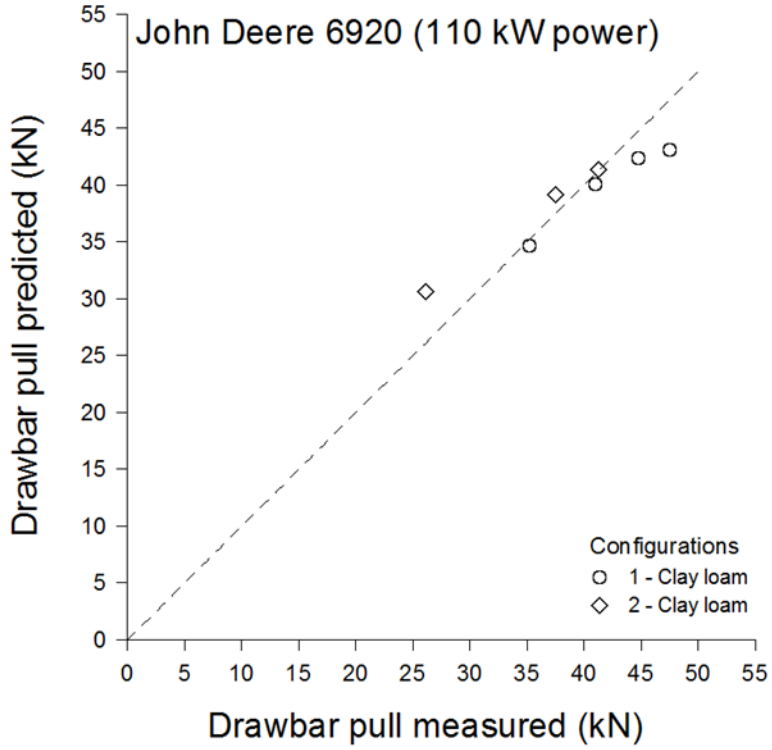

Fig. 68: Comparison between measured and simulated drawbar pull of tractor C on the clay loam (Table 5), for the different configurations considered (Table 3).

The overview of the comparison between measured and simulated drawbar pull for the tractor D on the loamy sand (Table 5), in configurations 1, 2, 3, and 4, is reported in Fig. 69. In this case, the overall mean error is 0.22 and the overall mean residual is 7.66 kN. Maximum and minimum values for the single configurations are 0.64 and 0.04 for the mean error, and 22.85 kN and 1.22 kN, for the mean residual. The maximum value of both the mean error and the mean residual is obtained in configuration 3 (Fig. 64*c*), whilst the minimum value of both the mean error and the mean residual corresponds to configuration 2 (Fig. 64*b*).
In Table 7 the accuracy of the simulation of the drawbar pull is reported in terms of mean residual and mean error for the different configurations and sites considered for the tractor A.
In Table 8, Table 9, and Table 10 the mean residual and the mean error related to simulations of drawbar pull, are reported for the different conditions considered for the tractors B, C, and D, respectively.

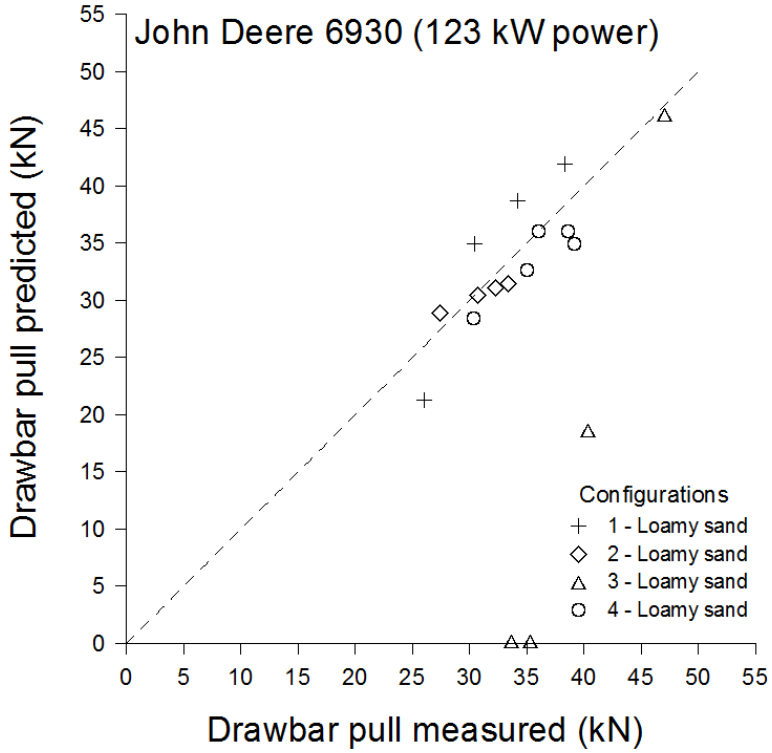

Fig. 69: Comparison between measured and simulated drawbar pull of tractor D on the loamy sand (Table 5), for the different configurations considered (Table 4).

Table 7: Accuracy of the *traction performance simulations for the tractor A.*

Tractor		Mean Residual [kN]	Mean Error
Hürlimann H488 DT 65 kW	Configuration	C / CL / SL / LS*	C / CL / SL / LS*
	1	1.00 / 1.86 /1.61 / 0.98	0.05 / 0.13 / 0.08 / 0.05
	2	0.94 / 1.21 / 1.69 / 0.31	0.05 / 0.09 / 0.10 / 0.02
	3	1.04 / 6.4 / 8.8 / -	0.03 / 0.31 / 0.53 / -
	4	1.66 / 2.26 /1.60 / -	0.06 / 0.10 / 0.12 / -
	5	- / - / 1.69 / 1.05	- / - / 0.06 / 0.06
	6	- / - / 1.31 / 0.54	- / - / 0.05 / 0.03
	7	- / - / 1.80 / 7.54	- / - / 0.06 / 0.33
	8	- / - / 1.61 / 3.00	- / - / 0.06 / 0.11
	9	- / - / 3.12 / -	- / - / 0.11 / -
	10	- / - / 1.90 / -	- / - / 0.07 / -
	11	- / - / 2.36 / -	- / - / 0.09 / -
	12	- / - / 2.44 / -	- / - / 0.09 / -

*C = Clay; CL = Clay loam; SL = Silty loam; LS = Loamy sand

Table 8: Accuracy of the *traction performance simulations for the tractor B.*

Tractor		Mean Residual [kN]	Mean Error
FIAT 50-66 DTS 40.4 kW	Configuration	C / CL / SL / LS*	C / CL / SL / LS*
	1	- / 0.73 / - / -	- / 0.05 / - / -
	2	- / 0.86 / - / -	- / 0.09 / - / -
	3	- / 0.16 / - / -	- / 0.01 / - / -
	4	- / 1.61 / - / -	- / 0.08 / - / -

*C = Clay; CL = Clay loam; SL = Silty loam; LS = Loamy sand

Table 9: Accuracy of the traction performance simulations for the tractor C.

Tractor		Mean Residual [kN]	Mean Error
John Deere 6920	Configuration	C / CL / SL / LS*	C / CL / SL / LS*
110 kW	1	- / 2.07 / - / -	- / 0.05 / - / -
	2	- / 2.71 / - / -	- / 0.10 / - / -

*C = Clay; CL = Clay loam; SL = Silty loam; LS = Loamy sand

Table 10: Accuracy of the traction performance simulations for the tractor D.

Tractor		Mean Residual [kN]	Mean Error
John Deere 6930	Configuration	C / CL / SL / LS*	C / CL / SL / LS*
123 kW	1	- / - / - / 4.35	- / - / - / 0.14
	2	- / - / - / 1.22	- / - / - / 0.04
	3	- / - / - / 22.85	- / - / - / 0.64
	4	- / - / - / 2.22	- / - / - / 0.06

*C = Clay; CL = Clay loam; SL = Silty loam; LS = Loamy sand

1.3.3 Influence of tyre inflation pressure and wheel load on traction performance

In the following the influence of tyre inflation pressure and wheel load on the traction performance of tractor A on an agricultural clay (C) Vertic Cambisol is compared on the basis of results of field traction tests as well as simulations with the semi-empirical soil-tyre interaction model adapted for MFWD vehicles, with a mechanistic interpretation of results.

The simulation of the soil-tyre contact surface and the contact stresses (normal σ and shear τ) together with the soil strength τ_{max} for the rear wheel at a slip of 10% in configurations 1, 2, 3, and 4 (Table 1) is represented in Fig. 70. The geometry of the soil-tyre contact surface is defined by the *x*-axis and the *z*-axis according to the reference system in Fig. 17. The stress condition at the soil-tyre contact together with the soil strength is defined by the *x*-axis and the *Stress*-axis. The geometry of the contact surface as well as the contact stresses and soil strength varied more noticeably with the increase in tyre pressure than with the increase in wheel load, with the former producing a deeper and shorter contact surface, and the latter creating a deeper and longer one.

The measured and simulated traction performance in terms of drawbar pull *DP* and traction coefficient μ_{tr} as a function of slip *i* are reported in Fig. 71. Lowering the inflation pressure produced an improvement in drawbar pull and traction coefficient both with and without ballasting the tractor. The increase in wheel load resulted in a higher drawbar pull at both 60 kPa and 160 kPa tyre inflation pressure, although it failed to produce noteworthy variations in terms of traction coefficient.

Fig. 72 shows the simulation of the traction coefficient as a function of slip (from 4% to 25%) and tyre inflation pressure (from 60 to 160 kPa) both without (Fig. 72*a*) and with ballasts (Fig. 72*b*). In this simulation, the slip base is assumed to vary according to the variation of the rolling radius reported in Fig. 39. Tyre pressure had a significant effect on traction coefficient, which decreased with increasing pressure. The increase in tractor weight (wheel load) resulted in a slight decrease in traction coefficient.

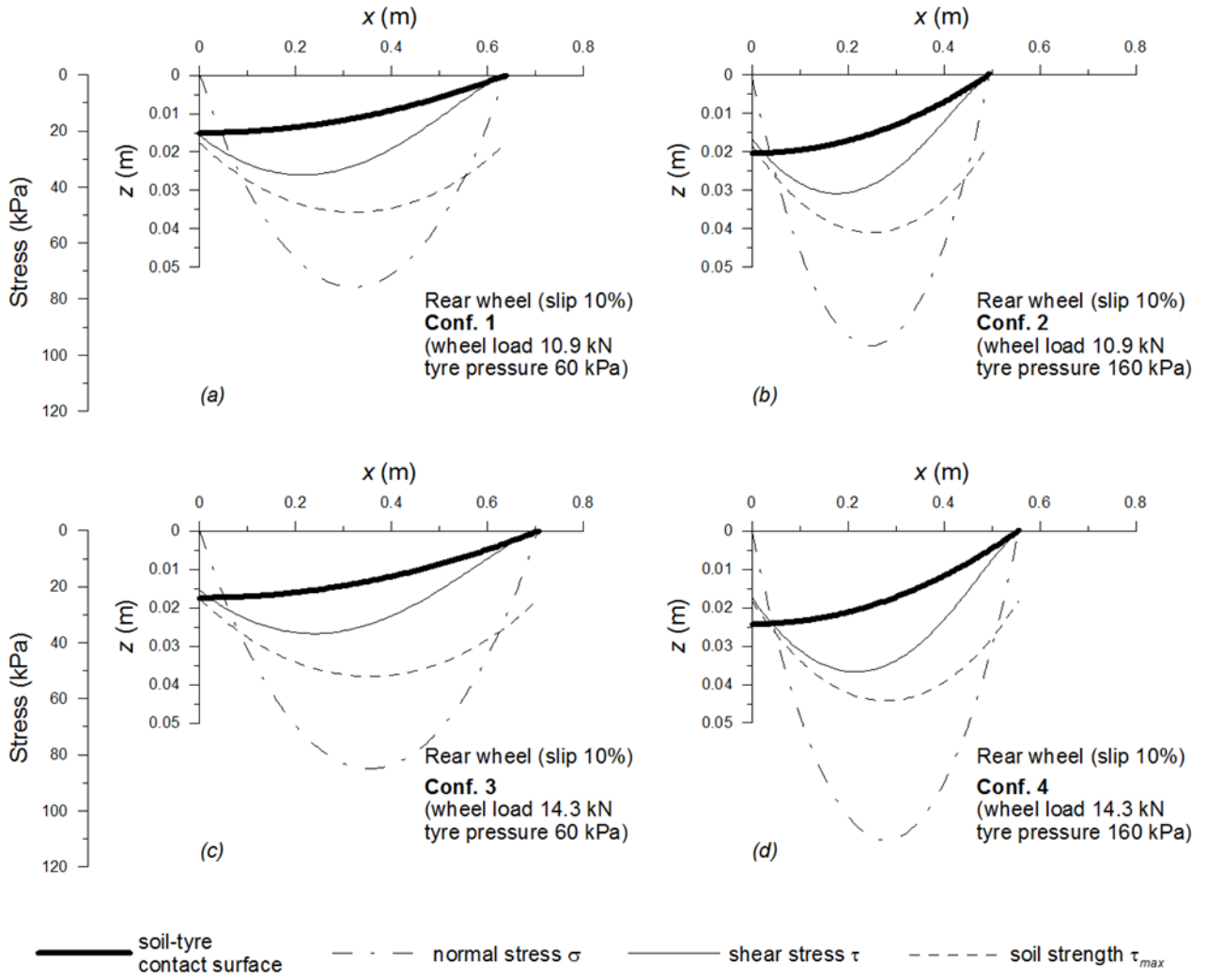

Fig. 70: Simulation of the geometry of the soil-tyre contact surface, the contact stresses (normal σ and shear τ), and the soil strength τ_{max} for the rear wheel (420 85R34 tyre) of tractor A at a slip of 10% in configurations 1, 2, 3, and 4 (Table 1), on the clay soil (Table 5).

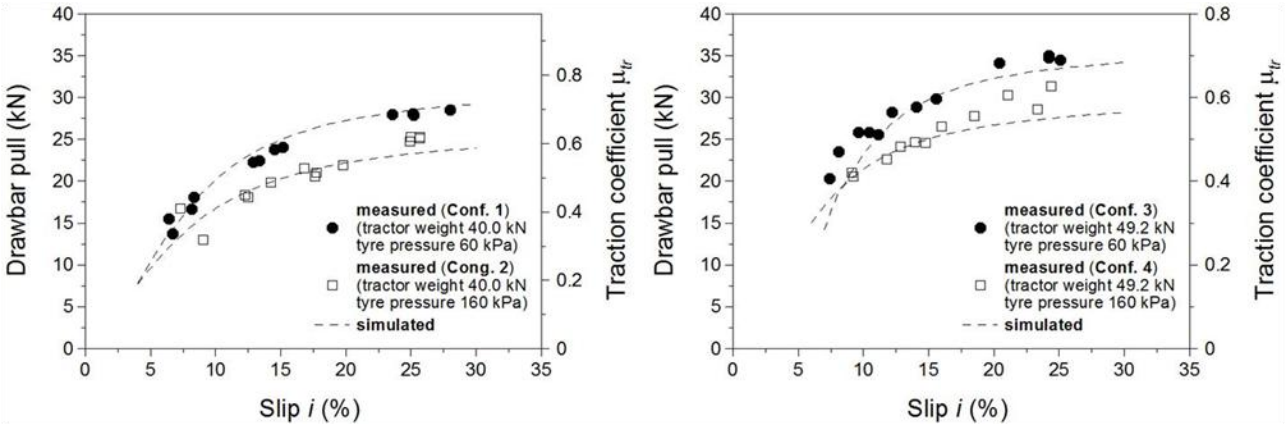

Fig. 71: Measured and simulated drawbar pull and traction coefficient as a function of slip, for the tractor A in configurations 1, 2, 3, and 4 (Table 1), on the clay soil (Table 5).

In order to properly measure the traction efficiency η_{tr}, a wheel torque dynamometer - not available for our tests - would be required. Traction efficiency was therefore merely simulated as a function of slip (from 4% to 25%) and tyre inflation pressure (from 60 to 160 kPa) without ballasts (Fig. 73*a*) and with ballasts (Fig. 73*b*).

It emerged that traction efficiency decreased along with an increase in both tyre pressure and wheel load, although the decrease owing to wheel load was less significant.

Values for power delivery efficiency η_{PD} and specific fuel consumption *SFC* (drawbar power basis) as a function of the slip are reported in Fig. 74 for the four tractor configurations considered (Table 1). The equivalent *PTO* was calculated on the basis of measured fuel consumption, according to Fig. 75.

During the tests, engine speed was kept at a constant 1700 rpm (68% rated speed) by means of the hand throttle. This engine speed corresponded to the highest torque and the lowest specific fuel consumption of the engine. The relationship between *PTO* (power-take-off) and fuel consumption in kg/h at 1700 rpm engine speed (Fig. 75) was derived in a laboratory test with a torque dynamometer (Schenck W700, Darmstadt, Germany).

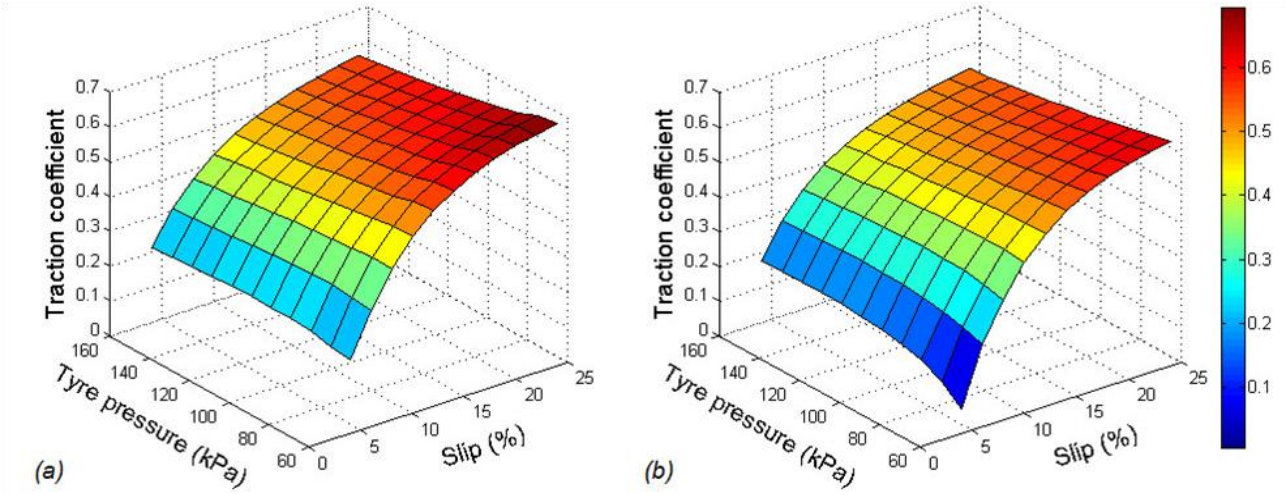

Fig. 72: Simulation of the traction coefficient of tractor A as a function of slip (from 4% to 25%) and tyre inflation pressure (from 60 to 160 kPa), without ballasts (tractor weight 40.0 kN) (a), and with ballasts (Tractor weight 49.2 kN) (b), on the clay soil (Table 5).

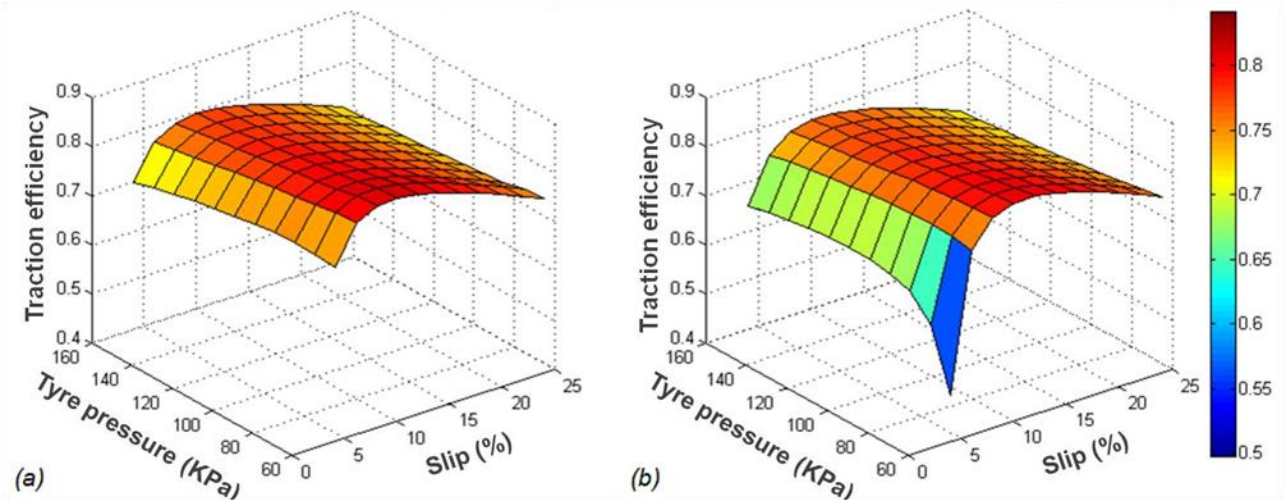

Fig. 73: Simulation of the traction efficiency of tractor A as a function of slip (from 4% to 25%) and tyre inflation pressure (from 60 to 160 kPa), without ballasts (tractor weight 40.0 kN) (a), and with ballasts (Tractor weight 49.2 kN) (b), on the clay soil (Table 5).

Power delivery efficiency and specific fuel consumption were fitted (least squares method) with the following equations:

$$\eta_{PD} = Ae^{\left(1-\frac{i}{l_A}\right)}\left(\frac{i}{l_A}\right)^{\left(1+\theta_A\frac{i}{l_A}\right)} \quad (57)$$

and

$$SFC = \frac{1}{Be^{\left(1-\frac{i}{l_B}\right)}\left(\frac{i}{l_B}\right)^{\left(1+\theta_B\frac{i}{l_B}\right)}} \quad (58)$$

wherein A, l_A, θ_A and B, l_B, θ_B are fitting parameters which mainly control: the positive peak of η_{PD} (parameter A), the negative peak of SFC (parameter B), the slip value at which the peak is reached (parameters l_A and l_B), and the slope of the curve beyond the peak (parameters θ_A and θ_B). Values of these parameters as well as the root mean square error $RMSE$ of the fitting are reported in Table 11.

An increase in tyre pressure resulted in lower power delivery efficiency and higher specific fuel consumption at both tractor weights, with a more significant variation at a tyre pressure of 60 kPa.

An increase in tractor weight, at least at a slip of less than 15%, resulted in a notable decrease in power delivery efficiency and an increase in specific fuel consumption at a tyre pressure of 60 kPa, as well as a slight decrease in power delivery efficiency with a more significant decrease in specific fuel consumption at a tyre pressure of 160 kPa.

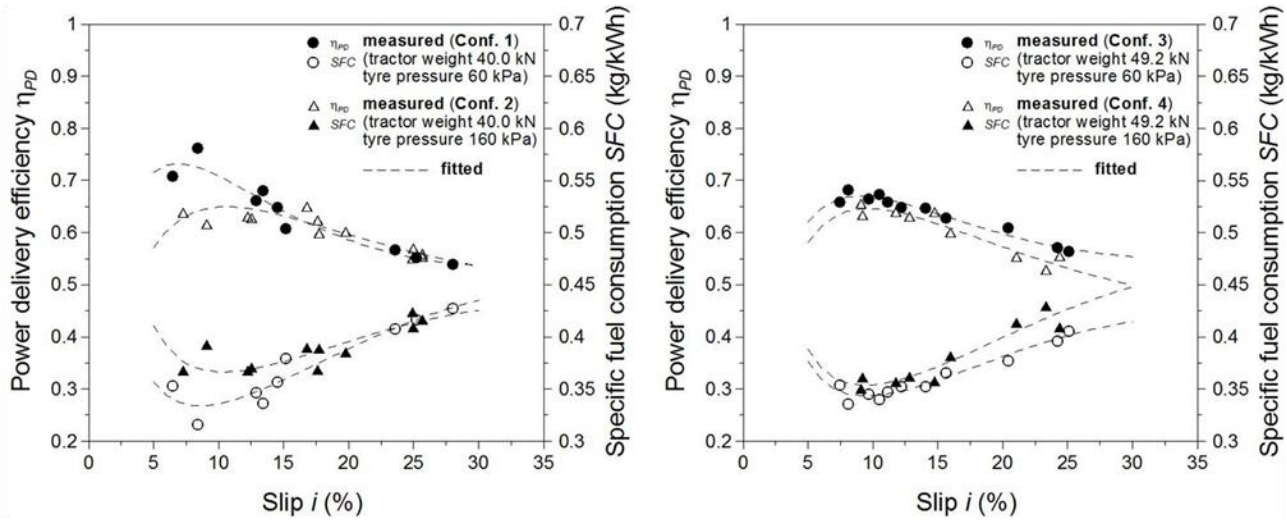

Fig. 74: Measured and fitted power delivery efficiency and specific fuel consumption (drawbar power basis) of tractor A as a function of slip, in configurations 1, 2, 3, and 4 (Table 1), on the clay soil (Table 5).

Table 11. Values of parameters A, l_A, θ_A and B, l_B, θ_B, and root mean square error RMSE from the fitting of the power delivery efficiency η_{PD} and the specific fuel consumption SFC (drawbar power basis).

	η_{PD}				SFC			
Conf.	A	l_A	θ_A	$RMSE$	B	l_B	θ_B	$RMSE$
	-	-	-	-	(kW h kg^{-1})	-	-	(kg kW^{-1} h^{-1})
1	0.67	3.77	0.28	0.019	2.74	4.62	0.28	0.011
2	0.59	5.98	0.29	0.016	2.47	5.26	0.29	0.010
3	0.61	4.68	0.29	0.007	2.65	4.94	0.29	0.005
4	0.60	5.98	0.27	0.012	2.59	5.08	0.28	0.009

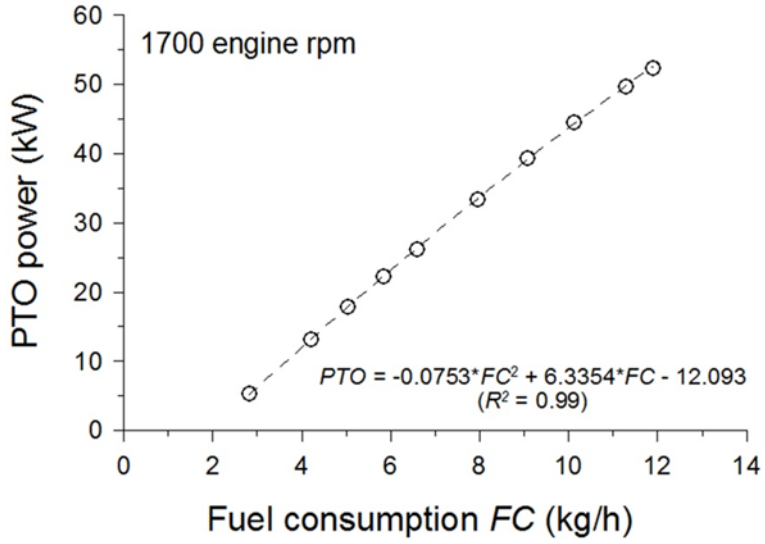

Fig. 75: Ratio between PTO and fuel consumption of tractor A at 1700 rpm engine speed.

1.3.4 Influence of soil mechanical properties on traction performance

In this paragraph the influence of soil mechanical parameters on the traction performance of tractor A is presented.

The four agricultural soils considered in this study are a clay, a clay loam, a silty loam, and a loamy sand with different water content, suction, and mechanical parameters (Table 5).

A comparison among the compression tests with the bevameter, executed in the four sites, is reported in Fig. 34 and Fig. 35. According to Bekker's indications (Bekker, 1960), the tests were performed with two round plates of 0.2 m and 0.3 m in diameter. This approach allows for the influence of the width of the contact patch on the soil reaction (Bekker, 1969).

The comparison points out noticeable differences in the stiffness under compression of the four soils. Such differences persist both in tests performed with the big plate and in tests performed with the small plate. Particularly, the loamy sand showed the highest stiffness, followed by the clay loam, whilst the silty loam and the clay showed a lower stiffness. The clay soil was the softest during the first load and the second load performed with the big plate (Fig. 35). In the compression tests with the small plate, the clay showed the weakest behaviour during the first load and a stiffness higher than the silty loam during the second load (Fig. 34). Results of the shear tests performed with the annular plate were elaborated according to the procedure described by Wong (1980). The envelopes of failure obtained for the four soils are reported in Fig. 38. The loamy sand has the highest cohesion (29.2 kPa) and the lowest angle of shear resistance (φ = 6.4°) This fact turns out in the highest strength at low vertical pressure and the lowest strength at high vertical pressure.

An opposite mechanical behaviour is shown by the clay loam which has the lowest cohesion (5 kPa) and the highest angle of shear resistance (φ = 30°). As a consequence, it has the lowest strength at low vertical pressure and the highest strength at high vertical pressure. The silty loam and the clay have values of cohesion and angle of shear resistance of 15.9 kPa and 25.6° and 24.4 kPa and 18°, respectively.

In the range of vertical pressure lower than 22 kPa the sandy loam shows the highest strength, in the range of vertical pressure from 23 kPa to 55 kPa the highest strength is shown by the clay. In the range of vertical pressure from 56 kPa to 110 kPa the highest strength is that of the silty loam, whilst beyond a vertical pressure of 110 kPa the highest strength is shown by the clay loam.

Results of the traction test on the four sites under consideration are reported in Fig. 76 for the tractor A in configuration 1 (Fig. 76*a*) and in configuration 2 (Fig. 76*b*). The two configurations are defined in Table 1. The experimental points are presented along with the simulations with the tractor-soil interaction model. The accuracy of the simulation was assessed in terms of the mean error and mean residual, the values obtained are reported in Table 7 (configurations 1 and 2). In all the cases considered, the highest mean error was 0.13, corresponding to a mean residual of 1.86 kN, which indicates a quite a good agreement between the experimental points and the simulation.

On all the four sites the increase in tyre pressure from 60 kPa to 160 kPa turned out in a decrease in drawbar pull.

At a tyre inflation pressure of 60 kPa the highest drawbar pull was measured on the clay and on the silty loam. Here the drawbar pull obtained was 28.5 kN at a slip of 28% on the clay, and 28.5 kN at a slip of 38.6 % on the silty loam. The drawbar pull measured on the clay loam and on the loamy sand was lower, with a maximum of 25.6 kN at a slip of 27.2% in the first case, and of 24.5 kN at a slip of 23.6% in the second case.

Also at a tyre pressure of 160 kPa the highest drawbar pull was measured on the clay and on the silty loam. In this case, the highest drawbar pull was 25.3 kN at a slip of 25.7% on the clay, and 25.9 kN at a slip of 46.7% on the silty loam. The maximum drawbar pull measured on the clay loam was 21.8 kN at a slip of 26.6%. The traction performance on the loamy sand was significantly lower than on the other soils with a maximum of 18.9 kN at a slip of 26.6%.

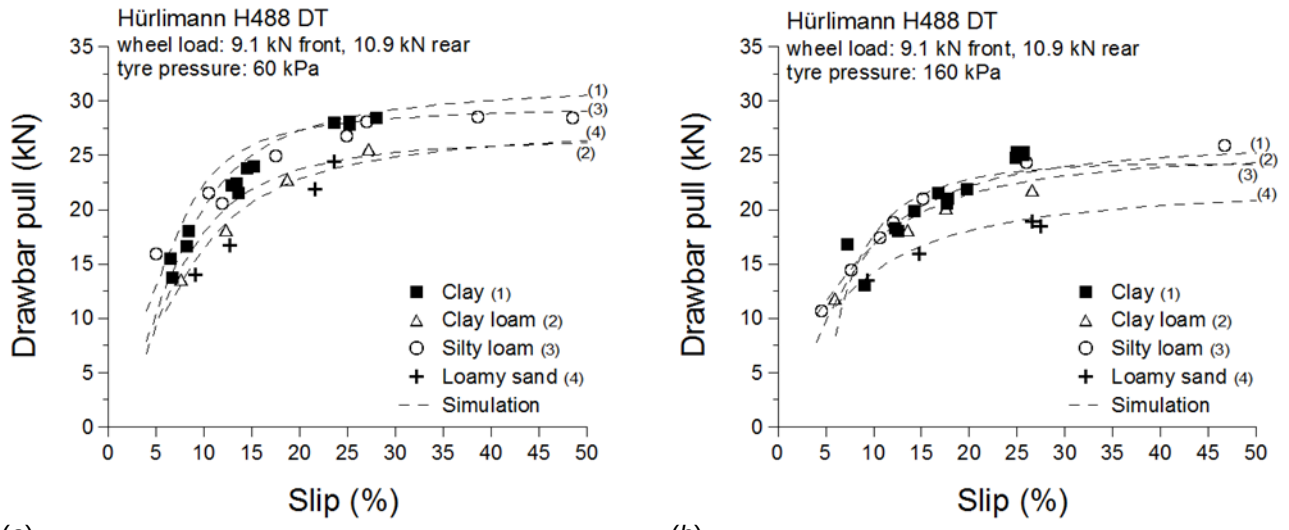

(*a*) (*b*)

Fig. 76: Measured and simulated drawbar pull of tractor A at a tyre pressure of 60 kPa (a) and at a tyre pressure of 160 kPa (b), on the four soils under consideration (clay, clay loam, silty loam and loamy sand).

Fig. 77 reports the specific fuel consumption *SFC* (drawbar power basis) as a function of the slip for the tractor A at a tyre pressure of 60 kPa (Fig. 77*a*) and at a tyre pressure of 160 kPa (Fig. 77*b*), on the four soils under consideration.

The distribution of the *SFC* shows a minimum in the range of slip from 7% to 15% both at a tyre pressure of 60 kPa and 160 kPa. The measured points were fitted with equation 58 and the accuracy was valued in terms of the root mean square error *RMSE* whose highest value was 0.029 at a tyre pressure of 60 kPa and 0.018 at a tyre pressure of 160 kPa (Table 12). In Table 12 the values of parameters B, l_B, θ_B of equation 58 are also reported.

At a tyre pressure of 60 kPa (Fig. 77*a*), the minimum *SFC* was 0.32 kg/kWh measured on the clay at a slip of 8%. On the silty loam the minimum *SFC* was 0.37 kg/kWh at a tyre slip of 11%, whilst on the loamy sand it was 0.37 kg/kWh at a tyre slip of 9% and on the clay loam it was 0.35 kg/kWh at a slip of 12%.

At a tyre pressure of 160 kPa (Fig. 77*b*) the minimum *SFC* was 0.36 kg/kWh obtained on the clay loam at a slip of 14%. On the clay the minimum *SFC* was 0.37 kg/kWh at a slip of 7%, whilst on the loamy sand it was 0.38 kg/kWh at a tyre slip of 15% and on the silty loam it was 0.40 kg/kWh at a tyre slip of 15%.

The increase of tyre inflation pressure from 60 kPa to 160 kPa turned out in an overall increase in *SFC*.

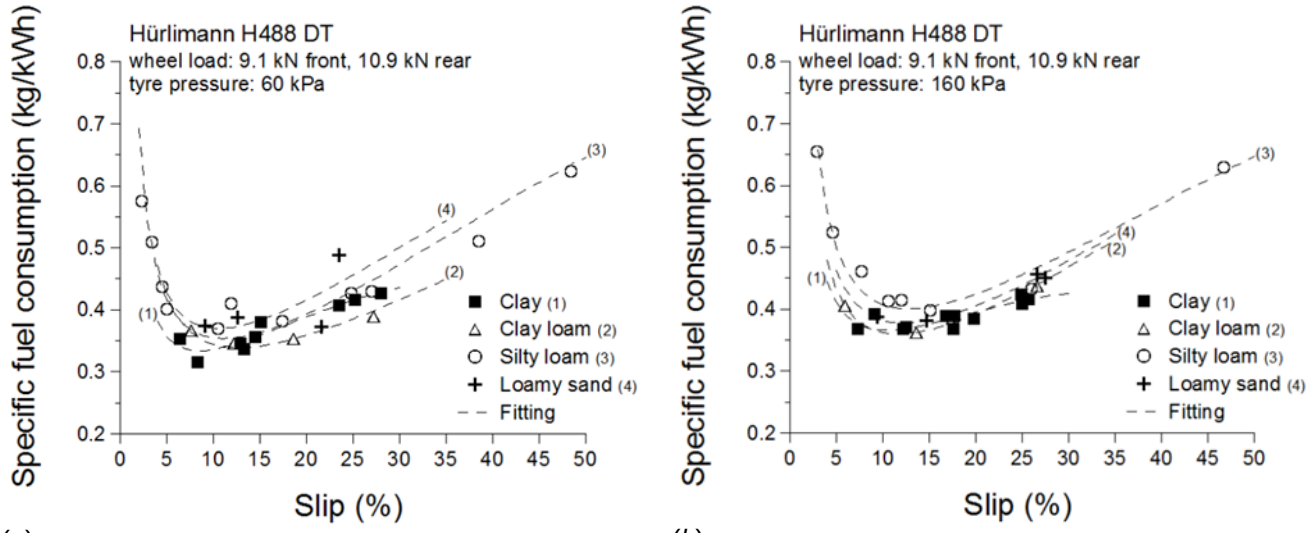

(*a*) (*b*)

Fig. 77: Measured and fitted specific fuel consumption SFC (drawbar power basis) of tractor A as a function of the slip, at a tyre pressure of 60 kPa (a) and at a tyre pressure of 160 kPa (b), on the four soils under consideration (clay, clay loam, silty loam and loamy sand).

Fig. 78 reports the distribution of the power delivery efficiency η_{PD}, defined according to equation 53, as a function of the slip in the four sites under consideration. The experimental points are seen along with a curve fitting based on equation 57, both at a tyre pressure of 60 kPa (Fig. 78*a*) and at a tyre pressure of 160 kPa (Fig. 78*b*). Values of the fitting parameters A, I_A, and θ_A, are reported in Table 13 together with the root mean square error *RMSE*. The latter had a highest value of 0.057, indicating a good agreement between the experimental points and the fitting curve.

At a tyre pressure of 60 kPa the highest η_{PD} was 0.76 measured on the clay at a slip of 8.4%. The lowest value was 0.64 measured on the loamy sand at a slip of 9.1%. On the silty loam the peak of η_{PD} was 0.69 measured at a slip of 10.5%, whilst on the clay loam it was also 0.69 at a slip of 12.3%.

At a tyre pressure of 160 kPa the highest η_{PD} was 0.66 measured at a slip of 13.6% on the clay loam. The lowest value was 0.62 measured on the loamy sand at a slip of 14.7%. On both the clay and the silty loam the peak value of η_{PD} was 0.65, in the first case measured at a slip of 16.8%, and in the second case measured at a slip of 15.2%.

The increase in tyre pressure from 60 kPa to 160 kPa turned out in an overall decrease in power delivery efficiency.

In most of the cases the peak of the η_{PD} corresponded to the minimum of the *SFC* and, in general, the range of slip between 7% and 15% where the *SFC* is minimized is also the range where the η_{PD} reaches its highest values.

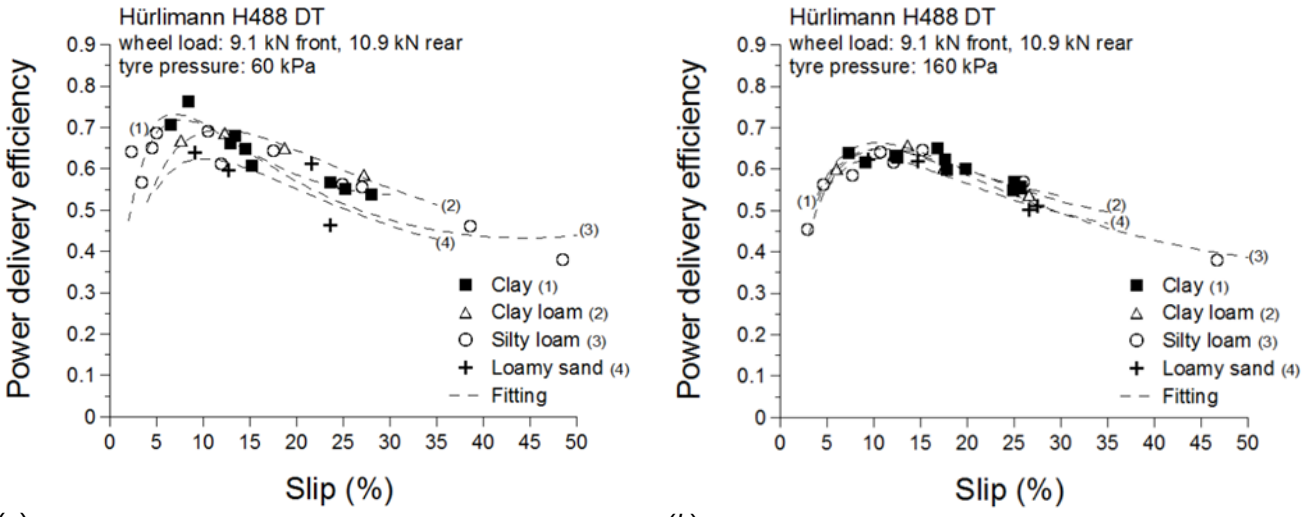

(*a*) (*b*)

Fig. 78: Measured and fitted power delivery efficiency η_{PD} of tractor A as a function of the slip, at a tyre pressure of 60 kPa (a) and at a tyre pressure of 160 kPa (b), on the four soils under consideration (clay, clay loam, silty loam and loamy sand).

Table 12. Values of parameters B, l_B, θ_B, and root mean square error RMSE from the fitting of the specific fuel consumption SFC.

Tyre pressure	60 kPa				160 kPa			
	B	l_B	θ_B	*RMSE*	*B*	l_B	θ_B	*RMSE*
Soil	(kW h kg^{-1})	-	-	(kg kW^{-1} h^{-1})	(kW h kg^{-1})	-	-	(kg kW^{-1} h^{-1})
Clay	2.74	4.62	0.28	0.011	2.47	5.26	0.29	0.010
Clay loam	0.11	3.04	10.52	0.006	0.11	2.99	11.02	0.004
Silty loam	0.11	2.84	11.00	0.028	0.09	3.04	10.52	0.018
Loamy sand	0.10	2.50	10.50	0.029	0.11	3.15	11.03	0.005

Table 13. Values of parameters A, l_A, θ_A, and root mean square error RMSE from the fitting of the power delivery efficiency η_{PD}.

Tyre pressure	60 kPa				160 kPa			
	A	l_A	θ_A	*RMSE*	*A*	l_A	θ_A	*RMSE*
Soil	-	-	-	-	-	-	-	-
Clay	0.67	3.77	0.28	0.019	0.59	5.65	0.29	0.016
Clay loam	0.65	0.07	0.27	0.008	0.61	0.06	0.28	0.012
Silty loam	0.67	0.04	0.27	0.057	0.60	0.06	0.27	0.028
Loamy sand	0.58	0.06	0.27	0.048	0.58	0.06	0.28	0.008

Results of the simulation with the tractor-soil interaction model for the tractor A on the four soils are reported in Fig. 79, Fig. 80, Fig. 81 and Fig. 82 in terms of drawbar pull *DP*, traction coefficient μ_{tr}, traction efficiency $\eta_{tr\ tractor}$, and motion resistance due to the soil compaction resistance R_c, as a function of the slip in the range from 5% to 25% and as a function of the tyre pressure in the range from 60 kPa to 160 kPa. In Fig. 79 the highest drawbar pull was obtained, on all the soils considered, at a tyre pressure of 60 kPa and a slip of 25%. The highest drawbar pull, 28.1 kN, was obtained on the clay, whilst the lowest drawbar pull, at the same conditions of slip and tyre pressure, was simulated on the loamy sand and it was 24.5 kN.

The highest drawbar pull on the silty loam and on the clay loam were 27.8 kN and 25.4 kN, respectively.

In all the sites considered, the drawbar pull increased with the slip and decreased with the tyre pressure, at least for high values of slip.

Simulations of the traction coefficient reported in Fig. 80 also confirm that the highest traction performance is simulated on the clay. Here the highest traction coefficient was 0.69 at a tyre pressure of 60 kPa and a slip of 25%. In the same conditions, the highest traction coefficient on the clay loam, on the silty loam and on the loamy sand were 0.62, 0.68, and 0.60, respectively. According to the distribution of the drawbar pull, also the traction coefficient increases with the slip and decreases with the tyre pressure for high values of slip.

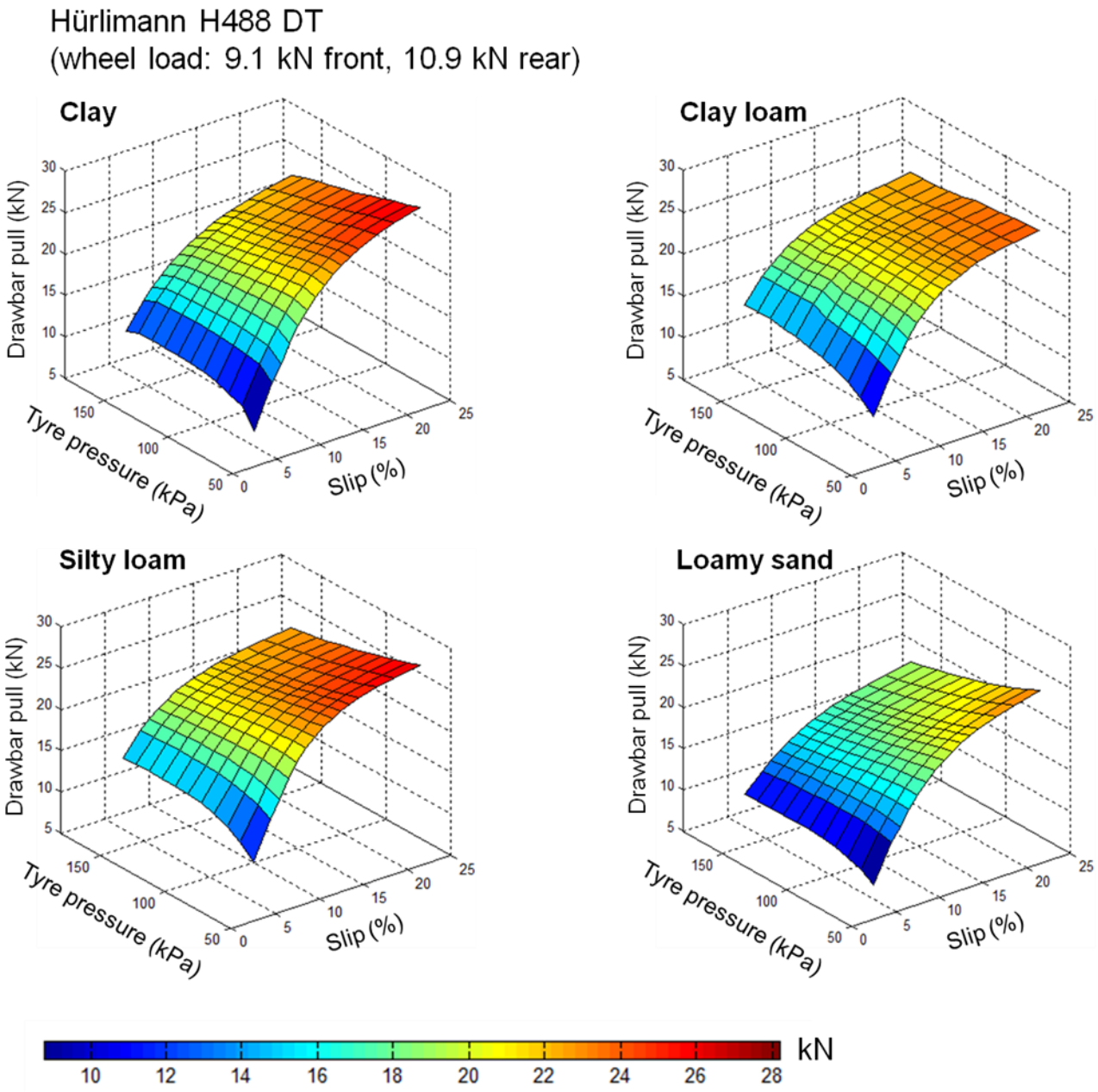

Fig. 79: Simulation of the drawbar pull of tractor A as a function of the slip and the tyre pressure on the four soils under consideration (clay, clay loam, silty loam, and loamy sand).

The simulation of the traction efficiency (Fig. 81) shows a peak in the range of slip values between 5% and 10%. The increase in tyre pressure makes for a decrease in traction efficiency. In Fig. 81 the highest traction efficiency is 0.95 reached on the loamy sand at a slip of 5%. The maximum traction efficiency on the clay, on

the clay loam, and on the silty loam were, in order, 0.86, 0.92 and 0.85, reached at a slip of 10%, 5%, and 9%, respectively. The motion resistance in Fig. 82 was calculated as the soil compaction resistance, according to equation 32. It increases with the tyre pressure in all the cases considered. An increase in slip turned out in a reduction of motion resistance on the clay and in no significant variations on the other soils. The highest motion resistance was obtained on the silty loam at a tyre pressure of 160 kPa and a slip of 5%, and it was 2.17 kN. The highest motion resistance on the clay was 1.82 kN obtained at a slip of 5% and a tyre pressure of 160 kPa.

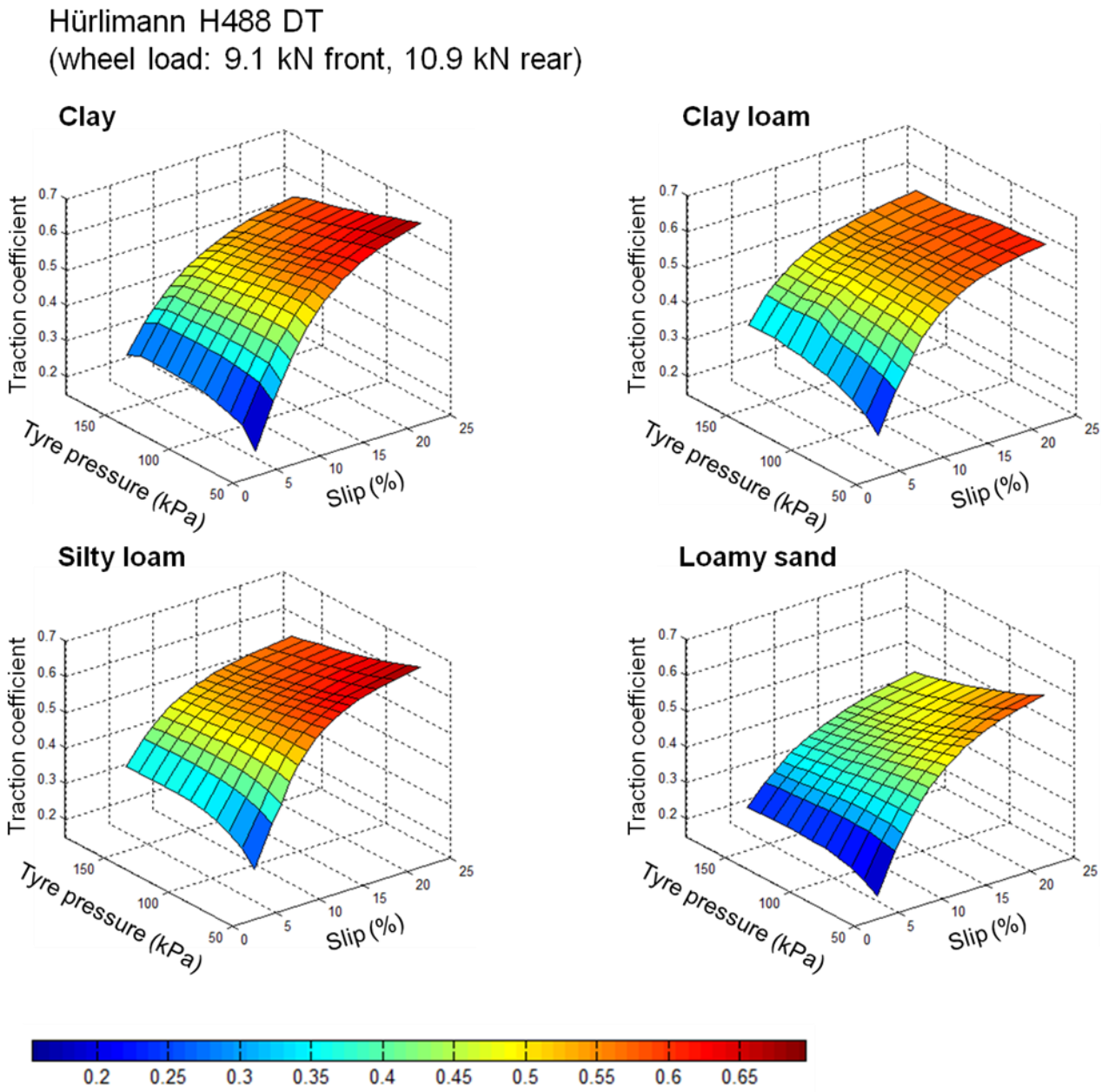

Fig. 80: Simulation of the traction coefficient of tractor A as a function of the slip and the tyre pressure on the four soils under consideration (clay, clay loam, silty loam, and loamy sand).

On the clay loam the maximum value of the motion resistance was 0.52 kN obtained also at a slip of 5% and a tyre pressure of 160 kPa. The maximum motion resistance on the loamy sand was 0.15 kN obtained at a

slip of 25% and at a tyre pressure of 160 kPa. The comparison among the motion resistance simulated on the different soils is in agreement with the results of the compression tests reported in Fig. 34 and Fig. 35.

Fig. 83 presents the simulation of the soil-tyre contact surface of the rear wheel of tractor A at a tyre pressure of 60 kPa and a slip of 10%, and the simulation of the contact stress in terms of both normal and shear stress. In addition, the soil strength is also shown. The rut depth was 0.015 m on the clay, 0.006 m on the clay loam, 0.028 m on the silty loam and 0.001 on the loamy sand. The different rut depths under the rear wheel are in agreement with the stiffness of the considered soils during the compression tests (Fig. 34 and Fig. 35).

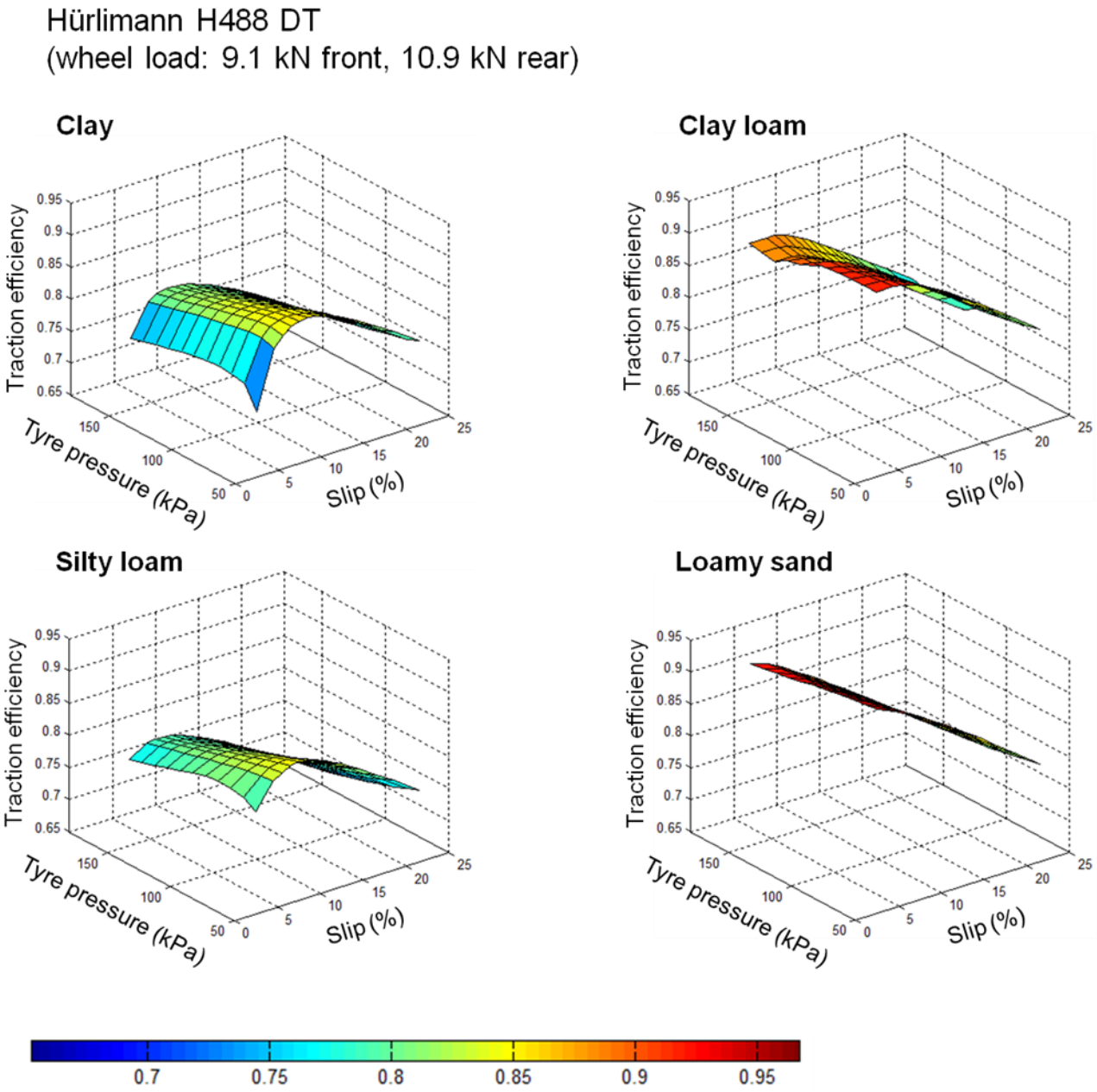

Fig. 81: Simulation of the traction efficiency of tractor A as a function of the slip and the tyre pressure on the four soils under consideration (clay, clay loam, silty loam, and loamy sand).

The higher the soil stiffness during compression, the lower the soil sinkage and the rut depth are. The length of the contact patch was 0.64 m on the clay, 0.62 m on the clay loam, 0.66 m on the silty loam, and 0.61 m on the loamy sand.

The maximum normal stress was 75.7 kPa on the clay, 77.7 kPa on the clay loam, 74.0 kPa on the silty loam, and 77.3 kPa on the loamy sand. The peak of shear stress was 35.7 kPa on the clay, 41.2 kPa on the clay loam, 43.2 kPa on the silty loam, and 26.8 kPa on the loamy sand. The maximum soil strength was 49.0 kPa on the clay, 49.8 kPa on the silty loam, 51.4 kPa on the silty loam, and 37.9 kPa on the loamy sand.

The same simulation of Fig. 83 is reported for a tyre pressure of 160 kPa in Fig. 84. Here the soil-tyre contact surface was deeper and shorter than at a tyre pressure of 60 kPa, moreover, the stress state at the soil-tyre contact was higher.

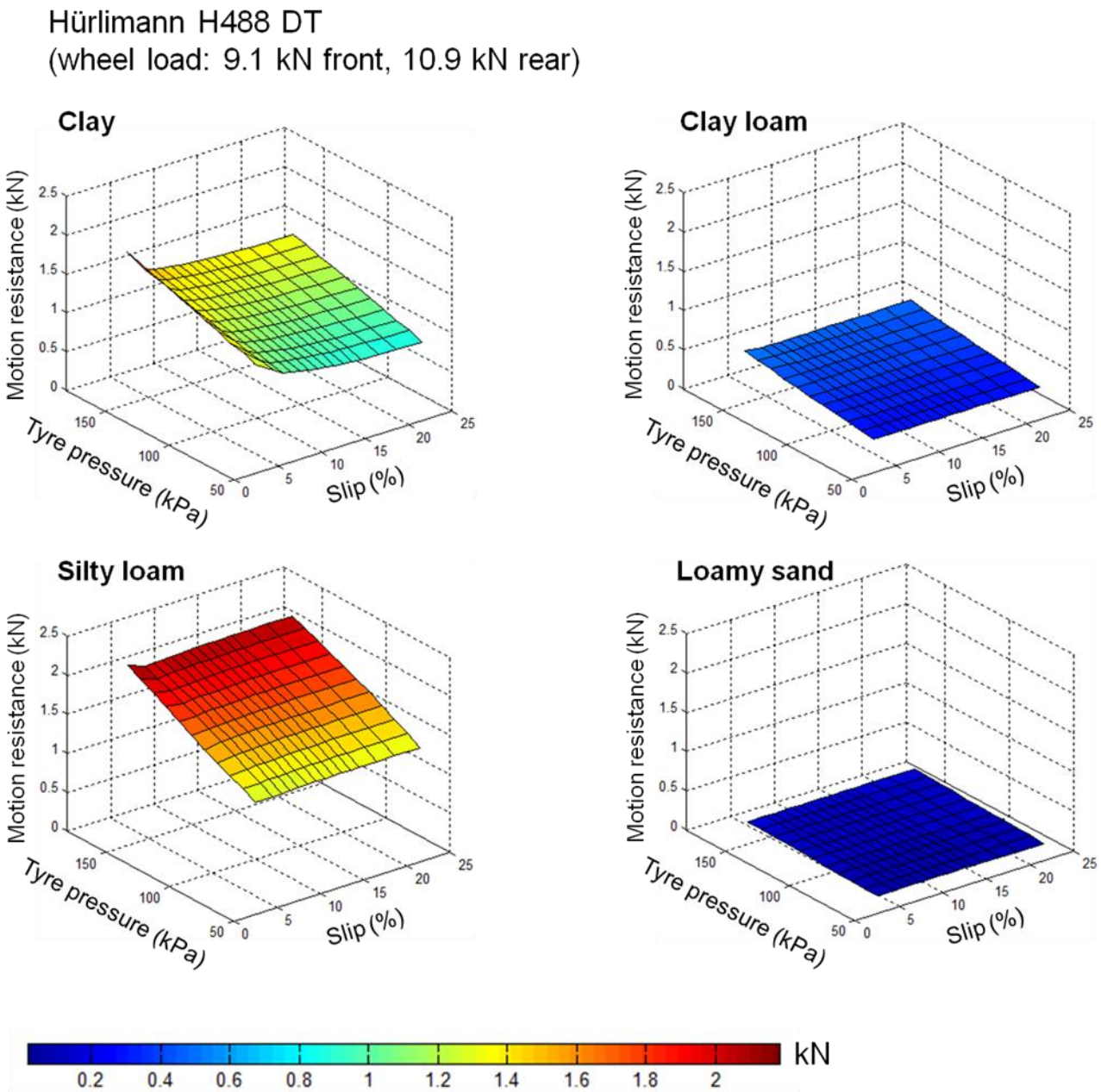

Fig. 82: Simulation of the motion resistance of tractor A as a function of the slip and the tyre pressure on the four soils under consideration (clay, clay loam, silty loam, and loamy sand).

On the clay soil the rut depth was 0.020 m. Values of the rut depth of 0.008 m, 0.037 m, and 0.002 m were simulated on the clay loam, on the silty loam and on the loamy sand, respectively.

The length of the contact patch assumed values of 0.49 m, 0.48 m, 0.53 m, and 0.45 m, on the clay, the clay loam, the silty loam and the loamy sand, respectively.

The maximum normal stress and shear stress on the clay were 95.9 kPa and 41.7 kPa, respectively. On the clay loam the maximum normal stress was 102.9 kPa and the maximum shear stress was 57.3 kPa. On the silty loam and on the loamy sand the maximum normal stress was 91.2 kPa and 103.2 kPa, respectively, whilst the shear stress was 55.0 kPa and 31.6 kPa, respectively.

The highest values reached by the soil strength were 55.6 kPa, 64.4 kPa, 59.4 kPa, and 40.8 kPa, on the clay, the clay loam, the silty loam, and the loamy sand, respectively.

Fig. 85 shows the simulated stress path along the soil-tyre contact surface of the rear wheel of tractor A at a slip of 10%. The simulation is repeated for a tyre pressure of 60 kPa (Fig. 85*a*) and for a tyre pressure of 160 kPa (Fig. 85*b*). The stress paths are represented in terms of mean stress and deviatoric stress.

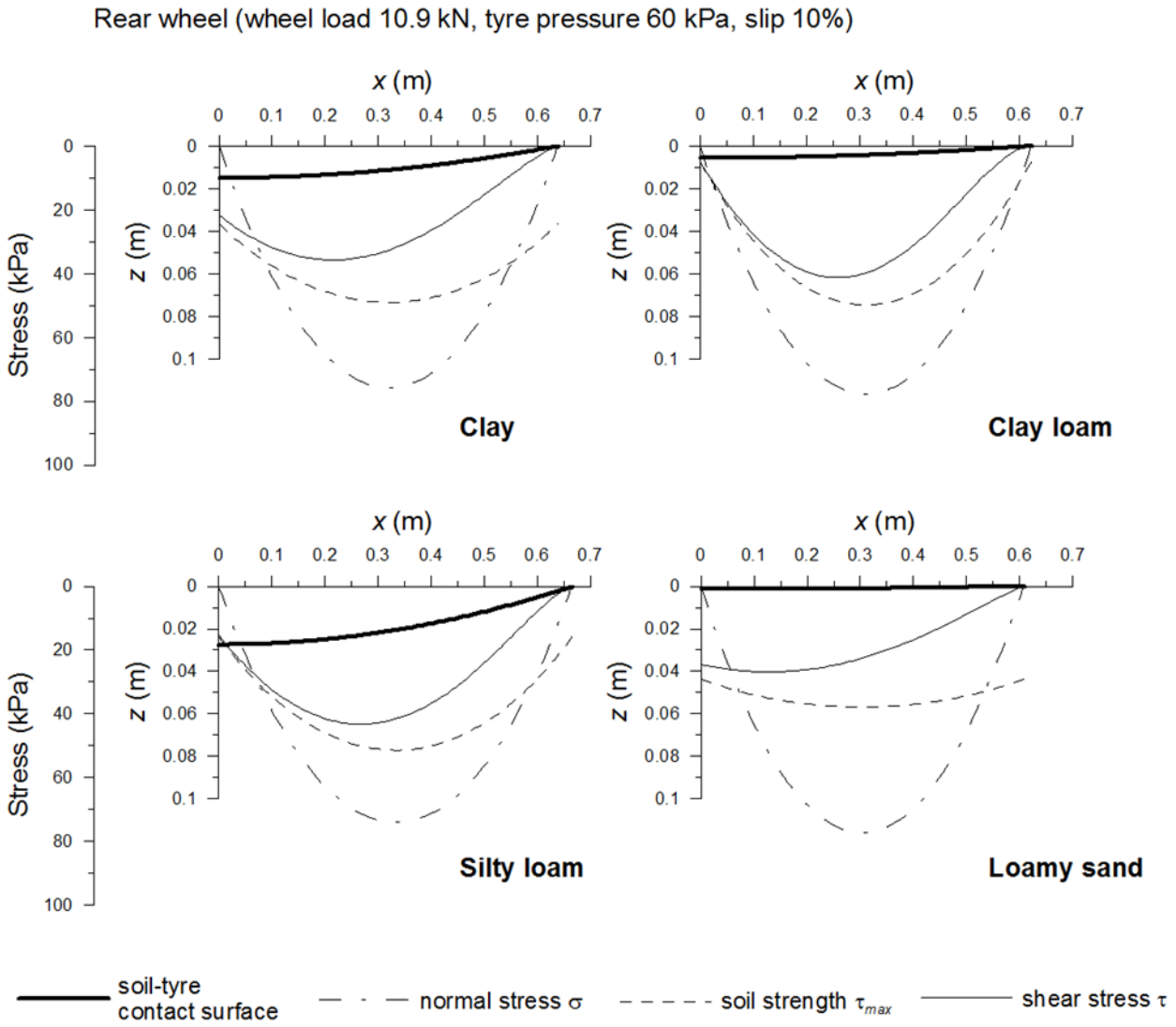

Fig. 83: Simulation of the geometry of the soil-tyre contact surface, the contact stresses (normal σ and shear τ), and the soil strength τ_{max} for the rear wheel (420 85R34 tyre) of tractor A at a slip of 10% in configuration 1 (Table 1), on the four soils considered (Table 5).

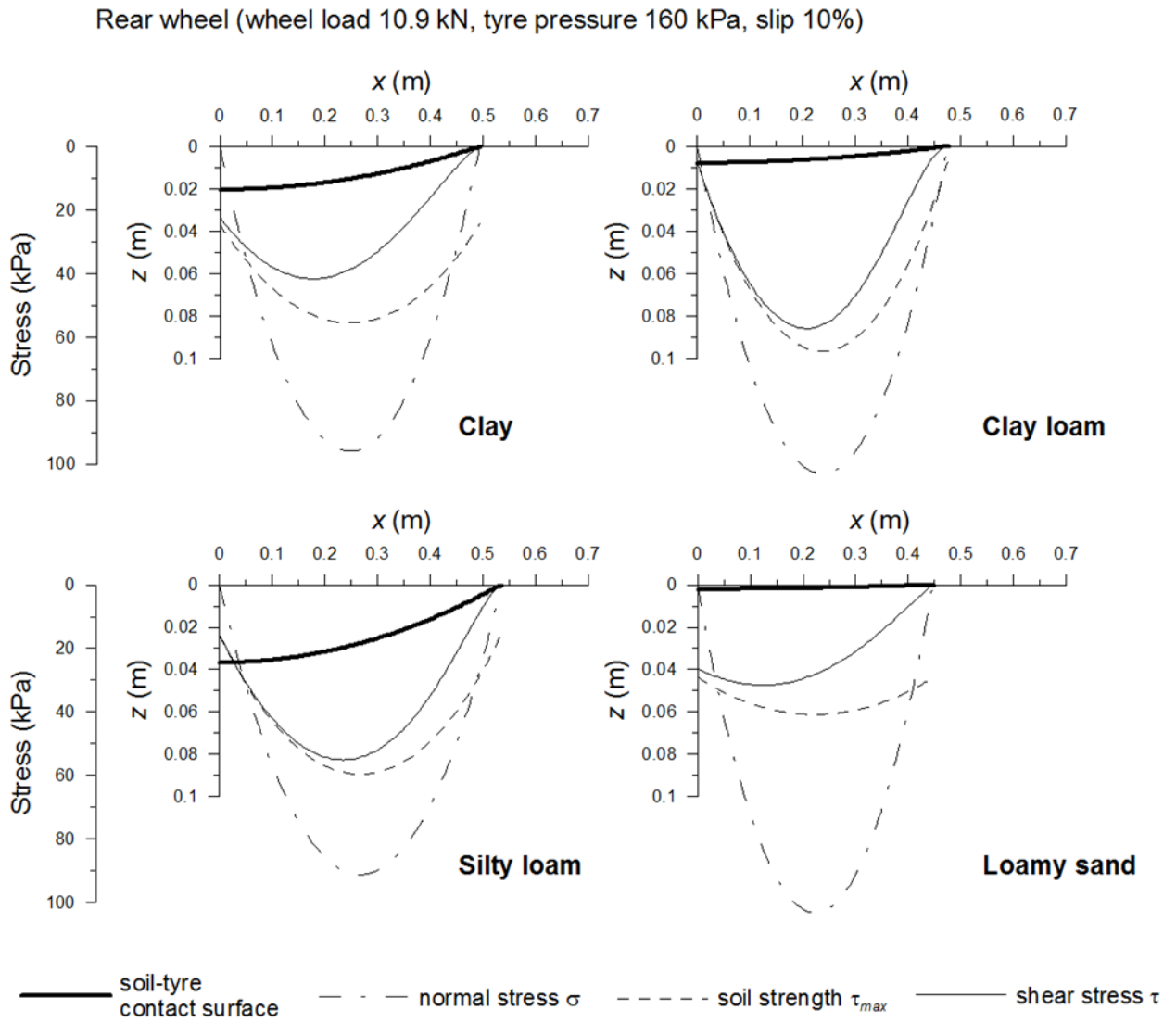

Fig. 84: Simulation of the geometry of the soil-tyre contact surface, the contact stresses (normal σ and shear τ), and the soil strength τ_{max} for the rear wheel (420 85R34 tyre) of tractor A at a slip of 10% in configuration 2 (Table 1), on the four soils considered (Table 5).

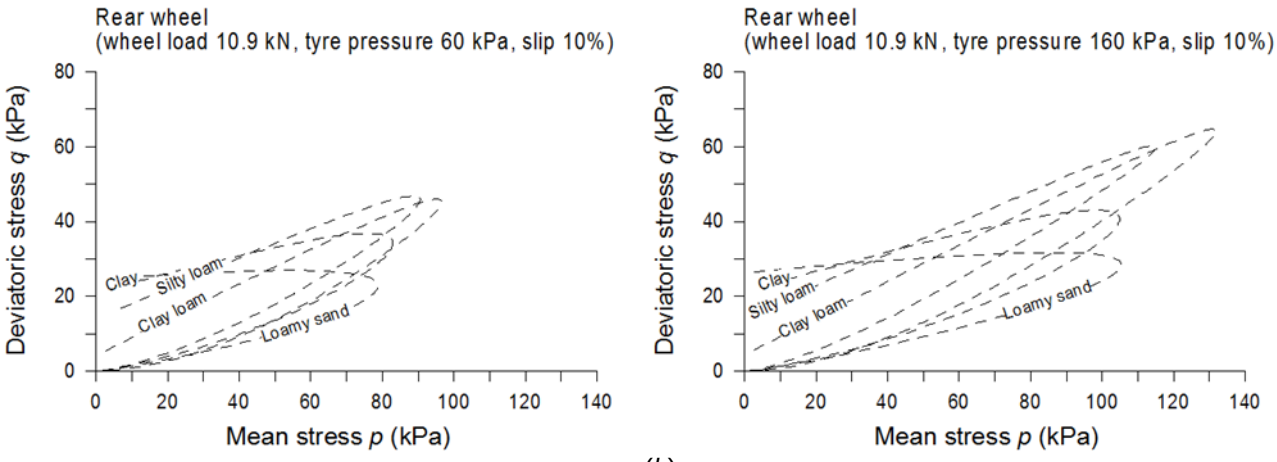

(*a*) (*b*)

Fig. 85: Simulation of the stress paths along the soil-tyre contact surface of the rear wheel (420 85R34 tyre) of tractor A at a slip of 10%, in configurations 1 (a) and 2 (b) (Table 1), on the four soils considered (Table 5).

At a tyre pressure of 60 kPa the highest mean stress and deviatoric stress were 83.0 kPa and 36.8 kPa, respectively, on the clay, 96.6 kPa and 45.9 kPa, respectively, on the clay loam, 90.6 kPa and 46.8 kPa, respectively, on the silty loam, and 78.8 kPa and 26.9 kPa, respectively, on the loamy sand.

At a tyre pressure of 160 kPa the stress state at the soil-tyre contact was noticeably higher. In this case, the mean stress assumed the highest value of 104.9 kPa, 131.8 kPa, 115.1 kPa and 105.4 kPa, on the clay, the clay loam, the silty loam and the loamy sand, respectively.

The deviatoric stress reached a maximum value of 43.0 kPa, 64.7 kPa, 60.3 kPa and 31.7 kPa, on the clay, the clay loam, the silty loam, and the loamy sand, respectively.

The mean normal stress and the mean shear stress over the soil-tyre contact surface of the rear wheel of tractor A at a slip of 10% and a tyre pressure of 60 kPa and 160 kPa are reported in Fig. 86 for the four soils under consideration. On the clay the mean normal stress was 50.5 kPa and the mean shear stress was 24.6 kPa at a tyre pressure of 60 kPa. At a tyre pressure of 160 kPa the mean normal stress was 64.1 kPa and the mean shear stress was 28.7 kPa. On the clay loam the mean normal stress was 51.7 kPa and the mean shear stress was 25.5 kPa at a tyre pressure of 60 kPa. They were 68.4 kPa and 35.6 kPa, respectively, at a tyre pressure of 160 kPa. On the silty loam the mean normal stress was 49.5 kPa at a tyre pressure of 60 kPa, and 60.8 kPa at a tyre pressure of 160 kPa. The mean shear stress was 29.0 kPa at a tyre pressure of 60 kPa, and 37.2 kPa at a tyre pressure of 160 kPa. On the loamy sand the mean normal stress was 51.4 kPa at a tyre pressure of 60 kPa, and 68.4 kPa at a tyre pressure of 160 kPa, whilst the mean shear stress was 18.8 kPa and 22.7 kPa at a tyre pressure of 60 kPa and 160 kPa, respectively.

The failure envelopes of the four soils are shown in Fig. 86 where the mechanical parameters cohesion and angle of shear resistance are also reported.

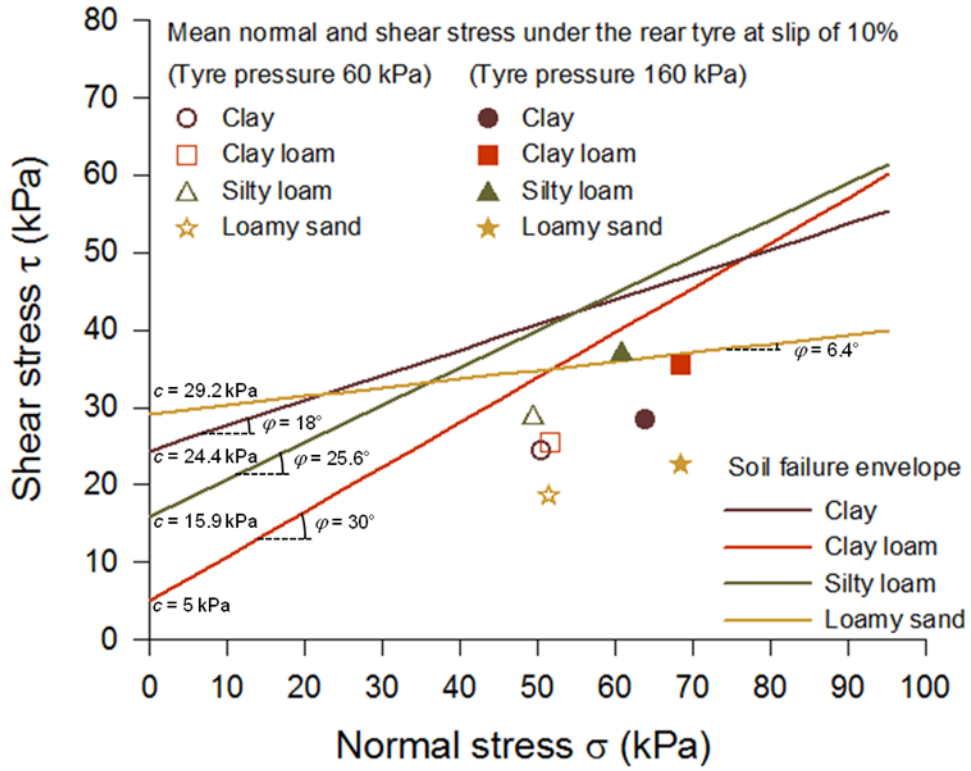

Fig. 86: Failure envelope according to Mohr-Coulomb and simulation of the mean normal and shear stress under the rear wheel (420 85R34 tyre) of tractor A at a slip of 10%, in configurations 1 and 2 (Table 1), for the four soils considered (Table 5).

1.4 Discussion

1.4.1 Analysis of measured and simulated traction performance of mechanical front-wheel drive (MFWD) tractors

Results of the full-scale traction tests with the four tractors clearly showed the improvement in the drawbar pull due to a decrease in the tyre pressure or an increase in the wheel load.

Turner (1993) and Zoz and Grisso (2003) also observed that an increase in tractor weight (wheel load) makes for higher drawbar pull. The benefits on traction performance of tractors of reduced inflation pressure were reported by many authors (Burt and Bailey, 1982; Wood and Mangione, 1992; Upadhyaya and Wulfsohn, 1993; Turner, 1993; Zoz and Grisso, 2003).

The comparison of the drawbar pull of tractor A measured on the four sites points out the influence of the soil mechanical behaviour on the traction performance, and confirms that this latter is not a characteristic of the tractor only, but it is a function of the tractor-soil system.

An analogous conclusion may be drawn on the basis of the results reported by Wismer and Luth (1973), Zoz (1987), Shell et al. (1997), Zoz and Grisso (2003), Saarilahti (2002), and Lyasko (2010).

The comparison of the traction performance on the four soils under consideration is analysed in detail in paragraph 1.3.4 and discussed in the paragraph 1.4.3.

The benefit in the drawbar pull developed on a cohesive soil from the use of dual tyres at the rear axle or at both the front and the rear axles is also pointed out by the experimental measurements.

Such a benefit is due to the wider contact surface which allows for a better use of the topsoil strength and is in agreement with the results reported by Grisso et al. (1992) and Turner (1993).

The model used presents a simple mathematical approach compared to the existing models by Bekker (1960), Fujimoto (1977), and Schmid (1995), as already remarked by Shmulevich and Osetinsky (2003).

Compared to some existing models for simulating the tractor drawbar performance based on the Wismer and Luth's equation (Wismer and Luth, 1973), like that presented by Sahay and Tewari (2004), the model used assures a more rigorous approach to describe the interaction between the tractor and the soil.

Results of the simulations reproduce the dependence of the drawbar pull, the traction coefficient, the traction efficiency and the motion resistance on the tyre pressure and on the wheel load.

Similar results were reported by Bart et al. (1979) and by Shmulevich and Osetinsky (2003) and Osetinsky and Shmulevich (2004).

Model simulations matched experimental measurements with general good agreement in the range of slip values considered (Fig. 58-Fig. 69 and Table 7-Table 10). When the four tractors are considered in all the configurations taken under consideration, the model simulates the traction performance, in terms of drawbar pull, with an overall accuracy corresponding to a mean error of 0.12 and a mean residual of 3.3 kN.

In most of the cases the simulated traction performance tended to cross the slip axis at values higher than zero. This implies that in order to develop net traction (drawbar pull) a certain slip is required. Such a result is due to the deflection of the tyre when it interacts with soil and depends on the distribution of the slip velocity along the soil-tyre contact surface, as explained in the description of the soil-tyre interaction model.

An evident underestimation of the drawbar pull is shown in many cases, at a low slip, when a high wheel load is combined with a low tyre inflation pressure, i.e. in configuration 3 (Fig. 58*c*, Fig. 59*c*, Fig. 60*c*, Fig. 62*c*, and Fig. 64*c*). This result is due to a not accurate enough simulation of the contact surface.

When dual tyres are used at the rear axle or at both the front and the rear axles (Fig. 66), the simplified approach which assumed a unique tyre having width and stiffness given by the sum of those of the two single tyres, gave results in sufficient agreement with the traction performance measured. However, a more rigorous analysis of the system of dual tyres seems to be needed in order to improve consistency of model simulations. The accuracy of the simulation is reduced due to the difficulty in a proper valuation of the rolling radius when dual tyres are used. Moreover, the soil pressure-sinkage relationship obtained with the bevameter vertical plates penetration tests results less precise for dual tyres or wide tyres than for narrow tyres. This is due to the fact that the compression plate employed were 0.2 m and 0.3 m in diameter, as a consequence, the dependence of the soil pressure-sinkage relationship on the width of the plate, or of the tyre, was consistent in a limited range around the plate diameters, becoming less consistent for tyres much wider than 0.3 m.

The model used doesn't describe the uneven stress state under the tyre tread due to the presence of the lugs. This aspect should be an object for a further development of the model.

In addition, a function which properly describes the elasto-plastic behaviour of the soil during a repetitive loading should be introduced in order to better simulate the interaction between the soil and the rear wheels.

The model presented can be a valid aid for the choice of a proper tractor configuration, this results in saving fuel and, therefore, in reducing the costs of tillage management.

1.4.2 Analysis of the influence of tyre inflation pressure and wheel load on traction performance

The traction performance of a wheeled tractor is the result of a stress-strain interaction between the tractor wheels and the topsoil. This interaction is affected by several factors, including the mechanical behaviour of the topsoil, power and geometry of the tractor (wheelbase and drawbar height), number of drive wheels, wheel load, wheel slip, tyre dimensions (width and diameter), tyre inflation pressure and stiffness, all of which exert a significant influence. While most of the above factors are more or less constrained, wheel load and tyre inflation pressure can be varied within wide ranges, allowing easy management of the traction performance of the tractor. Consequently, these factors are highly advantageous for practical applications. The influence of wheel load and tyre inflation pressure on tractor traction performance has been investigated using both a theoretical and an experimental approach.

With regard to the former approach, the semi-empirical models of interaction between soil and a pneumatic wheel based on Bekker's theory (Bekker, 1960) offer a valid framework for the better understanding and simulation of the effects of both tyre inflation pressure and wheel load on the traction performance of the tractor-soil system. In this context several approaches have been presented assuming the contact surface between soil and tyre to be a combination of a flattened portion and the unloaded contour (Bekker, 1960; Wong, 1989), or as an arc of an equivalent rigid wheel of larger diameter (Fujimoto, 1977), or also described as a parabolic configuration with its apex at the front point of contact (Schmid, 1995). More recently, Shmulevich and Osetinsky proposed their model based on a parabolic soil-tyre contact surface with its apex at the rear point of contact (Shmulevich and Osetinsky, 2003; Osetinsky and Shmulevich, 2004), which presents a simple mathematical treatment and allows a reliable simulation of traction performance.

With regard to the latter approach, many authors have reported experimental results showing some benefits of reduced tyre inflation pressure for tractor traction performance (Zombori, 1967; Gee-Clough et al., 1977; Burt and Bailey, 1982; Turner, 1993; Zoz and Grisso, 2003). Whilst evident for radial-ply tyres, these benefits in some cases turned out to be less or not at all significant for bias-ply tyres (Lee and Kim, 1997).

Serrano et al. (2009) studied the performance of a tractor (59 kW engine power) with two static ballasts, with and without liquid tyre ballast, and at three different inflation pressures. The use of liquid ballast in the tyres turned out not to improve work-rate and besides to increase fuel consumption per hectare of 5-10%. The use of higher tyre inflation pressures produced a slight reduction in work-rate (3-5%) with a large increase in fuel consumption per hectare (10-25%).

Burt et al. (1979) investigated the influence of dynamic wheel load on traction efficiency on both a compacted and an uncompacted soil, observing that, with constant travel reduction (slip), an increase in dynamic load produced in the former case an increase and in the latter case a decrease in traction efficiency.

Charles (1984) carried out tractor-traction tests on a low-plasticity silt soil in both a tilled (soft) and firm condition at different static loads and tyre inflation pressures. His findings show that both an increase in static load and a decrease in tyre pressure resulted in higher traction performance in terms of drawbar pull and traction efficiency for both of the soil conditions considered.

Lyne et al. (1984) reported results of traction tests with a 4WD tractor on a Westleigh clay in two soil conditions and with several combinations of static load and tyre pressure, showing that as static load increased at each inflation pressure, so did drawbar pull, drawbar power and power demand on the engine, with a corresponding decrease in specific fuel consumption (drawbar power basis). According to results reported by Turner (1993) and Zoz and Grisso (2003), an increase in tractor weight (wheel load), obtained with ballasts and tyre inflation pressure adapted to the weight, makes for higher drawbar pull, although it does not seem to result in a significant variation in terms of traction coefficient or power delivery efficiency.

Results of traction tests reported by Zoz and Grisso (2003) for a single 520/85R46 radial tyre with inflation pressure adapted for different wheel loads showed a negligible influence on maximum traction efficiency. Burt et al. (1983) and Burt and Bailey (1982) showed how, for a given drawbar pull, the traction efficiency of both radial-ply and bias-ply tyres can be maximised by selecting proper levels of dynamic load and inflation pressure.

Lyne et al. (1984) also pointed out the importance of an appropriate choice of both dynamic load and tyre inflation pressure in order to optimise the traction efficiency of a tractor. Moreover, it was observed that operating at optimum traction efficiency allows minimum specific fuel consumption (Lyne et al., 1984; Jenane et al., 1996).

Gee-Clough et al. (1982) demonstrated the key role of a wheel load properly matched to tractor power, speed, and drawbar pull at low tyre inflation pressure (110 kPa or less), in the optimisation of the power output of wheeled tractors in frictional-cohesive soils.

This variety of studies has produced results which in some cases appear to contradict one another. It should be pointed out, however, that the widely differing experimental conditions considered (soil and tyre types, wheel load range, tyre pressure range) make it difficult to draw proper comparisons, as do the different layouts and methodologies used for the traction tests.

According to our results, the advantages in decreasing tyre inflation pressure or ballasting the tractor may be greater or lesser, depending on the change in the interaction between soil and tyre. It emerged that the traction performance of the tractor considered depended on the geometry of the contact surface between tyre and soil, as well as on contact stresses and soil strength (Fig. 70). All of these factors varied significantly

with the inflation pressure, and less noticeably with the stationary wheel load in the four configurations considered (Fig. 70).

At low inflation pressure (Fig. 70*a* and Fig. 70*c*), the simulated contact surface was shallow and long. This implied, on the one hand, low soil strength due to low contact pressure, as well as high rolling resistance due to high tyre deformation, and on the other hand, low soil compaction resistance due to low soil sinkage, and the soil strength used on a more extended surface.

According to equation 27, soil strength is given by a cohesive component c and a frictional component $\sigma tan\varphi$ which depends on the normal stress σ. When the inflation pressure was reduced at constant wheel load, the improvement in traction performance was mainly due to the mobilisation of the cohesive component of the soil strength on a more extended contact area, i.e. a higher total contribution of the cohesive component of the soil strength along the contact surface. This allowed better use of the soil strength, which for the same slip resulted in a higher drawbar pull and traction coefficient (Fig. 71 and Fig. 72), higher simulated traction efficiency (Fig. 73), higher power delivery efficiency, and lower specific fuel consumption (Fig. 74).

When the stationary wheel load was increased at a constant tyre pressure, the simulated contact surface varied slightly, becoming longer and deeper (Fig. 70*a* and Fig. 70*c* and Fig. 70*b* and Fig. 70*d*). This implied, on the one hand, higher rolling resistance due to greater tyre deformation and higher soil compaction resistance due to greater soil sinkage, and on the other hand, higher soil strength due to greater normal contact stress and the soil strength used on a more extended surface.

The improvement of traction performance in terms of drawbar pull (Fig. 71) was partly due to a higher total contribution of the frictional component of the soil strength and partly due to a higher total contribution of the cohesive component of the soil strength along the contact surface. In spite of the higher drawbar pull, this way of using the soil strength did not result in any improvement in terms of traction coefficient (Fig. 71 and Fig. 72), simulated traction efficiency (Fig. 73), or power delivery efficiency (Fig. 74). At a slip of under 15%, the specific fuel consumption only decreased with increasing wheel load at a tyre pressure of 160 kPa.

1.4.3 Analysis of the influence of soil mechanical properties on traction performance

The major role of the soil mechanical behaviour in controlling the traction performance of a vehicle in off-road locomotion was pointed out from the origins of Terramechanics (Bekker, 1956; Bekker, 1960; Bekker, 1969; Wong, 1967; Wong and Reece, 1967).

Parameters describing the soil mechanical behaviour are present in the empirical, the semi-empirical, and the analytical methods used for analysing the tyre-soil interaction and predicting the trafficability of a terrain or the traction performance of an off-road vehicle.

In the context of the semi-empirical methods of tyre-soil interaction, like the one considered in this work, a thorough description of the mechanical tests with the bevameter was presented by Bekker (1956; 1960; 1969). Wong (1980) proposed an improved procedure to derive the soil mechanical parameters on the basis of the compression tests and the shear tests with a bevameter.

The major attention to a proper mechanical characterisation of the terrain for predicting trafficability and traction performance is testified by many works (Wills, 1963; Wong et al., 1979; Wong et al., 1982; Wong and Preston-Thomas, 1983). Upadhyaya et al. (1993) and Upadhyaya and Wulfsohn (1993) presented an instrumented device to obtain the soil parameters related to traction. More recently Garciano et al. (2010)

introduced an instrumented portable device that measures soil parameters useful in predicting tractive ability of off-road vehicles.

An analysis and quantitative evaluation of the effect of soil conditions on tractive performance of off-road wheeled and tracked vehicles was presented by Lyasko (2010). He concluded that in order to accurately calculate the tractive performance of a vehicle in a given soil condition, soil properties and parameters and their changes as functions of soil moisture content and density should be taken into account.

This paragraph aims to analyse the influence of the mechanical parameters of four Swiss agricultural soils (Table 5), having different textures and conditions, on the traction performance and the fuel consumption of a 65 kW MFWD agricultural tractor. Results are discussed both in qualitative and in quantitative terms, also on the basis of simulations with the tractor-soil interaction model.

The compression and shear tests performed with the tractor-mounted bevameter pointed out noticeable differences among the mechanical behaviour of the four soils under consideration.

Such differences are due to the variety of the soil textures and moisture conditions. Additional factors which affect the soil mechanical response under tractor traffic-induced stress are the soil structure and the presence of a stubble cover. These two aspects were not properly considered in this study and will probably be object of a further investigation. Other factors which control, to a great extent, the soil mechanical response, are the previous stress state that the soil underwent and the stress path.

The traction tests on the four agricultural soils were performed after the corn harvest, on the clay, the silty loam, and the loamy sand, and after the wheat harvest, on the clay loam. For these treatments, preliminary simulations with the Excel application TASCV2.0 have shown a close normal stress applied on the soil.

The driving conditions and the two tractor configurations considered were the same in all the tests, however, the simulated stress paths under the rear wheel varied significantly from one soil to the other (Fig. 85), mainly due to major differences in the shear stress applied along the soil-tyre contact surface (Fig. 83 and Fig. 84).

Mechanical parameters of several soils obtained from compression and shear tests performed with a bevameter were reported by Bekker (1969), Wong (1983), and Wong (1989). Such results were collected and listed by Wong (2008). An analysis of these results points out a rather wide variability of the soil parameters within the same texture of the soil, also for close values of the moisture content.

Our tests highlight a high stiffness under compression, described by the parameters K_c, K_φ and n, according to equation 2. Such a result depends on the fact that the soils under consideration were trafficked during the harvest. The cohesion of the loamy sand resulted quite high whilst the angle of shear resistance rather low. A possible reason for this result must be detected in the role of the stubble cover in affecting the shear resistance of the soil surface. The shear parameters measured on the other soils did not differ significantly from those reported by Wong (2008).

Both the measured and the predicted drawbar pull pointed out the major role of the soil mechanical strength in controlling the traction performance of the 40 kN tractor. At a slip of 10% and a tyre pressure of 60 kPa, the mean normal stress under the rear tyre ranged between 49.5 kPa on the silty loam and 51.7 kPa on the clay loam (Fig. 86). In this range of normal stress the strength of the clay and the silty loam were noticeably higher than those of the clay loam and the loamy sand. This fact makes for the higher drawbar pull on the clay and on the silty loam than on the clay loam and the loamy sand. At a slip of 10% the simulated drawbar

pull was 22.3 kN on the silty loam, 20.2 kN on the clay, 17.9 kN on the clay loam and 16.5 kN on the loamy sand.

At a tyre pressure of 160 kPa the mean normal stress ranged between 60.8 kPa on the silty loam and 68.4 kPa on the clay loam and the loamy sand. Within this range of normal stress, the strength of the clay is a little lower than that of the silty loam, the strength of the clay loam is close to that of the clay, whilst the loamy sand has a strength remarkably lower than the other soils.

The distribution of the drawbar pull as a function of the slip is in agreement with the above. At a slip of 10% the simulation of the drawbar pull gives 17.6 kN on the silty loam, 16.8 kN on the clay loam, 16.7 kN on the clay, and 14.3 kN on the loamy sand.

It must be remarked that the drawbar pull results also from the net traction of the front wheel whose mean stress state is not reported in Fig. 86. Moreover, the soil strength mainly controls the highest value of the drawbar pull, whilst the way the drawbar pull varies with the slip depends on the geometry of the contact surface and on the shear deformation modulus k. According to equation 27, the higher the shear deformation modulus, the slower the shear stress increases with the shear displacement and the slower the drawbar pull increases with the slip, for a given soil-tyre contact surface. This fact explains why, at a low slip, the drawbar pull on the clay is lower than that on the silty loam, whilst, at a high slip, it becomes higher.

The shear deformation modulus on the clay was 0.014 m, the highest among the soils considered (Table 5).

The same noticeable differences in the drawbar pull are observed in terms of the traction coefficient (Fig. 80). At a slip of 10% the traction coefficient assumed values of 0.56, 0.51, 0.45, and 0.41, on the silty loam, the clay, the clay loam, and the loamy sand, respectively, when the tyre pressure was 60 kPa. At the same slip and a tyre of 160 kPa the traction coefficient was 0.44, 0.42, 0.42, and 0.36, on the silty loam, the clay, the clay loam, and the loamy sand, respectively.

Saarilahti (2002) reported a comparison of different mobility models proposed by several authors, in terms of the rolling resistance coefficient, the thrust coefficient, and the drawbar pull coefficient as a function of the soil strength characterised by the penetration resistance. Both the thrust and the drawbar pull coefficient increase with the penetration resistance of the soil whilst the rolling resistance coefficient decreases.

Zoz and Grisso (2003) pointed out that the maximum net traction ratio reduces as the soil becomes less firm (lower net traction or drawbar pull at the same slip).

The motion resistance due to the soil compaction resistance (Fig. 82), according to equation 32, is deeply related to the firmness of the soil as well as to the rut depth z_0. The latter depends on the wheel load, the tyre dimension and the stiffness of both the tyre and the soil. For the same wheel load, tyre, and inflation pressure, the higher the soil firmness (Fig. 34 and Fig. 35), the lower the rut depth (Fig. 83 and Fig. 84). This results in a lower motion resistance in the firmest soils such as the loamy sand and the clay loam, where the soil-tyre contact is almost flat (Fig. 83 and Fig. 84). This effect persists both at a tyre pressure of 60 kPa and at a tyre pressure of 160 kPa.

It must be considered that both the clay loam and the loamy sand can be classified as firm soils, this implies, at least at a low slip, that the lugs support the entire wheel load, or a significant part of it if the carcass has a minimum contact with the soil. In such conditions, the effect of the lugs should be considered in order to proper describe the distribution of the normal pressure over the contact surface. Furthermore, the traction force developed should be calculated on the basis of both the shear stress-displacement curve of the soil-rubber contact, on the lug tip area, and the shear stress-displacement curve of the soil, on the shearing

surface between the lugs. This aspect is recognised as a major challenge for a further development of the Shmulevich and Osetinsky model.

The traction efficiency turned out to increase with the soil firmness (Fig. 81), this owing to a more favourable ratio of the drawbar pull developed to the torque applied to the wheels, for a given velocity and slip.

Zoz and Grisso (2003) pointed out that the peak of traction efficiency is reduced as the soil becomes softer and looser, but that it occurs at a net traction ratio which stays approximately constant.

The silty loam and the clay are the softest soils, but also the ones with the highest shear strength. This resulted in the highest drawbar pull and the highest motion resistance calculated as the soil compaction resistance. The clay loam and the loamy sand are the firmest soils with the lowest shear strength. This results in the lowest drawbar pull (Fig. 76, Fig. 79, and Fig. 80), and the lowest motion resistance (Fig. 82). The higher the motion resistance, the higher the fuel consumption. The specific fuel consumption measured did not vary significantly on the four soils, both at a tyre pressure of 60 kPa and at a tyre pressure of 160 kPa.

Such a result might be explained by the fact that the higher fuel consumption measured on the softest soils is balanced by the higher drawbar power developed. The clay and the clay loam showed a specific fuel consumption slightly lower than the other soils, whilst the specific fuel consumption on the silty loam was a little higher than on the other soils.

Similar results are reported by Šmerda and Čupera (2010) as a function of the drawbar pull for two values of the tyre inflation pressure.

A similar consideration could be made for the power delivery efficiency which also did not change remarkably on the four sites, particularly at a tyre pressure of 160 kPa. The higher the tractive power delivered, the higher the fuel consumption and, according to Fig. 75, the higher the equivalent power-take-off PTO. This turned out in an overall power delivery efficiency only slightly higher on the clay and slightly lower on the loamy sand, when the tyre pressure was set to 60 kPa, and without noticeable variations among the soil under consideration, when the tyre pressure was set to 160 kPa.

Results of this study point out that the traction performance depends on the tractor-soil system, as a consequence, a proper knowledge of the mechanical characteristics of an agricultural soil is the basis for a correct choice of the tractor configuration aimed at producing a benefit in the tillage management.

The overall traction performance in terms of drawbar pull, specific fuel consumption, and power delivery efficiency, was slightly better on the clay than on the other soils considered. A reason for such a result is that, compared to the clay loam and the loamy sand, the clay has a higher shear strength, at least in the stress-range of interest, and this allows for developing a higher drawbar pull. This effect seems to prevail on the lower firmness and higher motion resistance on the clay. Compared to the silty loam, the clay offers a little higher shear strength under the tyre inflated at a pressure of 60 kPa, and less strength under the tyre at 160 kPa of inflation pressure. However, it shows an overall higher firmness during the passage of the rear wheel, which turns out in a lower motion resistance.

This second aspect seems to prevail on the slight difference in shear strength at a tyre pressure of 160 kPa.

The lower drawbar pull developed on the clay at low slip is due to the higher shear deformation modulus and the different geometry of the contact surface. An evidence of these effects is that, at a slip of 10% (Fig. 83 and Fig. 84), the shear stress at the rear part of the contact surface does not reach the soil strength. Such a condition is, on the contrary, fully satisfied under the rear wheel on the silty loam.

2. Analysis of soil damage due to load and slip of tractor tyres

2.1 Introduction

2.1.1 Soil damage due to load and slip of tractor tyres

For more than four decades issues concerning subsoil compaction caused by agricultural machinery traffic have attracted the attention of researchers. Soil behavior under vertical loads and soil stress states during tyre or track passage have been widely studied in order to prevent deformations which may alter soil structure functionalities (Söhne, 1958; Vanden Berg and Gill, 1962; Raghavan et al., 1976; Arvidsson and Ristic, 1996; Gysi et al., 2001; Berli et al., 2003; Keller, 2005; Bastgen and Diserens, 2009). Different models to predict soil compaction have been proposed by Raghavan et al. (1977), O'Sullivan et al. (1999), Diserens et al. (2003), Van den Akker (2004), Keller et al. (2007).

While subsoil mechanical behavior has been considered for the above matters, the mechanical behavior of topsoil has mainly been examined in order to study the traction performance of tractors and resistance to tillage tools such as plows, which involve cutting the soil.

Tractor traction tyres interact with soil via a system of normal and tangential stresses along the soil-tyre contact surface. In this interaction both soil and tyre deform according to their own stress-strain relationships. Soil deformation results in the formation of a rut as well as in topsoil displacement along the soil-tyre contact surface. The topsoil displacement depends on shear stress which soil undergoes at contact with tyre. The shear stress-displacement relationship characterising the soil layer which interacts with the traction tyre has been studied for a long time as it strongly affects the relationship between traction force and wheel slip, usually referred to as traction performance of the soil-wheel system (Bekker, 1956; Janosi and Hanamoto, 1961; Wills, 1963; Wong and Preston-Thomas, 1983).

High traction forces are obtained by mobilising the strength of soil elements among tyre lugs, so it follows that they mainly depend on the strength of the soil which interacts with the tyre tread rather than on tyre material-soil interfacial resistance (Yong et al., 1984). As soon as the whole strength is mobilised, the soil elements among tyre lugs fail with the consequent formation of a strengthless layer (Fig. 87) and an underlying layer which shows high shear deformations.

The soil strength has long been recognised as one of the main factors limiting soil erosion processes (Fan and Wu, 2001; Nearing and West, 1988; Watson and Laflen, 1986). Effects of shear deformations on soil structure with regard to the alteration of the pore system functionalities have been pointed out by different researchers (Kirby, 1991; O'Sullivan et al., 1999).

Shear deformations have been proved to affect air permeability (Kirby, 1991; O'Sullivan et al., 1999) and gas diffusivity (O'Sullivan et al., 1999) in soil samples. The role of shearing, in addition to vertical compaction, in soil homogenisation and particle rearrangement with reduction of hydraulic conductivity was described by Horn (2003). More recently, also Alaoui et al. (2011) and Berisso et al. (2013) remarked the influence of shear stress-strain due to traffic of agricultural vehicles on the alteration of: the soil pore system, the soil hydraulic properties such as soil water retention curve and unsaturated hydraulic conductivity (Alaoui et al., 2011), and the air permeability and pore continuity (Berisso et al., 2013).

Moreover, the slip has been recognised to contribute in causing soil compaction pointed out by increased soil density (Raghavan et al., 1977; Raghavan et al., 1978), whereas Davies et al. (1973) showed how wheel slip is more important in causing compaction than additional wheel loading.

The remarkable influence of shear stress at wheel-soil interface on the magnitude of the major principal stress in the upper soil layer was pointed out by Olsen (1988). He also reported experimental results showing an increase in soil density due to the application of shear stress and observed shear strain under a simple shear plate in the upper 2 cm of soil below the plate.

Issues concerning topsoil damage due to tyre slip should be taken into account and further investigated (Diserens and Battiato, 2012). Although the slip is strictly related to the application of a traction force and, therefore, seems to be unavoidable, it should be controlled and properly limited in order to preserve topsoil structure and reduce erosion. In spite of this recognised need for limiting the slip of tractor tyres, no theoretical approaches have been presented so far to indicate a range of slip values where no topsoil damage occurs.

Moreover, the effects of shear deformation on soil structure, in terms of the alteration of pore-system functionalities, is an issue in need of further investigation, especially from the point of view of the relationship between mechanical stress and its impact on water movement in soil. This should aid in the development of more-suitable prediction models for soil damage (Alaoui et al., 2011).

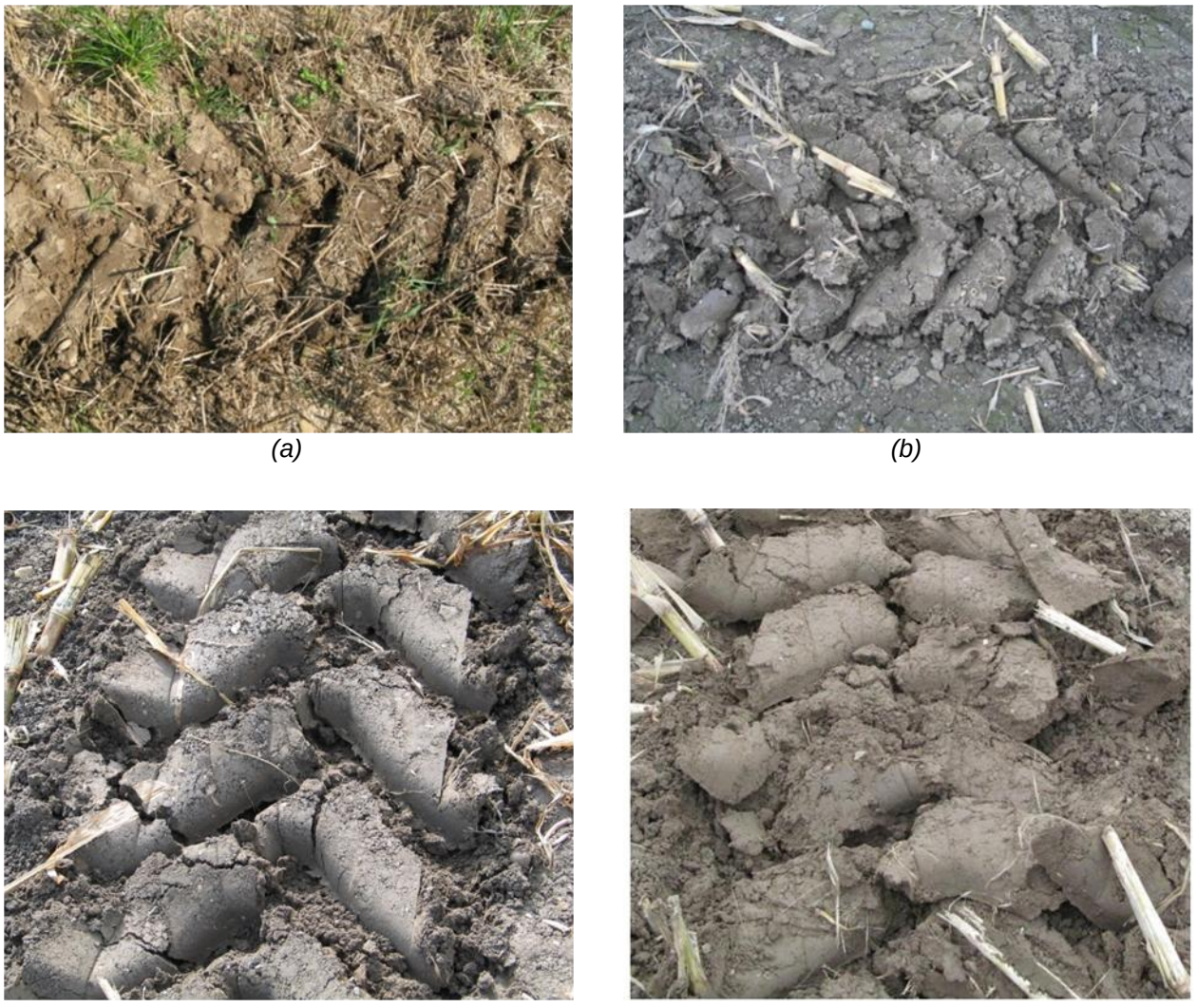

(a) *(b)*

(c) *(d)*

Fig. 87: Examples of soil cutting on cohesive soils with formation of a residual strengthless layer exposed to erosion: (a) clay loam with wheat stubble (Tänikon); (b) clay with corn stubble (Tänikon); (c) clay with corn stubble (Tänikon); (d) silty loam with corn stubble (Frauenfeld).

2.1.2 Aims of the research

The main aims of this work can be summarized as follows:

I. Definition of a mechanistic approach to define conditions which lead to soil failure due to slip of tractor tyres, and validation on the basis of field traction tests with a MFWD tractor on an agricultural silty loam (SL) Calcaric Fluvisol.

II. Evaluation of the soil stress state at the soil-tyre contact area during the passage of a tractor without and with slip. Assessment of soil deformation arising from the applied stress, and determination of the effects of such a deformation on the water movement in the soil.

III. Comparison of the effects of compression and shear deformation on the saturated hydraulic conductivity in laboratory tests.

2.2 Field test 1: Topsoil damage due to slip of tractor tyres: a mechanistic interpretation

2.2.1 Materials and methods

Field traction tests were aimed at investigating the effects of tyre slip on topsoil. The tests were carried out on an agricultural silty loam (SL) Calcaric Fluvisol with corn stubble (Table 5).

Several corridors 4 m wide and with a length ranging between 45 m and 85 m, according to the field geometry, were delimited in the field. Each corridor was driven in steady-state motion in which the slip of the pulling tractor was kept constant by controlling the developed net traction force with a braking tractor. The drawbar pull developed was varied from one corridor to the next and consequently also the slip. This latter ranged between 5% and 48%.

The longitudinal topsoil shear displacement due to tyre slip was chosen as a suitable indicator of the soil cutting effect and measured along the tracks of the pulling tractor after tractor passage. The pulling tractor and the braking tractor did not move in alignment during the test, which allowed the two tractors to have independent tracks and the longitudinal topsoil shear displacement to be measured on a track trafficked by the pulling tractor only.

In order to measure the longitudinal topsoil shear displacement a system of strips orthogonal to the tractor track was spray-painted on the topsoil surface, around 10 m apart, before tractor passage. The layout of the traction test in steady-state motion along a corridor and the specification of the system of spray painted strips for the measurement of the topsoil displacement are sketched in Fig. 88.

Fig. 89 shows a detail of the measurement of the longitudinal topsoil shear displacement. A strip width of 1.2 m allowed the ends to be far enough away from both the track of the pulling tractor and the track of the braking tractor, thus ensuring that the strip edges were undisturbed by the tractor passage and could be used as a reference system (points A, B, C, D in Fig. 90) for measuring the topsoil shear displacement due to tyre slip. The topsoil shear displacement was measured in each corridor with 2 or 3 repetitions.

The tractor A (Table 1) was employed as pulling tractor. The pulling effect was obtained by means of tractor C (Table 3), used as braking machine. The traction force, wheel slip, wheel load and tyre inflation pressure were measured as described in Chapter 1.2.2.1.

The traction tests were carried out using three configurations corresponding to cases 1, 2 and 11 in Table 1 and hereinafter referred to as cases 1, 2 and 3, respectively.

In order to obtain the highest traction performance, the tractor moved in a rectilinear direction with locked differential. The traction force in the longitudinal direction was obtained from the measured force by taking into account the angle γ of the steel cable used to connect the two tractors (Fig. 88). This angle was around 3° (in Fig. 88 a distorted scale is used). Traction tests were carried out with a mean forward speed of 0.76 m/s. The physical parameters of the silty loam (SL) Calcaric Fluvisol with corn stubble chosen as the location for the tests are listed in Table 5 along with the mechanical parameters for the soil-tyre interaction model. An additional repetitive shearing test at vertical pressure of 38 kPa, reported in Fig. 91, indicates three main phases of soil behaviour under shear stress: in a first very limited interval of displacements the soil seems to show an elastic behaviour, afterwards the elastic behaviour is associated with plastic deformations in a hardening elastoplastic phase, whereas the last phase is characterised by big plastic deformations under almost constant stress, indicating that soil failure is occurring. Parameters K_{carc} and ΔK_p which characterise tyre stiffness were determined on the basis of the tyre specifications as in Lines and Murphy (1991). Table 14 shows parameters used in the model of soil-tyre interaction. In case 3 the system of dual tyres can be

modelled, at least in first approximation, as one tyre having width and stiffness given by the sum of those of the two independent tyres.

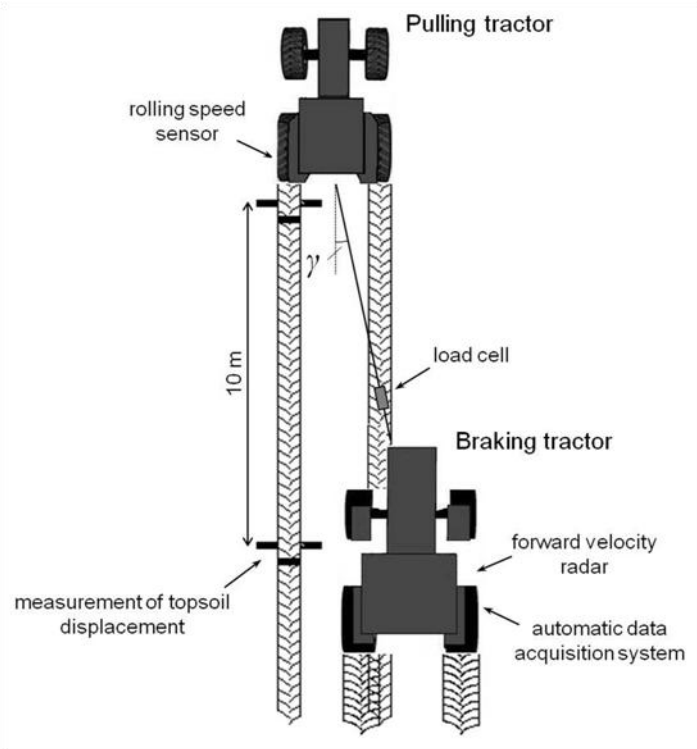

Fig. 88: Layout of the traction test in steady-state motion along a corridor and specification of the system of spray painted strips for the measurement of the topsoil displacement.

(a) *(b)*

Fig. 89: Spray-painted strip on topsoil surface for the measurement of longitudinal displacement: (a) before tractor passage, (b) after tractor passage.

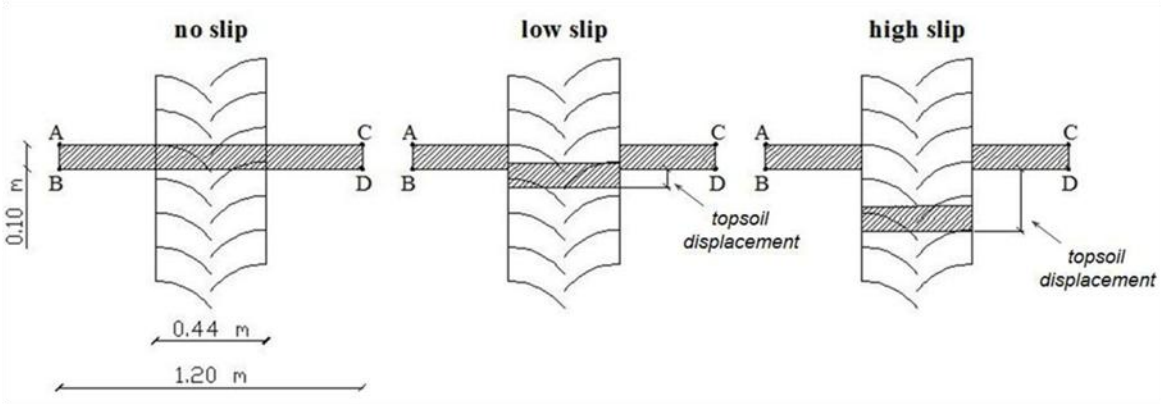

Fig. 90: Detail of the measurement of the longitudinal topsoil shear displacement due to tyre slip with a strip spray painted on the topsoil surface. Points A, B, C, D are used as a reference system.

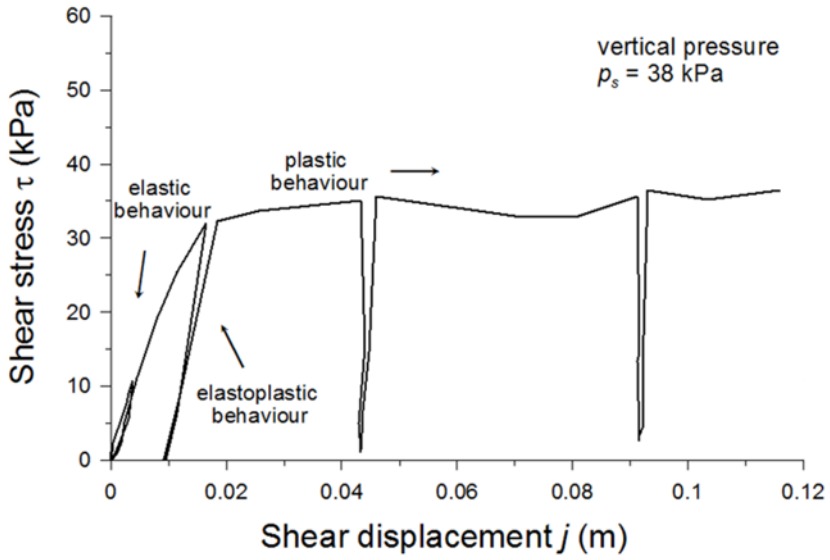

Fig. 91: Soil shear stress-displacement curve obtained in a horizontal plate shear deformation test with a bevameter at 38 kPa of vertical pressure. The repetitive shearing obtained by alternate loading and unloading phases.

Table 14: Parameters used in the soil-tyre interaction model.

	case 1		case 2		case 3	
Height of the drawbar h [m]	0.8		0.83		0.77	
Wheelbase pulling tractor L [m]	2.34		2.34		2.34	
	front axle	rear axle	front axle	rear axle	front axle	rear axle
Tyre	380/85R24	420/85R34	380/85R24	420/85R34	380/85R24	420/85R34
Dual tyre	-	-	-	-	11.2R28	11.2R42
Stationary wheel load W_0 [kN]	9.1	10.9	9.1	10.9	11.3	16.4
Tyre width b [m]	0.38	0.44	0.38	0.44	0.38/0.29*	0.44/0.30
Tyre unloaded radius R [m]	0.63	0.79	0.63	0.79	0.63/0.63	0.79/0.79
Tyre rolling radius R_r [m]	0.58	0.76	0.59	0.77	0.58	0.76
Tyre inflation pressure P_{in} [kPa]	60	60	160	160	60/60	60/60
Rim diameter D_{rim} [m]	0.61	0.86	0.61	0.86	0.61/0.71	0.86/1.07
Tyre stiffness [kN/m]	203	232	325	432	203/188	232 /199
Carcass stiffness K_{carc} [kN/m]	129.5	111.8	129.5	111.8	130/122	112/98
Inflation pressure dependence of the tyre ΔK_p [kN/mkPa]	1.22	2.00	1.22	2.00	1.22/1.09	2.00/1.69

* Second value refers to the dual tyre.

2.2.2 Results

The relationship between the drawbar pull developed by the tractor and the slip of tractor wheels is shown in Fig. 92. Here experimental measures are seen alongside the model simulation for the three cases under consideration. The highest traction performance in case 3 was due to the use of dual tyres, the tractor ballasting, and besides the low tyre inflation pressure. In case 1 the use of low tyre inflation pressure turned out in traction performance higher than in case 2. The model simulations showed general good agreement with the experimental results (root mean square error *RMSE* of 2.71 kN).

Simulations of the geometry of the soil-tyre contact surface and distributions of the normal stress σ, the shear stress τ and the soil strength τ_{max} along the soil-tyre contact surface are shown in Fig. 93 and Fig. 94. For each point of the contact surface, the normal stress and the shear stress are calculated according to Shmulevich and Osetinsky (2003).

Fig. 93 refers to the tractor configuration of case 1 and reports simulations for slip values of 5% and 15% for the front wheel (Fig. 93*a* and Fig. 93*c*, respectively) and for the rear wheel (Fig. 93*b* and Fig. 93*d*, respectively).

The load transfer effect caused the length of the contact surface and the rut depth of the front wheel to decrease as slip increased, with an opposite result for the rear wheel. The maximum normal stress at soil-tyre contact decreased with slip in the front wheel, and increased with slip in the rear wheel.

The shear stress at soil-tyre contact rose sharply with slip. At slip of 5% it assumed values very far from the soil strength, whereas at slip of 15% it approached the soil strength over a wide part of the contact surface.

At the rear point of the soil-tyre contact the shear stress was closer to the soil strength, and this latter, according to equation 27, corresponded to the soil cohesion *c*.

The ratio τ/τ_{max} varied along the contact surface as a function of the soil shear displacement *j*:

$$\frac{\tau}{\tau_{max}} = \left(1 - e^{-j/k}\right) \tag{59}$$

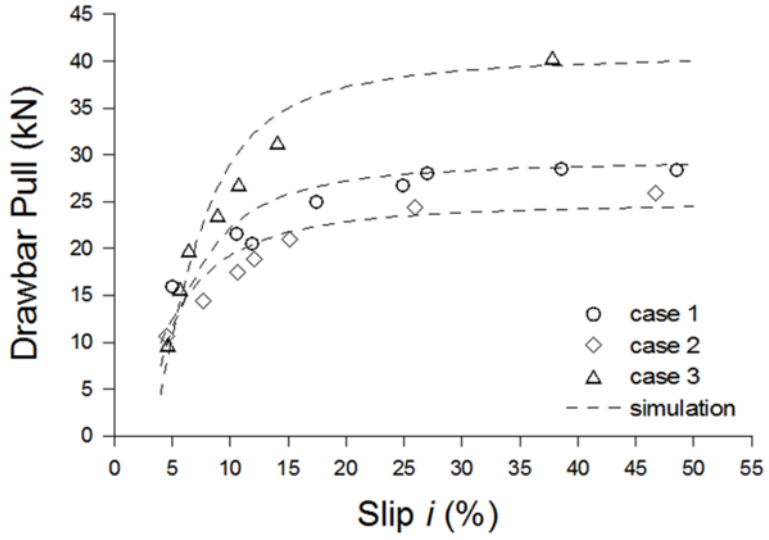

Fig. 92: Measured and simulated relationship between drawbar pull and wheel slip for tractor A in the three configurations considered: (case 1) tractor weight 40.0 kN and tyre inflation pressure 60 kPa; (case 2) tractor weight 40.0 kN and tyre inflation pressure 160 kPa; (case 3) tractor weight 55.4 kN, tyre inflation pressure 60 kPa, front and rear dual tyres.

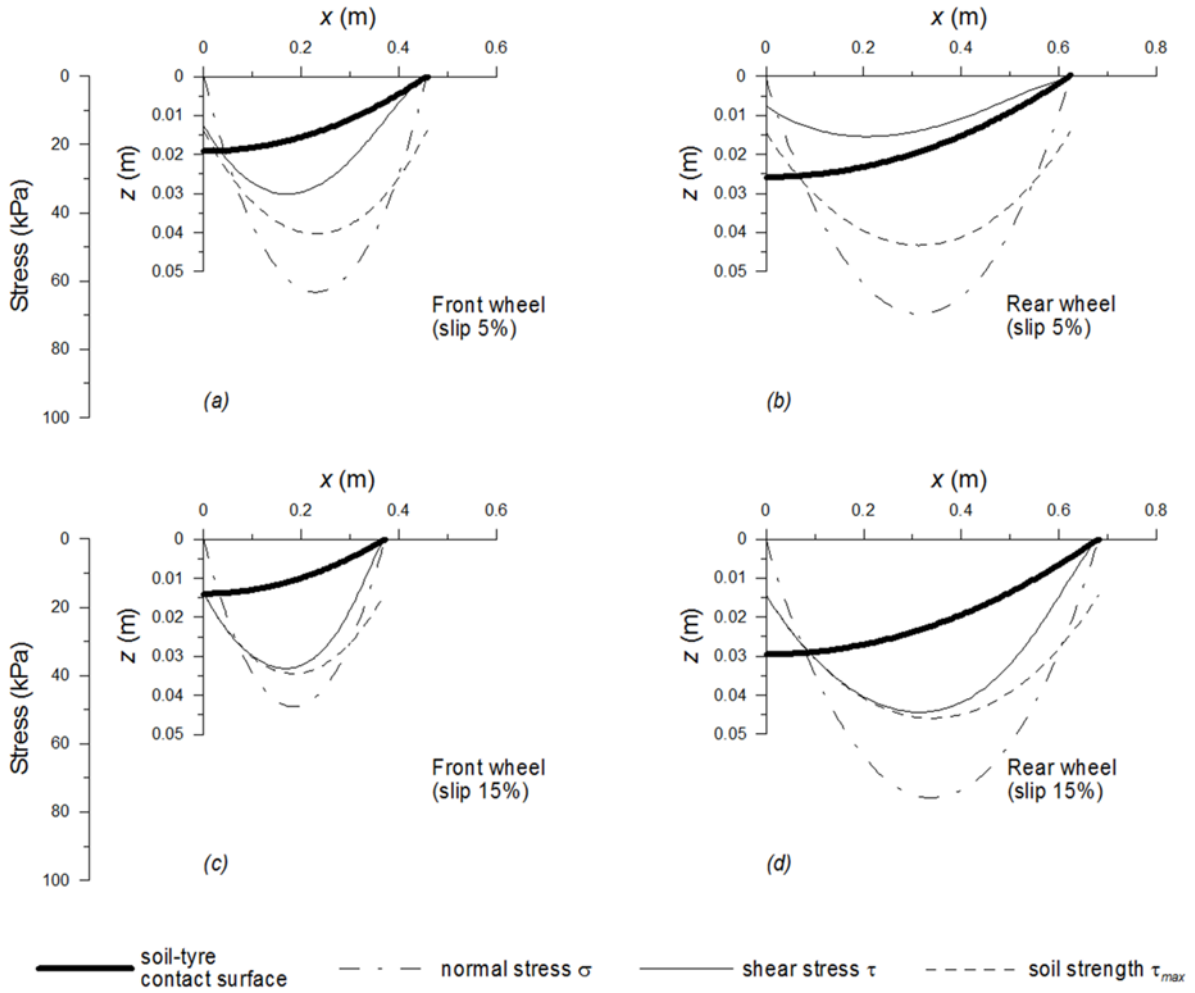

Fig. 93: Simulation of the soil-tyre contact surface with distribution of normal stress, shear stress and soil strength at slip of 5% and 15% for the front and the rear wheels of tractor A in case 1 (weight 40.0 kN, tyre inflation pressure 60 kPa): (a) front wheel at slip of 5%, (b) rear wheel at slip of 5%, (c) front wheel at slip of 15%, (d) rear wheel at slip of 15%.

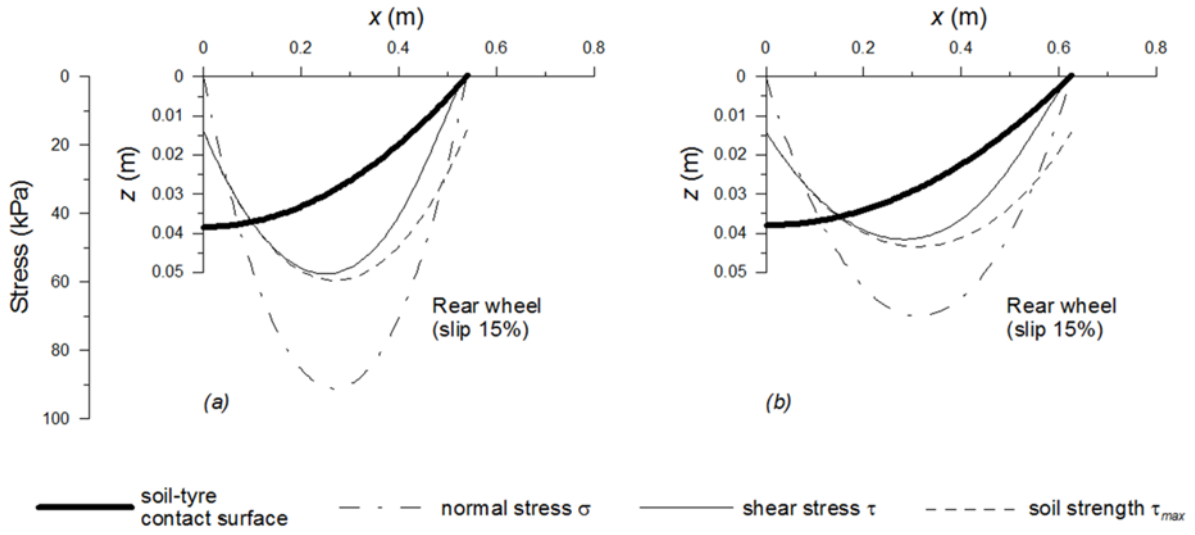

Fig. 94: Simulation of the soil-tyre contact surface with distribution of normal stress, shear stress and soil strength at slip of 15% for the rear wheel of tractor A in cases 2 and 3: (a) tractor weight 40.0 kN and tyre inflation pressure 160 kPa; (b) tractor weight 55.4 kN, tyre inflation pressure 60 kPa, front and rear dual tyres.

In Fig. 94 are reported the simulations of the geometry of the soil-tyre contact surface and the stress distribution at soil-tyre contact of the rear wheel at a slip of 15% for cases 2 and 3. In case 2 the contact surface was shorter and deeper than in case 1 (Fig. 93d), with higher maximum normal stress. In case 3 the contact surface was shorter than in case 1 and longer than in case 2, and the rut depth resulted close to case 2. The maximum normal stress was lower than in cases 1 and 2.

In Fig. 95 the soil stress paths along the contact surface with the tyre for the rear wheel in case 1 are represented in terms of mean stress $p = (\sigma_1+\sigma_3)/2$ and deviatoric stress $q = (\sigma_1-\sigma_3)/2$.

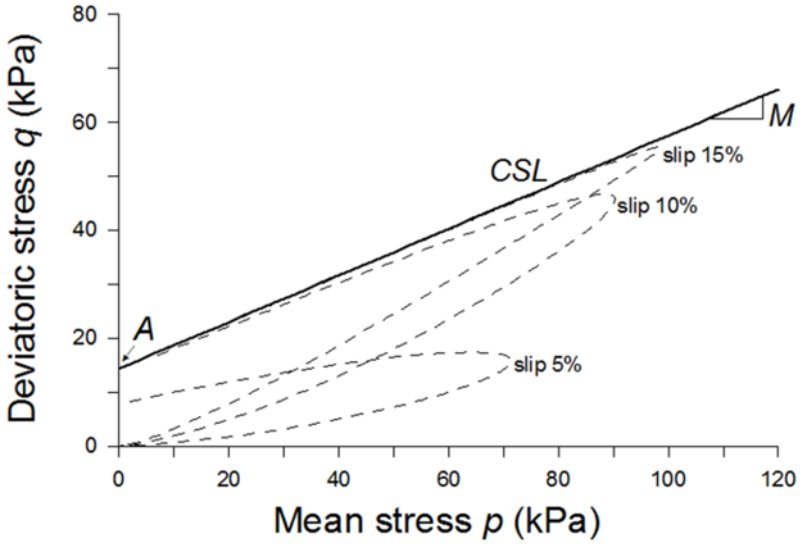

Fig. 95: Soil critical state line CSL and simulation od the stress paths along the soil-tyre contact surface at different slip for the rear wheel of tractor A in case 1 (weight 40.0 kN, tyre inflation pressure 60 kPa).

The stress paths at slip of 5%, 10% and 15% indicated that the soil stress state varied significantly along the contact surface and with slip. Moreover, the last point of the stress path which corresponded to the rear contact point turned out to be the closest to the critical state condition. At slip of 15% a wide part of the soil stress path lay on the critical state line *CSL,* indicating that the critical state condition was fully reached.

Fig. 96 shows the evolution of the measured topsoil shear displacement *j* with slip *i* for case 1 (Fig. 96*a*), case 2 (Fig. 96*b*) and case 3 (Fig. 96*c*). This is set alongside the evolution of the maximum ratio between shear stress τ and soil strength τ_{max} for the front and rear wheels.

As long as the shear stress along the contact surface of both the front tyre and the rear tyre with soil was considerably lower than soil strength and consequently the maximum ratio τ/τ_{max} assumed values to a great extent lower than 1, the topsoil shear displacements measured were very small, moreover they did not vary significantly with slip. When the maximum ratio τ/τ_{max} along the contact surface approached a value of 1, the topsoil shear displacements measured rose sharply in the three cases under consideration. According to equation 6 the ratio τ/τ_{max} assumes the value 1 as an asymptotic value, however, in practice a ratio τ/τ_{max} of 0.99 could be regarded as a limit beyond which soil strength is considered entirely mobilised. Such a limit was reached in case 1 at soil-front tyre contact for slip of 11% and at soil-rear tyre contact for slip of 13%, in case 2 at both soil-front tyre contact and soil-rear tyre contact for slip of 11%, and in case 3 at both soil-front tyre contact and soil-rear tyre contact for slip of 13%.

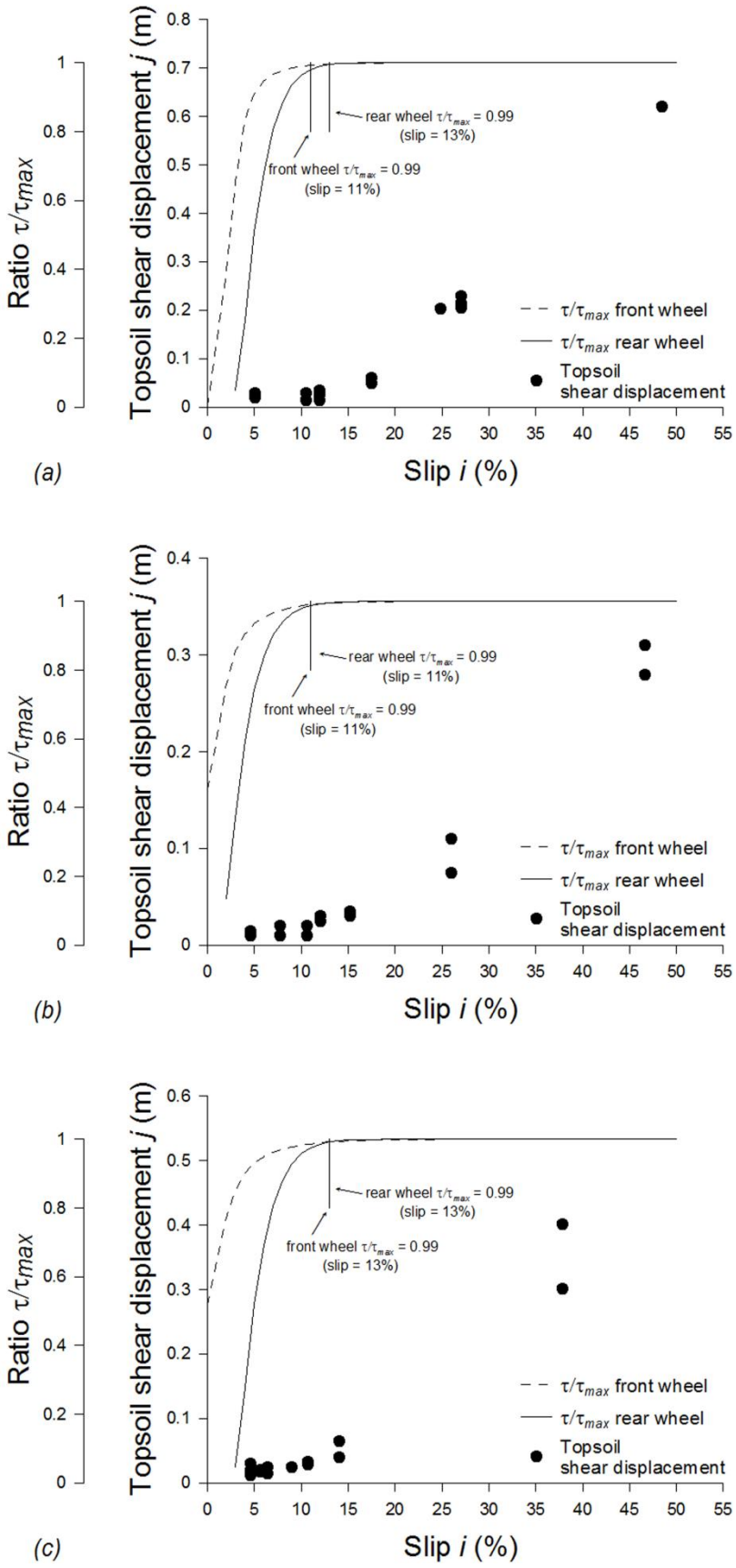

Fig. 96: Evolution of topsoil shear displacement with wheel slip compared with the simulated evolution of the maximum ratio τ/τ_{max} with wheel slip for the front wheel and the rear wheel of tractor A in the three configurations considered: (a) tractor weight 40.0 kN and tyre inflation pressure 60 kPa; (b) tractor weight 40.0 kN and tyre inflation pressure 160 kPa; (c) tractor weight 55.4 kN, tyre inflation pressure 60 kPa, front and rear dual tyres.

2.2.3 Discussion

Tractor traction tyres interact with soil via a system of normal and tangential stresses along the soil-tyre contact surface, in this interaction the traction force is developed by progressively mobilising the topsoil strength at contact with tyre, and as soon as the whole strength is mobilised the soil elements among tyre lugs fail (soil cutting effect), causing topsoil damage. This damage in terms of cutting effect due to slip of tractor tyres has never been properly considered so far (Diserens and Battiato, 2012).

The analytical approach presented was aimed at defining the mechanical condition at soil-tyre contact under which this topsoil damage occurs, and providing indicative limits of tyre slip for the conditions considered.

The soil-tyre interaction model used as a theoretical framework provided reliable simulations of traction performance in terms of drawbar pull and slip (Fig. 92) for the 65 kW MFWD tractor on the silty loam Calcaric Fluvisol (Table 5) in the three configurations considered (Table 14).

Simulations of the geometry of the soil-tyre contact surface and the distribution of stresses at soil-tyre contact (Fig. 93 and Fig. 94) indicated the influence of the tractor configuration, the slip of the wheels and the load transfer effect on the soil stress state at contact with tyre. The shear stress τ turned out to vary considerably with slip, approaching the soil strength τ_{max}. The ratio τ/τ_{max} varied over the contact surface with tyre as a function of the soil shear displacement j according to equation 59, and its maximum value rose sharply with slip as long as a value of 0.99 was reached (Fig. 96).

During shear tests the silt loam (SiL) Calcaric Fluvisol considered in this study showed an elastoplastic behaviour with hardening (Fig. 91). At low slip the soil was stressed in its domain of hardening behaviour and it deformed when shear stress increased. In this phase the soil was able to provide a high increase in traction force (drawbar pull) corresponding to small variations in slip (Fig. 92). The topsoil shear displacements measured were very small in this phase (Fig. 96), moreover, in spite of the big increase in traction (Fig. 92), they did not vary significantly with slip.

Soil failed as soon as its strength was approached, exhibiting a rise in topsoil shear displacements (Fig. 96). This condition may occur at different but close slip values for the soil-front tyre contact and the soil-rear tyre contact (Fig. 96). Once the soil strength was approached at the rear point of the soil-tyre contact, the traction force (drawbar pull) continued to increase with slip because the available soil strength was progressively mobilised on more extended areas of the contact surface (Fig. 93 and Fig. 94), but its gradient was greatly reduced (Fig. 92).

The value of the ratio τ/τ_{max} of 0.99 proved to be an indicative limit, suitable for practice, beyond which soil failure is expected to occur (Fig. 96). This limit is reached at a certain slip of the tyre which depends on soil mechanical behaviour and tyre parameters such as dimensions, rolling radius, carried load, inflation pressure, and stiffness. In the traction tests presented, the ratio τ/τ_{max} of 0.99 was reached at first at soil-front tyre contact for slip of 11% when the tyre inflation pressure was set to 60 kPa (Fig. 96*a*), at both soil-front tyre contact and soil-rear tyre contact for slip of 11% when the tyre inflation pressure was set to 160 kPa (Fig. 96*b*), and at both soil-front tyre contact and soil-rear tyre contact for slip of 13% when dual tyres were used at front and rear axles, the tractor was ballasted (from 40.8 kN to 56.6 kN), and the tyre inflation pressure was set to 60 kPa (Fig. 96*c*).

The elastic phase of soil behaviour, which might precede the elastoplastic phase according to Fig. 91, was not observable in the range of slip considered.

The choice of the tractor configuration is a matter of primary importance in tillage operations for the optimisation of traction performance, i.e. limiting slip of the wheels which involves a significant energy loss. To a great extent this aspect affects the fuel consumption and the time required for soil tillage. Moreover, as pointed out in this study, limiting slip concurs in the preservation of the topsoil. From this point of view, the limit values of slip obtained for the silty loam (SL) Calcaric Fluvisol in the three tractor configurations should be regarded as indicative limits not to be exceeded in field operations in order to avoid topsoil damage in the conditions considered.

2.3 Field test 2: Changes in soil hydraulic properties due to mechanical stress during tractor traffic with and without slip

2.3.1 Materials and methods

The following field tests were carried out in order to assess soil deformation arising from the passage of a tractor without and with slip and to determine how the soil deformation arising from these two treatments affects water movement in the soil.

2.3.1.1 Description of sites

The location of the tests was a clay loam agricultural field with wheat stubble (Table 5), here two sites were considered. The soil is described as albic luvisol (FAO classification, 2006). A detailed characterisation of the soil in the two sites, in terms of texture, organic carbon and pH, is reported in Table 15. On both sites, soil texture consists of clay loam to a depth of 0.45 m. Between 0.45 and 0.50 m, the material at site 1 (passage without slip) consists of clay, and that at site 2 (passage with slip) of clay loam. Soil organic carbon content (determined by weight loss on ignition) varies from 2% (topsoil) to 0.2% (subsoil). A pH of 7-7.2 was measured at the soil surface, increasing slightly to 7.4 in the subsoil.

The topsoil mechanical parameters for simulating soil-tyre interaction were derived by means of vertical plate penetration tests and horizontal plate shear deformation tests with the tractor-mounted bevameter, according to the procedure described in Chapter 1.2.2.2. In order to consider the multi-pass effect for the rear wheels, the bevameter tests were performed before passage of the tractor, as well as on the rut left by the passage of the front wheel; however, because soil parameters did not change significantly, a unique characterisation was adopted (Table 5).

Table 15: Texture, organic carbon and pH of the soil under consideration.

Depth interval (m)	Particle-size distribution (%)			Texture	Organic carbon OC (%)	pH
	Clay (< 2 μm)	Silt (2–60 μm)	Sand (> 60 μm)			
Site 1						
0.00–0.15	37.0	39.2	23.8	clay loam	2.0	7.0
0.30–0.45	36.7	37.2	26.1	clay loam	1.0	7.4
0.45–0.50	44.6	23.3	32.1	clay	0.2	7.4
Site 2						
0.00–0.15	36.3	41.0	22.7	clay loam	2.0	7.2
0.30–0.45	37.3	40.2	22.5	clay loam	1.0	7.4
0.45–0.50	35.2	30.1	34.7	clay loam	0.2	7.4

Site 1: Treatment without slip; Site 2: treatment with slip;
Textural classification according to USDA soil taxonomy

2.3.1.2 Traction tests

The aim of the field traction tests was to investigate the effects of tractor-tyre slip on the soil.

Corridors 4 m wide and 70 m long were marked out in the field (Fig. 97). In a first corridor (site 1), the tractor moved in a self-propelled, steady-state condition, whilst in a second corridor (site 2) the tractor moved in a steady-state condition with high drawbar pull and wheel slip. A drawbar pull of 21.8 kN was controlled by means of a braking tractor. Whereas almost no wheel slip was measured in the first corridor, there was a measured wheel slip of 27% in the second corridor.

The pulling tractor and the braking tractor did not move in alignment. This allowed the two tractors to have independent tracks, and enabled the soil at the study site to be trafficked by the pulling tractor only (Fig. 97).
The shearing process related to the slip was evaluated by marking the soil surface with two different-coloured dyes – blue and red – before the passage of the tractor. After the treatment, soil-layer displacement was measured.
The tractor A was employed as a pulling tractor. The braking tractor was a Massey Ferguson 8470 with 250 kW engine power and weighing 90.6 kN. The traction force, wheel slip, wheel load and tyre inflation pressure were measured as described in Chapter 1.2.2.1.
The rolling radius and the tyre stiffness were obtained according to as described in Chapter 1.2.2.3.
The theoretical speed ratio of the tractor wheels was determined during preliminary tests at zero drawbar pull on a smooth road. The technical specifications of the pulling and braking tractors are reported in Table 16. The actual forward velocity of the tractor was 1.6 m s^{-1} in the first corridor and 0.9 m s^{-1} in the second.

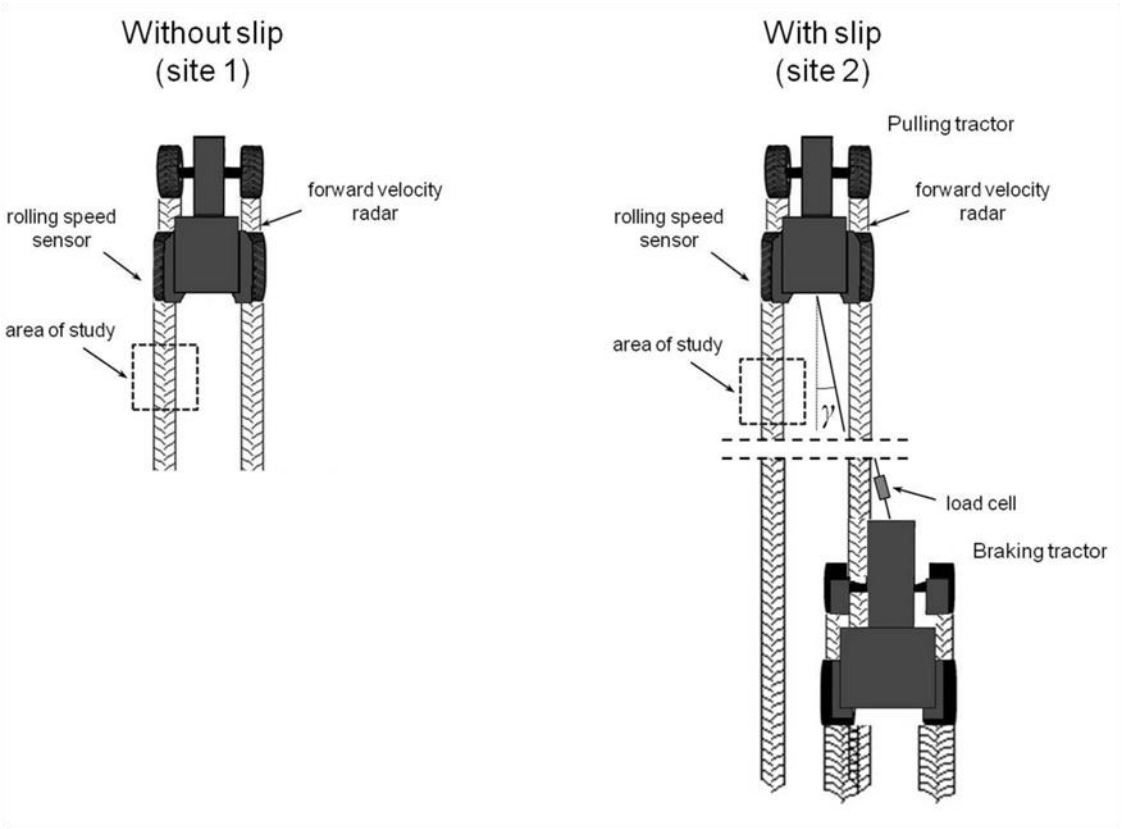

Fig. 97: Experimental design of the treatments.

2.3.1.3 Infiltration tests

From a pit, 1 m deep, three water content probes were installed horizontally under both sites (site 1 without slip and site 2 with slip).
The two plots were irrigated with a rainfall simulator of 1 m^2 area with intensities of 30 mm h^{-1} for 1 h. Water content was measured at the three depths of 0.15, 0.35 and 0.50 m with a time domain reflectrometer (TDR) (CR10X & TDR100, Campbell Scientific Inc.) with 0.20 m wave guides (two parallel rods of 6 mm diameter). Calibration was performed according to Roth et al. (1990). TDR measurements were made every 60 s.

Table 16: Some specifications of the tractors used in the traction tests.

Braking tractor	Massey Ferguson 8470
Power [kW]	250
Weight [kN]	90.6
Pulling tractor	Hürlimann H488 DT
Power [kW]	65
Weight [kN]	40
Wheelbase [m]	2.34
Tyre (front - rear)	380/85R24 - 420/85R34
Tyre width (front - rear) [m]	0.38 - 0.44
Tyre unloaded radius (front - rear) [m]	0.63 - 0.79
Tyre rolling radius (front - rear) [m]	0.58 - 0.76
Tyre inflation pressure (front - rear) [kPa]	160 - 160
Tyre stiffness (front - rear) [kN/m]	325 - 432
Stationary wheel load (front - rear) [kN]	9.1 - 10.9
Height of drawbar [m]	0.83
Theoretical speed ratio	0.99

The results obtained were analysed according to the increase in volumetric water content θ during water infiltration ($\Delta\theta_i$, defined as the difference between maximum water content and initial water content) and the decrease in θ after cessation of infiltration during the drainage phase ($\Delta\theta_d$, defined as the difference between maximum water content and the lowest water content measured within 2h after the maximum water content was reached) (Alaoui and Helbling, 2006). Low $\Delta\theta_d$ values indicate the draining of fine pores, whilst high values indicate the draining of larger pores such as macropores or cracks, and indicate preferential flow (Alaoui et al., 2003).

A dye infiltration experiment was carried out in order to visualise the heterogeneity of the tracer distribution pathways. To this end, 120 litres of dye tracer solution were prepared by diluting 440 grams of Brilliant Blue FCF powder – also known as food dye E133 (Flury and Flühler, 1995) – in ordinary tap water (concentration = 3.7 g l^{-1}). The prepared solution was applied in site 1 and site 2 for 3 hours at a constant rate of 24 mm h^{-1} using a rainfall simulator of 1 m^2 area (Alaoui and Goetz, 2008). Being neutral or anionic (depending on the pH), Brilliant Blue (BB) is not heavily adsorbed by negatively charged soil constituents. One day after infiltration, a soil pit was excavated and six vertical profiles (0, 0.20, 0.40, 0.60, 0.80 and 1 m from the edge of the area treated with the rainfall simulator) were prepared. A rubber string grid (1.0 x 0.7 m) was attached in front of each profile. The profiles were then photographed with a digital camera (hp photosmart 945; resolution: 5 megapixels). The resultant digital images had a resolution of approx. 2000 x 2000 pixels.

The final coverage of the stained areas was subsequently determined from profile images according to the following description: firstly, the pictures were processed with the Photoshop CS2 image editing program according to the procedure described by Alaoui and Goetz (2008), afterwards, the distribution of the dye coverage with depth was calculated for each image by horizontally counting the pixels indicating stained soil for each pixel row of the image.

To allow a quantitative insight with different BB concentrations, it was necessary to perform a calibration linking specific colours with corresponding BB concentration ranges. Ten standard solutions were therefore prepared (BB concentration: 0.1, 0.5, 1, 2, 4, 6, 20, 40, 80 and 150 g l^{-1}) in which the soil samples were saturated for 5 - 6 days. The samples were then left to dry for a couple of nights. Afterwards, about 3 mm of the bottom of each sample was scraped off with a knife to obtain smooth, homogenous surfaces. These

were then photographed with the same camera, under the same light conditions as in the field. The surface density of BB was then estimated up to a depth of 0.80 m for both sites (with and without slip).

2.3.1.4 Laboratory analyses: total porosity (TP), pore size distribution (PSD) and saturated hydraulic conductivity (Ksat)

Total porosity (TP) and pore size distribution (PSD) were determined for samples of undisturbed soil (five per depth) with a diameter of 55 mm and height of 42 mm. PSD was determined by a vacuum pressure membrane apparatus described by Dirksen (1999) with a hanging water column for a water suction $h < 31.6$ kPa and with a gas adsorption porosimetry using N_2 for 31.6 kPa < h < 1585 kPa.

TP was measured in the first 0.6 m at intervals of 0.15 m, whilst PSD was measured at depths of 0.05, 0.15, and 0.35 m. The samples were taken at intervals of about 0.15 m in a horizontal direction.

In this study, three pore classes were defined: macropores, i.e. pores larger than 50 µm; mesopores, measuring between 0.2 and 50 µm, and micropores, i.e. those smaller than 0.2 µm.

Saturated hydraulic conductivity was measured on undisturbed soil samples (five per depth) taken along the track trafficked without slip, along the track trafficked with slip (Fig. 97), and from an untrafficked area of the field (control). Samples from the topsoil surface (0 - 0.04 m) were taken after removal of the soil cut by the tyre lugs. Other samples were collected deeper in the topsoil (0.13 - 0.17 m) and in subsoil (0.33 - 0.37 m).

Water conductivity measurements were carried out by means of a permeameter using the falling head technique (Head, 1994).

2.3.1.5 Simulation of tyre-soil contact stress and its impact on soil hydraulic properties

The stress state at the soil-tyre contact surface and the traction performance of the MFWD tractor were simulated on the basis of the soil-tyre interaction model presented in chapther 1.2.1.

The soil mechanical parameters and the tractor specifications required for the simulation are reported in Table 5 and Table 16, respectively.

The MACRO model (Jarvis, 1994) is a dual-porosity model that simulates water and solute transport in macroporous soil. The model divides the total porosity into macropores and micropores. Water flow in micropores is calculated with the Richards equation (Richards, 1931), while macropore flow is simulated as a power-law function of the saturation level in macropores. The two domains are separated by a boundary water content (θ_b), a boundary saturated hydraulic conductivity (K_b), and a boundary tension (Ψ_b). An effective diffusion path length d controls mass exchange between the domains. In this study, the MACRO model is used to quantify water movement in site 1 (without slip) and site 2 (with slip).

2.3.2 Results

2.3.2.1 Soil stress and deformation

Whereas soil displacement was not apparent at site 1 (without slip), the soil was displaced by a distance of 0.35 m over a height of 0.08 m at site 2 (Fig. 98).

Below, the different mechanical conditions at sites 1 and 2 which caused these displacements, and their effects on the hydraulic properties of soil, are described.

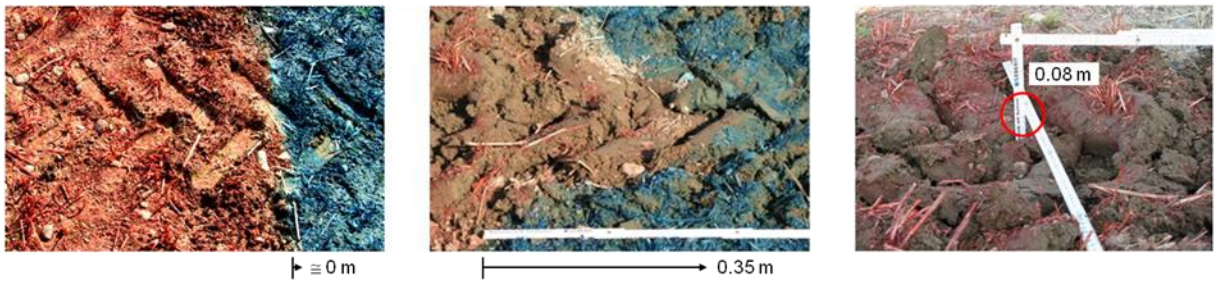

Fig. 98: Topsoil deformation due to tractor traffic: (a) longitudinal displacement on site 1 (without slip); (b) longitudinal displacement on site 2 (slip = 27%); (c) rut depth on site 2 (slip = 27%).

The reliability of the simulation with the soil-tyre interaction model was shown by Shmulevich and Osetinsky (2003) and Osetinsky and Shmulevich (2004).

In the conditions considered, the simulated traction performance in terms of net traction force of the tractor (drawbar pull) versus slip matched the measurements with good agreement (*RMSE* = 0.53 kN) (Fig. 99).

Fig. 100 shows the simulated geometry of the soil-tyre contact surface, the normal and shear contact stresses, and the soil strength for the front and rear wheels at slips of 1% (self-propelled condition) and 27%. The load acting on the front wheel decreased with increasing drawbar pull and slip (load-transfer effect), and caused the geometry of the contact surface to become shorter and shallower (Fig. 100*a* and Fig. 100*b*), and the maximum normal contact stress σ to decline (from 94.2 kPa to 71.6 kPa). The opposite effect characterised the rear wheel for which the maximum normal stress increased with slip (from 90.6 kPa to 104.4 kPa) (Fig. 100*c* and Fig. 100*d*). As the drawbar pull and slip increased, the maximum shear contact stress τ rose noticeably for both the front wheel (from 19.7 kPa to 42.6 kPa) and the rear wheel (from 6.0 kPa to 61.6 kPa), and approached the soil strength τ_{max} over a large part of the contact surface.

The evident underestimation of the rut depth in the presence of slip is due to the fact that the model does not simulate the digging effect which occurs at high slip. The variation with slip of the maximum values of normal stress and shear stress acting at soil-tyre contact surface for the front wheel and the rear wheel is reported in Fig. 101. At 1% slip the highest contact stresses occurred under the front wheel, whilst the highest contact stresses began to occur under the rear wheel when slip exceeded approx. 6%.

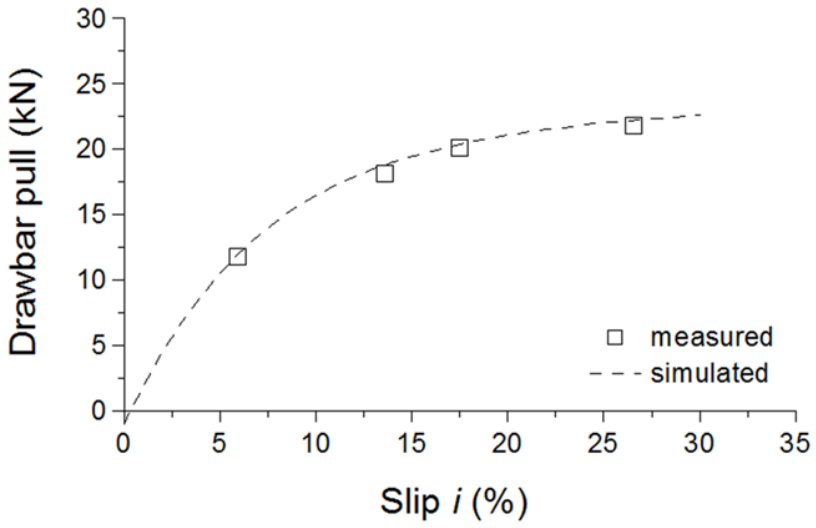

Fig. 99: Measured and simulated traction performance of tractor A (Table 1) on the clay loam (Table 5).

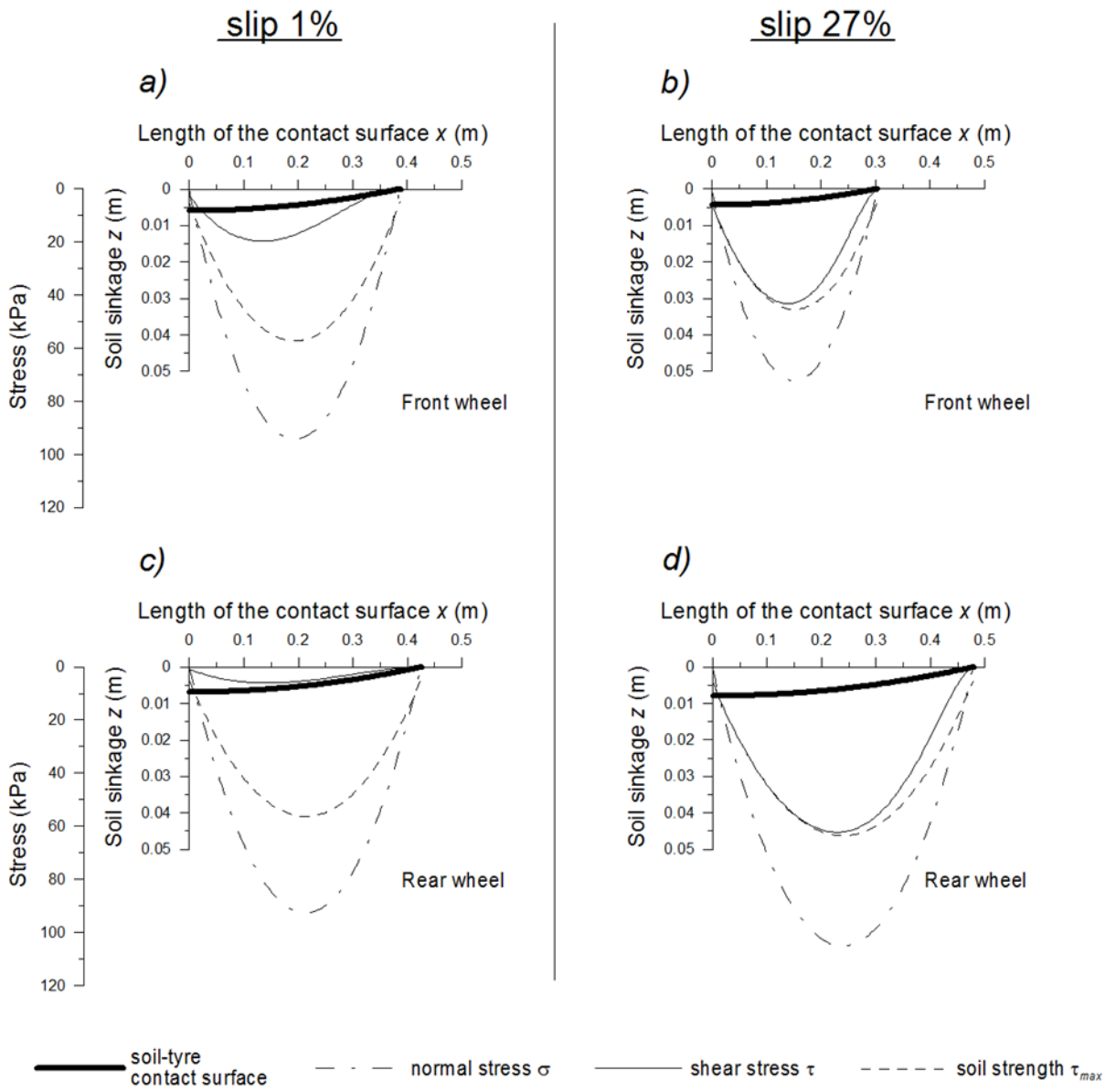

Fig. 100: Simulation of the geometry of the soil-tyre contact surface and the contact stresses: (a) front wheel at 1% slip; (b) front wheel at 27% slip; (c) rear wheel at 1% slip; (d) rear wheel at 27% slip.

2.3.2.2 Effects of deformation on soil porosity

According to the statistical analysis, total porosity at the soil surface (0 - 0.15 m) is significantly lower on the trafficked plot with slip (43%) than on the plot without slip (53.8%) (Fig. 102). Both values measured on trafficked plots with and without slip are significantly lower than the value measured on the control plot (without traffic) at 0.15 m depth (59%). This difference tends to persist at least between 0.15 and 0.45 m.

At the soil surface (0 - 0.05 m depth), macropores decreased from 5% in the control plot to 2% in site 1 (without slip) and to 0% in site 2 (with slip). Below this depth, no significant difference was observed between sites 1 and 2 in terms of macropores, whilst the macropore size distribution virtually disappeared at all depths in site 2 when compared to the control plot (Fig. 103).

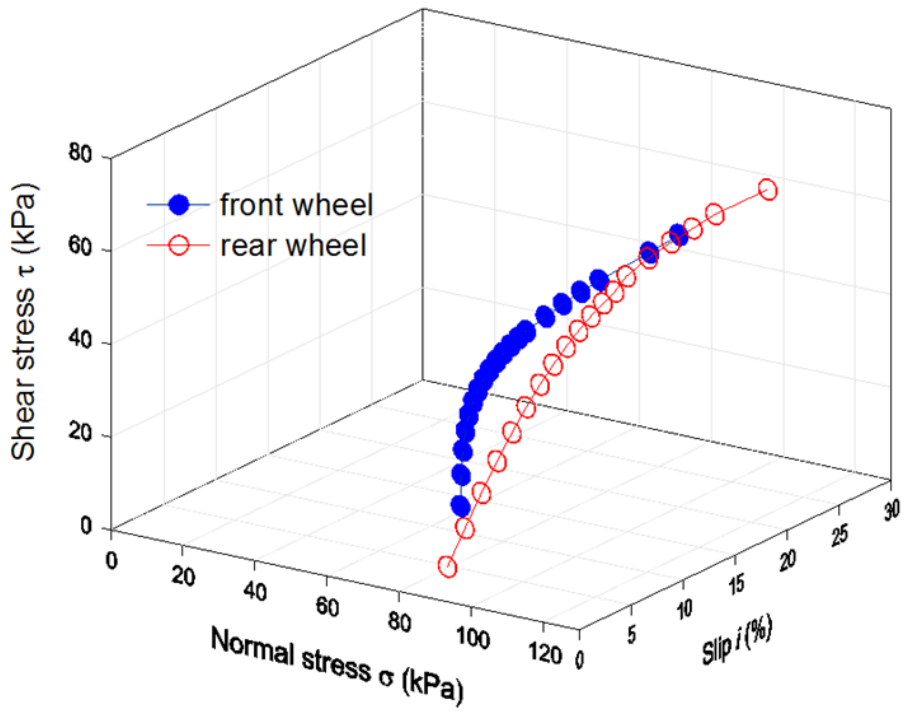

Fig. 101: Variation with slip of the maximum values of normal stress σ and shear stress τ acting at the soil-tyre contact surface for the front and rear wheels.

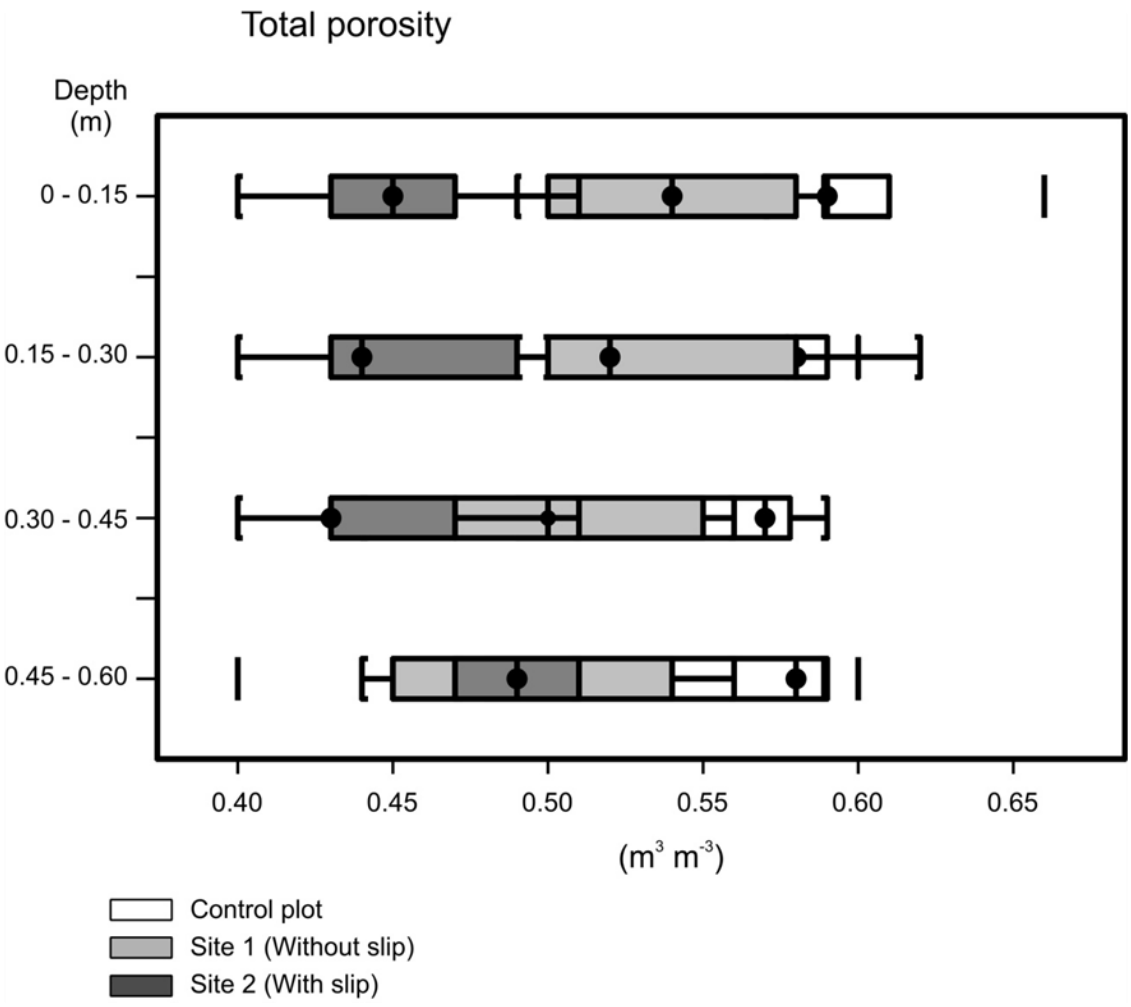

Fig. 102: Total porosity measured in the control plot, in site 1 (1% slip), and in site 2 (27% slip), at different depths.

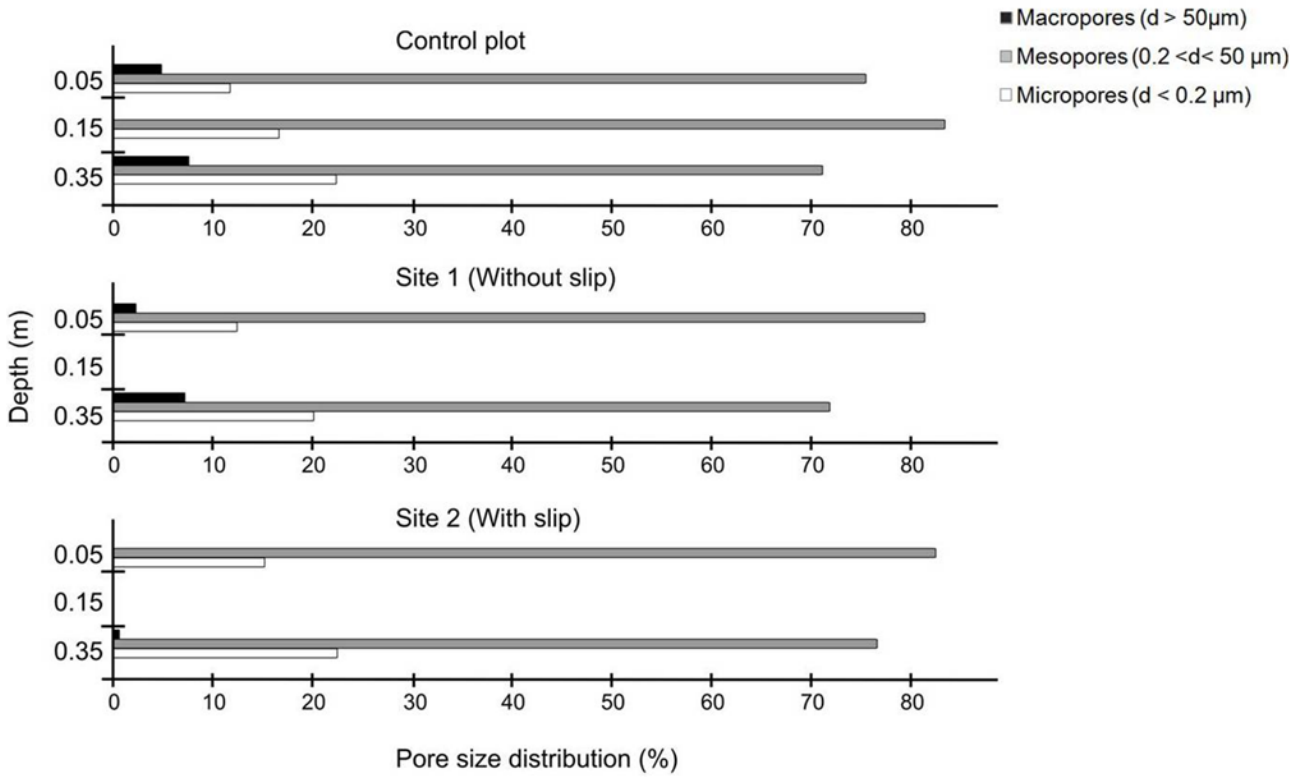

Fig. 103: Pore-size distribution in the control plot, in site 1 (1% slip), and in site 2 (27% slip), at three depths.

2.3.2.3 Effects of deformation on water movement in soil

A significant decrease in K_{sat} (mean value) was observed between the control plot (29.9 mm/h) and sites 1 (10.0 mm/h) and 2 (0.5 mm/h) at the soil surface between 0 and 0.04 m of depth (Fig. 104). No significant decrease of K_{sat} was observed below this depth.

In Fig. 105, the differences in K_{sat} at soil surface (0 - 0.04 m depth) between the control plot, site 1 and site 2, are related to the maximum stresses acting at the soil-tyre contact surface. As the stress condition at the soil-tyre contact surface increased, K_{sat} fell increasingly sharply. At 1% slip (site 1), the highest stress state was reached under the front tyre (σ = 94.2 kPa and τ = 19.7 kPa), and caused a drop of about 66% in K_{sat}. At 27% slip (site 2), the peak of the stress state was reached under the rear tyre (σ = 104.4 kPa and τ = 61.6 kPa), causing a reduction of about 98% in K_{sat}. The further decrease in K_{sat} from site 1 to 2 is most likely due primarily to the sharp increase in shear stress (210%), and only secondarily to the slight increase in normal contact stress (11%). Between 0.15 and 0.35 m, the continued existence of macropores as shown by K_{sat} (Fig. 104) is highlighted by dye-tracer density, which also reflects their existence. The weak dye-tracer density at 0.30 m depth on site 1 (without slip) demonstrates the existence of limited but efficient macropore flow (Alaoui and Goetz, 2008; Holden and Gell, 2009), supporting the theory that earthworm burrows act as dominant routes for preferential flow (Fig. 106). This observation implies that the greatest damage may occur in the topsoil above 0.30 m, characterised by a homogeneous, diffusive flow excluding macropore flow (Alaoui and Goetz, 2008; Holden and Gell, 2009), and that below this depth, the macropores may be considered to be intact. In the trafficked plot with slip (site 2), the zone of efficient macropores (0.30 m depth) disappears, most likely replaced by another type of pore reflected by the homogeneous distribution in the dye-tracer density throughout the entire soil profile (Fig. 107). These results are in accordance with the change in PSD presented in Fig. 103.

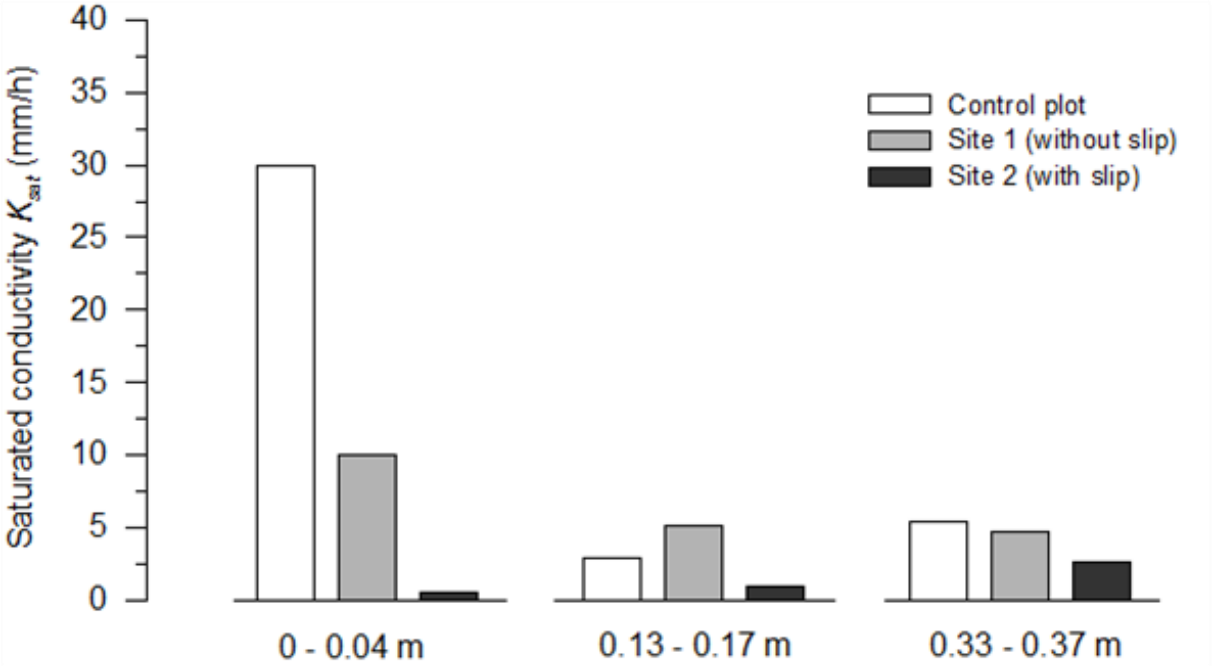

Fig. 104: Saturated hydraulic conductivity K_{sat} (mean value) measured in the control plot, in site 1 (1% slip), and in site 2 (27% slip), at different depths.

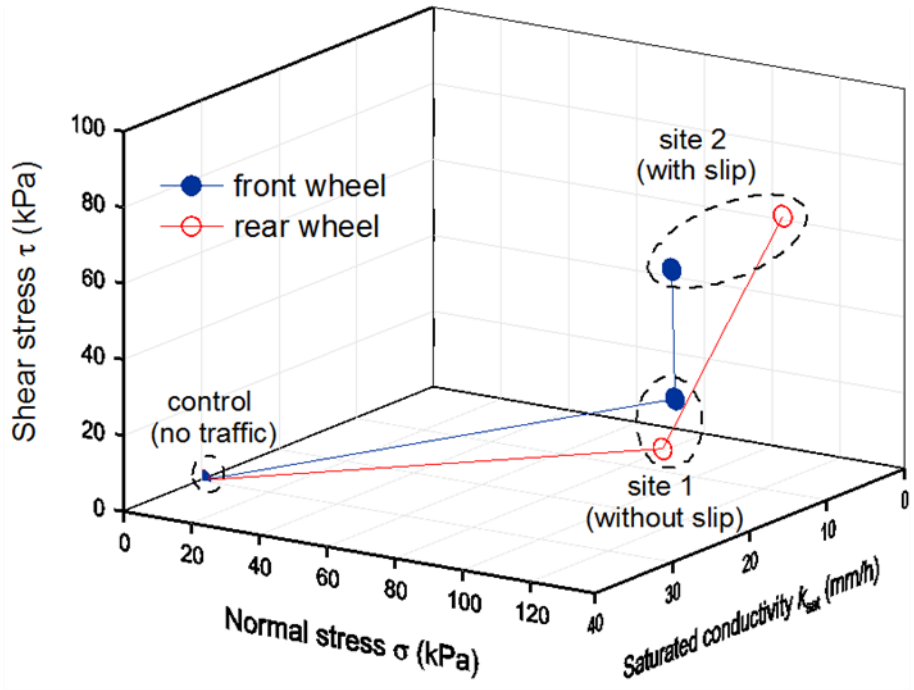

Fig. 105: Variation of K_{sat} at soil surface (0 - 0.04 m depth) between the control plot, site 1 (1% slip), and site 2 (27% slip), in relation to the maximum stresses acting at the soil-tyre contact surface.

Model calibration against water content (θ) measured at 0.15, 0.35 and 0.50 m yielded satisfactory results. The simulation reproduced the field measurements quite well, and the model efficiency (E) calculated according to Nash and Sutcliffe (1970) ranged between 0.53 and 0.83 (Fig. 108).

Once the model was calibrated for θ at different depths (Table 16), the volume of water out of macropores in the control plot, in site 1 (trafficked plot without slip), and in site 2 (trafficked plot with slip), was calculated (Fig. 109). A significant difference was observed between sites 1 and 2: at the soil surface (0.15 m), on the

trafficked plot without slip (site 1), the water out of macropores was 7 l whilst on site 2 it was 5 l, with a difference of about 30%. At 0.35 m, the difference was 52% (site 1: 5 l; site 2: 2.4 l). At 0.50 m, the difference was 76% (site 1: 3 l; site 2: 0.7 l). The comparison between the water volume out of macropores at sites 1 and 2 is consistent, especially at 0.15 and 0.35 m, because of the similar soil texture (Table 15), whilst at 0.50 m an additional effect owing to the difference in soil texture can be considered, but it does not significantly mask the difference in the water volume between the two sites.

Table 17: Model input parameters: soil hydraulic properties at site 1 (without slip) and site 2 (with slip).

Depth	*Parameters*									
Site 1										
(m)	θ_s† ($m^3\ m^{-3}$)	θ_b‡ ($m^3\ m^{-3}$)	θ_r‡ ($m^3\ m^{-3}$)	ψ_b‡ (cm)	K_{sat}† (mm h^{-1})	K_b‡ (mm h^{-1})	d ‡ (mm)	n* ‡ (-)	N‡ (-)	α‡ (cm^{-1})
0–0.15	0.54	0.45	0	1	70	0.1	20	4	1.108	0.027102
0.15–0.30	0.54	0.45	0	1	70	0.1	20	4	1.101	0.031269
0.30–0.45	0.50	0.43	0	1	50	0.1	20	4	1.096	0.027632
0.45–0.60	0.50	0.35	0	1	40	0.1	20	4	1.079	0.035064
Site 2										
0–0.15	0.45	0.20	0	1	40	0.1	6	4	1.050	0.000025
0.15–0.30	0.45	0.35	0	1	40	0.1	6	2	1.050	0.000062
0.30–0.45	0.45	0.33	0	1	40	0.1	5	2	1.140	0.022394
0.45–0.60	0.45	0.35	0	1	30	0.1	5	2	1.148	0.028195

† Measured parameters

‡ Parameters derived by calibration

θ_s: Saturated water content; θ_b: Boundary water content; θ_r: Residual water content; ψ_b: Boundary tension
K_{sat}: Saturated hydraulic conductivity; K_b: Boundary hydraulic conductivity; d: Effective diffusion-path length; n*: Reflects pore-size distribution index and tortuosity in the macropore system; N and α are van Genuchten parameters

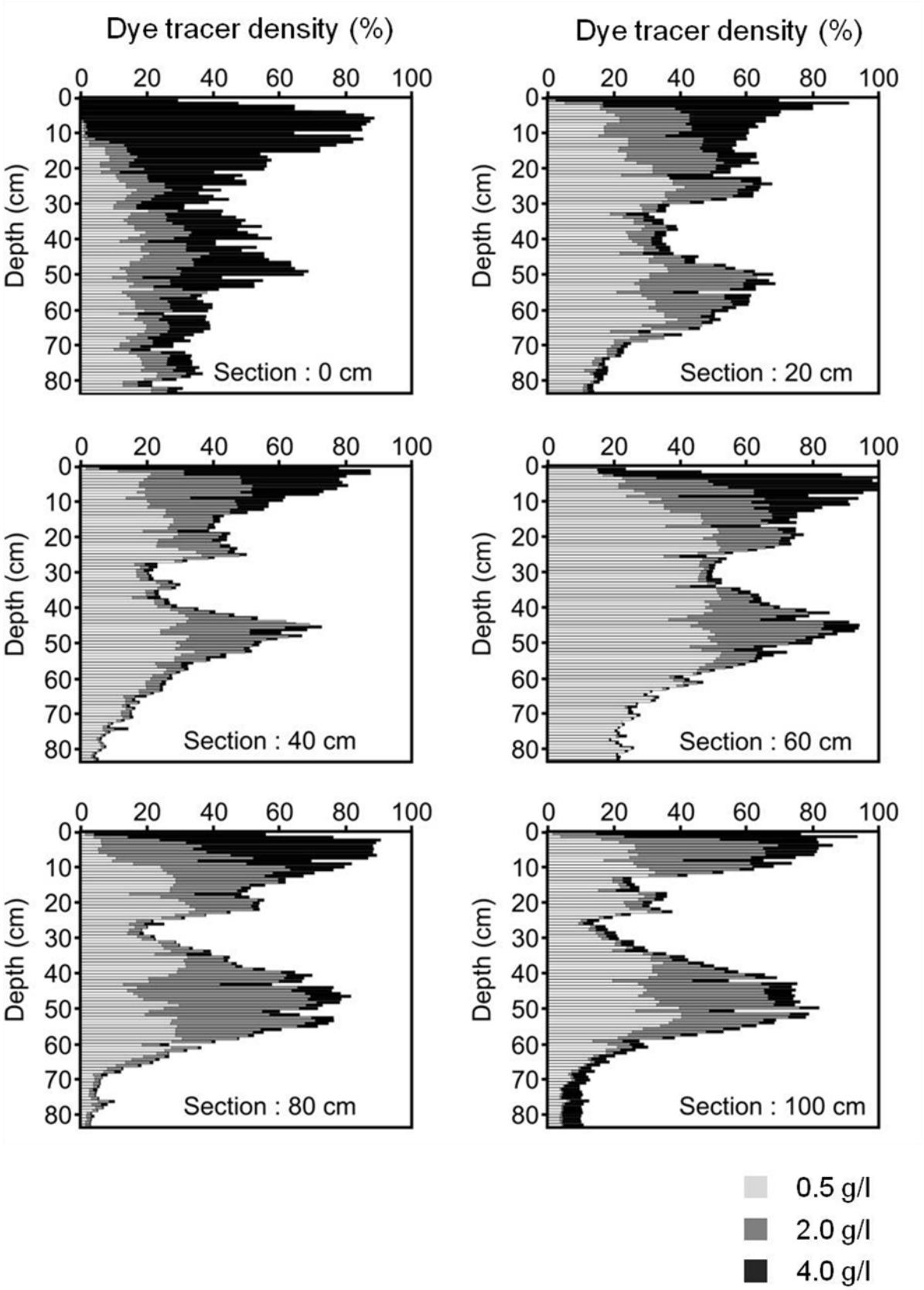

Fig. 106: Dye-tracer density versus depth measured on site 1 (without slip) in different vertical sections.

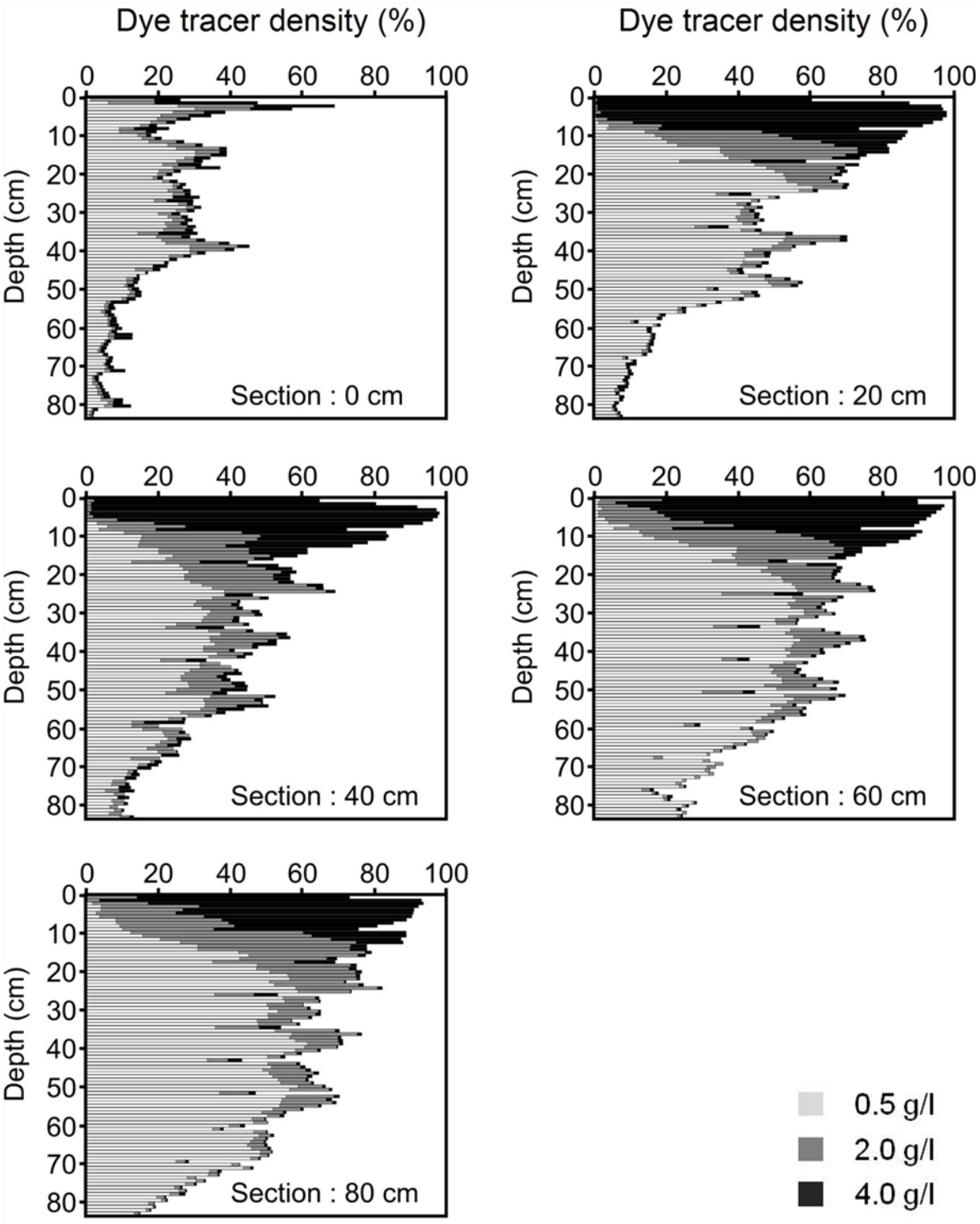

Fig. 107: Dye-tracer density versus depth measured on site 2 (with slip) in different vertical sections.

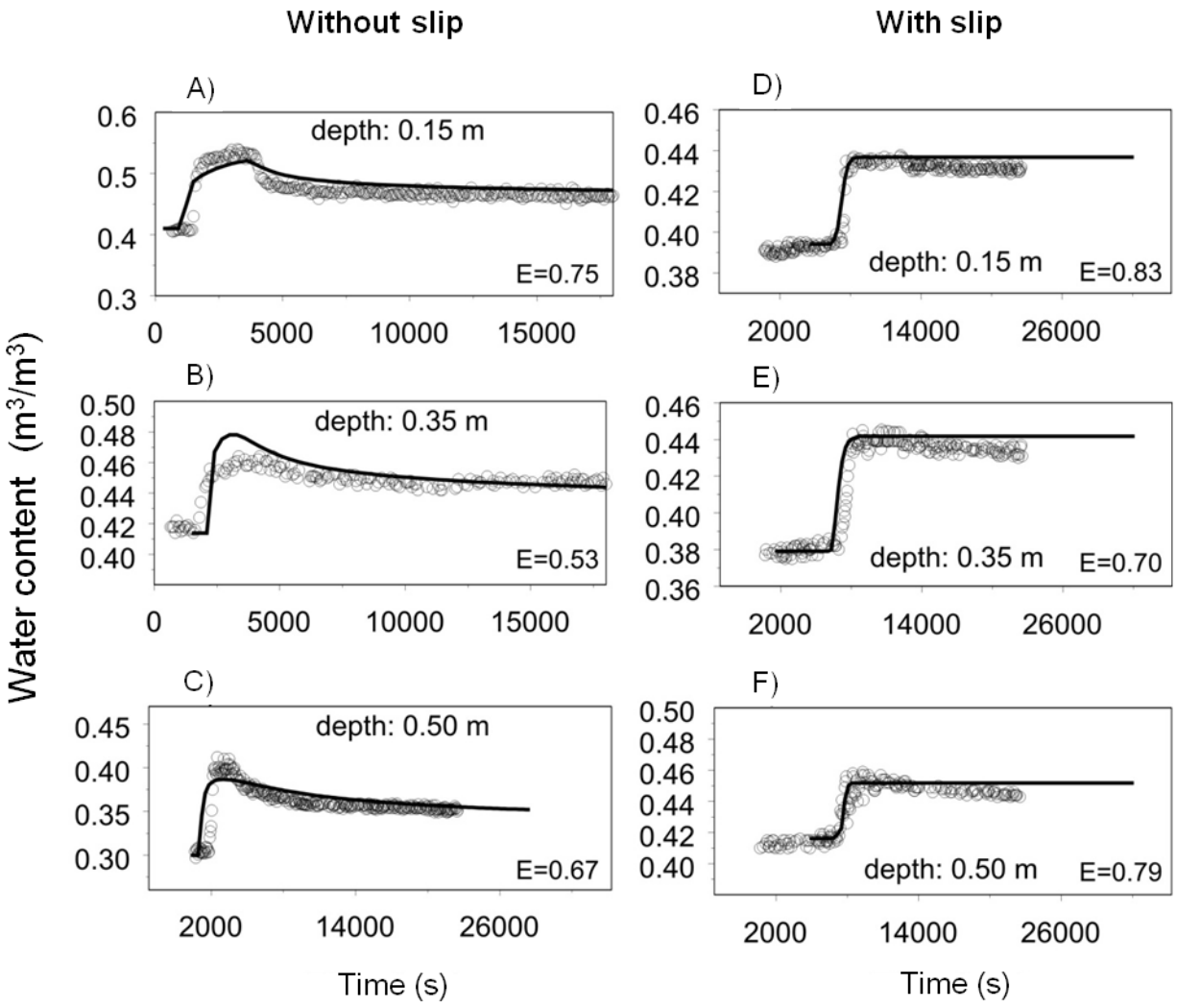

Fig. 108: Measured versus calculated water content on site 1 (A, B and C) and on site 2 (D, E and F).

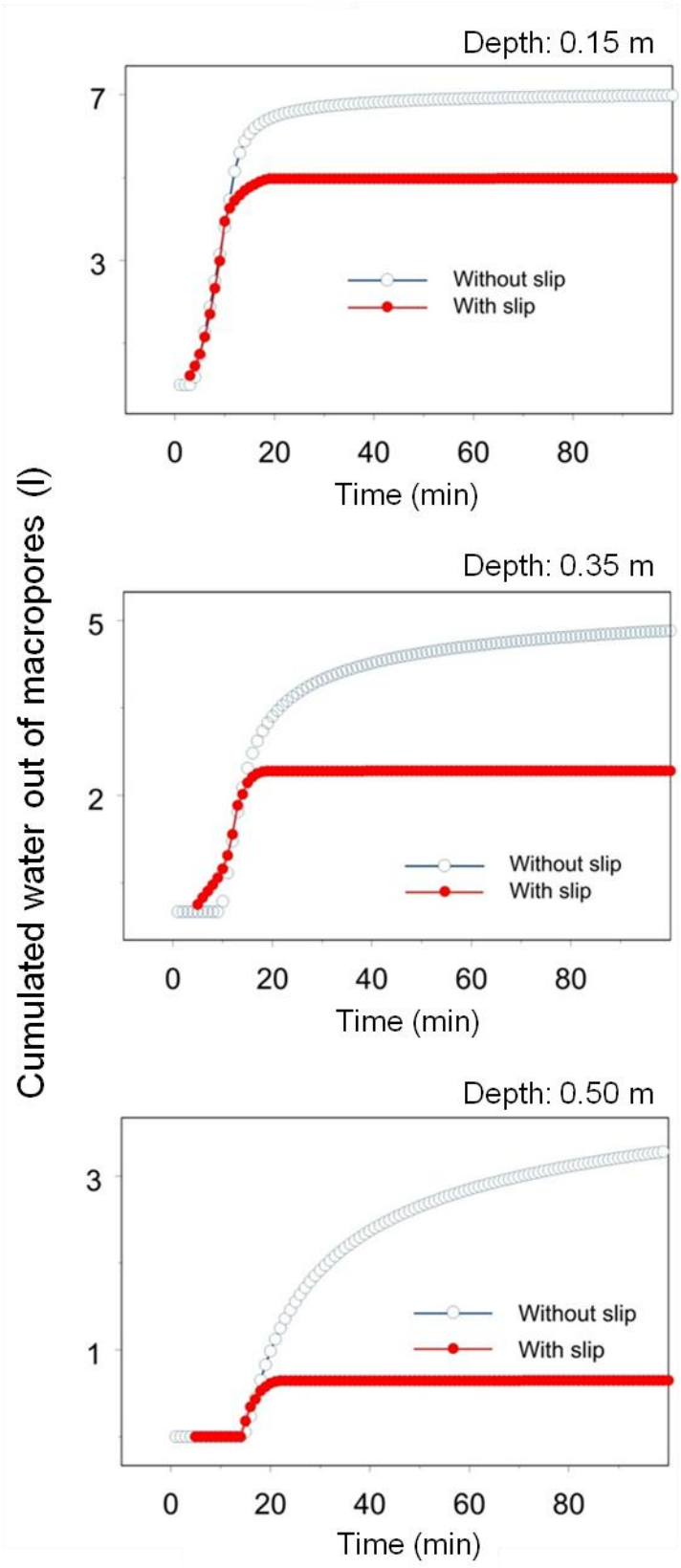

Fig. 109: Simulated water volume out of macropores on site 1 (without slip) and site 2 (with slip) at (A) 0.15 m (B) 0.35 m and (C) 0.50 m of depth.

2.3.3 Discussion

The results presented show influence of tractor working condition on soil stress (Fig. 100 and Fig. 101) and deformation, this latter in terms of change in total porosity (Fig. 102) and pore size distribution (Fig. 103), in addition to the change in pore system functionalities in terms of reduction of saturated hydraulic conductivity (Fig. 104 and Fig. 105) and infiltration capacity of a Brilliant Blue tracer (Fig. 106 and Fig. 107).

When the tractor moved in the self-propelled condition without wheel slip, or with high drawbar pull and wheel slip (Fig. 97), the soil was subject to both normal and shear stress at soil-tyre contact surface. In the first case, the shear stress was low, and the soil stress state was mainly characterised by the normal stress (Fig. 100*a* and Fig. 100*c*). In the second case, the shear stress rose, owing to the high traction force developed (Fig. 100b and Fig. 100d). Moreover, the load distribution between front and rear axles of the tractor changed in dynamic condition owing to the load transfer effect associated to the drawbar pull. Consequently, whereas the dynamic load on the front wheel was higher on site 1 (without slip) than in site 2 (with slip), the dynamic load on the rear wheel was higher on site 2 than on site 1.

The stress at the soil-tyre contact surface on site 2 differed, to a large extent, from that on site 1. The normal stress on site 2 was lower for the front wheel and higher for the rear wheel than on site 1, whilst the shear stress for both front and rear wheels was much higher on site 2 than on site 1.

Because of the different stresses applied, soil deformation on site 1 differed from that on site 2. The change in the soil pore system and its functionalities for water movement was more evident in the shallow layer (0 – 0.15 m) and more remarkable on site 2.

The differences with the control plot (no traffic) pointed out the soil sensitivity to stress caused by the passage of the tractor, whilst the differences between sites 1 and 2 highlighted the impact on soil degradation of the traction force developed by the tractor and the wheel slip.

In the first 0.15 m of depth, this degradation was clearly shown by a decrease in total porosity of 11% in site 1 and of 29% in site 2 (Fig. 102), with a reduction of macropores of about 60% and 100% respectively (Fig. 103). The simulated water volume out of macropores decreased from site 1 to site 2 by about 30% at 0.15 m depth, 52% at 0.35 m depth and 76% at 0.5 m depth (Fig. 109).

The saturated hydraulic conductivity of the shallow topsoil (0 – 0.04 m) decreased by about 66% on site 1 and about 98% on site 2 (Fig. 104). Accordingly, the risk of soil erosion due to rainwater runoff increases significantly when soil is trafficked with high slip. Moreover, as pointed out previously, traffic with high slip on agricultural soils may lead to the formation of a degraded, strengthless soil layer that is strongly exposed to erosion (Battiato and Diserens, 2011).

The quantitative relationship between maximum stress values applied on soil and saturated hydraulic conductivity reported in Fig. 105 is in need of further investigation based on the results of specific tests. The idea of a quantitative relationship for predicting changes in structure and permeability owing to soil deformation was previously proposed by Kirby and Blunden (1991) within the context of critical state soil mechanics. The same authors also recognised the need for further systematic studies.

This relationship is of particular interest for the hydrological aspects to be taken into account in hillside agricultural areas.

Similar results to those obtained for site 1 were reported by several authors who studied the response of different agricultural soils to stress caused by tractor traffic.

Alakukku et al. (2002) studied the response of a clay soil to stress caused by traffic of tractors of different size. They observed a reduction of saturated hydraulic conductivity of soil between 78% and 87% with a decrease in largest macroporosity (ϕ > 300 μm) between 34% and 63% in the layer 0 - 0.2 m.

Previously, Brown et al. (1992) had reported an increase of bulk density of about 17%, a decrease of air-filled porosity of about 74% with a reduction of saturated hydraulic conductivity of 90% at 0.05 - 0.125 m depth, owing to traffic of wheeled tractors on a silty clay loam. At depth 0.125 - 0.200 m the soil degradation was lower but still significant.

Pagliai et al. (2003) observed a reduction of transmission pores (elongated and continuous pores ranging from 50 to 500 μm) in the surface layer (0 - 0.1 m) of a clay soil from 24.2% to 9.3% due to one passage of a 48 kW wheeled tractor, and to 5.4% after four passages of the same tractor. The saturated hydraulic conductivity in the control was higher than 80 mm/h and reduced by more than 50% after one passage of the tractor and by more than 75% after four passages, with a highly significant correlation to the presence of elongated pores.

The effects of compaction of a silty clay soil due one passage and four passages of a four wheel drive tractor (113 kW engine power) were studied by Servadio et al. (2005). They measured a decrease in macroporosity, in particular of elongated pores in the soil layer 0 - 0.1 m depth, from 25.3% to 2.2% after one passage, and to 1.1% after four passages. In the soil layer 0.11 - 0.2 m the macroporosity decreased from 15.9% to 3.3% after one passage, and to 2.0% after four passages. The saturated hydraulic conductivity measured in the soil layer 0 - 0.1 m decreased from 15.8 mm/h to 2.8 mm/h after one passage, and to 1.6 mm/h after four passages.

Kim et al. (2010) reported, for the upper 0.10 m of a silt loam compacted by the passage of a tractor (504 International Harvester) pulling a water wagon (1.89 m^3 water), an increase of bulk density of 8%, with a decrease of computed tomography-measured number of pores of 71%, number of macropores of 69%, and number of coarse mesopores of 75%. The computed tomography-measured porosity and macroporosity decreased by 64%. The saturated hydraulic conductivity reduced due to compaction by 74%.

Specific tests aimed at investigating effects of wheel slip on soil compaction were carried out by Davies et al. (1973), Raghavan et al., (1977), and Raghavan and McKyes, (1977). Davies et al. (1973) observed that wheel slip was more important in causing soil compaction than additional wheel loading, with a more pronounced effect the greater the power of the tractor. Among their results, they reported the effects of traffic without and with slip around 30% of a medium powered tractor on a clay loam (Boxworth soil). They measured an increase of 48% of soil sinkage (from 0.071 m to 0.105 m) due to wheel slip. The decrease in total porosity due to traffic with slip compared to the untreated soil was 22% (from 0.72 to 0.56) at 0.05 m depth, 24% (from 0.68 to 0.52) at 0.10 m depth, and 20% (from 0.64 to 0.51) at 0.15 m depth. The water-entry rate reduced by 96% (from 710 mm/h to 27 mm/h) due to traffic without slip and was almost null (0.6 mm/h) due to traffic with slip.

Raghavan et al. (1977) evaluated soil compaction behaviour under different slip rates for various tyres in sand and sandy loam soils. They observed an increase in dry density due to slip of 50% in the sand and 100% in the sandy loam. Moreover, they identified the slip range, between 15% and 25%, where maximum compaction occurs.

Raghavan and McKyes (1977) studied the effects of slip-generated shear on compaction of sand and sandy loam soils in laboratory tests by means of a pure shear strain box fitted to a standard direct shear equipment.

The compaction was higher, for each normal pressure, with shear than without, and the dry density of the specimens increased due to shear forces between 20% and 50% for a constant normal pressure depending upon the moisture content in the range 10% - 38%.

Results of this study mainly confirm previous findings, and highlight the fact that the increase in soil density is to a large extent due to a reduction in macroporosity, which implies a significant degradation of soil hydraulic properties.

In addition to tractor configuration and soil condition, wheel slip plays a significant role in controlling stress at the soil-tyre contact surface as well as soil degradation in terms of reduction in macropore volume. Because macropores are of prime importance in controlling water movement in the soil and in reducing surface runoff, this degradation has a major impact on soil erosion and soil management.

In point of fact, surface runoff is responsible for severe erosion, especially in the hillside areas comprising the vast majority of agricultural zones in Switzerland, and is aggravated by a reduction in macropore vertical flow owing to soil compaction.

The influence of wheel slip on soil degradation appears to be of importance for both cohesive (clay loam) and granular (sand and sandy loam) soils. This topic merits more attention in future to enable the development of a proper soil-management approach and to help prevent soil erosion.

2.4 Laboratory tests: Hydro-mechanical behaviour of soil during compression and shearing

2.4.1 Materials and methods

2.4.1.1 Direct simple shear apparatus

The effects of stress-induced deformation on soil structure can be studied in the laboratory. A commonly used apparatus for soil testing is the triaxial cell (Head, 1994), however, it suffers from a number of limitations (O'Sullivan et al., 1999), such as the fact that the specimen has a large aspect ratio (height/diameter), this makes it unsuitable for examining the behaviour of thin layers of soil, furthermore, specimens of small diameter are unrepresentative (O'Sullivan et al., 1999). In addition, the structure of the specimens can be hardly analysed after triaxial testing due to the resulting shape of the sample.

In the direct shear test (Head, 1994) the plane along which the specimen fails is determined by the apparatus. In spite of a simple applicability for determining the strength of the soil, this apparatus is unsuitable for studying the effects of deformation on the structure, due to the nature of the deformation before failure.

The direct simple shear box represents a third alternative in which the specimen deforms such that a cross section parallel to the direction of deformation is a parallelogram (Fig. 110). Such a deformation is very close to the way the soil deforms under a driven tractor wheel (O'Sullivan et al., 1999).

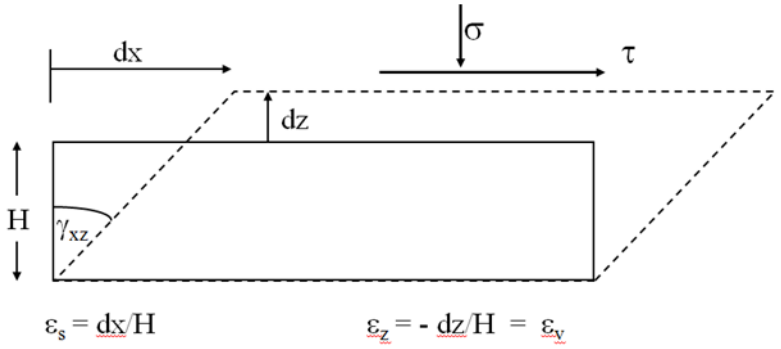

Fig. 110: Schema of stresses and deformations in simple shear test. During the simple shear test the soil sample deforms with the increasing shear stress τ under a constant vertical stress σ. The shear strain (deformation) ε_s is coupled to a vertical strain ε_z which also corresponds to the volumetric strain ε_v.

Among the advantages of the simple shear box, it must be mentioned that the principal stresses rotate as they do under a tractor wheel. Moreover, thanks to the relatively thin specimens, thin soil layers can be sampled. As a drawback, the principal stresses cannot be determined from the data, and this makes it hard to compare results to those obtained in the triaxial test. Another disadvantage is due to the disuniformity of the stress and the deformation within the specimen. Owing to the particular deformation of the specimen (Fig. 110), the soil in the acute angles of the parallelogram compacts more than the average, whilst the soil in the obtuse angles dilates.

Airey and Wood (1987) pointed out that the stress at the boundary may underestimate the stress on the central third of the specimen by up to 10%, however, the stress pattern at the boundary reproduces that on the central third. Another problem of the simple shear box is due to the fact that the forces applied on the shear box are not aligned, this produces a couple which may tilt the box during the test. In practical situations, the underestimation of stress is not a major disadvantage, and the simple shear box could produce data of reasonable quality (Airey and Wood, 1987). Furthermore, it is recognised that the simple

shear box is useful for investigating the soil behaviour before the failure takes place (O'Sullivan et al., 1999). Kirby (1991) and Harris and Bakker (1994) used the simple shear box for measuring the mechanical properties of agricultural topsoils.

A Geonor direct simple shear apparatus - DSS (Fig. 111) of the Soil Mechanics Laboratory LMS of the École Polytechnique Fédérale de Lausanne EPFL was employed.

The Geonor direct simple shear DSS apparatus was developed at the Norwegian Geotechnical Institute NGI by Bjerrum and Landva (1966). Since then it has been extensively used throughout the world.

A lever arm is used to amplify the vertical load applied by means of disc weights (Fig. 111). A ram, driven by an electric motor, applies a horizontal load on the specimen at constant speed. Different gears of the motor can be selected in order to control the speed of application of the shear load on the specimen and have the desired condition of drainage. Vertical and horizontal loads are measured by load cells having capacity of 20 kN, the horizontal and vertical displacements are measured by two linear variable differential transformers (LVDT). A datalogger is used for the data acquisition (Fig. 111), whilst a computer allows to process and display the data in real time. The simple shear box is placed on the bottom plate of the loading frame. The soil specimen is cylindrical, its cross-sectional area can vary from 0.2 10^{-2} to 1.04 10^{-2} m^2 whilst its height is usually 1.6 10^{-2} m. The specimen is placed inside a rubber membrane reinforced by a spiral wire (Fig. 112), such a membrane prevents radial deformation and allows the specimen to be deformed vertically and in simple shear. Testing procedures, including the sample preparation, have been developed by the American Society for Testing and Materials (ASTM) (ASTM D6528 - 07).

The test can be performed in drained or undrained conditions. According to Bjerrum and Landva (1966), the undrained condition can be simulated by continuously adjusting the vertical stress in order to keep constant the volume (or the height) of the specimen. In this case, it is assumed that the change in vertical stress is equal to the change in pore water pressure that would have occurred during a truly undrained test of a saturated sample (Bjerrum and Landva, 1966).

The top cap of the simple shear box was modified by realising a water drainage system with two pipes (Fig. 113), one allowing the water entry and one provided with a tap and used for the saturation of the drainage system with removal of possible air bubbles. The bottom cap was originally provided with a water tap. Thanks to this modification a water flow can be imposed through the sample and the hydraulic conductivity can be measured.

2.4.1.2 Samples preparation and tests execution

The tests were executed with samples of different textures (clay, clay loam, silty loam and loamy sand). In order to have comparable initial conditions for all the samples, the original aggregates were selected among the ones passing by the American Society for Testing and Materials (ASTM) sieve of 8 millimetres mesh and retained by the ASTM sieve of 4 millimetres mesh (Fig. 114), and reconstituted samples with cross-sectional area of 0.5 10^{-2} m2 and height 1.6 10^{-2} m were used (Fig. 115). This has also simplified the procedure of sample preparation since the sample was prepared directly inside the membrane by applying a minimum confining pressure. In order to avoid water to flow in between the sample and the membrane at low confining pressure, a thin mastic layer was placed at sample top (Fig. 115). The saturated water conductivity is obtained by the well known Darcy's law.

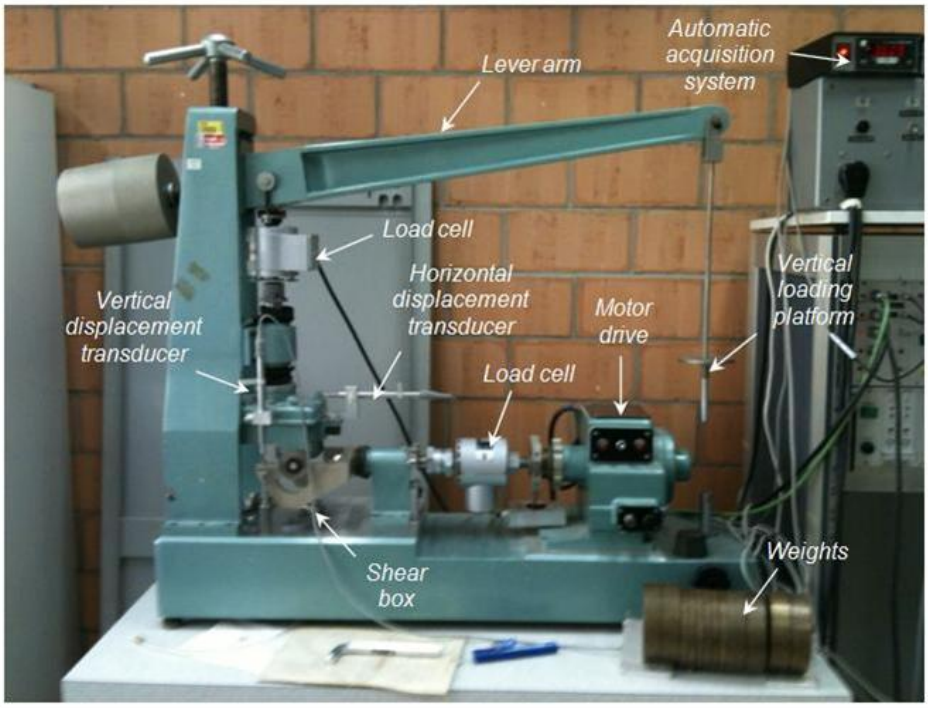

Fig. 111: The Geonor direct simple shear apparatus of the Soil Mechanics Laboratory LMS of the EPFL.

Fig. 112: The rubber membrane reinforced by a spiral wire.

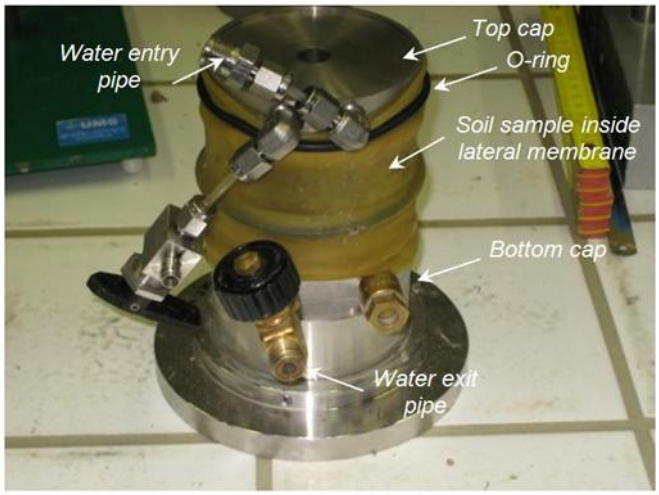

Fig. 113: Modified simple shear box.

(a) *(b)*

Fig. 114: Selected material for reconstituted samples: (a) the aggregates were selected among the ones passing by the American Society for Testing Materials ASTM sieve of 8 millimetres mesh and retained by the ASTM sieve of 4 millimetres mesh; (b) selected aggregates.

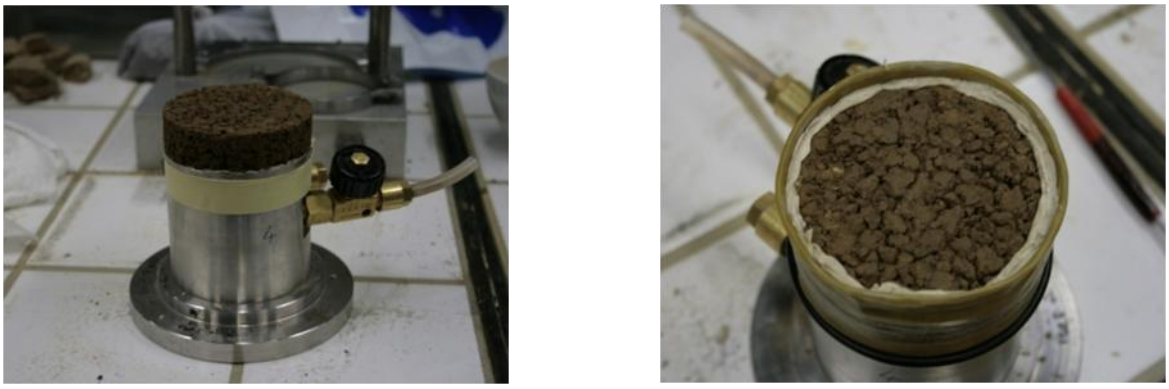

(a) *(b)*

Fig. 115: Reconstituted sample: (a) sample reconstituted with the aggregates selected; (b) sample inside the confining membrane with a thin mastic layer on top in order to avoid water to flow in between the sample and the surrounding membrane at low confining pressure.

A finite element simulation assuming a shear strain of 0.35 shows that water potential lines are nearly horizontal all over the sample an only boundary effects occur (Fig. 116), this allowing the water seepage through the sample to be reasonably assumed as vertical.

Vertical and horizontal forces applied on the sample as well as vertical and horizontal displacements were continuously recorded by the acquisition system during the test.

The aim of the tests with the simple shear apparatus was the comparison of compression and shear deformations on the saturated hydraulic conductivity. Sample deformation due to compression under vertical stress reproduces the effect under a tyre when no slip occurs. An additional distortional deformation due to shearing reproduces effects of tyre slip. The saturated hydraulic conductivity was first measured under a vertical pressure of 10 kPa which assured the correct contact between the apparatus and the shear box as well as a minimum confinement of the soil sample. The samples were consolidated under vertical pressures of 40 kPa, 80 kPa and 120 kPa. Stress paths along the horizontal plane are represented in Fig. 117. The saturated hydraulic conductivity was measured with the falling head conductivity method by means of a graduated burette. Preliminary tests have showed a watertight of the shear box, mainly limited by the o-rings

which fix the confining membrane, of 25 kPa. The conductivity measures were carried out with a hydraulic head of 10 kPa.

The shearing phase was stepped in order to execute hydraulic conductivity measurements at shear strains ε_s of 0.01, 0.1 and 0.35, under constant vertical pressure σ. The shear strain ε_s, the volumetric strain ε_v, the vertical stress σ and the horizontal stress τ are defined according to Fig. 110.

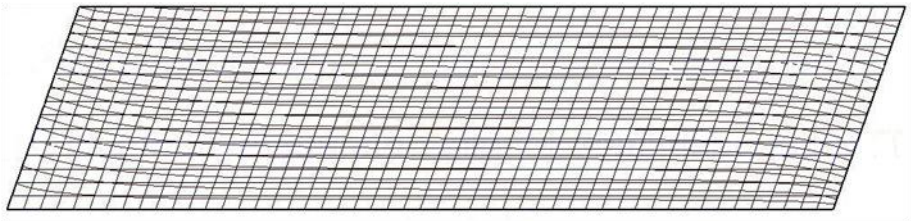

Fig. 116: Finite element simulation, assuming a shear strain ε_s of 0.35, shows that water potential lines are nearly horizontal all over the sample an only boundary effects occur.

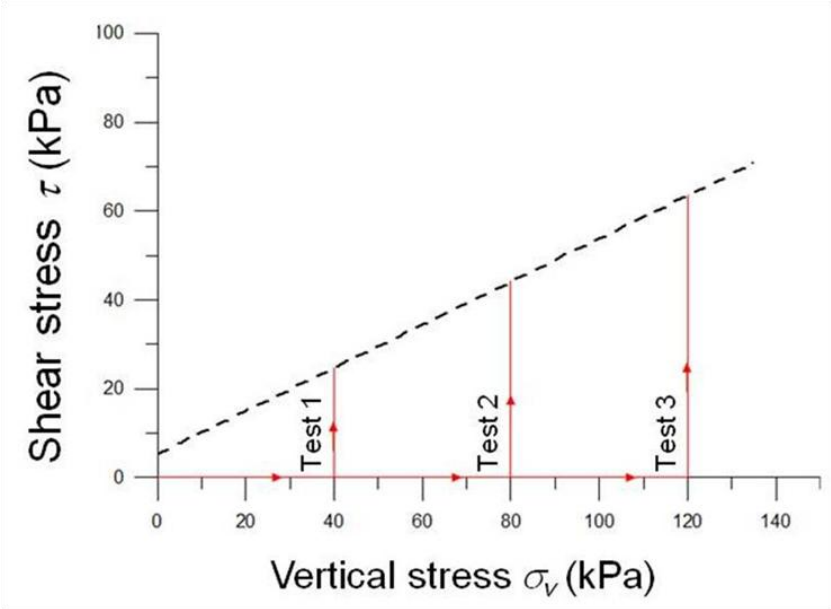

Fig. 117: Stress paths on the horizontal plane in the tests with the direct simple shear box.

2.4.2 Results

Examples of results from shear tests with the modified Geonor shear box are reported in Fig. 118 and Fig. 119.

Fig. 118 shows the evolution of the shear stress with the shear strain during shearing of reconstituted samples of loamy sand and clay loam (Table 5) at 120 kPa of vertical pressure.

Fig. 119 shows the evolution of the volumetric strain of the samples with the accumulated shear strain. Both the volumetric strain and the shear strain are defined according to Fig. 110.

Fig. 120 reports the evolution of the saturated hydraulic conductivity of the sample of loamy sand and that of clay loam before and after the consolidation and during the shearing, in function of the accumulated shear strain. The evolution of the saturated hydraulic conductivity is represented in a logarithmic scale.

During the consolidation phase, the sample of loamy sand accumulated a total volumetric strain of 0.12, whereas that of clay loam accumulated a volumetric strain of 0.176.

During the shear phase at 120 kPa of vertical pressure (Fig. 118), the shear stress rose progressively up to a maximum of around 65 kPa in both cases.

The saturated hydraulic conductivity of the samples decreased after the consolidation due to the volumetric deformation that occurred in this phase. The volumetric deformation was also measured during the shear phase (Fig. 119) and affected the saturated hydraulic conductivity.

Both the loamy sand and the clay loam showed a contraction behaviour (negative dilatancy) when they were sheared, this was pointed out by the positive volumetric strains registered in this phase (Fig. 119). According to this behaviour, the saturated hydraulic conductivity decreased in the shear phase.

The more the shear strain accumulated, the more the saturated water conductivity decreased (Fig. 120).

The saturated hydraulic conductivity of the sample of loamy sand decreased from 1.56 10^{-5} m/s to 1.28 10^{-5} m/s after the consolidation and from 1.28 10^{-5} m/s to 1.04 10^{-5} m/s after the shearing, the latter decrease results comparable to that induced by the consolidation.

The total variation of the saturated hydraulic conductivity was limited because of the high stiffness of sandy material and the low volumetric deformation occurred. It results nearly not readable in the logarithmic scale (Fig. 120). The initial saturated hydraulic conductivity of the sample of clay loam was 5.0 10^{-5} m/s, it decreased to 1.8 10^{-7} m/s after the consolidation and to 1.1 10^{-8} m/s after applying a shear strain ε_s of 0.35 (Fig. 120). The logarithmic scale seems to be suitable to visualize the change in saturated hydraulic conductivity in the clay loam sample which decreased sharply during the consolidation and less considerably during the shear phase (Fig. 120).

Fig. 121 reports the saturated hydraulic conductivity (in a decreasing logarithmic scale) in the intial condition, after the compression and after the shear of the samples of clay, clay loam and silty loam, at vertical pressures of 40, 80 and 120 kPa. For these three materials the compression is responsible for causing the great majority of the total decrease in the saturated hydraulic conductivity.

The variation of the saturated hydraulic conductivity of the samples of loamy sand due to the compression and the shear at vertical pressures of 40, 80, and 120 kPa is reported in Fig. 122. Here the variation of the hydraulic conductivity due to the shear phase was much higher than that due to the compression at 40 and 80 kPa of vertical pressure, moreover, it was positive. As already observed in Fig. 120, at 120 kPa of vertical pressure the shear produced a decrease in the hydraulic conductivity comparable to that due to the compression.

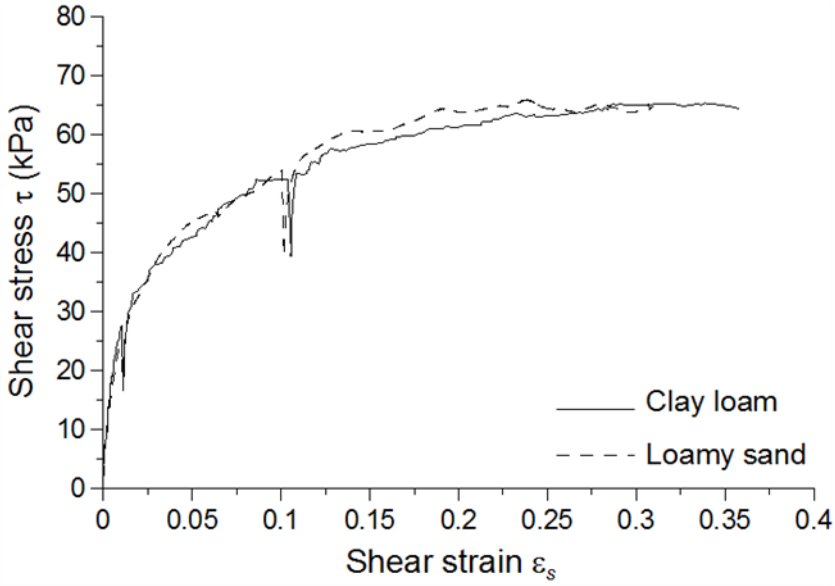

Fig. 118: Shear stress-strain relationship in a simple shear test for reconstituted samples of loamy sand and clay loam at 120 kPa of vertical pressure.

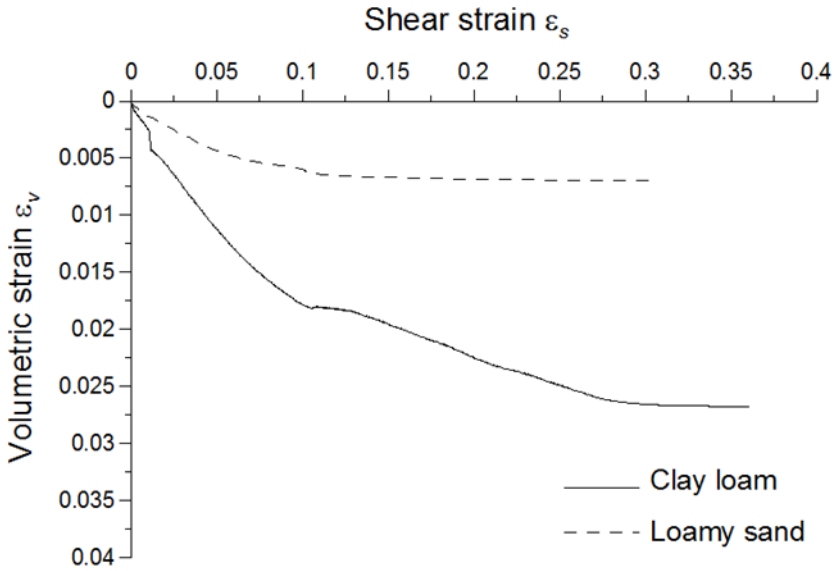

Fig. 119: Volumetric strain-shear strain relationship in a simple shear test for reconstituted samples of loamy sand and clay loam at 120 kPa of vertical pressure.

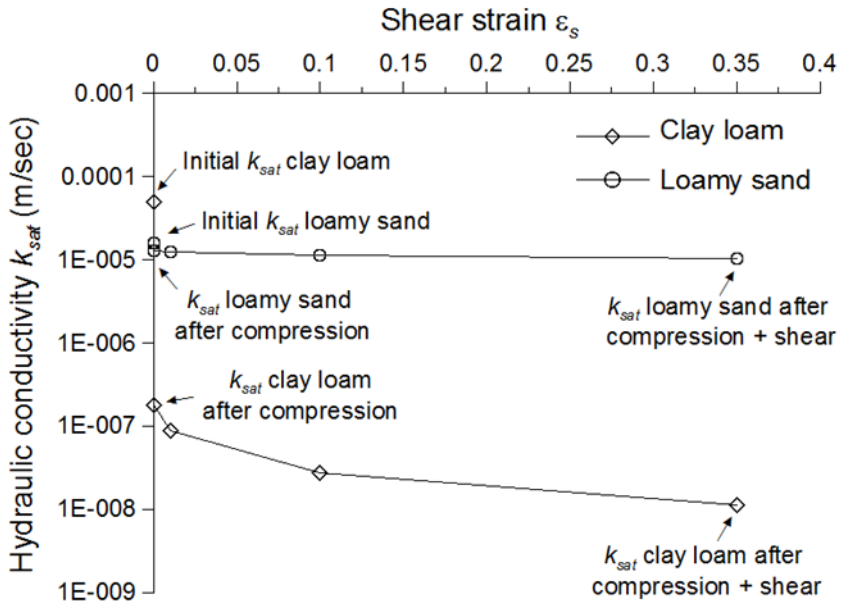

Fig. 120: Variation of the saturated hydraulic conductivity of the sample during the consolidation and the shear phase as a function of the shear strain for reconstituted samples of loamy sand and clay loam at 120 kPa of vertical pressure.

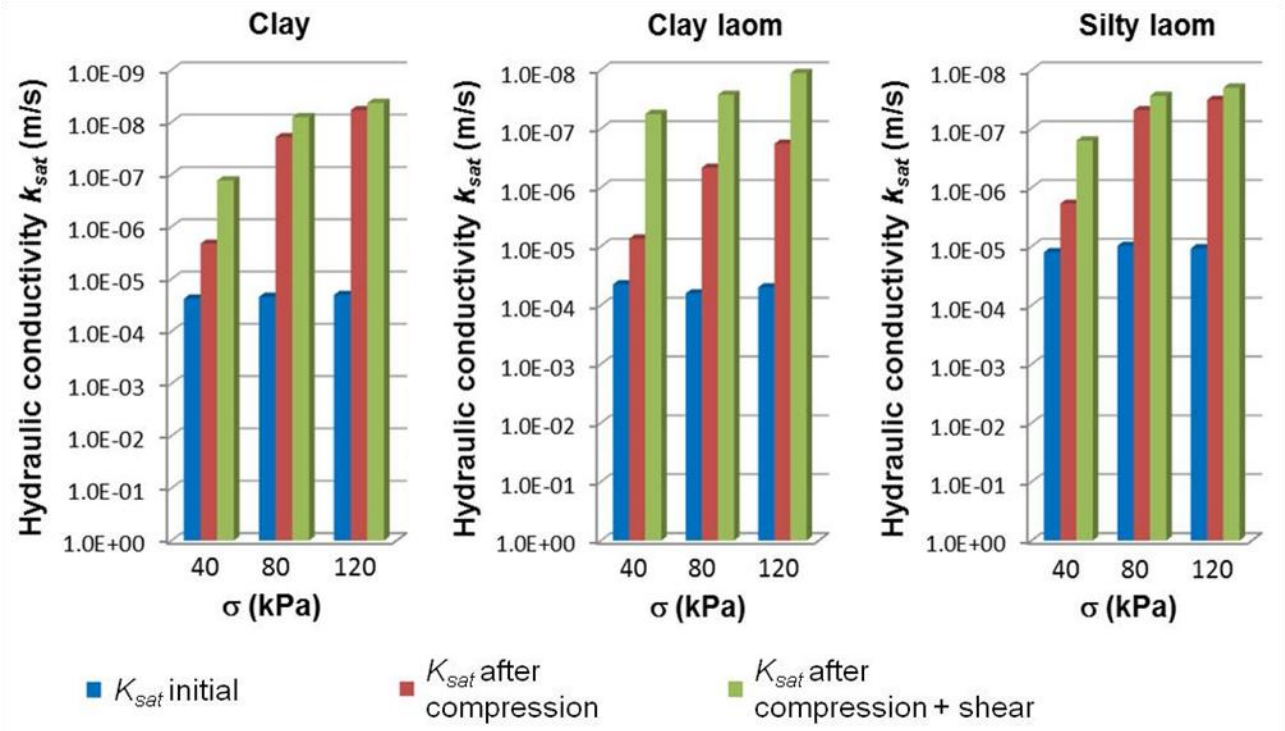

Fig. 121: Variation of the saturated hydraulic conductivity (in a decreasing logarithmic scale) of the samples of clay, clay loam, and silty loam after compression and after shear in the direct simple shear box, at vertical pressures of 40, 80, and 120 kPa.

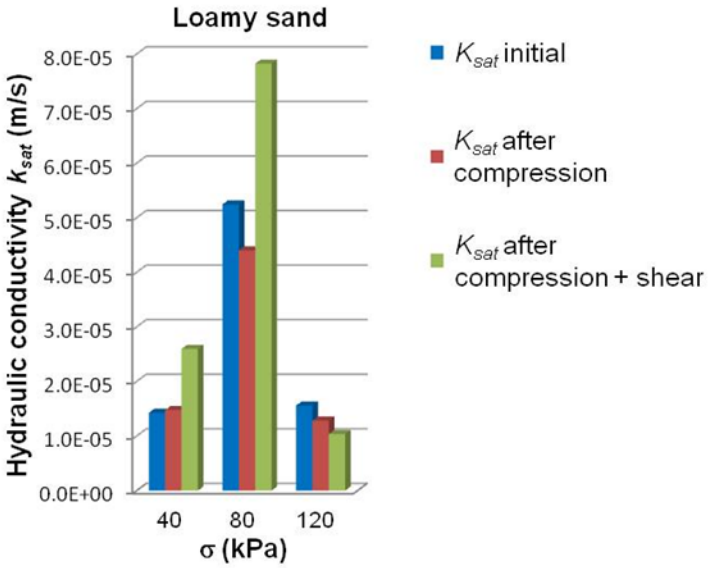

Fig. 122: Variation of the saturated hydraulic conductivity of the samples of loamy sand after compression and after shear in the direct simple shear box, at vertical pressures of 40, 80, and 120 kPa.

2.4.3 Discussion

Comparing the behaviour of the clay loam to that of the loamy sand (Fig. 118, Fig. 119 and Fig. 120) it results evident that, due to the lower stiffness, the clay loam strongly reduced its volume during the consolidation as well as significantly contracted when it was sheared.

The effects of the shear deformation on the hydraulic conductivity depended on the volumetric strain of the sample during shearing as well as on a certain modification or alteration of the pore system. The latter is not related to the variation of volume of voids but depends on possible distortional deformations of the water pathways into the sample.

In some cases, when the samples showed a dilation behaviour during the shear phase, the saturated hydraulic conductivity turned out to increase with the shear strain (Fig. 122).

Results indicate that the variation in voids volume of the soil pore system affects the hydraulic conductivity more than a pure distortional deformation which may alter the water pathways in the sample. Moreover, the variation of the saturated hydraulic conductivity during the shear phase resulted much higher in the samples which accumulated a bigger volumetric strain, being the shear strain always the same.

In the materials with high stiffness, like the samples of loamy sand, the volumetric deformation which occurred during the shear phase affected the saturated hydraulic conductivity significantly, causing a decrease nearly the same as that due to the consolidation at 120 kPa of vertical pressure (Fig. 120). At pressures of 40 and 80 kPa the variation in the hydraulic conductivity due to the shear phase was, to a great extent, bigger than that due to the compression, moreover, after the compression and the shear, the hydraulic conductivity of the sample was higher than its initial value (Fig. 122).

However, in the samples of loamy sand, the total variation in the hydraulic conductivity due to the consolidation and the subsequent shear was very little.

The samples which showed low stiffness, like the clayey or loamy materials, sharply reduced the saturated hydraulic conductivity due to the large amount of the volumetric deformation accumulated during the

consolidation, and the additional volumetric deformation in the shear phase resulted in nearly negligible variations in saturated hydraulic conductivity (Fig. 120 and Fig. 121).

O'Sullivan et al. (1999) observed that aggregate and intact samples of a sandy silt loam (eutric cambisol) subjected to simple shear up to a shear strain of 0.35 compacted roughly the equivalent to doubling the normal stress in the range from 30 kPa to 100 kPa.

Our results with the reconstituted samples of loamy sand in saturated condition pointed out a less significant effect of the shear deformation on compaction. At a vertical pressure of 120 kPa, the volumetric strain ε_v in the shear phase was about 6% of that recorded during the consolidation phase. However, the effect of the shear deformation in terms of variation in saturated hydraulic conductivity K_{sat} turned out to be almost equivalent to that of the consolidation at 120 kPa of vertical pressure. At vertical pressures of 40 and 80 kPa, the shear phase was associated to a dilation behaviour which resulted in an increase in saturated hydraulic conductivity (Fig. 122).

The effects of the shear deformation on the compaction of the samples of clay and silty loam also resulted less substantial that those observed by O'Sullivan et al. (1999).

Only the samples of clay loam showed a behaviour in agreement with that observed by O'Sullivan et al. (1999), since the shear phase at 40 kPa of vertical stress produced a volumetric strain (compaction) almost of the same amount of that produced by doubling the vertical stress. The hydraulic conductivity reduced after the shear at 40 kPa of vertical pressure, more than after the compression at 80 kPa (Fig. 121).

The volumetric strain accumulated by the samples of clay loam during the shear phase was around 0.03 in all cases, while the volumetric strain due to the consolidation phase varied significantly with the vertical stress applied. The ratio between the volumetric strain due to the shear and that due to the consolidation was 0.25 at a vertical stress of 40 kPa, 0.20 at a vertical stress of 80 kPa, and 0.15 at a vertical stress of 120 kPa. According to that observed by O'Sullivan et al. (1999), the influence of the shear strain on the compaction of the sample turned out to be less significant for higher vertical stress.

Shear strains in excess of 0.35 were observed to be unlikely to cause any significant further changes in volume (O'Sullivan et al., 1999), this result was also confirmed in almost all cases considered in our tests. At a shear strain ε_s of 0.35 the failure and the critical state condition were fully reached, this result is pointed out by a flat shear-stress shear-strain curve as well as a flat volumetric-strain shear-strain curve (Fig. 118 and Fig. 119). According to Kirby and Blunden (1991) who investigated the effects of soil shearing on the permeability to air, the shearing is responsible for causing a change in permeability. Both the uniaxial compression and the contraction during shear resulted in a decrease in permeability, whereas, an expansion during shear led to either a decrease or an increase in permeability.

As a consequence of the shear strain, the sample fabric was clearly aligned in the direction of shear, this effect was reported by Scott (1963), McKyes and Yong (1971), and Mitchell (1976). The effect of rearrangement of the initial fabric was limited at a low shear strain and, in general, at a shear stress much lower than the shear strength, this result is in agreement to that reported by Morgenstern and Tchalenko (1967), Barden (1972), and Dickson and Smart (1976). At a high shear strain, the deformation started to localize into thin zones of aligned particles (Morgenstern and Tchalenko, 1967; Dickson and Smart, 1976).

The consolidation phase which preceded the shear phase always resulted in a decrease in conductivity, this is due, in part, to the decrease in the volume of voids, and in part, to the increasing alignment of particles presenting a more tortuous path to the fluid (Kirby and Blunden, 1991; Blackwell et al., 1990; Kirby, 1991).

3. Conclusions and future prospects

This study aimed i) to develop a tractor-soil interaction model for predicting the traction performance of mechanical front-wheel drive MFWD agricultural tractors, ii) to substantiate the model on the basis of results of traction tests with four MFWD tractors of wide ranging power, in different configurations, and in four locations presenting soil textures ranging from clay to loamy sand, iii) to analyse the influence of soil strength, tyre pressure, wheel load, and dual tyres, on the traction performance of MFWD tractors, iv) to evaluate the quantitative effect of slip of tractor tyres on soil deformation, soil structure modification and alteration of water movement in soil, and v) to detect the mechanical conditions in soil-traction tyres interaction under which a topsoil damage may occur.

The main conclusions and future prospects of this study can be summarized as follows:

I. The experimental technique to perform full-scale tractor traction tests with MFWD tractors on agricultural soils allowed a proper control and monitoring of: the slip of the traction wheels, the traction force developed, and the fuel consumption. Experimental results were repeatable and reasonable, furthermore, a general qualitative agreement with other results presented in literature was observed.

   Additional traction tests should include the measurement of the torque acting on the wheels, with a torque dynamometer. This will allow the calculation of the traction efficiency.

II. Simulations with the soil-tractor interaction model matched measured traction performance with general good agreement (overall mean error of 12% and overall mean residual of 3.30 kN). The model proved to simulate consistently the traction performance in terms of drawbar pull as a function of the wheel slip, and to reliably reproduce the influence of tyre inflation pressure, wheel load, and soil strength, on the traction performance of the MFWD tractors considered. An evident underestimation of the drawbar pull is shown in many cases, at a low slip, when a high wheel load is combined with a low tyre inflation pressure. When dual tyres are used at the rear axle or at both the front and the rear axles, the simplified approach which assumes a unique tyre having width and stiffness given by the sum of those of the two single tyres gave results in appropriate agreement with the traction performance measured (overall mean error of 0.09 and overall mean residual of 2.36 kN). However, a more rigorous analysis of the system of dual tyres is needed in order to improve consistency of model simulations.

   The model presented can be a valid aid for the choice of a proper tractor configuration, this results in saving fuel and, therefore, in reducing the costs of tillage management.

   The introduction of the effects of the lugs is recognised as a major challenge for a further development of the model of soil-tyre interaction considered in this study. This is expected to result in a better simulation of the soil compaction resistance and the traction performance on firm soils. Furthermore, a function which properly describes the elasto-plastic behaviour of the soil during a repetitive loading should be introduced in order to better simulate the interaction between the soil and the rear wheels.

III. The analysis of the influence of tyre pressure and wheel load on the traction performance of the 40 kN tractor on the clay soil pointed out that, although the tractor developed higher drawbar pull both when tyre inflation pressure was decreased and wheel load was increased, only the decrease in tyre pressure produced improvements in terms of coefficient of traction, traction efficiency, power delivery efficiency,

and specific fuel consumption, while the only significant benefit due to the increase in wheel load was a reduction in the specific fuel consumption at a tyre pressure of 160 kPa and a slip of under 15%. A mechanistic interpretation of these results was proposed.

IV. The traction performance of the 40 kN tractor at a tyre pressure of 60 and 160 kPa was compared on the four agricultural soils under consideration. Compression and shear tests performed with the tractor-mounted bevameter pointed out noticeable differences in the mechanical behaviour of the soils. According to the different mechanical behaviour, the drawbar pull measured on the four soils was significantly disparate. Simulations with the tractor-soil interaction model also showed dissimilarities in the traction coefficient, the motion resistance, and the traction efficiency. In spite of the widely ranging mechanical parameters of the soils, only little dissimilarities were measured in terms of the specific fuel consumption and the power delivery efficiency, particularly at a tyre pressure of 160 kPa. The overall traction performance was slightly better on the clay soil than on the other soils. Results of this study confirm that the traction performance is a peculiarity of the tractor-soil system and not of the tractor only, and that a proper knowledge of the soil mechanical behaviour should aid in developing strategies to reduce the costs of tillage management.

V. High slip of tractor traction tyres causes topsoil damage in terms of soil cutting effect with the formation of a strengthless layer strongly exposed to erosion and an underlying layer where shear deformations contribute to the alteration of soil structure functionalities. In the silt loam agricultural field, the soil failure was clearly indicated by longitudinal topsoil shear displacement. This latter turned out not to vary significantly at a low slip. As soon as the soil strength was approached, topsoil shear displacement rose, indicating that soil failure was occurring. A ratio τ/τ_{max} of 0.99, as a maximum value along the soil-tyre contact surface, was identified as the indicative limit beyond which soil failure is expected to occur. This limit corresponds to a certain tyre slip which depends on soil mechanical behaviour and tyre parameters such as dimensions, rolling radius, carried load, inflation pressure, and stiffness. In the traction tests executed on the silt loam, a ratio τ/τ_{max} of 0.99 was reached at first at soil-front tyre contact for slip of 11% when the tyre inflation pressure was set to 60 kPa, and at both soil-front tyre contact and soil-rear tyre contact, for slip of 11% when the tyre inflation pressure was set to 160 kPa, and for slip of 13% when dual tyres were used at front and rear axles, the tractor was ballasted (from 40.8 kN to 56.6 kN), and the tyre inflation pressure was set to 60 kPa. These slip values should be regarded as indicative limits not to be exceeded in tillage operations in order to avoid topsoil damage in the conditions considered.

As pointed out in this study, limiting slip concurs in the preservation of the topsoil. A similar study needs to be extended to soils having texture and conditions different from those considered, moreover, additional traction tests should involve tractors of different size, power, and traction system, in order to lead to a better knowledge of the tractor-soil interaction which can assure more appropriate tillage management.

VI. The stress state at the soil-tyre contact surface increased significantly when the tractor moved with slip rather than without slip, mostly in terms of shear stress. As a consequence, the severity of tractor-traffic-

induced soil degradation increased appreciably. The change in soil structure and hydraulic properties measured in the clay loam agricultural field was more pronounced in the first 0.15 m where the total porosity decreases by 11% without slip and 29% with slip, with a reduction of macropores of about 60% and 100%, respectively. The saturated hydraulic conductivity of the shallow topsoil (0 - 0.04 m) turned out reduced of about 66% without slip and of about 98% with 27% slip. These results are in agreement with data reported by other authors. A mechanistic interpretation of the influence of slip on soil damage was provided on the basis of the increase in vertical pressure due to the load transfer effect, as well as of the contraction behaviour of slightly consolidated soils during shearing.

The influence of wheel slip on soil degradation appears to be of importance for both cohesive (clay loam) and granular (sand and sandy loam) soils. This topic merits more attention in future to enable the development of a proper soil-management approach and to help prevent soil erosion.

VII. A Geonor simple shear box was successfully modified in order to perform soil hydraulic conductivity measurements in saturated conditions during the compression phase and the shear phase of the test. Results obtained on reconstituted samples confirmed that shear deformations may contribute to damage topsoil structure functionalities, decreasing, in most cases, the hydraulic conductivity. The decrease in hydraulic conductivity due to shear-induced soil deformations turned out to be almost comparable to that induced by compression, in the loamy sand at a vertical pressure of 120 kPa. At pressures of 40 and 80 kPa, the saturated hydraulic conductivity varied due to the shear-induced deformations more than due to the compression phase, moreover, it increased with the accumulated shear strain. In the clay, the clay loam, and the silty loam, the decrease in the saturated hydraulic conductivity was mainly controlled by the deformation during compression. Only in the samples of clay loam, at low vertical stress (σ = 40 kPa), the shear phase produced a volumetric strain (compaction) almost of the same amount of that induced by doubling the vertical stress, and a decrease in the saturated hydraulic conductivity bigger than that due to the compression at 80 and 120 kPa.

The effects of shearing on the saturated hydraulic conductivity were mainly controlled by the volumetric strain coupled to the shear strain, and the variation in voids volume of the pore system affected the hydraulic conductivity more than a pure distortional deformation which may alter the water pathways in the sample.

4. TASC V3.0 Module 2: Traction, energy and topsoil damage

Tillage operations require traction forces developed by stress interactions between tractor tyres and topsoil. In this interaction both the tyres and the soil deform and wheel slip occurs. Limiting wheel slip is an issue of high interest since it means saving fuel and avoiding precocious wear of tyres. Moreover, high wheel slip corresponds to high shear stress on topsoil surface which can lead to a topsoil damage involving soil cutting due to the tyre lugs and alteration of the soil pore system functionalities due to intense shear deformations. In spite of the above considerations, wheel slip seems to be unavoidable when driving on soil and the challenge is mostly finding out the best tractor configuration to have the highest traction with the lowest wheel slip. In this context, a new module “Traction and Energy analysis“ was developed for the third version of the Excel application TASC V3.0 (Tyres/Tracks And Soil Compaction) (Fig. 123). This module aims to simulate the tractor traction performance and to prevent any topsoil damage. The net traction force and the wheel slip limit values beyond which topsoil damage is expected to occur, are provided as output of the simulation. These limit values are calculated according to the criterion presented by Battiato et al., (2013). In parallel, the dynamic load by pulling is also given, this allows an even better assessment of the risks of severe compaction (Module 1 – Stress propagation and soil damage).

Additionally, the tractor traction performance is presented in terms of the net traction force (or drawbar pull), the engine power and the fuel consumption, as a function of the wheel slip, and furthermore, the specific fuel consumption (drawbar power basis) and the tractive efficiency, as a function of the traction force.

The engine power is simulated assuming an inner loss of 15% from the engine to the tractor wheels.

In addition, the draft requirement of tillage tools and seeding implements can be calculated according to the ASAE 497.7 (2011), as a function of the tool properties, the tilling depth, and the soil texture and velocity. Results are reported in a table form (Fig. 124) and a graphical form (Fig. 125 and Fig. 126).

The Traction and Energy analysis module simulates the traction performance of the tractor-soil system on the basis of the model presented in this work and by Battiato and Diserens (2013).

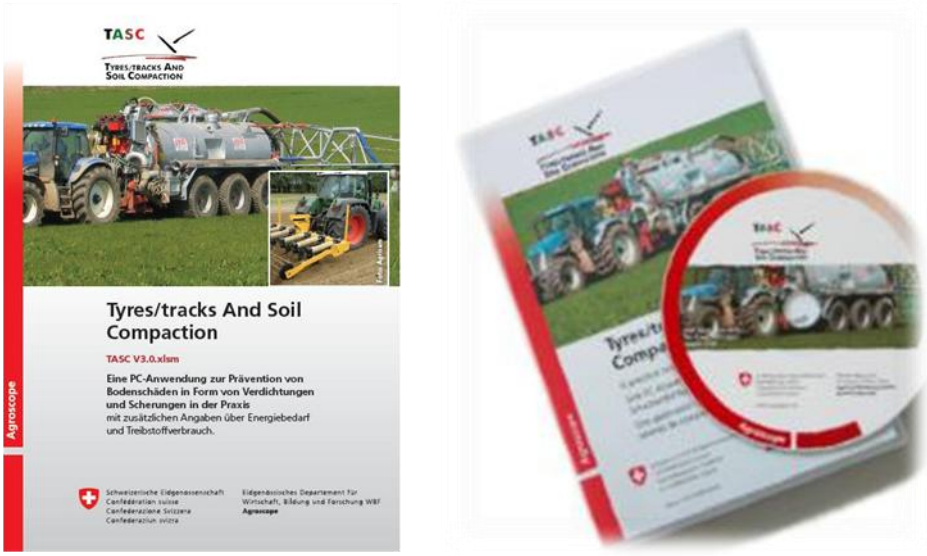

Fig. 123: The new TASC V3.0 (www.AgroscopeTASC V3.0).

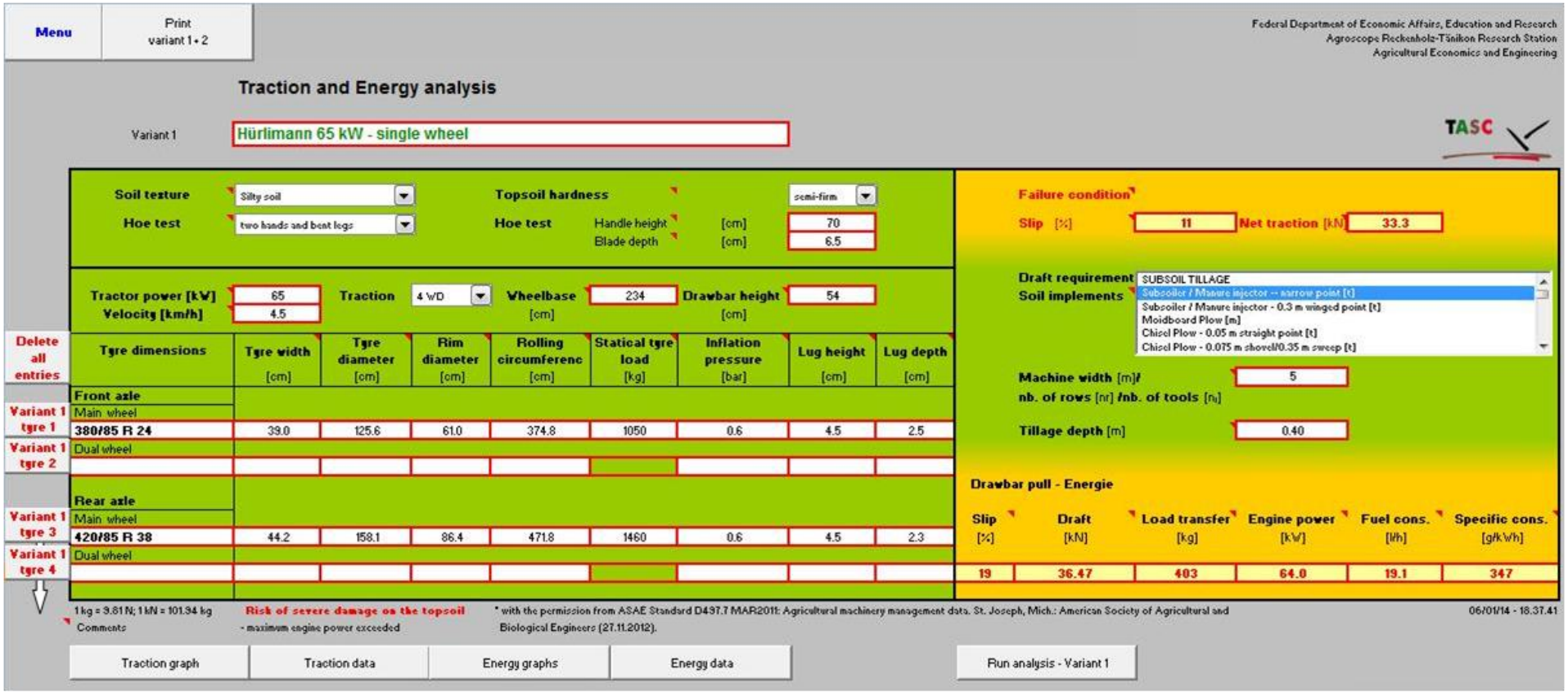

Fig. 124: The interface of the module Traction and Energy analysis of the TASC V3.0 with the input data (green background of the table) and the main output data (yellow background of the table).

Input data (Fig. 124) involve soil mechanical parameters and machine parameters included the driving speed. The soil mechanical behaviour is characterised by means of five parameters: two parameters of compression stiffness, one parameter of shearing stiffness and two parameters of shear strength. These parameters are derived on the basis of practical tests to be executed on field. Five classes of soil texture can be chosen: clay soil, silty soil, silty loam and loam, sandy loam and loamy sand, sandy soil. The soil mechanical behaviour is described on the basis of four simple tests: the screwdriver test, the hoe test, the finger test (tactile test) and the rut depth test.

The screwdriver test was already presented in the data input for the TASC – Stress Propagation module where it's used in order to characterise the topsoil stability (Diserens et al., 2003). In this case the screwdriver test is employed to provide an indicative value of the modulus of shear deformation *k* of the topsoil. The relationship between the topsoil penetration resistance *P.R.* [kg] measured with the screwdriver and the modulus of shear deformation *k* [m] was derived empirically on different agricultural soils (Diserens and Battiato, 2013).

The hoe test is the most important. It provides, in fact, the soil strength parameter *c* [kPa] which strongly affects the tractor traction performance. The test requires a hoe to be employed and allows the soil cohesion *c'* to be calculated on the basis of the force applied to cut a soil clod. The force applied is estimated on the basis of the position assumed to pull the hoe and cut the soil clod. In this, five classes are considered: 1 hand, 2 hands, 1 hand and bent legs, 2 hands and bent legs, and no possible. The resistance of the soil clod is calculated by means of the method of stress characteristics (Reece, 1965) assuming a two dimensional soil failure mechanism.

The tactile test provides a simple determination of the angle of soil shear resistance φ which characterises the ultimate soil strength. The values of the soil shear resistance φ adopted in the TASC V3.0 are reported in the TASC User Guide and were selected on the basis of several values reported in literature.

The rut depth test provides a simple determination of the soil parameters K and n, respectively the modulus of deformation and the exponent of deformation. These two parameters define the soil pressure-sinkage relationship according to Bekker's theory (Bekker, 1956; Bekker 1960).

The wheel characteristics which affect the traction analysis are the load, the tyre inflation pressure, the tyre dimensions such as the width and the unloaded outer diameter, and the rim diameter. The tyre radial stiffness is defined by two parameters: the carcass stiffness and the stiffness from the inflation pressure. These two parameters are calculated according to Lines and Murphy (1991).

Additional input parameters are the tractor power, the velocity, the number of driven wheels (4WD or 2WD), the wheelbase of the tractor, and the drawbar height.

The tyres can be selected from a very comprehensive database and the use of dual tyres can also be simulated.

This new TASC module is a practical tool which allows the user to compare tractor traction performance, to assess soil vulnerability and fuel consumption corresponding to different tractor configurations, on several soils under various conditions. Number of driven wheels, number of tyres, tyre type and inflation pressure, wheel load and driving velocity can be varied in order to find out the best configuration. This new TASC module is also validated on the basis of several field tests.

A detailed description of the input and output parameter and the computation procedure used in the module Traction and Energy of the TASC V3.0 is provided in the TASC User Guide and by Diserens and Battiato (2013).

Additional information about the Excel application TASC are given at the following websites:

Order form d/e/f

http://www.agroscope.admin.ch/praxis/00220/06773/06774/index.html?lang=de.

Flyer d/e/f/

http://www.agroscope.ch/praxis/00220/06773/06777/index.html?lang=de

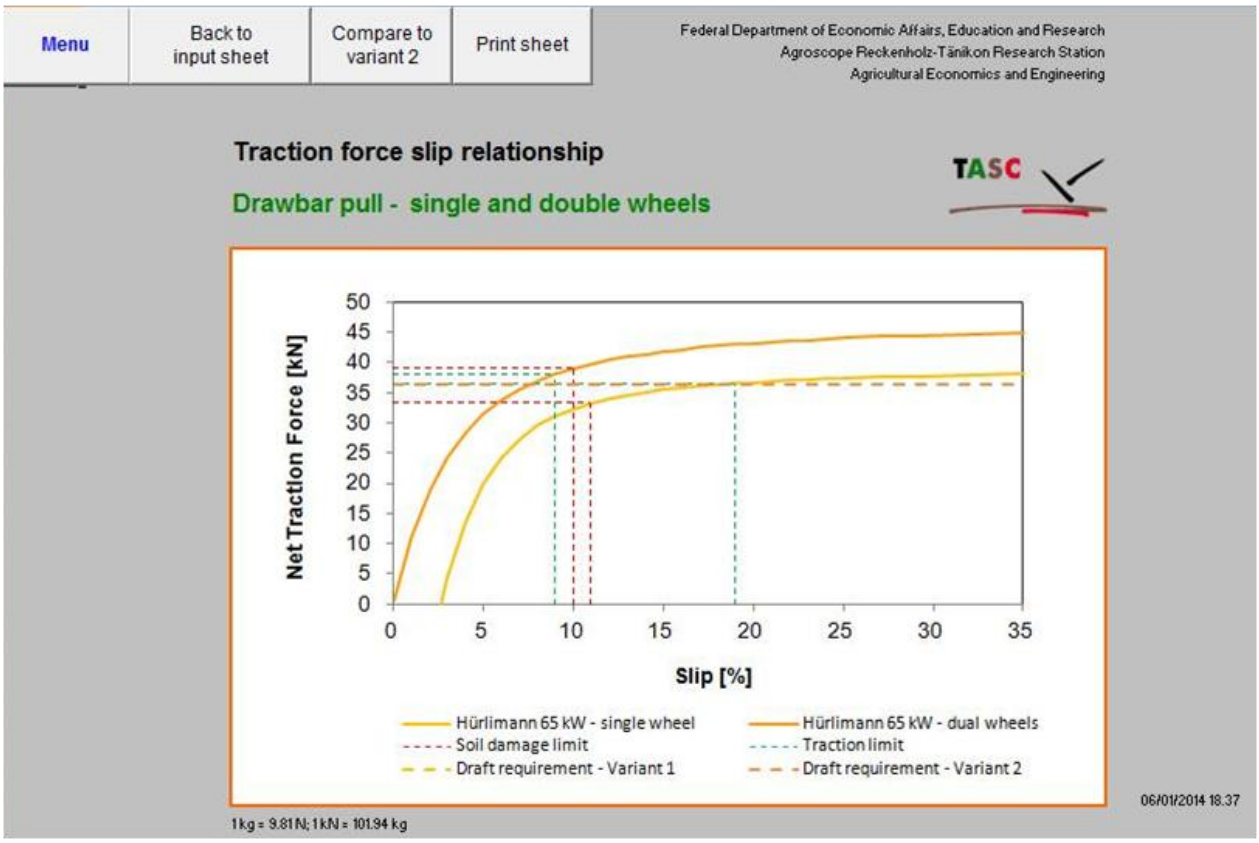

Fig. 125: The traction force as a function of the slip is one of the graphical output of the module Traction and Energy analysis of the TASC V3.0.

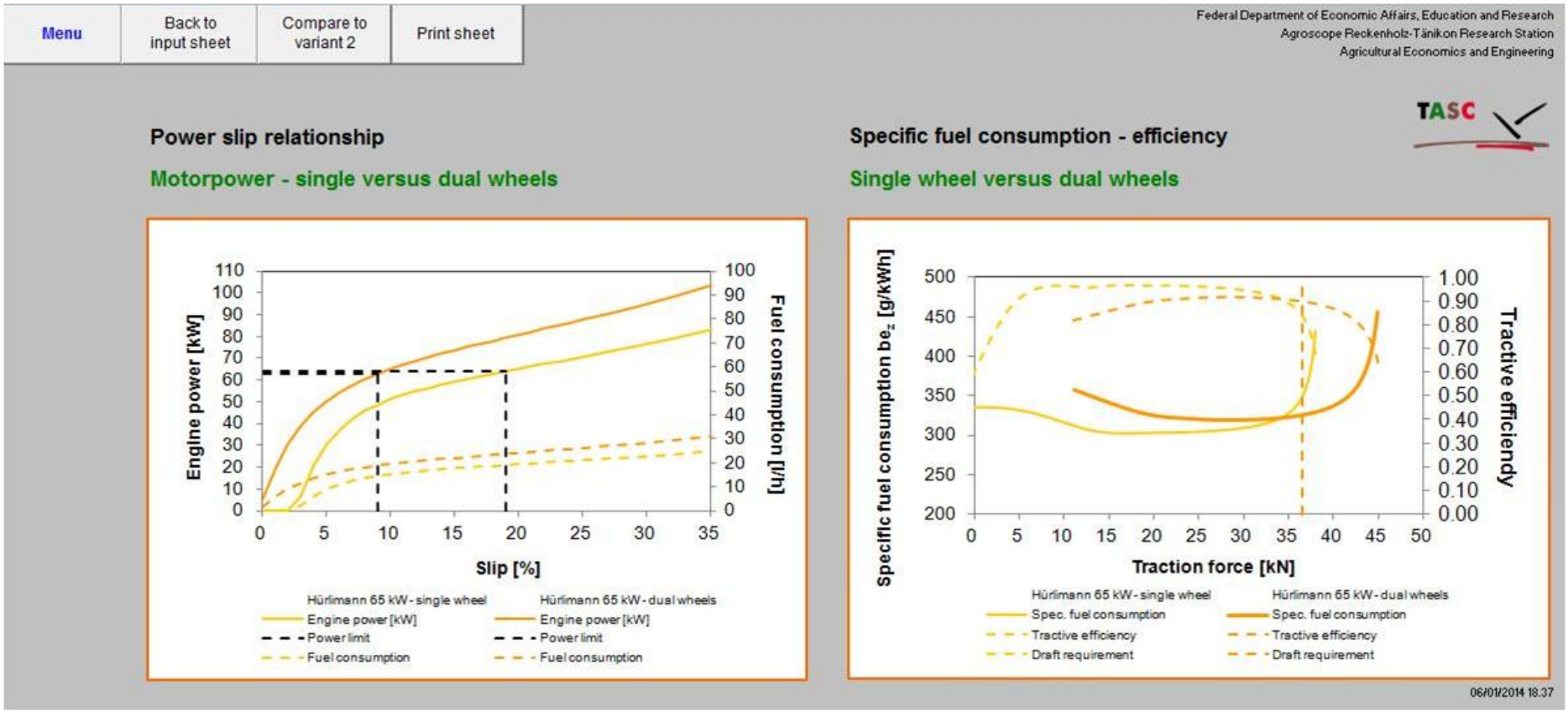

Fig. 126: The engine power and the fuel consumption as a function of the slip together with the specific fuel consumption and the tractive efficiency as a function of the traction force are also among the graphical results of the module Traction and Energy analysis of the TASC V3.0.

Acknowledgements

I wish to acknowledge the Swiss Federal Office for the Environment FOEN and the tyre manufacturer Michelin for the financial support for this study.

I would like to express my gratitude to many people of the Agroscope Reckenholz-Tänikon Research Station ART who have contributed in the accomplishment of this work. In particular, I sincerely thank Dr. Etienne Diserens for his supervision and remarkable collaboration, and besides, his help and encouragement. I'm very grateful to Dr. Thomas Anken for the valuable discussions and comments which contributed to improve this work, as well as for his continuous support. I'm particularly grateful to Mr. Beat Kürsteiner, Mr. Jakob Heusser and Mr. Isidor Schiess, for the precious help they provided for the field tests, and to Mr. Marco Landis for providing data reported in Fig. 75.

I profoundly thank professor Luigi Sartori of the Land, Environment, Agriculture and Forestry Department of the University of Padua for accepting me among his PhD students and for being a good and available supervisor. My thanks go also to professor Lyesse Laloui of the Laboratory of Soil Mechanics of the Polytechnic of Lausanne, for guiding and addressing me in the early approach to this study, and to professor Abdallah Alaoui of the Hydrology Group of the Department of Geography of the University of Bern, for his help in the development of the second part of this work and during the field experiments.

I wish to thank professor Camillo Airò Farrulla and professor Calogero Valore of the Department of Civil, Environmental, Aerospace and Materials Engineering of the University of Palermo, for stimulating my interest in issues dealing with soil mechanics, and Dr. Alessio Ferrari of the Laboratory of Soil Mechanics of the Polytechnic of Lausanne who, besides being a good friend, represented to me a sort of mentore.

I would also like to thank Mr. Patrick Dubey of the Laboratory of Soil Mechanics of the Polytechnic of Lausanne for his help with the laboratory tests.

Warm thanks go to Ms Regula Wolz and to Ms Janet Stoves for kindly proofreading this text.

I finally thank my parents for their fondness and their support, and my wife Paola for helping me in the writing out of some parts of this work and for lovingly putting up with me talking about matters of soil mechanics and traction performance of tractors at home.

5. Bibliography

AESCO, “Matlab/Simulink Module AESCO Soft Soil Tyre Model (AS^{2}TM) User’s Guide”, 2003.

Airey, D.W., Wood, D.M., 1987. An evaluation of direct simple shear tests on clay. Géotechnique, 37, 25-35.

Alakukku, L., Ahokas, J., Ristolainen, A., 2002. Response of clay soil macroporosity to stress caused by tracked tractors. Advances in GeoEcology 35, 319-330. Marcello Pagliai and Robert Jones (Eds).

Alaoui, A., Germann, P., Jarvis N., Acutis, M., 2003. Dual-porosity and kinematic wave approaches to assess the degree of preferential flow in an unsaturated soil. Hydrol. Sci. J. 48 (3), 455-472.

Alaoui, A., Helbling, A., 2006. Evaluation of soil compaction using hydrodynamic water content variation: Comparison between compacted and non-compacted soil. Geoderma 134, 97-108.

Alaoui, A., Goetz, B., 2008. Dye tracer and infiltration experiments to investigate macropore flow. Geoderma 144, 279-286.

Alaoui, A., Lipiec, J., Gerke, H.H., 2011. A review of the changes in the soil pore system due to soil deformation: A hydrodynamic perspective. Soil & Tillage Research, 115-116, 1-15, 2011.

Arvidsson, J., Ristic, S., 1996. Soil stress and compaction effects for four tractor tyres. J. Terramech. 33 (5), 223-232.

ASAE D497.7, 2011. Agricultural Machinery Management Data, ASABE Standard (American Society of Agricultural and Biological Engineers).

Asaf, Z., Rubinstein, D., Shmulevich, I., 2005. Determination of discrete element model parameters required for soil tillage. In Proc. 15th International Conference of the ISTVS, International Society for Terrain-Vehicle Systems.

Asaf, Z., Rubinstein, D., Shmulevich, I., 2006. Evaluation of link-track performances using DEM. J. Terramech. 43 (2), 141-161.

ASTM Standard ASTM D6528 - 07, "Standard Test Method for Consolidated Undrained Direct Simple Shear Testing of Cohesive Soils" ASTM Geotechnical Engineering Standards, 2007.

Aubel, T., 1994. The interaction between the rolling tyre and the soft soil. In Proc. 6th European Conf. of the ISTVS, International Society for Terrain-Vehicle Systems, pp. 169-188.

Barden, L., 1972. The influence of structure on deformation and failure in clay soil. Geotechnique, 22, 159-163.

Bastgen, H.M., Diserens, E., 2009. q value for calculation of pressure propagation in arable soils taking topsoil stability into account. Soil Till. Res. 102 (1), 138-143.

Battiato, A., Diserens, E., 2011. Predicting topsoil damage from slip of tractor tires. Bodenkundliche Gesellschaft der Schweiz - Bulletin 32, pp. 21-26.

Battiato, A., Diserens, E., and Sartori, L., 2011. Predicting topsoil damage from slip of tractor tyres: analysis of the soil cutting effect from the tread of traction tyres. 69th International Conference on Agricultural Engineering – LAND.TECHNIK AgEng 2011, Hannover, Germany, VDI-Report pp. 445-450.

Battiato, A., Diserens, E., 2013. Influence of tyre inflation pressure and wheel load on the traction performance of a 65 kW MFWD tractor on a cohesive soil. Journal of Agricultural Science 5 (8), 197-215.

Battiato, A., Diserens, E., Laloui, L., Sartori, L., 2013. A mechanistic approach to topsoil damage due to slip of tractor tyres. Journal of Agricultural Science and Applications (JASA) 2 (3), 160-168.

Battiato, A., Diserens, E., Alaoui, A., Sartori, L., 2013. Response of a clay loam agricultural soil to mechanical stress from tractor traffic with and without slip. 71st International Conference on Agricultural Engineering – LAND.TECHNIK AgEng 2013, Hannover, Germany, VDI-Report pp. 205-211.

Bekker, M.G., 1956. Theory of Land Locomotion. Ann Arbor, Mich., University of Michigan Press.

Bekker, M.G., 1960. Off-the-Road Locomotion. Ann Arbor, Mich., University of Michigan Press.

Bekker, M.G., 1969. Introduction to Terrain-Vehicle Systems. Ann Arbor, Mich., University of Michigan Press.

Berisso, F.E., Schjønning, P., Lamande´, M., Weisskopf, P., Stettler, M., Keller, T., 2013. Effects of the stress field induced by a running tyre on the soil pore system. Soil & Tillage Research, 131, 36-46.

Berli, M., Kirby, J.M., Springman, S.M., Schulin, R., 2003. Modelling compaction of agricultural subsoils by tracked heavy construction machinery under various moisture conditions in Switzerland. Soil Till. Res. 73, 57-66.

Bjerrum, L., Landva A., 1966: Direct simple shear tests on a Norwegian quick clay. Geotechnique, 16. (1), 1-20.

Blackwell, P.S., Ringrose-Voase, A.J., Jaywardane, N.S., Olsson, K.A., McKenzie, D.C., Mason, W.K., 1990. The use of air-filled porosity and intrinsic permeability to air to characterise structure of macropore space and saturated hydraulic conductivity of clay soils. J. Soil Sci. 41, 215-228.

Brixius, W.W., 1987. Traction prediction equations for bias ply tires. ASAE paper No. 87-1622.

Burt, E.C., Bailey, A.C., Patterson, R.M., Taylor, J.H., 1979. Combined effects of dynamic load and travel reduction on tire performance. Trans. ASAE 22 (1), 40-45.

Burt, E.C., Bailey, A.C., 1982. Load and inflation pressure effects on tires. Trans. ASAE 25 (4), 881-884.

Burt, E.C., Lyne, P.W.L., Meiring, P., Keen, J.F., 1983. Ballast and inflation effects on tire efficiency. Trans. ASAE 26, 1352-1354.

Charles, S.M., 1984. Effects of ballast and inflation pressure on tractor tire performance. Agricultural engineering 65 (2), 11-13.

Cundall, P.A., 1971. A computer model for simulation progressive large-scale movement in blocky rock system. In Proc. Symp. ISRM, No. 8. International Society for Rock Mechanics.

Cundall, P.A., Strack, O.D.L., 1979. A discrete numerical model for granular assemblies. J. Geotechnique 29 (1), 47-65.

Davies, D.B., Finney, J.B., Richardson, S.J., 1973. Relative effects of tractor weight and wheel-slip in causing soil compaction. J. Soil Sci. 24 (3), 399-409.

Dickson, J.W., Smart, P., 1976. Some interaction between stress and microstructure of kaolin. In: Modification of Soil Structure. W.W. Emerson, R.D. Bond, A.R. Dexter. Wiley, Brisbane.

Dirksen, Ch., 1999. Soil Physics Measurements. Reiskirchen: Catena Verl. GeoEcology, ISBN 3-923881-43-3.

Diserens, E., 2002. Ermittlung der Reifen-Kontaktfläche im Feld mittels Rechenmodell. FAT-Berichte Nr. 582. 12pp.

Diserens, E., Spiess, E., Steinmann, G., 2003. TASC: a new practical computer tool to prevent soil compaction damage in arable farming. In: Proceedings of the International Conference on Geo-Environmental Engineering, Singapore, pp. 85-92.

Diserens, E., Steinmann, G., 2003. In-situ determination of the fracture point of an agricultural soil using the plate penetration test, comparison with the oedometer method and validation. In: Proceedings of the International Conference on Geo-Environmental Engineering, Singapore, pp. 93-106.

Diserens, E., Défossez, P., Duboisset, A., Alaoui, A., 2011. Prediction of the contact area of agricultural traction tyres on firm soil. Biosyst. Eng. 110, 73-82.

Diserens, E., 2011. Calculating the contact area of trailer tyres in the field. Soil Till. Res., 103 (2), 302-309.

Diserens, E., Battiato, A., 2012. Traction force in arable farming: agronomic and environmental aspects after field data acquisition and modelling. International Conference of Agricultural Engineering, CIGR-AgEng, Valencia, Spain.

Diserens, E., Battiato, A., 2013. TASC V3.0 - Prognose Bodengefährdung und Treibstoffverbrauch : Eine PC-Anwendung zur Beurteilung der Bodenbeanspruchung im Ober- und Unterboden in der Land- und Forstwirtschaft sowie zur Schätzung des Energie- und Treibstoffbedarfs im Ackerbau. ART-Bericht. 766, 2013, 1-8.

Du Plessis, H.L.M., and Venter, G., 1993. Soft surface lateral forces and force modelling for a tractor tyre. J. Terramech. 30 (2), 101-110.

Fan, J.C., Wu, M.F., 2001. Effects of soil strength, texture, slope steepness and rainfall intensity on interrill erosion of some soils in Taiwan. in: D.E. Stott, R.H. Mohtar, and G.C. Steinhardt (eds), Sustaining the Global Farm, Selected papers from the 10th International Soil Conservation Organization Meeting, pp. 588-593.

Fervers, C.W., 1997. Effects of traction and slip, Investigation with FEM. In Proc. 7th European Conf. of the ISTVS, International Society for Terrain-Vehicle Systems, pp. 117-124.

Fervers, C.W., 2004. Improved FEM simulation model for tire-soil interaction. J. Terramech. 41 (2-3), 87-100.

Flury, M., Flühler, H., 1995. Tracer characteristics of Brilliant Blue FCF. Soil Sci. Soc. Am. J., 59, 22-27.

Freitag, D.R., 1965. A dimensional analysis of performance of pneumatic tyres in soft soils. WES Technical report No. 3-688.

Fujii, H,F., Oida, A., Nakashima, H., Miyasaka, J., Momozu, M., 2003. Analysis of interaction between lunar terrain and treaded wheel by distinct element method. In Proc. 14th International Conf. of the ISTVS, International Society for Terrain-Vehicle Systems.

Fujimoto, Y., 1977. Performance of elastic wheels on yielding cohesive soils. J. Terramech. 14 (4), 191-210.

Gao, Y., Wong, J.Y., 1994. The development and validation of a computer-aided method for design evaluation of tracked vehicles with rigid links. Proceedings Institution of Mechanical Engineers, part D, Journal of Automobile Engineering, vol. 208. no. D3.

Garciano, L.O., Upadhyaya, S.K., Jones, R.A., 2010. Measurement of soil parameters useful in predicting tractive ability of off-road vehicles using an instrumented portable device. J. Terramech. 47 (5), 295-305.

Gee-Clough. D., 1976. The Bekker theory of rolling resistance amended to take account of skid and deep sinkage. J. Terramech. 13 (2), 87-105.

Gee-Clough, D., McAllister, M., Evernden, D.W., 1977. Tractive performance of tractor drive tyres II. A comparison of radial and cross-ply carcass construction. J. agric. Engng Res. 22, 385-395.

Gee-Clough. D., 1978. A comparison of the mobility number and Bekker approaches to the traction mechanics and recent advances in both methods at the N.I.A.E. Proceedings of the 6th International ISTVS conference, Vienna, Austria, pp. 735-755.

Gee-Clough, D., 1980. Selection of tyre sizes for agricultural vehicles. Journal of agricultural engineering research 25 (3), 261-278.

Gee-Clough, D., Pearson, G., McAllister, M., 1982. Ballasting wheeled tractors to achieve maximum power output in frictional-cohesive soils. J. agric. Engng Res. 27, 1-19.

Golob, T.B., 1981. Effects of soil strength parameters on terrain classification. Proceedings of the 7th International ISTVS Conference, Calgary, Canada, pp. 901-927.

Grahn, M., 1991. Prediction of sinkage and rolling resistance for off-the-road vehicles considering penetration velocity. J. Terramech. 28 (4), 339-347.

Grahn, M., 1996. Einfluß der Fahrgeschwindigkeit auf die Einsinkung und den Rollwiderstand von Radfahrzeugen auf Geländeböden. Ph.D. Thesis. Universität der Bundeswehr Hamburg, Germany.

Grisso, R.D., Al-Hamed, S.A., Taylor, R.K., Zoz, F.M., 1992. Demonstrating tractor performance trends using lotus templates. Applied Engineering in Agriculture 8 (6), 733-738.

Gysi, M., Maeder, V., Weisskopf, P., 2001. Pressure distribution underneath tires of agricultural vehicles. Trans. ASAE 44 (6), 1385-1389.

Harris, H.D., Bakker, D. M., 1994. A servo-controlled simple shear box. Soil Till. Res., 31, 23-35.

Head, K.H., 1994. Manual of soil laboratory testing. John Wiley and Sons.

Holden, J., Gell, K.F., 2009. Morphological characterization of solute flow in a brown earth grassland soil with cranefly larvae burrows (leatherjackets). Geoderma 152, 181-186.

Holm, C., Hefer, G.J., Hinze, D., 1987. The influence of shape and size of a penetration body on the pressure-sinkage relationship. Proceedings of the 9th International ISTVS Conference, Barcelona, Spain, pp. 28-36.

Horn, R., 2003. Stress-strain effects in structured unsaturated soils on coupled mechanical and hydraulic processes. Geoderma 116, 77-88.

Hovland, H.J., 1973. Mechanics of wheel-soil interaction. Final report for research phase: trafficability. Space science laboratory, series 14, issue 23. University of California, Berkeley.

ISTVS, 1977. International Society For Terrain-Vehicle Systems Standards. J. Terramech. 14 (3), 153-182.

Janosi, Z., Hanamoto, B., 1961. The analytical determination of drawbar pull as a function of slip for tracked vehicles in deformable soils. In: Proceedings of the 1st International Conference on the Mechanics of Soil-Vehicle Systems, Edizioni Minerva Tecnica, Torino, Italy, pp. 707-736.

Jarvis, N.J., 1994. The MACRO model Version 3.1 – Technical description and sample simulations. Reports and Dissertations no. 19, Department of Soil Science, Swedish University of Agricultural Sciences, Uppsala, Sweden, 51 pages.

Jenane, C., Bashford, L.L., Monroe, G., 1996. Reduction of fuel consumption through improved tractive performance. J. agric. Engng Res. 64, 131-138.

Karafiath, L.L., Nowatzki, E.A., 1978. Soil mechanics for off-road vehicles engineering. Trans Tech Publications (Series on Rock and Soil Mechanics Vol. 2, No. 5), Clausthal, Germany.

Keira, H.M.S., 1979. Effects of vibration on the shearing characteristics of soil engaging machinery. Thesis, Carleton University, Ottawa, ON, Canada.

Keller, T., 2005. A model for the prediction of the contact area and the distribution of vertical stress below agricultural tyres from readily available tyre parameters. Biosyst. Eng. 92, 85-96.

Keller, T., Défossez, P., Weisskopf, P., Arvidsson, J., Richard, G., 2007. SoilFlex: A model for prediction of soil stresses and soil compaction due to agricultural field traffic including a synthesis of analytical approaches. Soil Till. Res. 93 (2), 391-411.

Kim, H., Anderson, S.H., Motavalli, P.P., Gantzer, C.J., 2010. Compaction effects on soil macropore geometry and related parameters for an arable field. Geoderma 160, 244-251.

Kirby, J.M., Blunden, B.G., 1991. Interaction of soil deformations, structure and permeability. Aust. J. Soil Res. 29, 891-904.

Kirby, J.M., 1991. The influence of soil deformations on the permeability to air. J. Soil Science. 42, 227-235.

Knight, S.J., Rula, A.A., 1961. Measurement and estimation of the trafficability of fine-grained soils. Proceedings of the 1st International ISTVS Conference, Torino-Saint Vincent, Italy, pp. 371-384.

Lee, D.R., Kim, K.U., 1997. Effect of inflation pressure on tractive performance of bias-ply tires. J. Terramech. 34 (3), 187-208.

Li, R., Li, Y., Zhuang, J., 1990. Study on passing probability of automobile combination on soft ground. Proceedings of the 10th International ISTVS Conference, Kobe, Japan, pp. 349-358.

Liu, C.H., Wong, J.Y., 1996. Numerical simulations of tire-soil interaction based on critical state soil mechanics. J. Terramech. 33 (5), 209-221.

Liu, C.H., Wong, J.Y., Mang, H.A., 2000. Large strain finite element analysis of sand: model, algorithm and application to numerical simulation of tire-sand interaction. Computers and Structures, 74 (3), 253-265.

Lines, J.A., Murphy, K., 1991. The stiffness of agricultural tractor tyres. J. Terramech. 28 (1), 49-64.

Lyasko, M.I., 2010. How to calculate the effect of soil conditions on tractive performance. J. Terramech. 47 (6), 423-445.

Lyne, P.W.L., Burt, E.C., Meiring, P., 1984. Effect of tire and engine parameters on efficiency. Trans. ASAE 27 (1), 5-7.

Maclaurin, E.B., 1981. The effect of tread pattern on the field performance of tyres. Proceedings of the 7th International ISTVS Conference, Calgary, Canada, pp. 699-735.

McKyes, E., Yong, R.N., 1971. Three techniques for fabric viewing as applied to shear distortion of a clay. Clay and Clay Minerals 19, 289-293.

McKyes, E., Ali, O.S., 1977. The cutting of soil by narrow blades. J. Terramech. 14 (2), 43-58.

McKyes, E., 1985. Soil Cutting and Tillage. Developments in Agricultural Engineering 7. Elsevier, Amsterdam, The Netherlands.

Mitchell, J.K., 1976. Foundamentals of Soil Behaviour. Wiley, New York.

Morgenstern, N.R., Tchalenko, J.S., 1967. Microscopic structures in kaolin subjected to direct shear. Geotechnique 17, 309-328.

Muro, T., 1993. Tractive performance of a driven rigid wheel on soft ground based on the analysis of soil-wheel interaction. J. Terramech. 30 (5), 351-369.

Muro, T., 1997. Comparison of the traction performance of a two-axle four wheel drive (4WD), rear wheel drive (RWD), and front wheel drive (FWD) vehicle on loose sandy slopped terrain. J. Terramech. 34 (1), 35-55.

Nash, J.E., Sutcliffe, J.V., 1970. River flow forecasting through conceptual models, Part I – A discussion of principles, J. Hydrol., 10, 282-290.

Nearing, M.A., West, L.T., 1988. Soil strength indices as indicators of consolidation. American Society of Agricultural Engineers 31, 471-476.

Oida, A., Schwanghart, H., Ohakubo, S., 1999. Effect of tire lug cross-section on tire performance simulation by distinct element method. In Proc. 13th International Conf. of the ISTVS, International Society for Terrain-Vehicle Systems, pp. 345-352.

Onafeko, O., Reece, A.R., 1967. Soil stresses and deformations beneath rigid wheels. J. Terramech. 4 (1), 59-80.

Osetinsky, A., Shmulevich, I., 2004. Traction performance simulation of a pushed/pulled driven wheel. Trans. ASAE 47 (4), 981-994.

O'Sullivan, M.F., Henshall, J.K., Dickson, J.W., 1999. A simplified method for estimating soil compaction. Soil Till. Res. 49, 325-335.

O'Sullivan, M.F., Robertson, E.A.G., Henshall, J.K., 1999. Shear effects on gas transport in soil. Soil Till. Res. 50 (1), 73-83.

Pagliai, M., Marsili, A., Servadio, P., Vignozzi, N., Pellegrini, S., 2003. Changes in some properties of a clay soil in Central Italy following the passage of rubber tracked and wheeled tractors of medium power. Soil Till. Res. 73, 119-129.

Paul, T., 1984. Performance prediction of pneumatic tyres on sand. Proceedings of the 8th International ISTVS Conference, Cambridge, UK, pp. 87-96.

Perumpral, J.V., Liljedal, J.B., Perloff, W.H., 1971. A numerical method for predicting the stress distribution and soil deformation under a tractor wheel. J. Terramech. 8 (1), 9-22.

Pope, R.G., 1969. The effect of sinkage rate on pressure sinkage relationships and rolling resistance in real and artificial clays. J. Terramech. 6 (4), 31-38.

Pope, R.G., 1971. The effect of wheel speed on rolling resistance. J. Terramech. 8 (1), 51-58.

Raghavan, G.S.V., McKyes, E., Chassé, M., 1976. Soil compaction patterns caused by off-road vehicles in eastern Canadian agricultural soils. J. Terramech. 13 (2), 107-115.

Raghavan, G.S.V., McKyes, E., 1977. Laboratory study to determine the effect of slip-generated shear on soil compaction. Can. Agric. Eng. 19 (1), 40-42.

Raghavan, G.S.V., McKyes, E., Beaulieu, B., 1977. Prediction of clay soil compaction. J. Terramech. 14 (1), 31-38.

Raghavan, G.S.V., McKyes, E., Beaulieu, B., 1978. Clay soil compaction due to wheel slip. Trans. ASAE 21 (4), 646-649.

Reece, A.R., 1965. The fundamental equation of earthmoving mechanics. Symposium of Earthmoving Machinery, Institute of Mechanical Engineers, 179, Part 3F, London.

Reece, A.R., 1965. Principles of Soil-Vehicle Mechanics. Proceedings of the Institution of Mechanical Engineers, vol. 180, part 2A.

Reece, A.R., Peca, J.O., 1981. An assessment of the value of the cone penetrometer in mobility prediction. Proceedings of the 7th International ISTVS Conference, Calgary, Canada. pp. 1-33.

Richards, L.A., 1931. Capillary conduction of liquids in porous mediums. Physics 1, pp. 318-333.

Roth, K., Schulin, R., Flühler, H., Attinger, W., 1990. Calibration of time domain reflectrometry for water content measurement using a composite dielectric approach. Water Resour. Res. 26, 2267-2274.

Rowland, D., 1972. Tracked vehicle ground pressure and its effect on soft ground performance. Proceedings of the 4th International ISTVS Conference, Stockholm, Sweden.

Rowland, D., 1975. A review of vehicle design for soft ground operation. Proceedings of the 5th International ISTVS Conference, Detroit, U.S.A.

Rubinstein, D., Upadhyaya, S.K., Sima, M., 1994. Determination of in-situ engineering properties of soil using a response surface methodology. J. Terramech. 31 (2), 67-92.

Sahay, C.S., Tewari, V.K., 2004. Computer simulation of tractor single-point drawbar performance. Biosyst. Eng. 88 (4), 419-428.

Sargana, M.A., Gee-Clough, D., Gupta, C.P., 1985. A dynamic equation for the pressure-sinkage relationship in saturated clay soils. J. Terramech. 22 (2), 111-120.

Schmid, I.C., 1995. Interaction of vehicle and terrain results from 10 years research at IKK. J. Terramech. 32 (1), 3-26.

Serrano, J. M., Peça, J. O., Silva, J. R., & Márquez, L. (2009). The effect of liquid ballast and tyre inflation pressure on tractor performance. Biosyst. Eng. 102, 51-62.

Servadio, P., Marsili, A., Vignozzi, N., Pellegrini, S., Pagliai, M., 2005. Effects on some soil qualities in central Italy following the passage of four wheel drive tractor fitted with single and dual tires. Soil Till. Res. 84 (1), 87-100.

Seta, E., Kamagawa, T., Nakajima, Y., 2003. Prediction of snow/tire interaction using explicit FEM and FVM. Tire science and technology, TSTCA, 31 (3), 173-188.

Scott, R.F., 1963. Principles of soil mechanics. Addison-Wesley: Reading, Mass.

Shell, L.R., Zoz, F.M., Turner, R.L., 1997. Field performance of rubber belt and MFWD tractors in Texas soils. In: Belt and Tire Traction in Agricultural Vehicles (SP-1291), 65-73. SAE technical paper series 972729. SAE.

Shigeta, Y., Aruga, K., 2005. Application of 3D distinct element method to track shoe model. Proceedings of the 15th International ISTVS Conference, Hayama, Japan.

Shmulevich, I., 1975. Laboratory criteria for selecting alternative vehicle tires. Thesis, Technion Israel Institute of Technology, Haifa, Israel.

Shmulevich, I., Osetinsky, A., 2003. Traction performance of a pushed/pulled drive wheel. J. Terramech. 40, 35-50.

Shoop, A.S., 1993. Thawing soil strength measurements for predicting vehicle performance. J. Terramech. 30 (6), 405-418.

Shoop, A.S., 2001. Finite element modeling of tire terrain interaction. ERDC/CRREL TR−01−16. Vicksburg, Miss.: U.S. Army Corp of Engineers, Engineer Research and Development Center.

Šmerda, T., Čupera, J., 2010. Tire inflation and its influence on drawbar characteristics and performance – Energetic indicators of a tractor set. J. Terramech. 47, 395-400.

Söhne, W., 1958. Fundamentals of pressure distribution and soil compaction under tractor tires. Agric. Eng. 39, 276-290.

Thangavadivelu, S., Taylor, R., Clark, S., Slocombe, J., 1994. Measuring soil properties to predict tractive performance of an agricultural drive tire. J. Terramech. 31 (4), 215-225.

Turnage, G.W., 1972a. Tire selection and performance prediction for off-road wheeled-vehicle operations. Proceedings of the 4th International ISTVS Conference, Stockholm-Kiruna, Sweden, pp. 62-82.

Turnage, G.W., 1972b. Using dimensionless prediction terms to describe off-road wheel vehicle performance. ASAE Paper No. 72-634.

Turnage, G.W., 1978. A synopsis of tire design and operational considerations aimed at increasing insoil tire drawbar performance. Proceedings of the 6th International ISTVS Conference, Vienna, Austria, pp. 757-810.

Turnage, G.W., 1984. Prediction of in-sand tyre and wheeled vehicle drawbar performance. Proceedings of the 8th International ISTVS Conference, Cambridge, UK, pp. 121-150.

Turner, R.J., 1993. Single, dual and triple tires and rubber belt tracks in prairie soil conditions. ASAE/CSAE meeting presentation, ASAE paper No. 93-1516. St. Joseph, Mich.: ASAE.

Turner, R.J., 1993. A simple system for determining tractive performance in the field. ASAE/CSAE meeting presentation, ASAE paper No. 93-1574. St. Joseph, Mich.: ASAE.

Turner, R.J., Shell, L.R., Zoz, F.M., 1997. Field performance of rubber belt and MFWD tractors in southern Alberta soils. In: Belt and Tire Traction in Agricultural Vehicles (SP-1291), 75-85. SAE technical paper series 972730. SAE.

Upadhyaya, S.K., Wulfsohn, D., Jubbal, G., 1989. Traction prediction equations for radial ply tyres. J. Terramech. 26 (2), 149-175.

Upadhyaya, S.K., Wulfsohn, D., 1990. Traction prediction for radial ply tyres. Proceedings of the 10th International ISTVS Conference, Kobe, Japan, pp. 447-451.

Upadhyaya, S.K., Wulfsohn, D., Mehlschau, J., 1993. J. Terramech. 30 (1), 1-20.

Upadhyaya, S.K., Wulfsohn, D., 1993. Traction prediction using soil parameters obtained with an instrumented analog device. J. Terramech. 30 (2), 85-100.

Upadhyaya, S.K., and A. K. Rosa. 1997. Prediction of traction and soil compacting. In Proc. 3rd International Conf. on Soil Dynamics, 19-58. Tiberias, Israel.

Upadhyaya, S.K., Sime, M., Raghuwanshi, N., Adler, B., 1997. Semi-empirical traction prediction equations based on relevant soil parameters. J. Terramech. 34 (3), 141-154.

Van den Akker, J.J.H., 2004. SOCOMO: a soil compaction model to calculate soil stresses and the subsoil carrying capacity. Soil Till. Res. 79, 113-127.

Vanden Berg, G.E., Gill, W.R., 1962. Pressure distribution between a smooth tire and the soil. Trans. ASAE 5, 126-129.

Watson, D.A., Laflen, J.M., 1986. Soil strength, slope and rainfall effects of interrill erosion. Transactions of the ASAE, 29, 98-102.

Wiley, J.C., Turner, R.J., 2008. Power Hop Instability of Tractors. ASABE (American Society of Agricultural and Biological Engineers) Distinguished Lecture Series No. 32.

Wills, B.M.D., 1963. The measurement of soil shear strength and deformation moduli and a comparison of the actual and theoretical performance of a family of rigid tracks. J. Agric. Eng. Res. 8 (2), 115-131.

Wismer, R.D., Luth, H.J., 1973. Off-road traction prediction for wheeled vehicles. J. Terramech, 10 (2), 49-61.

Wong, J.Y., 1967. Behaviour of soil beneath rigid wheels. J. Agric. Eng. Res. 12 (4), 257-269.

Wong, J.Y., Reece, A.R., 1967. Prediction of rigid wheel performance based on the analysis of soil-wheel stresses, part I. J. Terramech. 4 (1), 81-98.

Wong, J.Y., Reece, A.R., 1967. Prediction of rigid wheel performance based on the analysis of soil-wheel stresses, part II. J. Terramech. 4 (2), 7-25.

Wong, J.Y., 1977. Discussion on prediction of wheel-soil interaction and performance using the finite element method. J. Terramech. 14 (4), 249-250.

Wong, J.Y., Garber, M., Radforth, J.R., Dowell, J.T., 1979. Characterization of the mechanical properties of muskeg with special reference to vehicle mobility. J. Terramech. 16 (4), 163-180.

Wong, J.Y., 1980. Data processing methodology in the characterization of the mechanical properties of terrain. J. Terramech. 17 (1), 13-41.

Wong, J.Y., Radforth, J.R., Preston-Thomas, J., 1982. Some further studies of the mechanical properties of muskeg in relation to vehicle mobility. J. Terramech. 19 (2), 107-127.

Wong, J.Y., Preston-Thomas, J., 1983. On the characterization of the shear stress-displacement relationship of terrain. J. Terramech. 19 (4), 225-234.

Wong, J.Y., Preston-Thomas, J., 1983. On the characterization of the pressure-sinkage relationship of snow covers containing an ice layer. J. Terramech. 20 (1), 1-12.

Wong, J.Y., Garber, M., Preston-Thomas, J., 1984. Theoretical prediction and experimental substantiation of the ground pressure distribution and tractive performance of tracked vehicles. Proceedings Institution of Mechanical Engineers, part D, Transport Engineering, vol. 198. no. D15.

Wong, J.Y., 1984. Wheel-soil interaction. J. Terramech. 21 (2), 117-131.

Wong, J.Y., Bekker, M.G., 1985. Terrain Vehicle Systems Analysis. Monograph, Department of mechanical and aerospace Engineering, Carleton University, Ottawa, ON, Canada.

Wong, J.Y., Preston-Thomas, J., 1986. Parametric analysis of tracked vehicle performance using an advanced computer simulation model. Proceedings Institution of Mechanical Engineers, part D, Transport Engineering, vol. 200. no. D2.

Wong, J.Y., Preston-Thomas, J., 1988. Investigation into the effects of suspension characteristics and design parameters on the performance of tracked vehicles using an advanced computer simulation model. Proceedings Institution of Mechanical Engineers, part D, Transport Engineering, vol. 202. no. D3.

Wong, J.Y., 1989. Terramechanics and off-road vehicles. The Netherlands: Elsevier Science, Amsterdam.

Wong, J.Y., 1992. Optimization of the tractive performance of articulated tracked vehicles using an advanced computer simulation model. Proceedings Institution of Mechanical Engineers, part D, Journal of Automobile Engineering, vol. 206. no. D1.

Wong, J.Y., Irwin, G.J., 1992. Measurement and characterization of the of the pressure-sinkage data for snow obtained using a rammsonde. J. Terramech. 29 (2), 265-280.

Wong, J.Y., 1994. On the role of mean maximum pressure as an indicator of cross-country mobility for tracked vehicles. J. Terramech. 31 (3), 197-213.

Wong, J.Y., 1995. Application of the computer simulation model NTVPM-86 to the development of a new version of the Infantry Fighting vehicle ASCOD. J. Terramech. 32 (1), 53-61.

Wong, J.Y., 1998. Optimization of design parameters of rigid-link track systems using an advanced computer-aided method. Proceedings Institution of Mechanical Engineers, part D, Journal of Automobile Engineering, vol. 212. no. D3.

Wong, J.Y., Huang, W., 2005. Evaluation of the effects of design features on tracked vehicle mobility using an advanced computer-simulation model. International Journal of Heavy Vehicle Systems, 12 (4), 344-365.

Wong, J.Y., Huang, W., 2006. An investigation into the effects of initial tracked tension on soft ground mobility of tracked vehicles using an advanced computer simulation model. Proceedings Institution of Mechanical Engineers, part D, Journal of Automobile Engineering, vol. 220 (6), 695-711.

Wong, J.Y., Huang, W., 2008. Approaches to improving the mobility of military tracked vehicles on soft terrain. International Journal of Heavy Vehicle Systems, 15 (2), 127-151.

Wong, J.Y., 2008. Theory of Ground Vehicles. John Wiley and Sons, Hoboken, New Jersey.

Wong, J.Y., 2010. Terramechanics and off-road vehicle engineering. The Netherlands: Elsevier Science, Amsterdam.

Wood, R.K., Mangione, D.A., 1992. Tractive benefits of properly adjusted inflation pressure: Farmer experiences. ASAE paper No. 92-1583. St. Joseph, Mich.: ASAE.

Yong, R.N., Fattah, E.A., 1976. Prediction of wheel-soil interaction and performance using the finite element method. J. Terramech. 13 (4), 227-240.

Yong, R.N., Fattah, E.A., Skiadas, N., 1984. Vehicle traction mechanics. The Netherlands: Elsevier Science, Amsterdam.

Zhang, T., Lee, J.H., Liu, Q., 2005. Finite element simulation of tire-snow interaction under combined longitudinal and lateral slip condition. Proceedings of the 15th International ISTVS Conference, Hayama, Japan.

Zombori, J., 1967. Drawbar pull tests of various traction devices on sandy soils. J. Terramech. 4 (1), 9-17.

Zoz, F.M., 1987. Predicting tractor field performance (updated). ASAE paper No. 87-1623. St. Joseph, Mich.: ASAE.

Zoz, F.M., Turner, R.J., Shell, L.R., 2002. Power delivery efficiency: a valid measure of belt and tire tractor performance. Trans. ASAE 45 (3), 509-518.

Zoz, F.M., Grisso, R.D., 2003. Traction and tractor performance. ASAE distinguished lecture series (Tractor design No. 27), ASAE publication No. 913C0403. St. Joseph, Mich.: ASAE.

6. Appendices

6.1 Appendix 1

Integral (19):

$$j = \int_0^t V_j dt \tag{19}$$

where (see Fig. 20):

$$V_j = V_{wj} - V_{\alpha j} = wr\cos\alpha_{\omega j} - Va\cos\alpha$$

The integral can be rewritten as:

$$-\int_{\alpha_{V\omega o}}^{\alpha_{V\omega}} \left(\omega r\cos\alpha_{\omega j} - V_a\cos\alpha\right) d\frac{\left(\alpha_{V\omega}\right)}{\omega} =$$

$$\int_{\alpha_{V\omega}}^{\alpha_{V\omega o}} \left(r\cos\alpha_{\omega j} - \frac{V_a}{\omega}\cos\alpha\right) d\alpha_{V\omega} \tag{1.1}$$

being:

$$\omega = \frac{d\alpha_{V\omega}}{dt}$$

and:

$$dt = \frac{d\alpha_{V\omega}}{\omega}$$

Equation (1.1) is now expressed as a function of *x* (see Fig. 19).

The radius vector *r* can be written as follows:

$$r = r(x) = \sqrt{(x - e_0)^2 + \left(\sqrt{R^2 - {e_0}^2} - ax^2\right)^2} \tag{1.2}$$

while:

$$\cos\alpha_{\omega j} = \cos\alpha_{\omega j}(x) = \frac{1}{\sqrt{1 + \left(\tan\alpha_{\omega j}(x)\right)^2}} \tag{1.3}$$

being:

$$\alpha_{\omega j} = \alpha_{V\omega} - \alpha$$

Using the subtraction formulas for tangent, one gets:

$$\tan\alpha_{\omega j} = \frac{\dfrac{(x - e_0)}{\sqrt{R^2 - {e_0}^2} - ax^2} - 2ax}{1 + \dfrac{2ax(x - e_0)}{\sqrt{R^2 - {e_0}^2} - ax^2}} \tag{1.4}$$

where:

$$\tan\alpha_{V\omega} = \frac{(x - e_0)}{\sqrt{R^2 - {e_0}^2 - ax^2}}$$

and

$$\tan\alpha = 2ax$$

this latter is the angular coefficient of the straight line tangent to the contact surface corresponding to the derivative of the parabolic function ax^2.

Simplifying the above expression (1.4), equation (1.3) can be rewritten as:

$$\cos\alpha_{\omega j} = \frac{1}{\sqrt{1 + \left[\frac{(x - e_0) - 2ax\sqrt{R^2 - {e_0}^2 - ax^2}}{\sqrt{R^2 - {e_0}^2 - ax^2} + 2ax(x - e_0)}\right]^2}} \tag{1.5}$$

With regard to the term $\cos\alpha$ in integral (1.1), it can be written as:

$$\cos\alpha = \cos\alpha(x) = \frac{1}{\sqrt{1 + (\tan\alpha(x))^2}} = \frac{1}{\sqrt{1 + (2ax)^2}} \tag{1.6}$$

Finally, rewriting term $d\alpha_{V\omega}$ as a function of *x*:

$$d\alpha_{V\omega} = \alpha'_{V\omega}(x)dx \tag{1.7}$$

being:

$$\alpha_{V\omega} = \alpha_{V\omega}(x) = arctg\,\frac{(x - e_0)}{\sqrt{R^2 - {e_0}^2 - ax^2}} \tag{1.8}$$

one has:

$$\alpha'_{V\omega} = \frac{d}{dx}\left[arctg\,\frac{(x - e_0)}{\sqrt{R^2 - {e_0}^2 - ax^2}}\right]$$

this is a common derivative which results, after being simplified, in:

$$\alpha'_{V\omega} = \frac{\sqrt{R^2 - {e_0}^2 - ax^2} + 2ax(x - e_0)}{\left(\sqrt{R^2 - {e_0}^2 - ax^2}\right)^2 + (x - e_0)^2} \tag{1.9}$$

Thus, rewriting integral (1.1) with all components in terms of *x*, one obtains:

$$\int_{x}^{x_0}\left[\frac{\sqrt{(x-e_0)^2+\left(\sqrt{R^2-{e_0}^2}-ax^2\right)^2}}{\sqrt{1+\left[\frac{(x-e_0)-2ax\sqrt{R^2-{e_0}^2}-ax^2}{\sqrt{R^2-{e_0}^2}-ax^2+2ax(x-e_0)}\right]^2}}-\frac{\frac{V_a}{\omega}}{\sqrt{1+(2ax)^2}}\right]\frac{\sqrt{R^2-{e_0}^2}-ax^2+2ax(x-e_0)}{\left(\sqrt{R^2-{e_0}^2}-ax^2\right)^2+(x-e_0)^2}dx \tag{1.10}$$

The above equation can be simplified in the form:

$$j=\int_{x}^{x_0}\frac{\left[ax(x-2e_0)+\sqrt{R^2-e_0^2}-\frac{V_a}{\omega}\right]\left[ax(x-2e_0)+\sqrt{R^2-e_0^2}\right]}{\sqrt{1+(2ax)^2}\left[\left(\sqrt{R^2-e_0^2}-ax^2\right)^2+(x-e_0)^2\right]}dx$$

6.2 Appendix 2

Integral (34):

$$We_t = \int_0^{x_0} K_v \delta x dx \tag{34}$$

being δ defined as follows:

$$\delta = \sqrt{R^2 - (x - e_0)^2} - \sqrt{R^2 - e_0^2} + ax^2$$

equations (34) can be written:

$$e_t = \frac{K_v}{W} \int_0^{x_0} \left[\sqrt{R^2 - (x - e_0)^2} - \sqrt{R^2 - e_0^2} + ax^2 \right] x dx = \tag{2.1}$$

$$e_t = \frac{K_v}{W} \int_0^{x_0} \sqrt{R^2 - (x - e_0)^2}\, x dx - \int_0^{x_0} \sqrt{R^2 - e_0^2}\, x dx + \int_0^{x_0} ax^3 x dx = \tag{2.2}$$

Development of the first term:

$$e_t = \frac{K_v}{W} \int_0^{x_0} \sqrt{R^2 - (x - e_0)^2}\, x dx \tag{2.3}$$

Rewriting only the integral as:

$$\int_{-e_0}^{y_0} \sqrt{R^2 - y^2}\, (y + e_0) dy \tag{2.4}$$

where:

$$y = x - e_0$$

Using the technique of integration by parts, one gets:

$$\frac{1}{2} \left[\left(R^2 arcsen \frac{y}{R} + y\sqrt{R^2 - y^2} \right) (y + e_0) \right]_{-e_0}^{y_0} - \frac{1}{2} \int_{-e_0}^{y_0} \left(R^2 arcsen \frac{y}{R} + y\sqrt{R^2 - y^2} \right) dy \tag{2.5}$$

The solution of the first terms is then:

$$\frac{(y_0 + e_0)}{2} R^2 arcsen \frac{y_0}{R} + \frac{(y_0 + e_0)}{2} y_0 \sqrt{R^2 - y_0^2} \tag{2.6}$$

Rewriting remaining integrals as:

$$-\frac{1}{2} \int_{-e_0}^{y_0} R^2 arcsen \frac{y}{R} dy - \frac{1}{2} \int_{-e_0}^{y_0} y\sqrt{R^2 - y^2}\, dy \tag{2.7}$$

for the first term:

$$-\frac{1}{2} \int_{-e_0}^{y_0} R^2 arcsen \frac{y}{R} dy \tag{2.8}$$

using the following change of variable:

$$z = \frac{y}{R} \tag{2.9}$$

$$dz = \frac{1}{R} dy$$

one obtains:

$$-\frac{1}{2} R^3 \int_{-\frac{\varepsilon_0}{R}}^{z_0} arcsenz dz \tag{2.10}$$

this is a common integral which results in:

$$-\frac{1}{2} R^3 \left[z arcsenz + \sqrt{1 - z^2} \right]_{-\frac{\varepsilon_0}{R}}^{z_0} \tag{2.11}$$

Rewriting equation (2.11) using the change of variable (2.9),

$$-\frac{1}{2} R^3 \left[\frac{y}{R} arcsen \frac{y}{R} + \sqrt{1 - \left(\frac{y}{R} \right)^2} \right]_{-e_0}^{y_0}$$

being:

$$arcsen(-x) = -arcsenx$$

one gets the following solution:

$$-\frac{1}{2} R^2 y_0 arcsen \frac{y_0}{R} - \frac{1}{2} R^2 \sqrt{R^2 - {y_0}^2} + \frac{1}{2} R^2 arcsen \frac{e_0}{R} + \frac{1}{2} R^2 \sqrt{R^2 - {e_0}^2} \tag{2.12}$$

With regard to the second term of the integral (2.7)

$$-\frac{1}{2} \int_{-e_0}^{y_o} y \sqrt{R^2 - y^2} dy$$

the above integral has the following known solution:

$$\frac{1}{6} \left(R^2 - {y_0}^2 \right) \sqrt{R^2 - {y_0}^2} - \frac{1}{6} \left(R^2 - {e_0}^2 \right) \sqrt{R^2 - {e_0}^2} \tag{2.13}$$

thus, collecting terms (2.6), (2.12) and (2.13) one obtains solution of integral (2.4):

$$\frac{(y_0 + e_0)}{2} R^2 arcsen \frac{y_0}{R} + \frac{(y_0 + e_0)}{2} y_0 \sqrt{R_2 - {y_0}^2} - \frac{1}{2} R^2 y_0 arcsen \frac{y_0}{R} - \frac{1}{2} R^2 \sqrt{R^2 - {y_0}^2} + \frac{1}{2} R^2 arcsen \frac{e_0}{R} + \frac{1}{2} R^2 \sqrt{R^2 - {e_0}^2} + \frac{1}{6} \left(R^2 - {y_0}^2 \right) \sqrt{R^2 - {y_0}^2} - \frac{1}{6} \left(R^2 - {e_0}^2 \right) \sqrt{R^2 - {e_0}^2} \tag{2.14}$$

Development of the second term in equation (2.2):

$$-\int_0^{x_0}\sqrt{R^2-{e_0}^2}\,x\,dx$$

this is a common integrals which results in:

$$-\sqrt{R^2-{e_0}^2}\,\frac{{x_0}^2}{2} \tag{2.15}$$

Finally, last term of equation (2.2)

$$\int_0^{x_0} ax^3\,dx$$

it gives the following solution:

$$a\,\frac{{x_0}^4}{4} \tag{2.16}$$

the above solution can be rewritten as:

$$\frac{{z_0}^2}{4a} \tag{2.17}$$

being:

$$z = z_0 - ax^2$$

Thus, rewriting the equation (2.2) with all solutions found, one obtains:

$$e_t = \frac{K_v}{W}\left[\begin{array}{l}\frac{(y_0+e_0)}{2}R^2 arcsen\frac{y_0}{R}+\frac{(y_0+e_0)}{2}y_0\sqrt{R^2-y_0^2}-\frac{1}{2}R^2 y_0 arcsen\frac{y_0}{R}-\frac{1}{2}R^2\sqrt{R^2-{y_0}^2}+\\ \frac{1}{2}R^2 arcsen\frac{e_0}{R}+\frac{1}{2}R^2\sqrt{R^2-{e_0}^2}+\frac{1}{6}\left(R^2-{y_0}^2\right)\sqrt{R^2-{y_0}^2}-\frac{1}{6}\left(R^2-{e_0}^2\right)\sqrt{R^2-{e_0}^2}-\\ \sqrt{R^2-{e_0}^2}\,\frac{{x_0}^2}{2}+\frac{{z_0}^2}{4a}\end{array}\right]$$

Changing the variable *y* with *x* ($y = x - e_0$), the above equation can be simplified by grouping similar terms to get:

$$e_t W = K_v\left\{\begin{array}{l}\frac{1}{2}e_0R^2\left[arcsen\frac{x_0-e_0}{R}\,arcsen\frac{e_0}{R}\right]+\frac{\sqrt{R^2-(x_0-e_0)^2}}{3}\left[(x_0-e_0)\left(x_0+\frac{e_0}{2}\right)-R^2\right]+\\ \frac{\sqrt{R^2-{e_0}^2}}{3}\left[R^2+\frac{{e_0}^2}{2}-\frac{3{x_0}^2}{2}\right]+\frac{{z_0}^2}{4a}\end{array}\right\}$$

6.3 Appendix 3

Measured and simulated drawbar pull (Figs. 59-64)

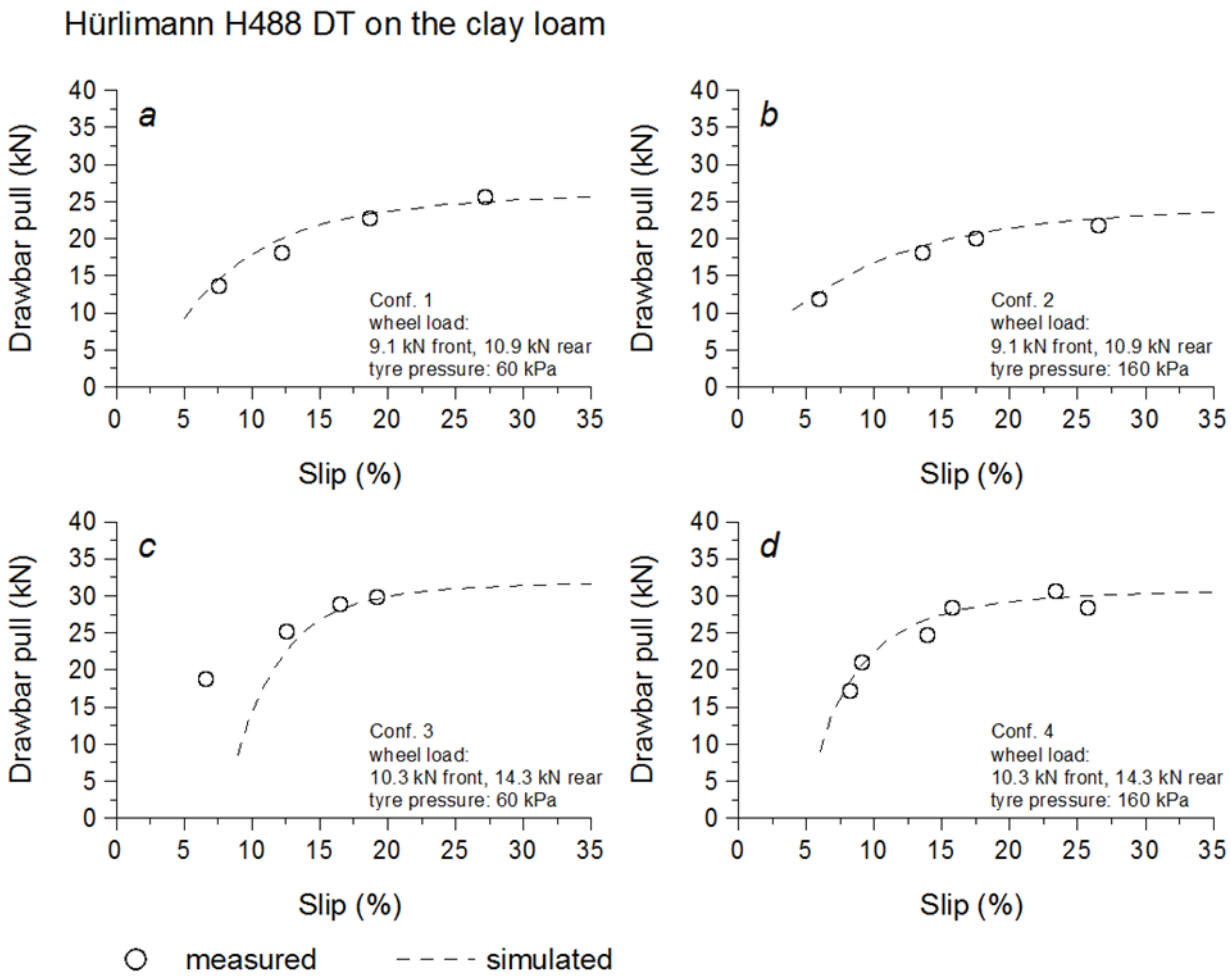

Fig. 59: Measured and simulated drawbar pull of tractor A on the clay loam.

Hürlimann H488 DT on the silty loam

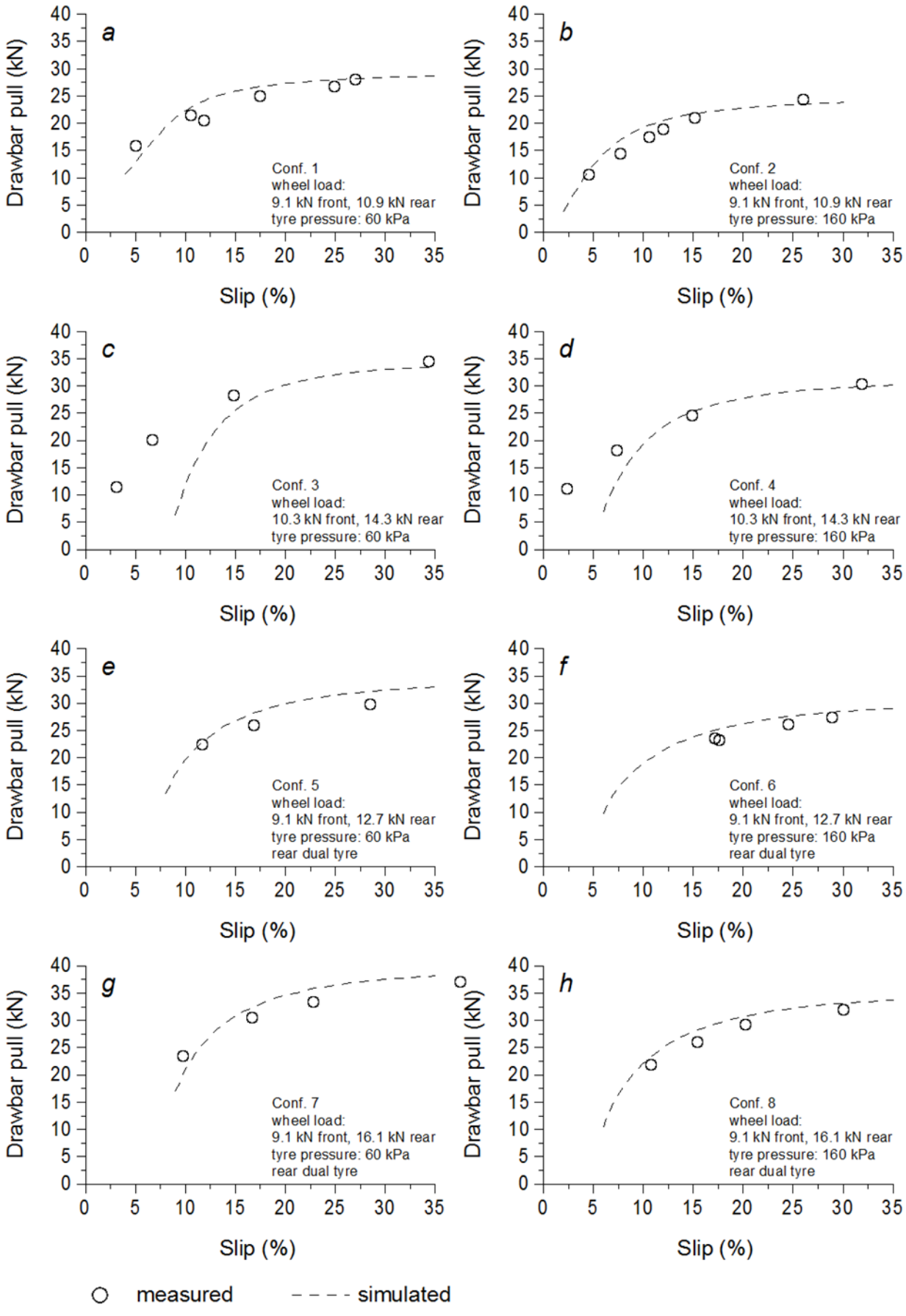

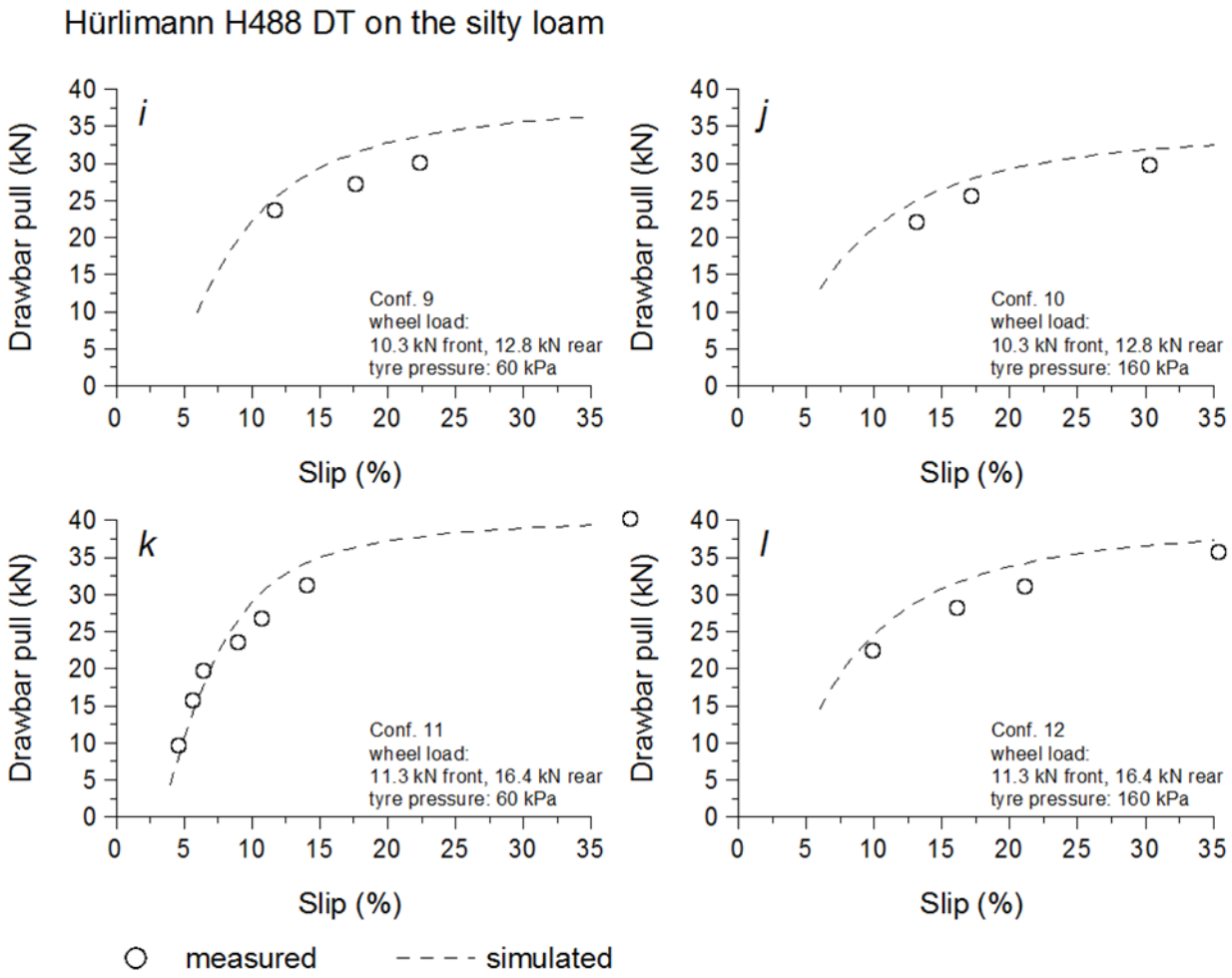

Fig. 60: Measured and simulated drawbar pull of tractor A on the silty loam.

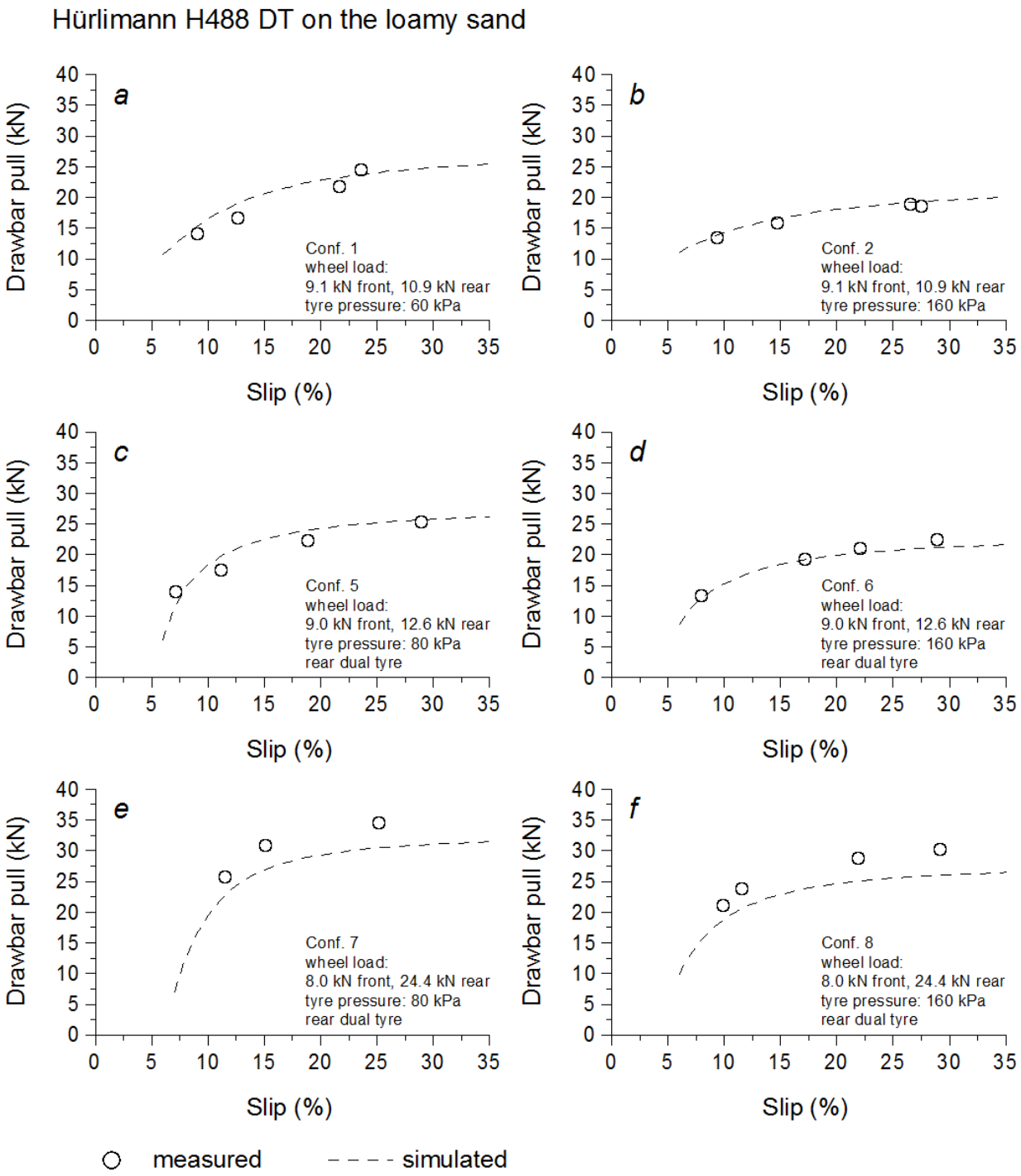

Fig. 61: Measured and simulated drawbar pull of tractor A on the loamy sand.

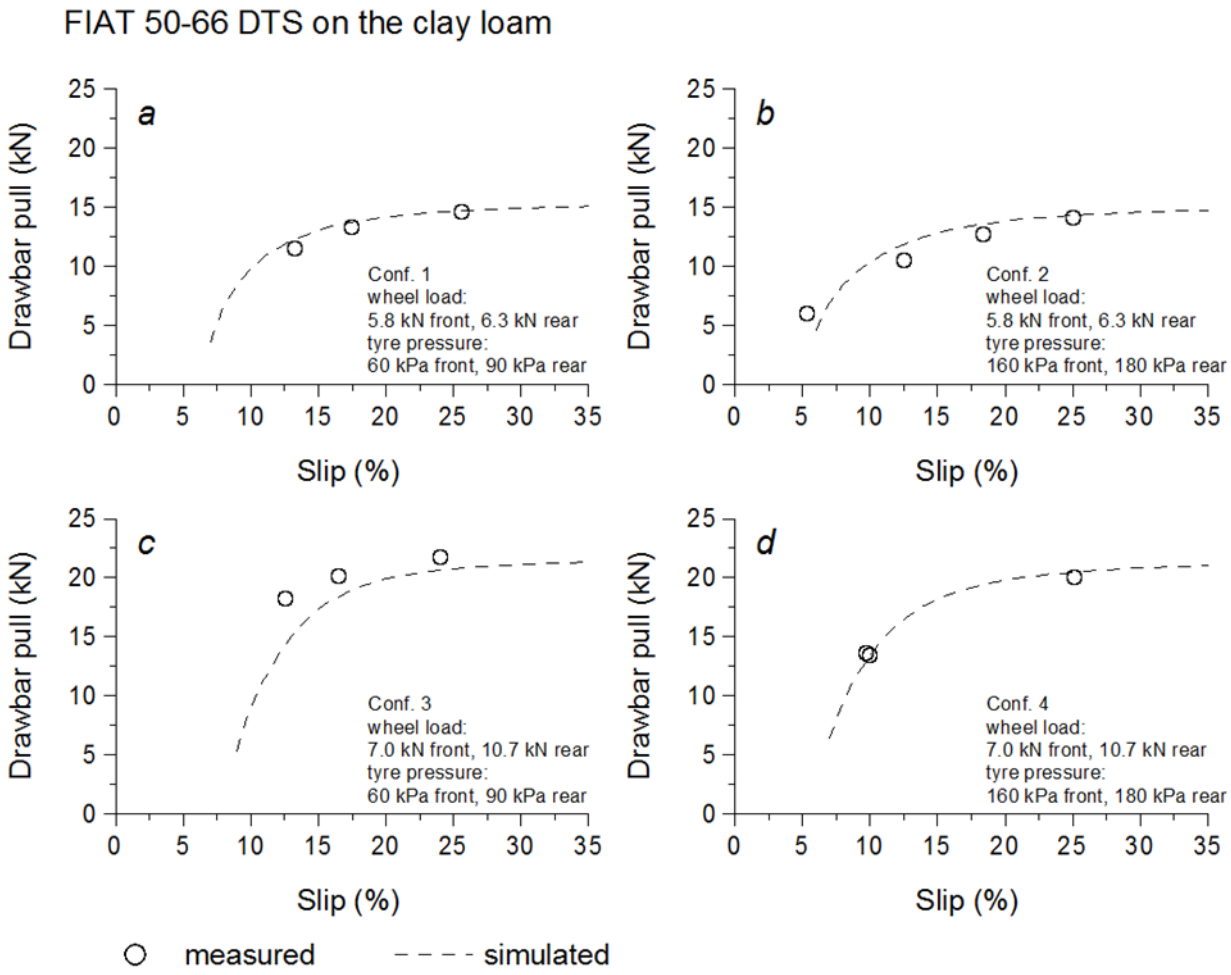

Fig. 62: Measured and simulated drawbar pull of tractor B on the clay loam.

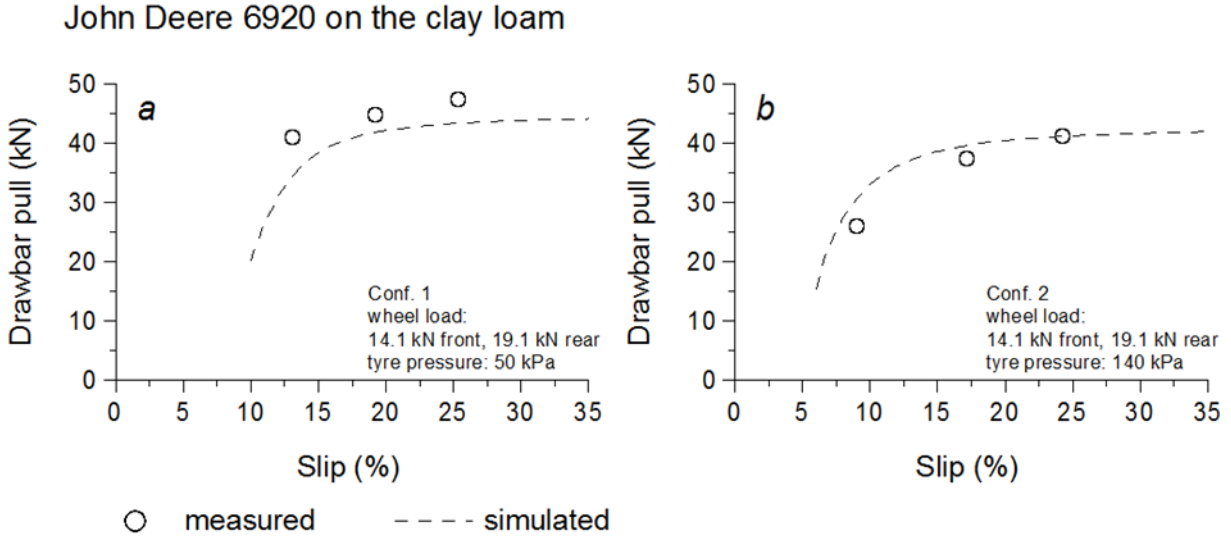

Fig. 63: Measured and simulated drawbar pull of the tractor C on the clay loam.

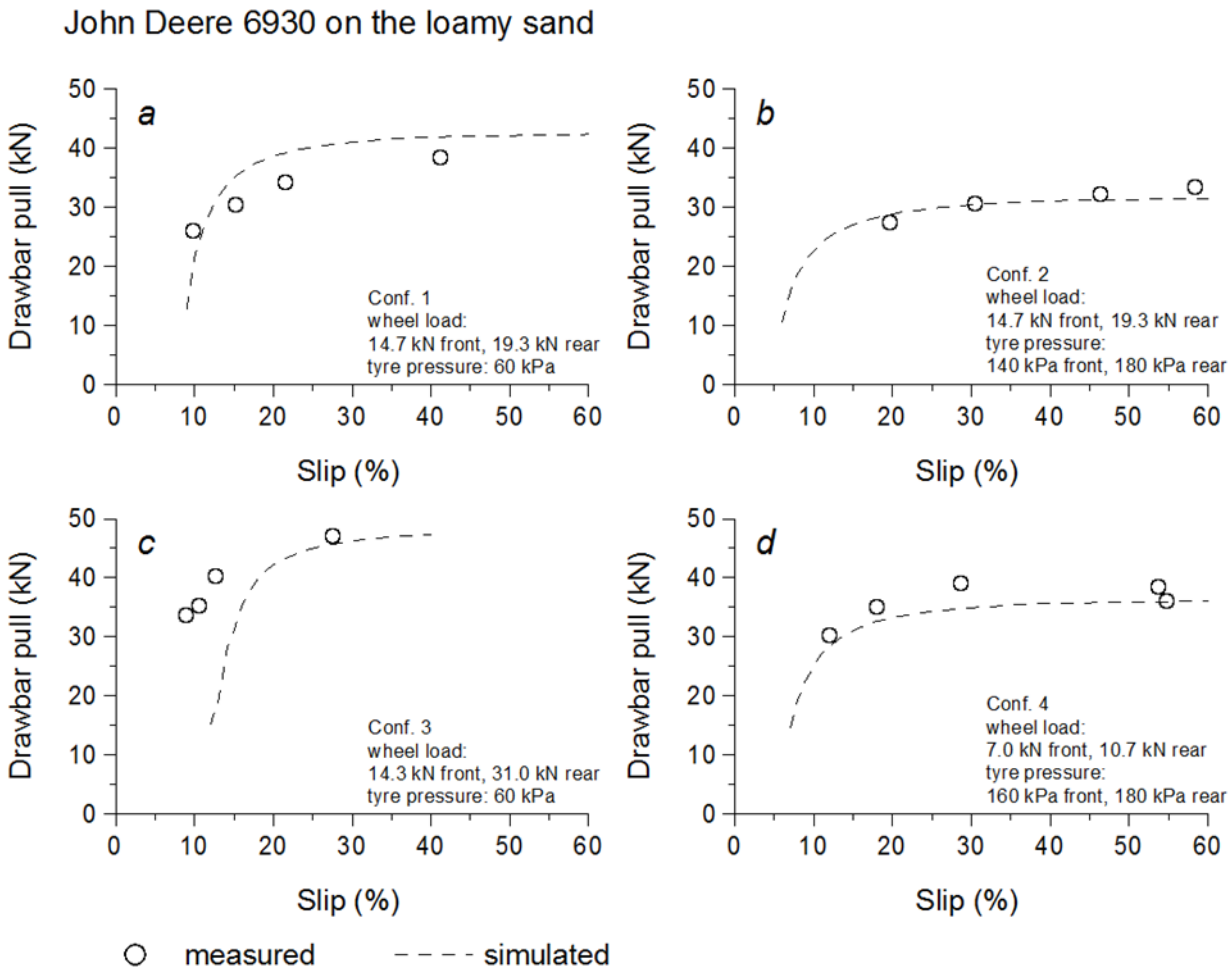

Fig. 64: Measured and simulated drawbar pull of tractor D on the loamy sand.